Dublin City University

School of Physical Sciences

Growth and chemical characterisation studies of Mn silicate barrier layers on SiO_2 and CDO

Justin Bogan B.Sc

Doctor of Philosophy

February 2012

Supervised by Professor Greg Hughes

Dedications and Acknowledgements

Firstly, I would like to thank my supervisor Greg Hughes, for the help, support, knowledge and respect he has given me throughout my years in DCU. I cannot thank him enough for the opportunities he has given me.

From DCU, I would like to thank everyone in the Surface and Interfaces Research Group for all of their help over the past 4 years; to Paddy, Rob, Barry, Anthony, Lee, Lalit, Rajesh, Stephen and Kumar. All of you make coming into college every day a pleasure. Special thanks go to Juan Lozano in University of Oxford for all his TEM images and analysis. Many thanks also to Pat Wogan and Des Lavelle for all of their help on the technical side of things.

Thank you to all my friends in Dublin; especially Declan, Mike, Davey, Brian, Ann-Marie and Niamh for their friendship and support throughout the years.

I would like to acknowledge Science Foundation Ireland for the financial support of this work.

Finally, I would like to thank my parents for all they have done for me throughout my life. I thank them for showing me the value and importance of education and I dedicate this thesis to them.

Declaration

I hereby certify that this material, which I now submit for assessment on the programme of study leading to the award of doctor of Philosophy is entirely my own work, that I have exercised reasonable care to ensure that the work is original, and does not to the best of my knowledge breach any law of copyright, and has not been taken from the work of others save and to the extent that such work has been cited and acknowledged within the text of my work.

Signed: _____ (Candidate)

ID No.: 53340589

Date: _____

Abstract

This thesis investigates the suitability of manganese silicate ($MnSiO_3$) as a possible copper interconnect diffusion barrier layer on both a 5.4 nm thick thermally grown SiO_2 and a low dielectric constant carbon doped oxide (CDO), with the focus of understanding the barrier formation process. The self forming nature of this diffusion barrier layer resulting from the chemical interaction of deposited Mn with the insulating substrate has potential application in future generations of copper interconnect technologies as they are significantly thinner than the conventional deposited barrier layers. The principle technique used to study the interface chemistry resulting from the interaction of deposited manganese with the insulating substrates to form a $MnSiO_3$ layer was x-ray photoelectron spectroscopy (XPS). Transmission electron microscopy (TEM) measurements provided information on the structure of the barrier layers which could be correlated with the XPS results. Significant differences in the extent of the interface interaction which resulted in the formation of the $MnSiO_3$ barrier layer were found to depend on whether the deposited Mn was partially oxidised. The studies performed on the 5.4 nm thermally grown SiO_2 confirmed that the growth of the $MnSiO_3$ resulted in a corresponding reduction in the SiO_2 layer thickness. Interactions between residual metallic Mn and subsequently deposited copper layers were also investigated and showed that in order to reduce the width of the barrier layer, it was preferable that all the deposited Mn was fully incorporated into the silicate. TEM measurements were also used to investigate thicker thermally deposited Mn/Cu heterostructures on SiO_2 which were subsequently annealed in order to study the diffusion interactions between copper and manganese. The formation of Mn silicate layers on low dielectric constant carbon doped oxide (CDO) was also investigated and compared with the formation characteristics on the thermally grown SiO_2.

Publications arising from this work

Barrier behaviour and interdiffusion in thermally evaporated Mn/Cu heterostructures onto SiO_2 substrates

J. G. Lozano, J. Bogan, B. Brennan and G. Hughes

Applied Physics Letters **98**, (2011)123112

Synchrotron radiation photoemission study of in-situ manganese silicate formation on SiO_2 for barrier layer applications

Patrick Casey, Barry Brennan, Justin Bogan and Greg Hughes.

Applied Physics Letters **98**, (2011) 113508.

Chemical and structural investigation of the role of both metallic manganese and manganese oxide in the formation of manganese silicate barrier layers on SiO_2

P.Casey, J. Bogan, J.G Lozano, P.D. Nellist, G. Hughes.

Journal of Applied Physics **110,** (2011) 054507

Photoemission study of carbon depletion from ultra low-κ carbon doped oxide surfaces during the growth of Mn silicate barrier layers

P.Casey , J. Bogan, G. Hughes,

Journal of Applied Physics, *Accepted for publication November 2011.*

Conference Proceedings

Interdiffusion in Cu/Mn based barrier layers for copper interconnects.

Justin Bogan, Juan G. Lozano, Barry Brennan and Greg Hughes

18th Interdisciplinary Surface Science Conference (ISSC-18) (4th-7th April 2011)

Awarded best student poster at conference.

Manganese based Diffusion Barriers for Cu Interconnects

Justin Bogan, Patrick Casey, Juan Lozano and Greg Hughes, Intel ERIC conference 12th-14th October 2010, Leixlip, Co.Kildare, 13th Oct 2010

Barrier layer formation and interdiffusion in Cu/Mn heterostructures for interconnect technologies

J.G. Lozano, J. Bogan, B. Brennan, P.D. Nellist and G. Hughes, IMC17 Sept 2010.

(S)TEM analysis of the interdiffusion and barrier layer formation in Mn/Cu heterostructures on SiO_2 for interconnect technologies

J. G. Lozano, S. Lozano-Perez, J. Bogan, Y.C. Wang, B. Brennan, P. D. Nellist and G. Hughes

EMAG 2011 - Quantifying the Nanoworld - Electron Microscopy and Analysis Group Conference - 6–9 September 2011, Birmingham, UK

Chemical and structural investigation of the formation of manganese silicate copper diffusion barrier layers on SiO_2

Bogan Justin , Casey Patrick, Brennan Barry, Lozano Juan, Nellist Peter, Hughes Greg

Intel ERIC 2011 12th – 14th Oct 2011 Leixlip, Dublin.

Table of Contents

Table of Figures

Chapter 1

Introduction

This chapter serves as a brief introduction to the main topics covered in the thesis. The focus of this study is to investigate and characterise the chemical and structural properties of interface formation between manganese/copper films and various dielectric substrates. This will give an insight into the factors that could influence the potential use and integration of manganese silicate as a self-forming interconnect barrier layer into the next generation of high speed semiconductor devices. In this chapter, the history and importance of interconnects within the modern integrated circuit (IC) will be reviewed. The challenges facing the semiconductor industry in interconnect processing, and how new materials may be used to find solutions to these problems, are then discussed.

1.1 Interconnect Overview

Integrated circuit device fabrication can be divided into two main processing sections; front-end-of-line (FEOL) and back-end-of-line (BEOL). FEOL is concerned with the formation of individual logic devices (transistors, capacitors, resistors) patterned on a semiconducting substrate. After the final FEOL step, there are as many as ~1×10^9 isolated transistors per microprocessor device. The back-end-of-line is concerned with connecting these devices together in a meaningful way. This process involves fabricating metal wires (interconnects) surrounded by insulating dielectric layers. The function of these interconnects is to distribute clock and other signals, and to provide power/ground connections, to the various circuit/system functions on the chip. Shown

in Figure 1.1 is a schematic diagram of a typical microprocessor with a hierarchical wiring approach for multilevel interconnects. In 2011, advanced microprocessors from the 32nm technology node from the International Technology Roadmap for Semiconductors (ITRS) may consist of 10 or more layers of metallisation [**1**]. The following section will discuss the development of these metal layers.

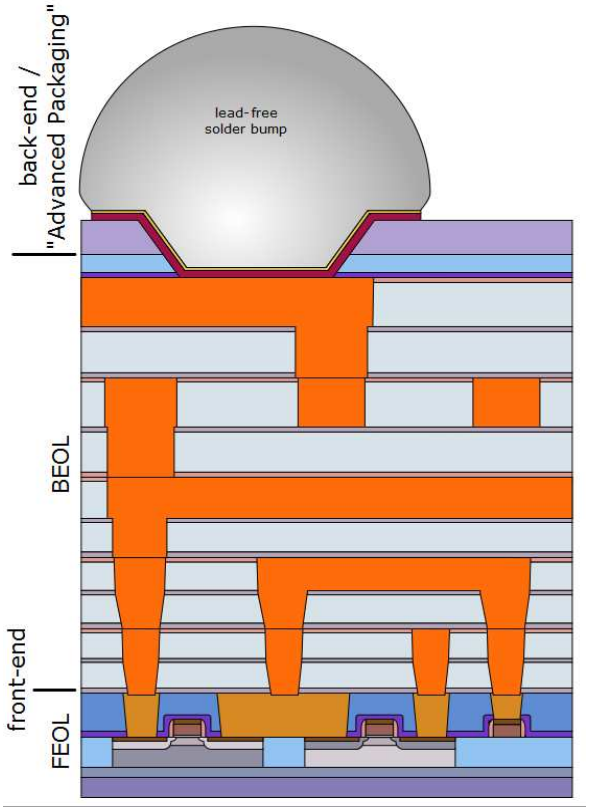

Figure 1.1: Schematic diagram of a microprocessor with a hierarchical wiring approach for multilevel interconnects

Historically, aluminium (Al) has been used as the interconnect metal because of its relatively low resistivity (2.7$\mu\Omega$/cm). Also, it can be easily deposited through either sputtering or vapour deposition, and the photoresist masking/plasma etching processes used to pattern aluminium are well known. Silicon dioxide (SiO_2) was used as the inter-

layer dielectric (ILD) material as it was very well characterised and easy to deposit/etch. However, diffusion of the aluminium into the surrounding dielectric has been a problem since the fabrication of the first IC in 1959 [**2**].

Silicon is soluble in aluminium as shown in the phase diagram in Figure 1.2 and hence will migrate into the aluminium contact when the chip is in operation. The aluminium can then diffuse into the voids left by the movement of the silicon. This movement of the interconnect material causes spiking which results in large leakage current and creation of an open circuit in the device. Initially this problem was addressed by doping the aluminium with a small amount of silicon which prevented further silicon from migrating into the wire. This became the basis for IC metallisation until 1983. By that time the technology had moved into the 2µm node and the contact resistance and leakage became too high once more and it became impossible to balance the aluminium spiking via silicon doping. The solution to this problem became the introduction of a physical barrier layer between the aluminium and the silicon.

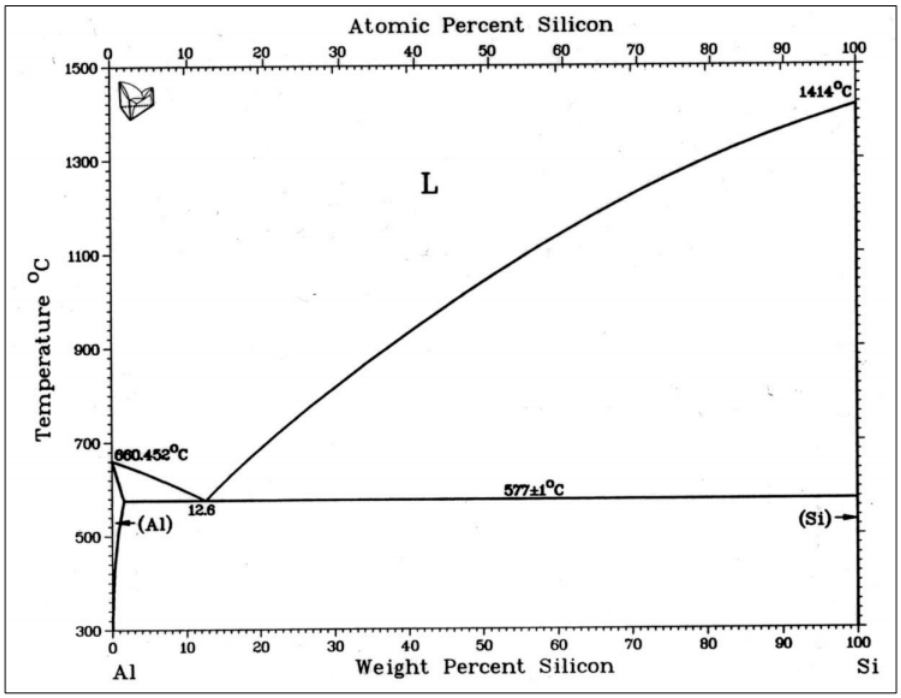

Figure 1.2: Al/Si Phase diagram [3]

Initially, titanium (Ti) was used as the barrier material because like aluminium, it was well understood and, because it is highly reactive it formed a good contact between the aluminium and the SiO_2. This Ti barrier worked for a time but soon the interaction of the titanium with the aluminium became a problem as the Ti was used up in the formation of $TiAl_3$ and the barrier properties of the film were lost. This problem was solved by the introduction of a further barrier layer of TiN on top of the initial Ti barrier. This titanium nitride layer was used because it was very unreactive and easy to form via the introduction of nitrogen during Ti deposition. This combination of aluminium interconnects, silicon dioxide insulators, and Ti/TiN barrier layers effectively solved the problem of interconnect contact reliability up to the 250nm technology node. However, in 1997, IBM announced the first copper based microchip; referring to the replacement of the aluminium interconnects with wires made from copper. This was hugely relevant as the idea of using copper as the interconnect material was something that had eluded chip manufacturers for decades [**4**].

1.1.1 Why copper?

Over the past two decades, the overall speed of integrated circuits has increased considerably. This increase has typically been made possible through advances in lithography processes in FEOL manufacturing making it possible to create smaller and smaller transistor channel lengths, allowing manufacturers to fit more devices on a single die. This increase in the number of features naturally improves performance, while also decreasing the gate switching delay due to the transistors being physically closer together on the chip. However, as the transistor gate delay decreases, other factors in the device begin to have a larger impact on speed. With gate miniaturisation, the interconnect delay increases due to increased wire density which results in smaller wires which carry less current, and have an increased electrical resistivity. This delay is due to both resistance of the conducting metal line, and the capacitance between adjacent lines surrounded by the dielectric. The product of the resistance and the

capacitance is known as the RC time constant and the intrinsic speed limit of the IC is now determined by this factor [**5**][**6**] as illustrated in Figure 1.3.

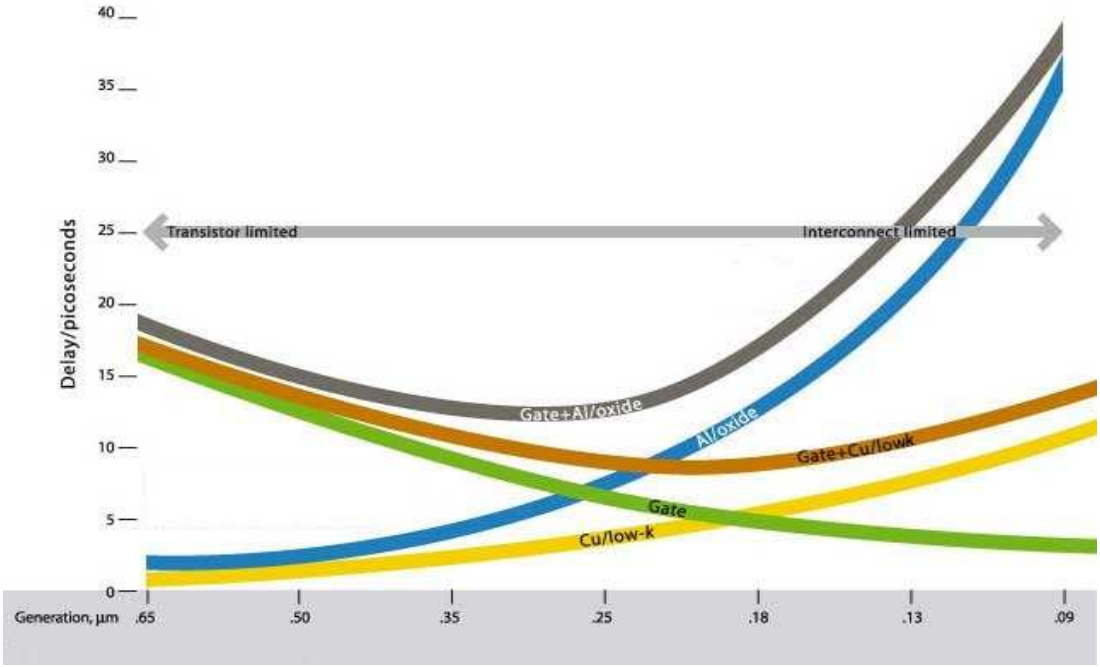

Figure 1.3: RC delay as a function of the gate length. The gate delay can be simply reduced by shorter feature size. The interconnect delay (RC delay) starts to dominate the overall delay at shorter feature size [7].

The resistance (R) of a typical interconnect line shown in Figure 1.4 is expressed by Equation 1.1. It is determined by both the resistivity of the material and the geometry of the device.

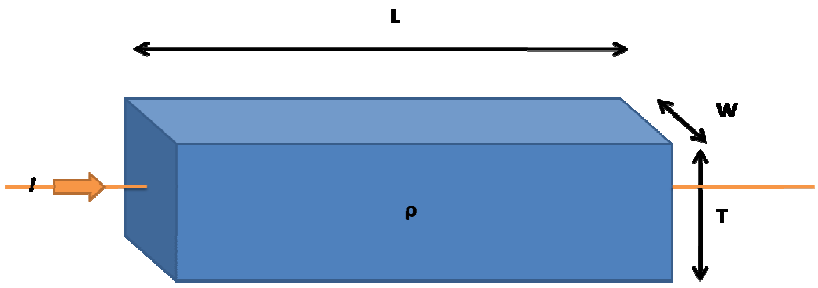

Figure 1.4: Basic resistive structure, where R=resistance, ρ=resitivity of material, L,W,T are the length, width and thickness of material

$$R = \frac{\rho L}{WT} \tag{1.1}$$

Similarly, the capacitance (C) between two interconnect lines surrounded by dielectric is shown in Figure 1.5 and expressed by Equation 1.2. The capacitance is again dependent upon the geometry and the relative permittivity of the dielectric.

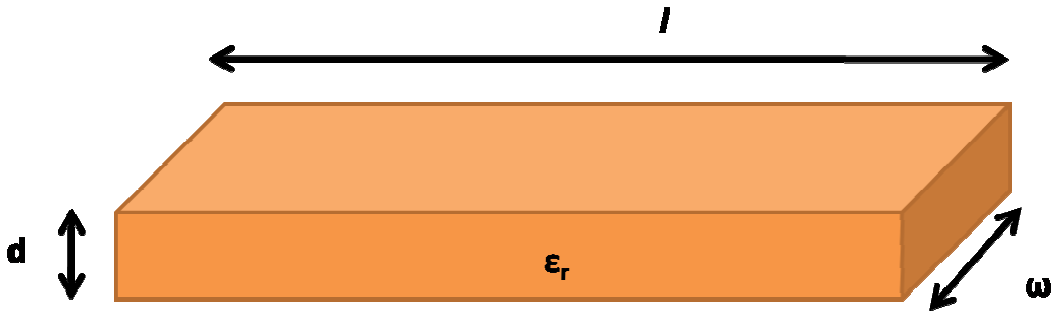

Figure 1.5: Basic capacitive structure where, ε_0=permittivity of free space, ε_r=relative permittivity of the dielectric material and l,w,d are length, width, and distance between plates

$$C = \frac{\varepsilon_0 \epsilon_r lw}{d} \tag{1.2}$$

The RC time constant of a typical multilayered interconnect stack illustrated in Figure 1.6 can be calculated as:

$$R_w C_w = 2R_w(C_V + C_L)$$

$$= \frac{2\rho L}{WT}\left(\frac{\varepsilon_0 \varepsilon_r WL}{H} + \frac{\varepsilon_0 \varepsilon_r TL}{X}\right) \tag{1.3}$$

$$= 2\rho\varepsilon_0\varepsilon_r \frac{L}{WT}\left(\frac{WL}{H} + \frac{TL}{X}\right)$$

$$= 2\rho\varepsilon_0\varepsilon_r \left(\frac{L^2}{TH} + \frac{L^2}{WX}\right)$$

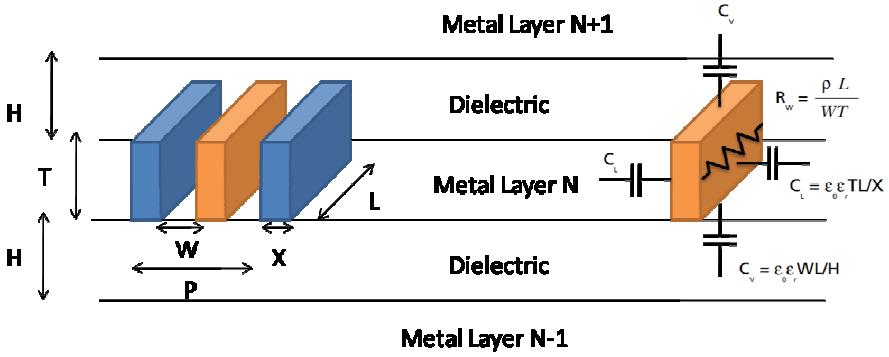

Figure 1.6: Typical multilayer interconnect stack illustrating the various capacitances to be accounted for when calculating the RC time constant.

Where:

R_w = Resistance of the interconnect

$C_{w=}$ Capacitance associated with the interconnect

C_V = Inter-layer capacitance

C_L = Intra-layer capacitance

L = Length of the interconnect

W = Width of the interconnect

T = Thickness of the metal layer

H = Height of the dielectric layer

X = Spacing between adjacent interconnects

P = Pitch of the line

If it is assumed that the height of the interconnect is equal to the height of the dielectric layer (T=H) and that the spacing between adjacent interconnects is equal to the width of the interconnects (W=X=P/2), then the equation may be further simplified to

$$R_w C_w = 2\rho\varepsilon_0\varepsilon_r L^2\left(\frac{1}{T^2}+\frac{4}{P^2}\right) \tag{1.4}$$

This shows that the RC time constant and hence the overall chip delay can be reduced by either reducing the resistivity of the interconnect material, using a dielectric with a lower permittivity, or shortening the interconnect line lengths. The last of these three is not an option, as it is the increase in overall interconnect length due to miniaturisation which causes the increasing delay in the first place. The use of low-k dielectric materials as insulating layers reducing capacitance is viable, and will be discussed further at the end of this chapter. Still, the most favourable choice is the reduction of the interconnect resistivity by replacing the aluminium with a different material.

However, considering that aluminium is already an excellent conductor somewhat limits the choice of replacement materials. Gold, silver and copper are some of the few metals which display a higher electrical conductivity. However, copper (Cu) proves to be the clear choice as both gold and silver are far too expensive for large scale integration. The electrical conductivity of copper is 5.9×10^7 S/m; roughly 1.5 times the conductivity of aluminium, resulting in the resistivity of copper (1.7μ**Ω**/cm) being approximately 40% less than that of aluminium (2.7μ**Ω**/cm) [**8**]. Hence, as the RC time constant is directly proportional to the resistivity, a ~40% decrease in overall delay can be achieved by using copper rather than aluminium.

Added advantages to using copper include the fact that copper has twice the thermal conductivity of aluminium and offers higher reliability due to its higher melting point

(1085 vs. 660 °C for Al) making it significantly more resistant to electromigration. Electromigration can be defined as the process by which a metal conductor changes shape under the influence of the electric current flowing through it. In a circuit, if the electron current density is sufficiently high, an "electron wind" effect is created within the conductor. Although the size, mass and consequent momentum of an electron is very small compared to an atom, if enough electrons collide with an atom it will eventually move, especially if the atom is at the edge of a grain boundary and not held in place very tightly. As one atom is moved due to the electron bombardment the remaining current flowing through the line is pushed through a smaller area putting more pressure on the remaining atoms of the grain which are not so tightly bound. The result is that these atoms then also get pushed away. This may lead to decreased performance and a potential open circuit along the conducting line as shown in Figure 1.7

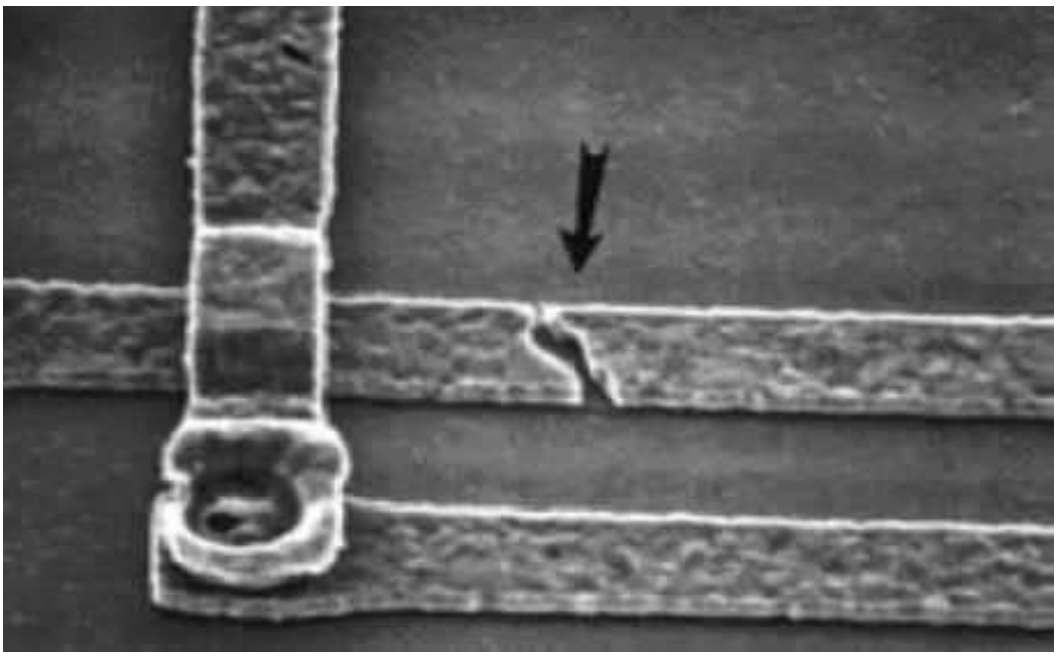

Figure 1.7: Effects of Electromigration on a metal track in an IC [9].

This proved to be another problem with aluminium interconnects of the past. As aluminum is a relatively light atom, the current density was enough to move the interconnect material causing unintended electrical connections known as hillocks within

the circuit and shorting the line. The old solution to this problem was the addition of titanium shunt layers which rerouted the current if a void did occur. In contrast to aluminium, copper atoms are strongly bound together [**10**], which accounts for it being far less likely to form hillocks when compared to Al.

However, although copper possesses multiple advantages over aluminium in terms of interconnect performance, major challenges exist in terms of its implementation in semiconductor processing. As stated previously, chip manufacturers had long recognized the benefits in using copper, but the transition to it only occurred after solutions were found to various processing problems. The traditional subtractive aluminium interconnect process, consisting of photoresist masking and plasma etching could not be used as there were major difficulties in etching copper due to the fact that it requires much higher temperatures to form the volatile compounds used in the etching process. Also, unlike aluminium, copper could not be efficiently deposited via chemical vapour deposition. For these reasons industry needed to develop a completely new process in order to introduce copper into the microprocessor interconnects. The development of the damascene and dual-damascene processes allowed copper to be deposited on a pre-patterned dielectric via electroplating eliminating the need for etching of copper.

The remaining reason which initially prohibited the use of copper as an interconnect metal was its interaction with both silicon and the dielectric insulating materials used in back end processing. The next section will discuss this, and the increased importance of the diffusion barrier layers.

1.2 Research Motivation - The need for a new barrier material

Despite the advantages of Cu, there exists a serious diffusion problem with copper if it is deposited directly on silicon (Si). Cu reacts with silicon and silicon dioxide at low temperatures [**11**] and is a fast diffuser in these materials due to its relatively high mobility. The diffusivity of Cu in Si ranges from 5×10^{-5} to $5\times10^{-4}cm^2s^{-1}$ with activation energy E_a of about 1.0 eV for temperature range from 900 to 1300° C, while the diffusivity for Al ranges from 1×10^{-14} to $4\times10^{-10}cm^2s^{-1}$ -with activation energy E_a of about 3.4 eV for the same temperature range. These high diffusion rates of elemental copper have required the further development of the physical barriers between dielectric and interconnect to prevent interdiffusion across the interface as Cu diffusion into the silicon will degrade device performance by introducing deep electronic levels into the Si band gap resulting in the reduction in minority carrier lifetime [**12**]. Furthermore, the formation of Cu-Si compounds affects the reverse leakage current of p-n junctions.

A number of criteria must be met in the selection of a barrier material. The optimal barrier needs to limit copper diffusivity, be conformal, adhere to both copper and dielectric, exhibit resistance to mechanical stresses and most importantly have low resistivity. The barrier layers currently used to fulfil this function are composed of a $Cu/Ta/TaN/SiO_2$ layered structure shown in Figure 1.8, as the Ti/TiN barrier layers used for Al are no longer effective as a barrier against copper due to the formation of a bulk alloy between the Cu and Ti. However, as device geometry continues its downward trend, there is a need to develop a scalable barrier layer technology alternative, to the Ta/TaN layers as they tend to have poor electrical conductivity and exhibit poor adhesion to the copper necessitating the use of a copper seed layer. Also, as device miniaturisation continues the thickness of the barrier region becomes more important. Too thick a barrier and the overall barrier metal/copper film will have a greater total

resistance than aluminium interconnects, eliminating any benefit. For this reason the barrier layer should be as thin as possible.

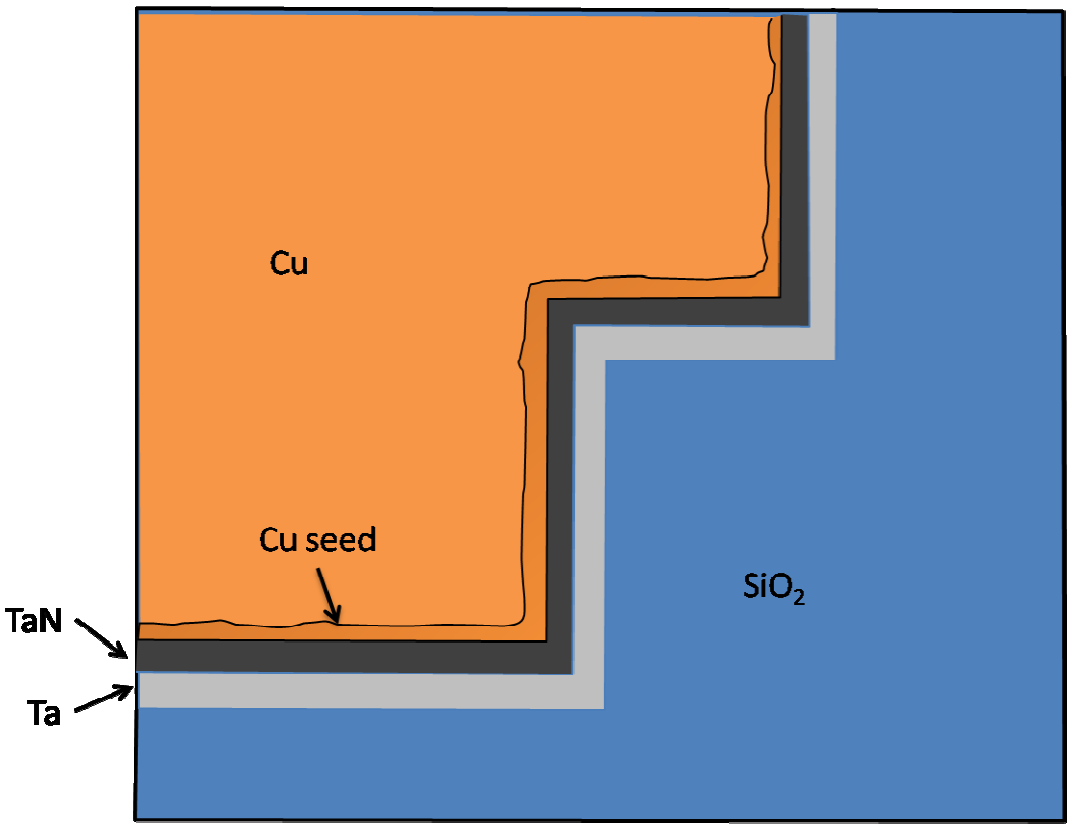

Figure 1.8: Current technology using Ta/TaN barriers. [13]

Furthermore, while all current barrier layer deposition strategies involve physical vapour deposition (PVD) technologies, future barrier layers will have to address conformal deposition techniques such as atomic layer deposition (ALD) growth. Non-uniform coverage of side walls and trenches will eventually limit the further thickness reduction in conventional PVD barrier layer deposition. However, while ALD can deposit very thin films with uniform coverage, the slow deposition rates and reliability issues require the exploration of alternative solutions including the so called self-forming barrier process which could be a possible route to satisfying the essential requirements of barrier layer formation for future device technologies. The next section will discuss the concept of the self forming barrier as well as the choice of barrier candidate materials.

1.3 Self Forming Barrier

The idea of self-forming barrier layer involves the co-deposition of a copper/barrier metal alloy directly onto the dielectric layer. Subsequent anneals should lead to the segregation of the alloying metal to the copper/SiO_2 interface where it chemically reacts with the SiO_2 forming a thin barrier region. The methodology of this is schematically shown in Figure 1.9.

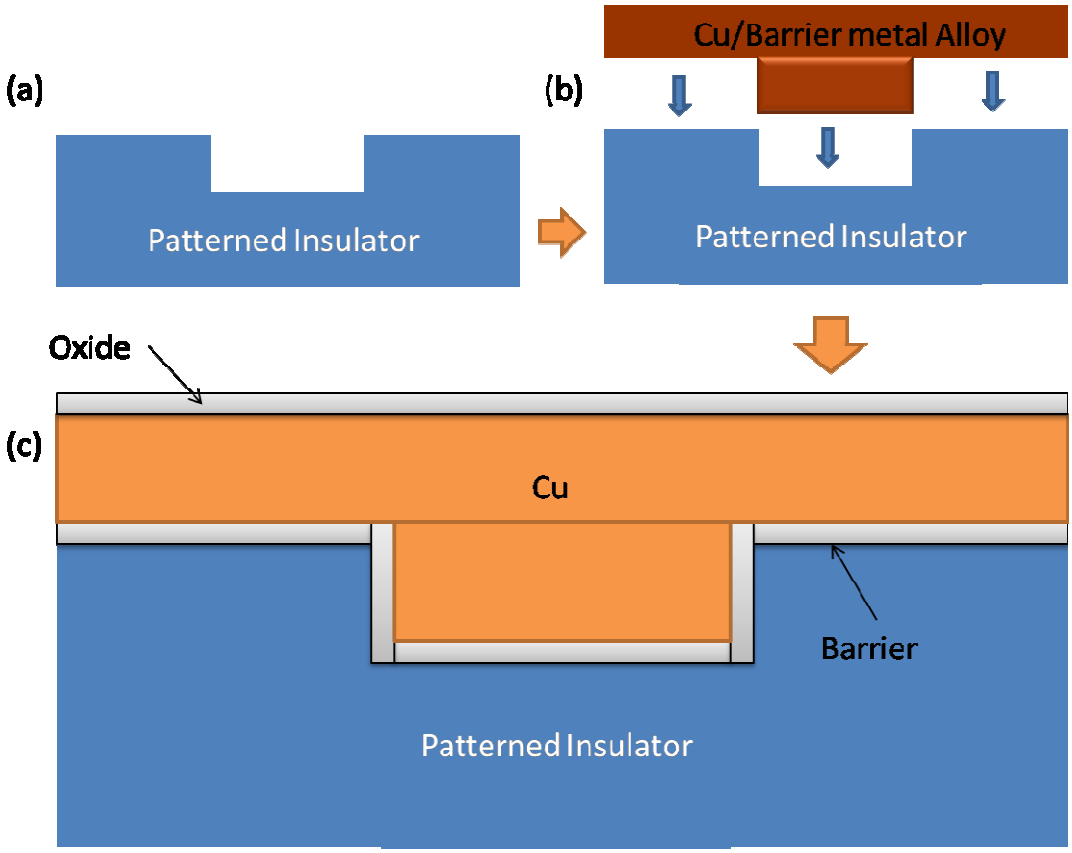

Figure 1.9: The concept of the self forming barrier.

Starting with a pre-patterned ILD (a), an alloy consisting of the copper interconnect and barrier materials is deposited (b). Upon thermal anneal the barrier metal is expelled from the copper and migrates to the ILD interface forming a stable compound which was low mobility, resulting in high purity copper in the bulk. Any residual unreacted barrier metal in the copper film may be removed from the bulk copper

through oxygen exposure during anneal resulting in a barrier metal oxide at the top surface, thereby immobilizing it. It can then be subsequently removed from the top surface by either etch or by a chemo-mechanical polishing (CMP) step. Ideally, the barrier should not occupy any of the volume reserved for Cu forming what's known as a zero-thickness barrier where the alloying material becomes completely incorporated into the dielectric. Hence, this method could also potentially solve the problem of uniform coverage of the sidewalls and trenches.

Recent publications [**14**][**15**] have suggested manganese as a suitable alloying material as its diffusivity is faster than that of copper and Cu/Mn alloy compositions have been shown to be capable of forming effective barrier layers 3-4nm thick which meets the requirements of the 2009 ITRS target barrier layer thickness for the 24nm node.

1.3.1 Why Use Manganese?

For any potential alloying metal in copper the important properties for use as an interconnect barrier are barrier effectiveness, rapid migration to the interface on annealing, stable barrier formation, adhesion to the substrate and negligible impact on the resistivity of interconnect material after barrier formation. Manganese was chosen as a possible alloying element because of its ability to satisfy most of the criteria over other potential barrier elements such as Mg and Al which have been previously explored [**16**].

With regards to barrier formation, it is essential that the alloying element will form a stable oxide barrier at the interconnect/dielectric interface. However, this reaction must happen before any diffusion of copper into the bulk can occur. The rate of atomic diffusion of Mn in Cu is faster than the self-diffusivity of Cu by an order of magnitude at 450 ° C meaning that Mn atoms are expected to migrate to the SiO_2 interface before noticeable reaction occurs between Cu and Si or SiO_2, fulfilling this criterion.

Once the alloying element reaches the interface the driving force for stable compound formation can be assessed with the heat of formation and, more accurately, with the

standard free energy of oxide formation. It has previously been reported that when magnesium is used at an alloying element in copper it rapidly forms MgO at the dielectric interface due to its relatively high standard free energy, and this is accompanied by a reduction of SiO_2 and freed Si atoms can then diffuse into the Cu layer increasing the resistivity of the copper [**16**]. Hence the standard free energy of oxide formation should be negative but not much larger than that of SiO_2. The standard free energy parameter of Mn oxide however is slightly larger than that of SiO_2, so that when manganese forms an oxide at the SiO_2 interface the reduction reaction is not expected to be as thermodynamically favourable as is the case for Mg. The most favourable reaction would be the formation of a metal silicate, which would include the barrier metal and both silicon and oxygen addressing the problem of the freed Si atoms seen in oxide formation studies using Mg as the alloying metal.

The third factor effecting the choice of barrier material is the adhesion between the interconnect and dielectric material. This is expected to become an important aspect in future technology nodes as Cu has poorer adhesion to SiO_2 than Ta and TaN [**13**] effecting the reliability of the chip. Thus, enhancing the adhesion by means of a self-forming diffusion layer is also an important issue. Moreover, the electromigration resistance was reported to be strongly related to the interfacial adhesion between the Cu interconnect and capping material. Therefore, the measurement of the adhesion of the interface between Cu and the dielectric is important in terms of electromigration as well. The adhesion of manganese to the SiO_2/Cu interface is as yet unknown and will be explored in future investigations.

Finally, as mentioned previously any increase of the resistivity of the interconnect material due to solute scattering should be minimized, because the performance is strongly related to the resistivity of the interconnect material. To ensure that the alloying material is completely expelled from the copper, the activity coefficient which is defined as a measure of chemical interaction between solute and solvent atoms in a solid solution alloy must be less than that of the interconnect material. The activity

coefficient (which is defined as the factor to account for deviations from ideal behaviour) of Mn in Cu is larger than 1, while that of Mg and Al in Cu is less than 1. This indicates that Mn can be easily expelled from Cu when a more favourable reaction can take place with an adjacent material, such as SiO_2. In contrast, Mg and Al tend to remain in Cu because of their strong chemical interaction with Cu. If Mn is expelled completely from the original Cu–Mn alloy, interconnect resistivity can potentially be reduced to the level of pure Cu.

All of these factors indicate that manganese is an ideal candidate for choice of alloying material with a view to simultaneous deposition of interconnect and barrier layer material, and the growth of a self forming barrier. Transmission electron microscopy (TEM) studies of deposited Cu/Mn alloys on SiO_2 [**14**] have shown that thin (2-3 nm) Mn silicate layers formed at the dielectric interface act as effective barriers to Cu, O and H_2O diffusion [**14**][**17**]. The work of Gordon *et al* [**18**] has reported promising electrical characteristics for Cu interconnects on Mn silicate using techniques such as sheet resistance and capacitance measurements [**18**][**19**]. However, studies using analysis techniques such as electron energy loss spectroscopy (EELS) and secondary ion mass spectroscopy (SIMS) have produced contradictory results relating to the chemical composition of the barrier layer. In particular, doubt remains over the presence of manganese oxide [**20**], Mn silicate [**18**] or both [**21**], within the Mn/SiO_2 interfacial region. In their analysis of electron energy loss spectroscopy (EELS) spectra, Koike *et al.* [**14**] first reported a Mn^{3+} valence state consistent with Mn_2O_3 being the main constituent of the barrier; while Abblet *et al.* [**22**] reported the valence state of Mn in the barrier as +2 by means of x-ray absorption near-edge spectroscopy and extended x-ray absorption fine structure, being mainly constituted of a mixture of MnO and $MnSiO_3$. A possible reason for these inconsistencies is the reported electron screening interaction which occurs between metallic Mn and Cu atoms, which is known to affect the profile of EELS Mn-L3 spectra [**21**] and Mn photoemission [**23**] spectra taken from Mn/Cu alloys. In addition to this the *ex-situ* sample preparation methods

required for techniques such as EELS may result in the ambient oxidation of Mn [**24**], creating uncertainty as to whether the Mn oxide species are due to air exposure or due to the inherent chemical state within the barrier layer.

The scope for this study deals predominantly with the initial growth and chemical characterisation of manganese thin films on silicon oxide based insulating substrates as little in-depth analysis of the interfacial chemistry of the individual layers has been previously published. Only after determining the interfacial chemistry of Mn films as a function of annealing temperature on SiO_2 layers, were further studies of the analysis of sequentially deposited and co-deposited Mn/Cu barrier layers investigated.

1.4 Alternative substrate materials (CDO)

As previously discussed, the interconnect delay (RC time constant) in IC's has started to dominate the overall delay and determine the intrinsic speed limit of the overall circuit. The replacement of the Al interconnect material by Cu reduces the resistivity (R), hence reducing the time constant.

Nonetheless, there is an ever increasing interest in using low-κ materials defined as having a dielectric constant less than the SiO_2 value of 3.9.The introduction of these materials provides another path of solving the RC delay problem by reducing the capacitance(C) of the interlayer dielectric. Carbon doped oxides (CDO) are a family of modified dielectric materials which can have k values as low as 2.5 depending on the percentage incorporation of carbon. In a CDO material, some of the Si-O bonds are replaced by Si-CH_3 bonds. This results in the formation of less polar bonding which reduces the dielectric constant of the material. These substrates are studied in the final chapter of this thesis.

1.5 Thesis Layout and Organisation

Chapter 2 presents the surface analysis techniques used in this study, along with the principles behind their operation. The primary technique used in this work was conventional X-ray photoelectron spectroscopy (XPS). Other techniques such as synchrotron based XPS, transmission electron microscopy (TEM) and atomic force microscopy (AFM) were also used and are described in detail.

Chapter 3 describes the ultra high vacuum (UHV) systems used for these experiments, along with the thin film deposition and semiconductor surface cleaning techniques employed throughout the study. The deposition techniques used in this study include electron beam (e-beam) evaporation and thermal hot filament deposition which were used to deposit thin films of Mn and Cu. The curve fitting approach used for both synchrotron and conventional XPS spectra are also outlined in this chapter.

Chapter 4 focuses on the suitability of Mn silicate as a potential diffusion barrier on SiO_2. This investigation is divided into two separate sections consisting of the characterisation of the interfacial properties of Mn thin films on SiO_2 and the role of oxygen in silicate formation. High resolution synchrotron based XPS studies show that Mn deposition onto SiO_2 results in the formation of a Mn silicate interfacial region after thermal anneal. Further XPS studies indicate that the presence of oxygen is important in controlling the extent of this reaction.

In Chapter 5 the introduction of copper into the barrier formation process is investigated. Studies relating to the mobility of Mn and Cu in thicker films are explored using TEM. Further investigations using XPS indicate that both sequentially grown and co-deposited Mn/Cu films impacts on the formation of the silicate layers due to the presence of copper.

Chapter 6 presents an initial investigation into how the replacement of the SiO_2 substrate with that of a low-k CDO dielectric impacts on the formation of the silicate

barrier layer at the Mn/CDO interfaces and how the interface reactions can be modified and potentially improved. Using conventional XPS the formation of both Mn silicate and Mn carbide is observed. Finally, methods to minimise/remove this carbide are explored.

Chapter 7 draws together the main findings of this work and outlines some possible future directions which further studies could explore.

1.6 References

[1] "International Technology Roadmap for Semiconductors," Interconnect, 2009.

[2] J. R. Black, "Metallization Failures In Integrated Circuits," RADC Technical Report, 1968.

[3] http://www.mrl.ucsb.edu/~edkramer/LectureVGsMat100B/99Lecture14VGs/Image133.jpg

[4] T. Gupta, *Copper Interconnect Technology*, 1st ed. Springer, 2009.

[5] M. Liu, "Pore characterization of ultralow-k dielectric thin films using positronium annihilation spectroscopy," PhD Thesis, 2008.

[6] K. Buchanan, "The evolution of interconnect technology for silicon integrated circuitry," in *GaAsMANTECH*, 2002.

[7] http://spectrum.ieee.org/images/mar04/images/0304chipf1.jpg

[8] (2011, Oct.) Wolframm Alpha. [Online]. http://www.wolframalpha.com/

[9] [Online]. http://www.dwpg.com/contentdata/images/tn_576804216.pjpeg

[10] C. M. Tan and G. Zhang, "Overcoming intrinsic weakness of ULSI metallization electromigration performances," *Thin Solid Films*, vol. 462-463, pp. 263-268, Sep. 2004.

[11] D. B. Butrymowicz and J. R. R. M. E. Manning, "Diffusion in Copper and Copper Alloys," *J. Phys Chem. Ref. Data*, vol. 2, no. 3, pp. 643-655, 1973.

[12] J. B. e. al., "Investigation of Copper Metallization Induced Failure of Diode Structures with and without Barrier Layer," *Microelectronic Engineering*, vol. 33, pp. 283-291, 1997.

[13] H. Y. Wong, N. F. Mohd Shukor, and N. Amin, "Prospective development in diffusion barrier layers for copper metallization in LSI," *Microelectronics Journal* , vol. 38, pp. 777-782, Jun. 2007.

[14] J. Koike and M. Wada, "Self-forming diffusion barrier layer in Cu-Mn alloy metallization," *Appl. Phys. Lett*, vol. 87, no. 041911, Jul. 2005.

[15] e. a. T. Usui, "Highly reliable copper dual-damascene interconnects with self-formed MnSiO barrier layer," *IEEE Trans. Electron Devices*, vol. 53, no. 10, p. 2492, 2006.

[16] M. J. Frederick, R. Goswami, and G. Ramanah, "Sequence of Mg segregation, grain growth, and interfacial MgO formation in Cu-Mg alloy films on SiO2 during vacuum annealing," *J. Appl. Phys.*, vol. 93, no. 10, pp. 5966-5972, May 2003.

[17] Y. Au, et al., "Selective Chemical Vapor Deposition of Manganese Self-Alighned Capped Layer for Cu Interconnections in Microelectronics," *J. Electrochem. Soc.*, vol. 157, no. 6, pp. 341-345, Apr. 2010.

[18] R. G. Gordon and H. Kim, "Self-Aligned Barrier Layers for Interconnects," U.S. Manufacturing WO 2009/117670 A2, Sep. 24, 2009.

[19] J. Iijima, Y. Fujii, K. Neishi, and J. Koike, "Resistivity reduction by external oxidation of Cu-Mn alloy films for semiconductor interconnect application," *J. Vac. Sci. Technol., B*, vol. 27, no. 4, pp. 1963-1968, Jul. 2009.

[20] S. ,. M. Chung and J. Koike, "Analysis of dielectric constant of a self-forming barrier layer with Cu-Mn alloy on TEOS-SiO2," *J. Vac. Sci. Technol, B.*, no. 27,

p. 28, Sep. 2009.

[21] Y. Otsuka, J. Koike, H. Sako, K. Ishibashi, and N. Kawasaki, "Graded composition and valence states in self forming barrier layers at Cu-Mn/SiO2 interface," *Appl. Phys. Lett*, vol. 96, no. 012101, Jan. 2010.

[22] J. M. Ablett, J. C. Woicik, Z. Tokei, and S. List, "Phase identification of self-forming Cu-Mn based diffusion barriers on p-SiOC:H and SiO2 dielectrics using x-ray absorption fine structure," *Appl. Phys. Lett.*, vol. 94, no. 042112, Jan. 2009.

[23] U. Manju, D. Topwal, G. Rossi, and I. Vobornick, "Electronic structure of the two-dimensionally ordered Mn/Cu(110) magnetic surface alloy," *Phys. Rev. B*, vol. 82, no. 035442, Jul. 2010.

[24] C. Yoon and D. L. Cocke, "Oxidation studies of copper-manganese alloys - A basis for model catalyst preparation," *Appl. Surf. Sci.*, vol. 31, no. 118, pp. 118-150, Aug. 1988.

Chapter 2

Experimental Techniques

2.1 X-Ray Photoelectron Spectroscopy

The principle analytical technique used in this study was x-ray Photoelectron Spectroscopy (XPS). XPS; also known as Electron Spectroscopy for Chemical Analysis (ESCA) is a highly surface sensitive analysis technique used to determine surface composition and chemical bonding of the top 5-10 nm of solid materials. Surface analysis by XPS is accomplished by irradiating a sample with mono-energetic soft x-rays and analysing the kinetic energy of the electrons emitted from the material due to the photoelectric effect [**1**] as shown in Figure 2.1.

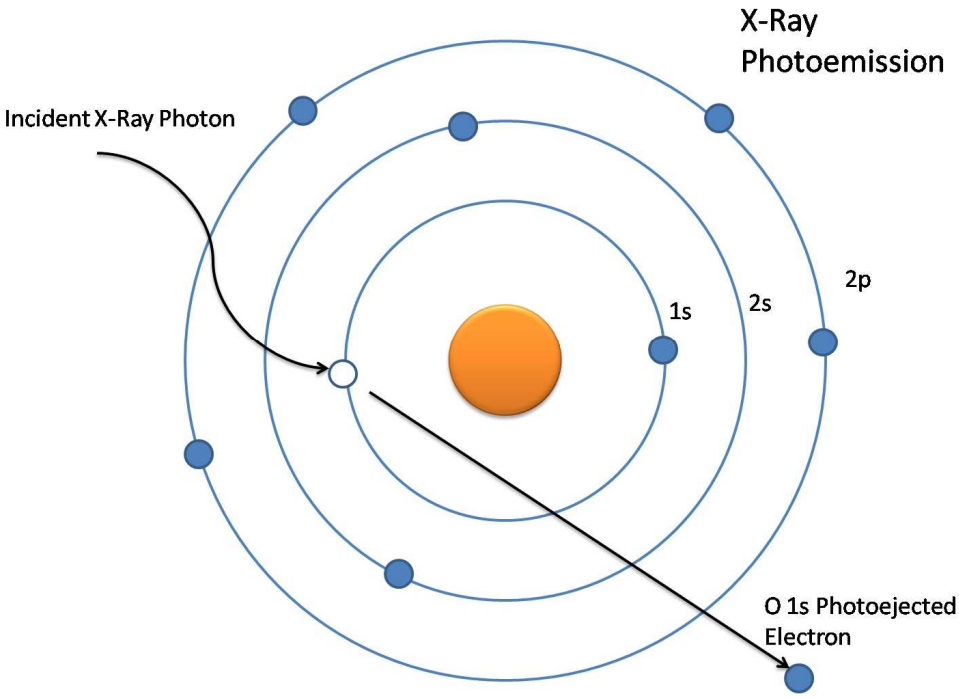

Figure 2.1 Schematic showing photoemission of an electron from the oxygen 1s orbital

2.1.1 Principles of XPS

The typical experimental set up for conventional XPS analysis is shown in Figure 2.2, consisting of an x-ray source, a grounded sample under analysis, electron collection lens, electron kinetic energy analyser and detection system, and an external computer system to display the detector output.

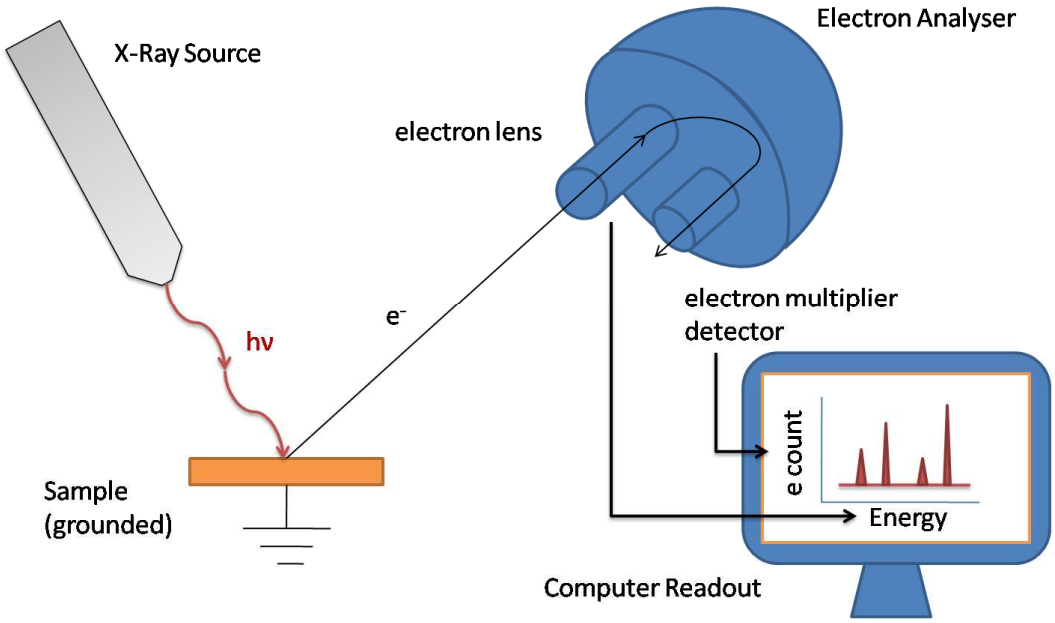

Figure 2.2 A schematic diagram showing the experimental setup for conventional XPS

The surface to be analysed is first placed in a vacuum environment and then irradiated with x-rays. The x-rays are produced by a twin anode x-ray source, which consists of a copper, water cooled anode target coated with a combination of aluminium and magnesium films which can be selected independently. Electrons from a hot tungsten filament are accelerated using a high voltage, ranging from 10 – 15 kV, towards the water cooled Mg or Al anode. Upon striking the selected target, core holes are created, which when filled by an electron transition from a higher energy level can result in the emission of an x-ray. In the case of Mg or Al anodes, two distinct x-ray emission lines with photon energy 1253.6 eV (Mg Kα) or 1486.6 eV (Al Kα) are

produced, which are routinely used in XPS measurements. When an x-ray photon impinges upon an atom on the surface of the sample one of three events can occur; (1) the photon can pass through the atom without any interaction; (2) the photon can interact with the atom leading to partial energy loss leading to Compton scattering; and (3) the photon may be absorbed, transferring all of its energy to an atomic orbital electron, leading to the emission of that electron from the atom as shown previously in Figure 2.1. The third process forms the basis of XPS. These emitted electrons are subsequently separated according to kinetic energy (KE) using an electron energy analyser and counted using an electron detector similar to those shown schematically in Figure 2.2.

The basic physics of the photoemission process is given by Einstein's equation;

$$E_b = h\nu - \mathrm{KE} \tag{2.1}$$

where E_b is the binding energy of the electron in the atom with respect to the Fermi level, $h\nu$ is the energy of the photon from the x-ray source, and KE is the kinetic energy of the emitted photoelectron. Thus, the binding energy may be obtained by measuring the kinetic energy of the emitted electron, as the energy of the x-ray source is known. Given that every energy level of each element has a discrete binding energy, the elemental composition of a sample can be determined by comparing the measured binding energies to known spectra.

At this point it is worth commenting on the measurement of the electron binding energy in relation to the XPS system. For gases, the binding energy of an electron in a given orbital is identical to the ionization energy of that electron [**2**]. In conducting solids however the influence of the surface is felt, and additional energy in the form of the sample workfunction is needed to remove the electron from the surface. Hence equation 2.1 becomes

$$E_b = h\nu - \mathrm{KE} - \Phi_s \tag{2.2}$$

where Φ_s is the sample material's workfunction which is defined as the energy difference between the vacuum level and Fermi level ($E_{vac} - E_F$). However, once the sample and the spectrometer are in electrical contact, the Fermi level of the sample lines up with the Fermi level of the spectrometer by grounding both the sample and the spectrometer as shown in Figure 2.3.

It is now clear from Figure 2.3 that the sum of the electron's initial binding energy measured up to the Fermi level (E_B^F), and its kinetic energy after being emitted (E_{kin}^1), does not equal the photon energy of the impinging x-rays.

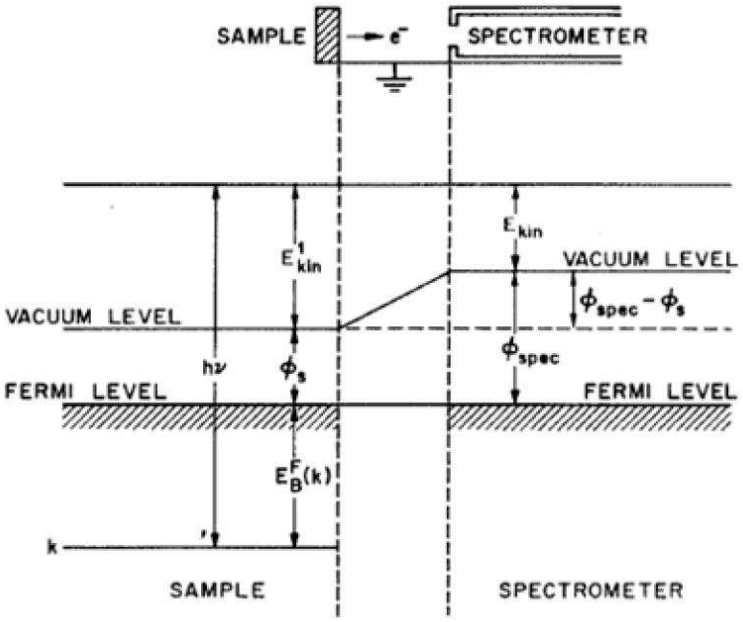

Figure 2.3 Energy level diagram for the photoemission process showing a sample and spectrometer in electrical contact [3].

Feldman and Mayer [**3**] explain how the measured kinetic energy value (E_{kin}) may differ from the actual kinetic energy of the emitted electrons (E_{kin}^{1}). It has been shown that an electron passing from the sample to the spectrometer experiences a potential difference equal to the difference between the workfunction of the sample $\Phi_{material}$ and that of the spectrometer(Φ_{spec}). The measured kinetic value can therefore be defined by equation (2.3).

$$E_{kin} = E_{kin}^{1} + (\Phi_s - \Phi_{spec}) \tag{2.3}$$

By substituting this into equation (2.2), the expression given in equation (2.4) can be found.

$$E_b = h\nu - \mathrm{KE} - \Phi_{\mathrm{spec}} \tag{2.4}$$

This equation allows the binding energy of an electron to be obtained once the x-ray photon energy and spectrometer workfunction values are known. Thus the measurement of E_b is shown to be independent of the sample workfunction, Φ_s, but is dependent on the spectrometer work function, Φ_{spec}. The spectrometer workfunction is commonly determined using a reference sample of known binding energy such as gold (4f = 83.98 eV), with measured spectra being shifted to compensate for this value. The linearity of the binding energy scale may then be calibrated by adjusting the energy difference between two widely spaced spectral lines of known values (e.g., the 3p = 75 eV and 2p = 933 eV peaks of copper).

2.1.2 Inelastic Mean Free Path and Sampling Depth

As illustrated in Figure 2.4 x-rays typically illuminate and cause emission of electrons from a sample area of approximately 1 cm^2. However, only electrons from a $1mm^2$ area are counted in order to facilitate depth profiling which is discussed later in this chapter.

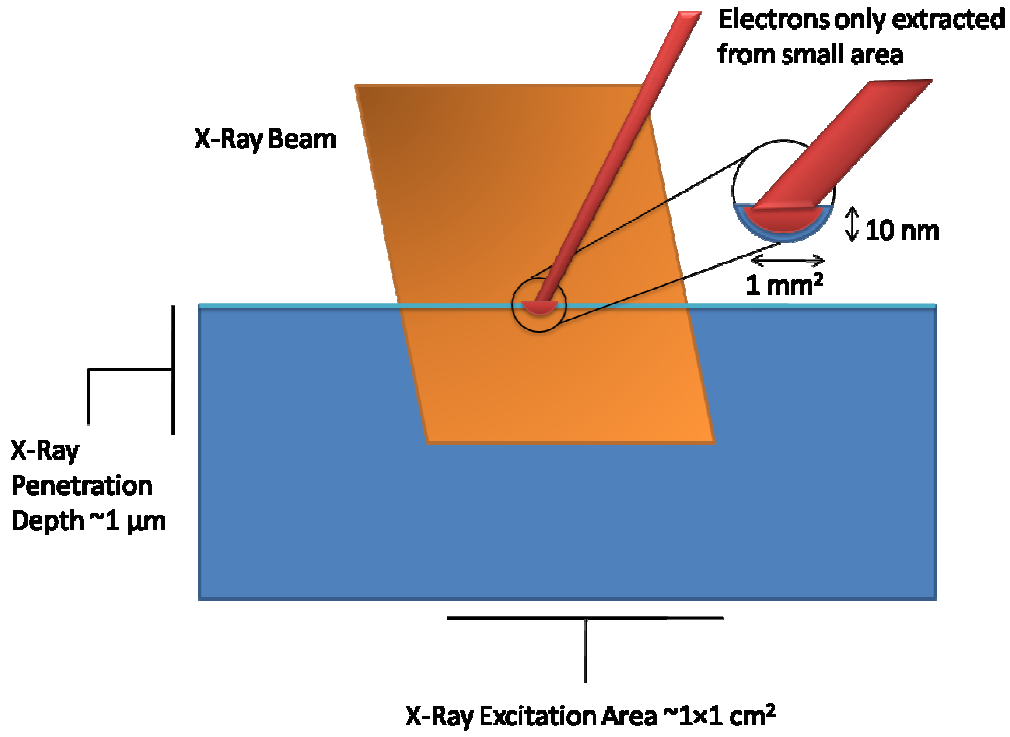

Figure 2.4 Diagram showing x-ray beam incident on sample [2]

With regards to the penetration of the x-ray beam, it is important to note that while the typical penetration depth of a 1 KeV photon beam into solid matter is in the order of ~1µm, the escape depth of electrons at this energy is considerably smaller (approximately 10 nm). This difference is due to the fact that photoemitted electrons from within the sample interact strongly with matter and may lose kinetic energy via inelastic collisions with other atoms, which can occur within the solid before the photo-excited electrons emerge from the surface. The probability of such interactions can be statistically predicted based on the inelastic mean free path (IMFP) of the given material, which is dependent on the initial kinetic energy of the electron and the nature of the material and is represented by the universal mean free path curve in Figure 2.5.

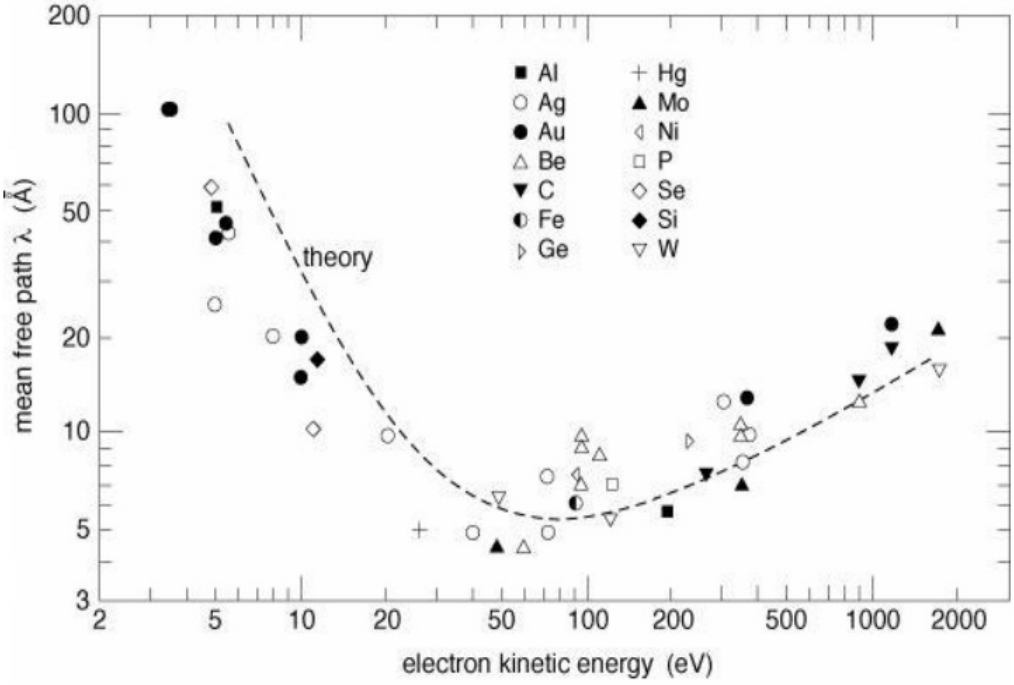

Figure 2.5 Universal mean free path (MFP) curve, showing a range of materials [4].

The IMFP is defined as the average distance (in nanometres) that an electron travels between successive inelastic collisions. The IMFP may be expressed as follows

$$P(d) = \exp(-\frac{d}{\lambda}) \tag{2.5}$$

Where P(d) is the probability of an electron travelling a distance d, through a solid without undergoing scattering; and λ is the IMFP for the electrons of a given energy. Figure 2.6 illustrates that the likelihood of an electron escaping decays very rapidly and is essentially zero for a distance $d > 5\lambda$.

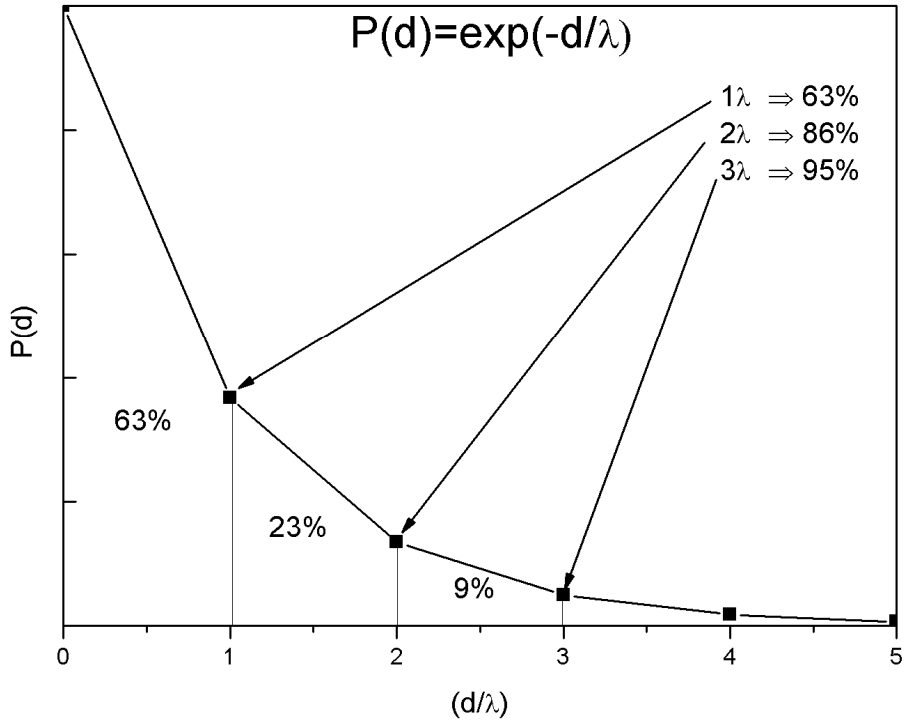

Figure 2.6 Graph showing probability of unscattered electron emission as a function of depth

By integrating under the curve it can be seen that virtually all unscattered electrons come from within 3λ of the surface. This is known as the sampling depth and accounts for 95% of detected unscattered electrons. In an XPS experiment, we are only concerned with the unscattered photoelectrons as they have kinetic energies which can be related back to the original binding energy value. These unscattered electrons produce narrow and intense photoemission peaks, such as those shown in Figure 2.7, and the binding energy of these peaks can be related to the elements present at the surface. Electrons emitted from the surface zone that have lost some energy due to inelastic interactions emerge from the sample with various kinetic energies, and add to the background of the spectrum.

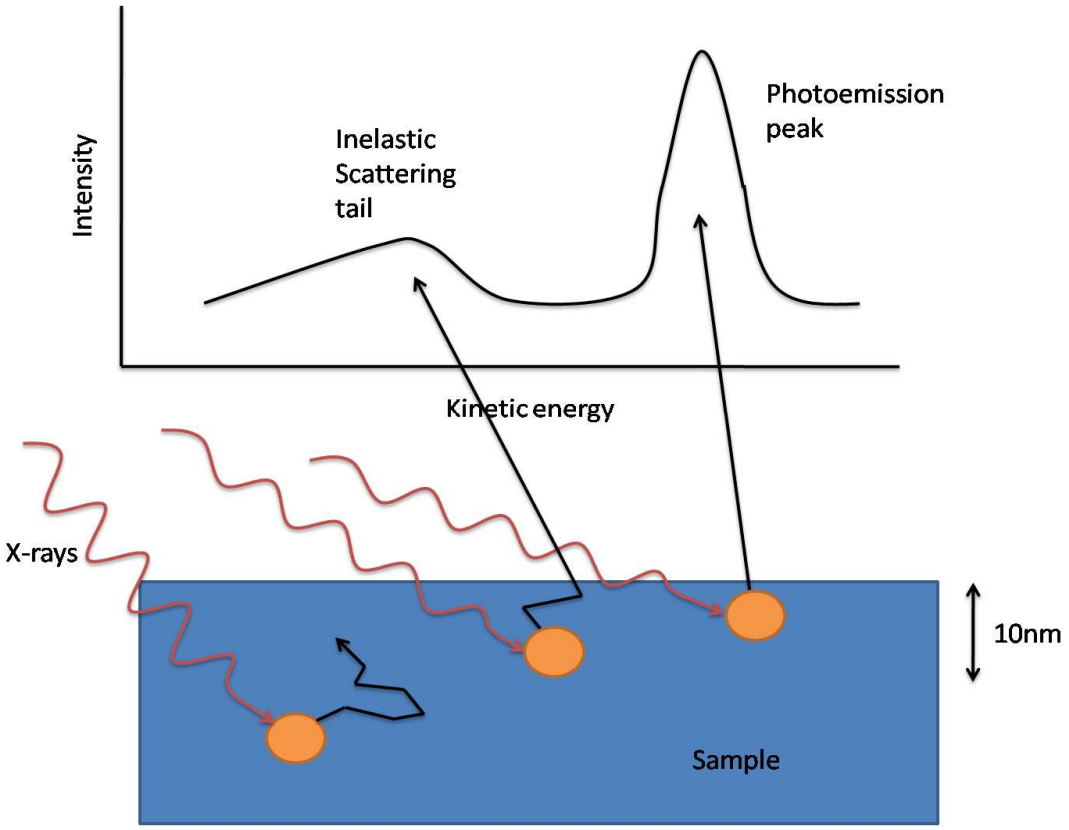

Figure 2.7: Diagram showing various electron emissions making up a typical photoemission peak. [2]

It is for this reason that XPS is considered an extremely surface sensitive technique, as while the photoemission process may occur from as deep as the x-ray penetration depth, only electrons from near the sample surface and are detected.

Upon escaping the sample surface electrons are focussed by a series of lenses, filtered according to kinetic energy using an energy analyzer and finally counted by an electron detector. The spectrometer is setup to scan across the different electron energies in order to count and store the number of detected electrons for a given energy for a given detection time. This data is then outputted to an external computer system. The details of the electron spectrometer used in this work are expanded upon in Chapter 3.

2.1.3 Spectral Features

The spectra obtained from the spectrometer displays a plot of the number of electron counts per second as a function of the electron binding energy. As previously discussed the position on the kinetic energy scale equal to the x-ray excitation energy minus the spectrometer work function corresponds to a binding energy of 0 eV. It is for this reason that a binding energy scale with zero at that point and increasing to the left is commonly used. In typical XPS analysis of a sample, the first step generally is to undertake a broad energy survey scan from this 0 eV binding energy position to ~1000 eV. Figure 2.8 shows the spectrum of a carbon doped silicon oxide sample. The photoemission process will cause electrons with specific energies related to the atomic core level binding energies to be emitted. Any electrons that have lost energy increase the level of the background at kinetic energies lower than the peak energy. The background is continuous because of the random nature of the loss processes. Any noise in the spectrum is due to the collection of single electrons randomly spaced in time.

Rising above the background we can examine two distinct types of peaks. These are the photoemission peaks associated with core-level events and x-ray induced Auger lines. The most intense photoelectron lines are typically the narrowest lines observed in the spectra and are relatively symmetrical. However, metals exhibit considerable asymmetry due to coupling with conduction electrons. Auger lines are groups of lines caused by the transition of a core level electron to deeper lying empty energy level which results in the transfer of energy to another bound electron giving it sufficient kinetic energy to be emitted from the surface. These lines can be readily distinguished by changing the energy of the x-ray source as the kinetic energy of the Auger lines will remain the same due to the interaction being dependant on the energy separation of the core levels while the photoemission lines will shift by the energy difference between the Mg and Al x-ray sources. Tables of

measured and calculated binding energies for almost all elements are widely available to aid in the identification process. [**5**] [**6**] [**7**]

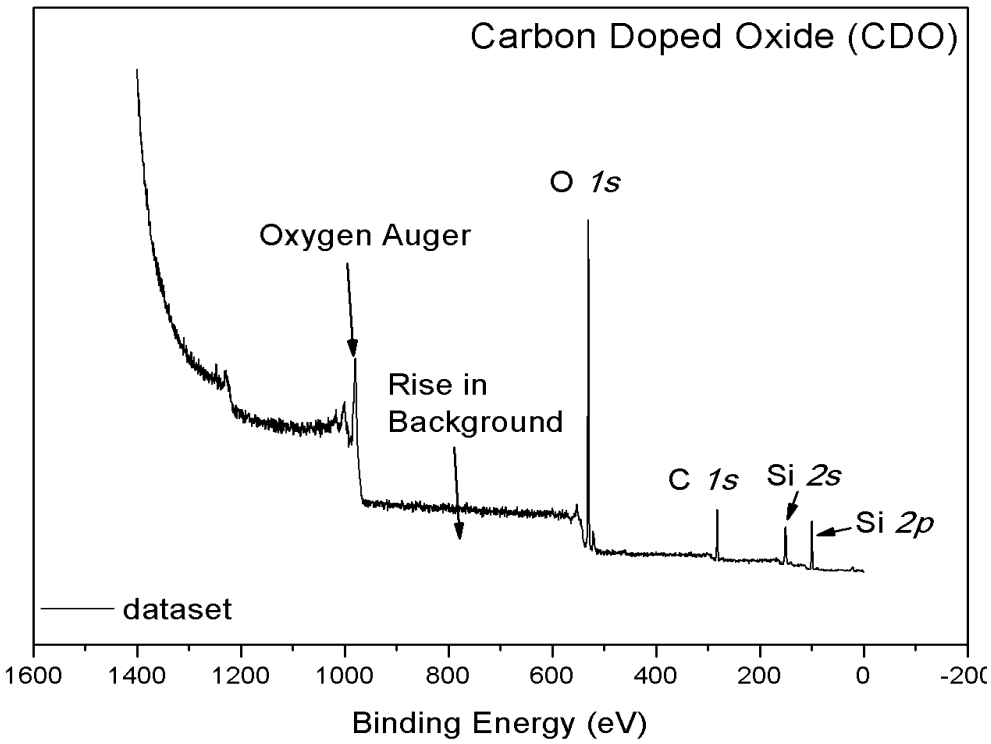

Figure 2.8: Survey scan taken from a carbon doped oxide (CDO) surface. By analysing the binding energy positions of the photoemission peaks the elements Si, O and C can be identified.

After identification of the relevant photoemission peaks from the survey scan, more detailed information may be obtained from high resolution narrow energy scans.

An x-ray satellite as shown in Figure 2.9 is a feature that will be seen when using a non-monochromated x-ray source. The non-monochromatic source may excite the sample with x-ray components at higher energies. These low-intensity x-rays will produce minor photoemission peaks at approximately 10 eV higher kinetic energy than that of the primary peak. These features may be removed by the use of an x-ray

monochromator which uses quartz crystals to eliminate residual Bremsstrahlung and significantly narrows the peak width of the photoemission lines.

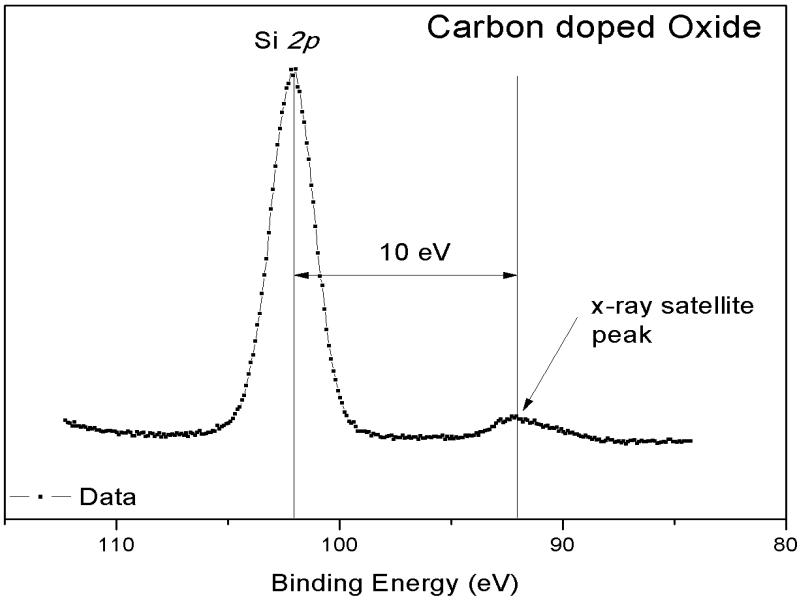

Figure 2.9: Mg x-ray satellite observed in the Si 2p spectrum of CDO.

Further features often seen within high-resolution scans are those of shake-up lines and multiplet-splitting. Shake-up satellites as shown in Figure 2.10, occur when photoelectrons lose energy through the promotion of valence electrons. While regarded as loss peaks, these satellites, in contrast to the inelastic scattering background have discrete energies because the energy loss is equivalent to a specific energy transition in the atom.

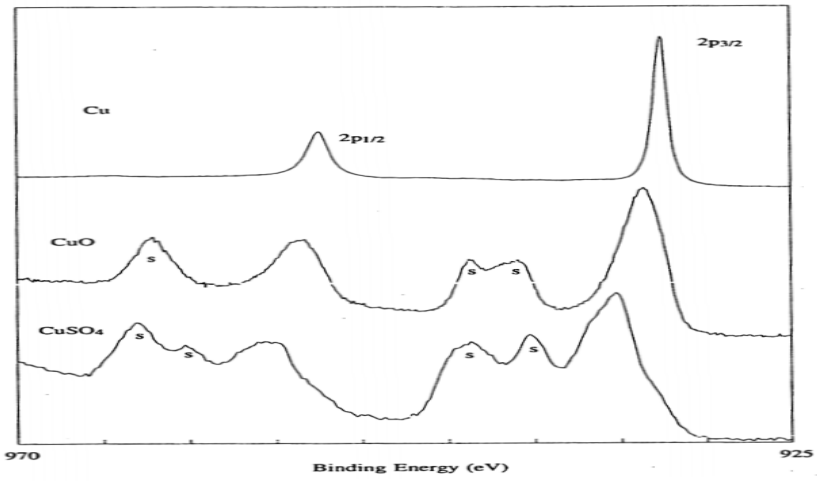

Figure 2.10: Examples of shake-up lines of the Cu 2p peak in copper compounds [7]

Multiplet splitting occurs because electrons in an atom can create a vacancy in more than one way because of their spin, i.e. two energetically equivalent final states are possible. The coupling of an unpaired electron from a s-type orbital with other unpaired orbitals within the atom can create an ion which can result in an asymmetric photoelectron line with several components similar to the one shown in Figure 2.11.

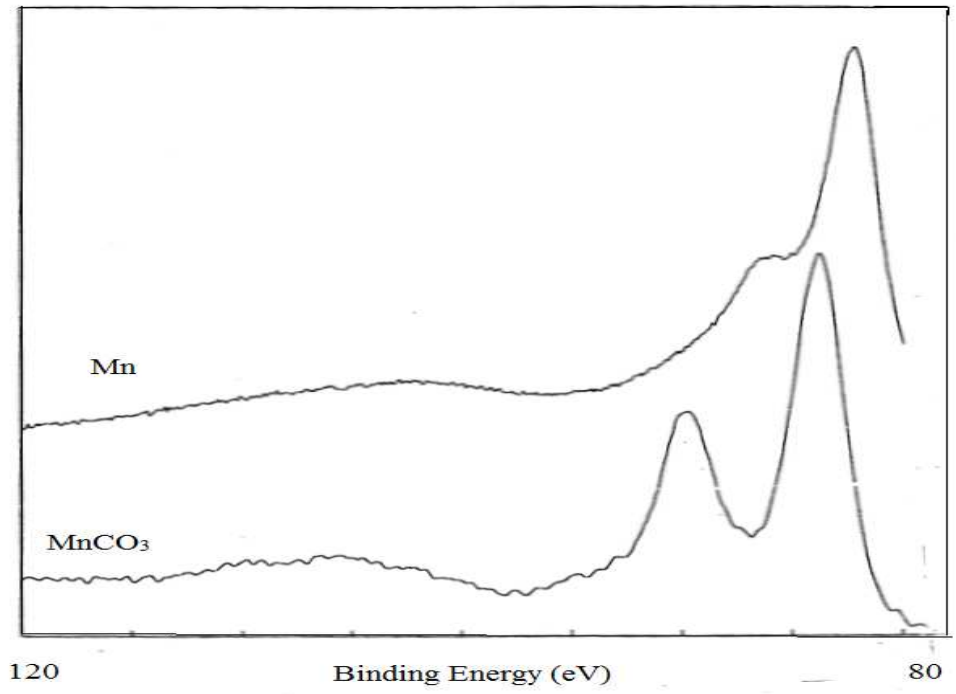

Figure 2.11: Multiplet splitting of the Mn 3s [7].

2.1.4 Element Identification

Standard XPS can be used to identify the presence of elements which are at atomic concentration levels greater than approximately 0.1 – 1 %. Elements are commonly identified by the presence of their strongest spectral feature, in the case of silicon this is the Si 2p peak at 99.3 eV seen in Figure 2.12. However, binding energy positions are not unique to specific elements and different peaks may often overlap within the spectrum i.e. the Ga 3p and Si 2p peaks at ~ 103 eV [**8**]. In this situation the presence of secondary core level features, such as the Si 2s, may be used to identify the elements.

2.1.5 Chemical Shifts

In addition to identifying the elements present on the surface, one of the most important aspects of XPS is the ability to distinguish between different chemical environments of the same element. This is possible because the binding energy of an electron within an atom depends on the bonding environment of that atom. Therefore, changes in chemical bonding can result in changes in the charge density around the atoms, which causes a "chemical shift" in the binding energy of the electrons which emerge from these atoms. This process is described in greater detail with reference to the silicon/silicon dioxide system, using the Si 2p spectrum in Figure 2.12.

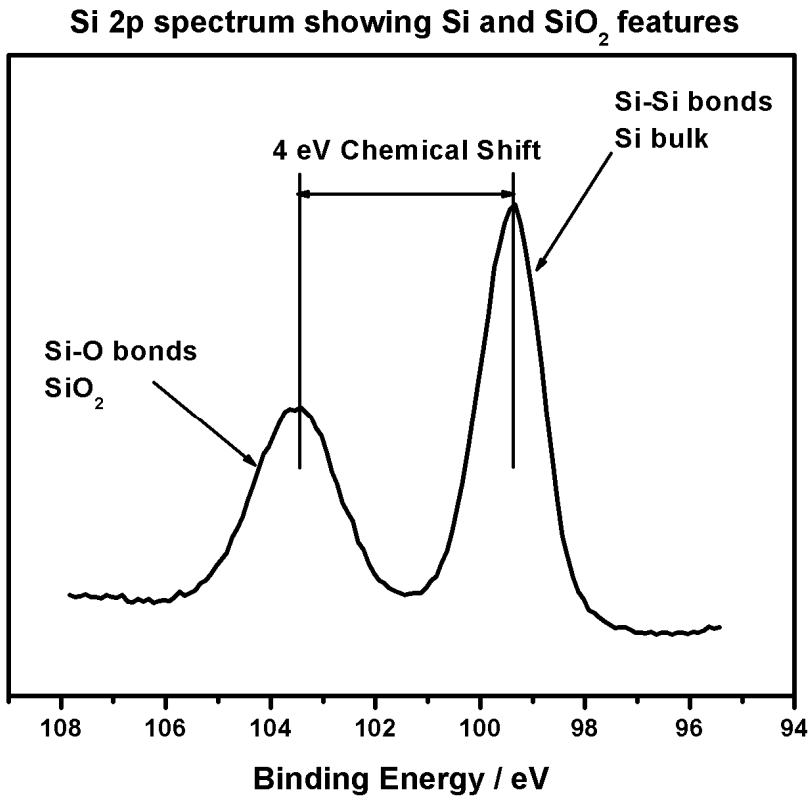

Figure 2.12: Si 2*p* spectrum showing a 4 eV chemical shift between component peaks which indicates the presence of Si and SiO_2.

Figure 2.12 shows a Si 2p spectrum taken from a thin (~ 4 nm) SiO_2 layer which was thermally grown on a Si (111) substrate. It can be seen that electrons excited from the Si substrate appear at a binding energy of ~ 99.3 eV, while those from the SiO_2 over layer appear at a higher binding energy position, chemically shifted from the bulk by ~ 4 eV. This is due to the different bonding environment present within the two chemical species. The covalent Si-Si bonding system seen within the Si bulk allows the valence electrons to be shared equally among each of the Si atoms involved in the bonding structure. However, the incorporation of O atoms, which have considerably greater electronegativity than Si, results in the transfer of electron density toward the O atoms. As such, Si-O bonds are more ionic and electrons which are excited from these silicon atoms are leaving an atom which has a slightly greater positive charge than those

within the Si bulk. The effect of this positive charge is to reduce the kinetic energy of the emitted electrons, which is apparent from the increased binding energy of the SiO_2 peak seen in Figure 2.12. As such, the relative electronegativity values of the elements within a sample can be used to identify chemical interactions. For example, the formation of a spectral component at the lower binding energy (LBE) side of the Si bulk peak indicates that Si atoms are bonded to an element with a lower electronegativity than that of Si, commonly seen in the form of a metal silicate as will be shown in Chapter 4 of this study.

2.1.6 Quantification

Semi-quantitative analysis of the relative concentration of different elements in a material can be achieved by comparing the intensity of the relevant core level peaks. However, there are a number of factors which must be taken into account in order to accurately quantify chemical composition using XPS peak intensities. This is analysed in further detail in reference to Mg 2p and O 1s spectra taken from an MgO thin film deposited on Si (111), shown in Figure 2.13.

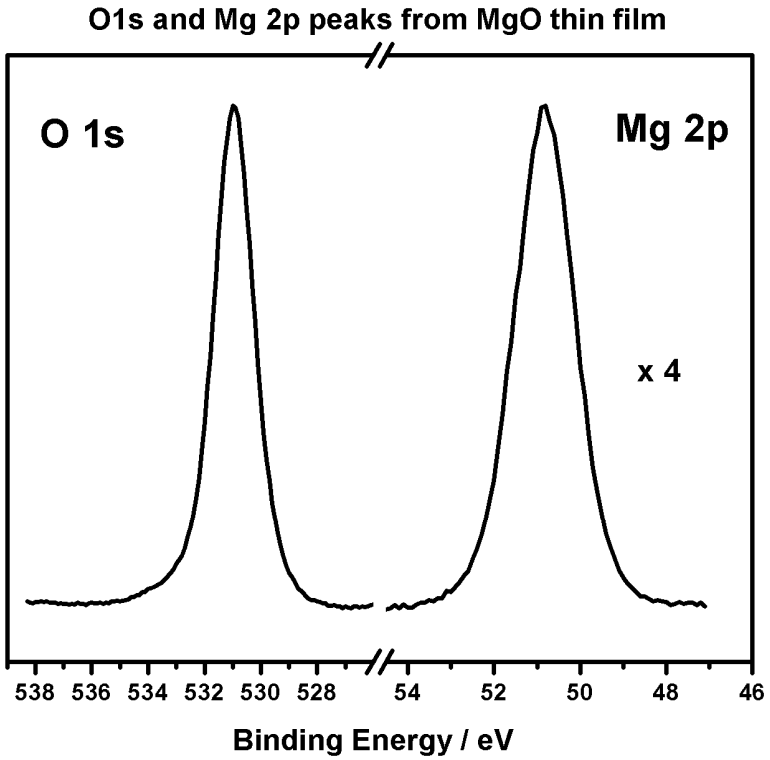

Figure 2.13 O 1*s* and Mg 2*p* spectra taken from a 20 nm stoichiometric MgO thin film.

In order to determine stoichiometry using the spectra in Figure 2.13 it must be assumed that the MgO film is chemically homogenous, as if the chemical composition perpendicular to the surface is non-uniform within the XPS sampling depth, no definitive elemental ratios can be extracted. The relative binding energies of the two peaks must also be taken into account given that electron IMFP is strongly dependant on kinetic energy. As such, it can be said that electrons emerging from the Mg 2p peak (BE 50 eV, KE 1200 eV) may emerge from a greater depth than O 1s electrons (BE 531 eV, KE 720 eV). Further factors include the photo-ionisation cross-section of that specific core-level which is the probability that an electron of that core-level will be excited [**9**]. Finally there is the transmission function of the analyser which determines the relative sensitivity of the analyser to electrons of different kinetic energies.

Based on these criteria relative sensitivity factors (RSF) can be obtained for the core level peaks of each element, and using these RSF values, chemical composition can be analysed. Published RSF values are available from XPS reference manuals [**7**] and allow semi-quantitative analysis of chemical composition to be achieved. In reference to the spectra in Figure 2.13, the published RSF values of O 1s and Mg 2p are 0.711 and 0.129 respectively [**7**]. Therefore, for stoichiometric MgO the integrated area of the O 1s peak should be ~ 5.5 times greater than that of the Mg 2p. This analysis is at best semi-quantitative and the use of reference materials is common for more accurate quantification studies. In this study, quantitative analysis has been performed in an attempt to directly compare differently prepared samples, rather than for the purpose of extracting absolute values.

2.1.7 Depth Profiling using ARXPS

Although XPS is considered a highly surface sensitive technique, if we estimate that the sampling depth is 8 nm and consider that deposited thin films can be ~1 nm then the surface region detected by XPS could consist of multiple atomic layers. This is illustrated schematically in Figure 2.14. Each of these layers may have a different chemical composition and the XPS spectrum that we obtain is a convolution of these layers.

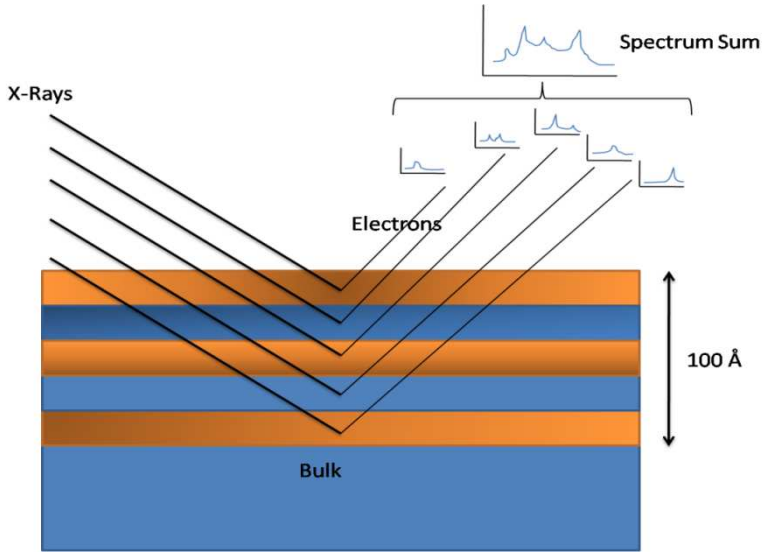

Figure 2.14 Diagram showing convoluted signals from sampling depth [2]

Angular resolved XPS (ARXPS) allows non-destructive depth profiling to be achieved for a thickness into the sample surface which is comparable to the sampling depth. Previous discussions relating to the emission of photoelectrons assume that they escape using the shortest path, which is that perpendicular to the sample surface. Therefore, the maximum sampling depth is achieved by aligning the sample so that the electrons which emerge normal to the surface are detected by the analyser. However, electrons emerging from shallower angles with respect to the surface may also be analysed by rotating the sample relative to the analyser. This has the effect of reducing the actual sampling depth from which the photoemitted electrons emerge as is schematically shown in Figure 2.15.

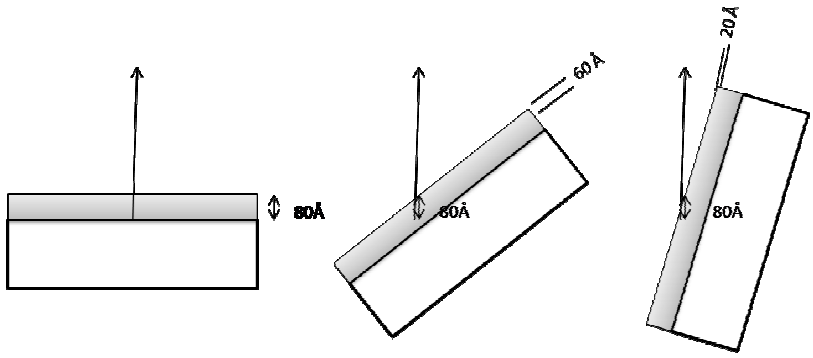

Figure 2.15 Concept of ARXPS showing effective sampling depth

It can be seen from Figure 2.15 that electrons emerging perpendicular to the surface have the same sampling depth as those emerging at the glancing angles i.e. 8 nm. However, in the rotated samples the perpendicular depth from which the electrons escape from the surface is considerably less than for normal emission. As such, core level spectra taken at an increased angle are more surface sensitive than those taken at normal emission. This is further evidenced by Si 2*p* spectra in Figure 2.16 which are taken from a SiO_2 surface (~ 5 nm) at emission angles equal to 0 ° (normal emission) and 60 °. It can be clearly seen that the spectrum taken at 60 ° shows an increased intensity from the Si oxide overlayer.

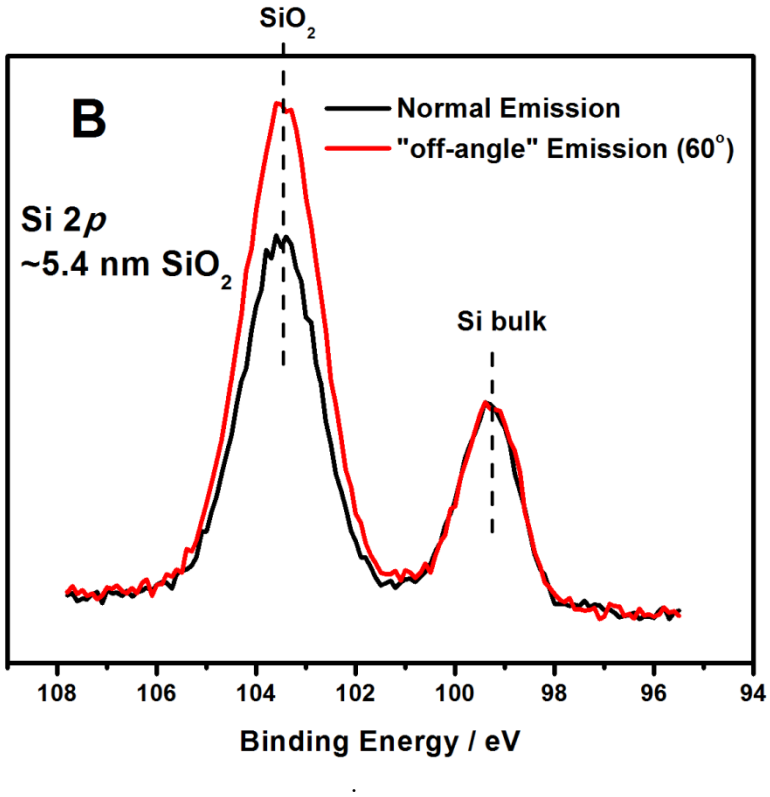

Figure 2.16: Si 2*p* spectra taken from a 5.4 nm SiO_2 layer on silicon showing the increased surface sensitivity using ARXPS.

2.1.8 Thickness Calculations

XPS may be used to approximate the thickness of thin (less than approximately 10 nm) overlayers by comparing the intensity of core level peaks taken from the substrate and overlayer, respectively.

XPS thickness calculations used in this study can be divided into two categories. The overlayer thickness can be estimated based on the suppression of the substrate peak by the presence of an overlayer. Alternatively, when the same element is present in distinguishably different chemical environments in the overlayer and substrate, the overlayer thickness calculations are simplified.

For a sample of material A which forms a thin uniform layer of thickness d on a substrate of material S, the following equation can be written for the relative intensity of the substrate (I_S) and overlayer (I_A) XPS signals (assuming exponential attenuation of the overlayer) [**10**] [**11**].

$$\frac{I_A}{I_S} = \frac{I_A^{\infty}\left\{1 - exp\left[\frac{-d}{\lambda_{A,A}(\cos\theta)}\right]\right\}}{I_S^{\infty} exp\left[\frac{-d}{\lambda_{S,A}(\cos\theta)}\right]} \qquad (2.6)$$

The angle θ in this equation is the emission angle of the excited electrons and is measured with respect to the surface normal. Factors I_A^{∞} and I_S^{∞} are peak intensities taken from samples of materials A and B of effectively infinite thickness. The parameters $\lambda_{A,A}$ and $\lambda_{S,A}$ are the effective attenuation lengths of electrons emerging from the overlayer and the substrate respectively [**12**]. The effective attenuation length (EAL) is known to differ from the inelastic mean free path (IMFP) due to elastic-scattering which causes the photoelectrons signal to decay in a non-exponential manner [**13**]. This variation from the IMFP value is dependent on the composition of the sample

but, in general, changes in physical properties such as an increased density will result in a reduction of the EAL.

For the case of SiO_2 on Si, where the kinetic energy of the substrate and overlayer signals differ by approximately 4 eV the values $\lambda_{A,A}$ and $\lambda_{S,A}$ are approximately equal and can be replaced by a single term λ [**12**], making d the subject of the expression equation 2.6 is found.

$$d = \lambda \cos\theta \ln\left[1 + \frac{\left(\frac{I_A}{I_A^{\infty}}\right)}{\left(\frac{I_S}{I_S^{\infty}}\right)}\right] \tag{2.7}$$

The ratio $\frac{I_S^{\infty}}{I_A^{\infty}}$ can be referred to as K [**14**] [**12**] [**15**] leaving;

$$d = \lambda \cos\theta \ln\left[1 + K\left(\frac{I_A}{I_S}\right)\right] \tag{2.8}$$

As stated previously, equation 2.7 relates only to situations where the kinetic energy of the substrate and overlayer peaks are comparable. In this study equation 2.7 was used to calculate the thickness of Si oxide overlayers on Si, with the parameter K being found experimentally using SiO_2 and Si samples of effectively infinite thickness and a value for λ found in the literature [**12**].

Thickness calculations based on this method can be achieved using software such as NIST Electron EAL Database [**6**].

2.2 Synchrotron radiation photoemission spectroscopy

2.2.1 Advantages over XPS

The principle of synchrotron based photoemission (SRPS) is similar to that of conventional XPS, with the energy of emitted photoelectrons being analysed to determine the composition of a material. However, SRPS allows for considerably improved resolution and greater surface sensitivity than conventional XPS.

Synchrotron radiation is characterised by:

- High brightness and high intensity, many orders of magnitude more than that offered by X-rays produced in conventional X-ray tubes
- High brilliance, exceeding other natural and artificial light sources by many orders of magnitude: 3rd generation sources typically have a brilliance greater than 10^{18} photons/s/mm^2/mrad^2/0.1%BW, where 0.1% BW denotes a bandwidth 10^{-3} ω centred on the frequency ω.
- High collimation, i.e. small angular divergence of the beam
- Low emittance, i.e. the product of source cross section and solid angle of emission is small
- Widely tuneable in energy/wavelength by monochromatisation (sub eV up to the MeV range)
- High level of polarization (linear or elliptical)
- Pulsed light emission (pulse durations at or below one nanosecond, or a billionth of a second)

2.2.2 Principles of Operation

The layout of a typical synchrotron light source consists of an electron gun, linear accelerator, booster and storage rings and array of magnets is shown in Figure 2.17.

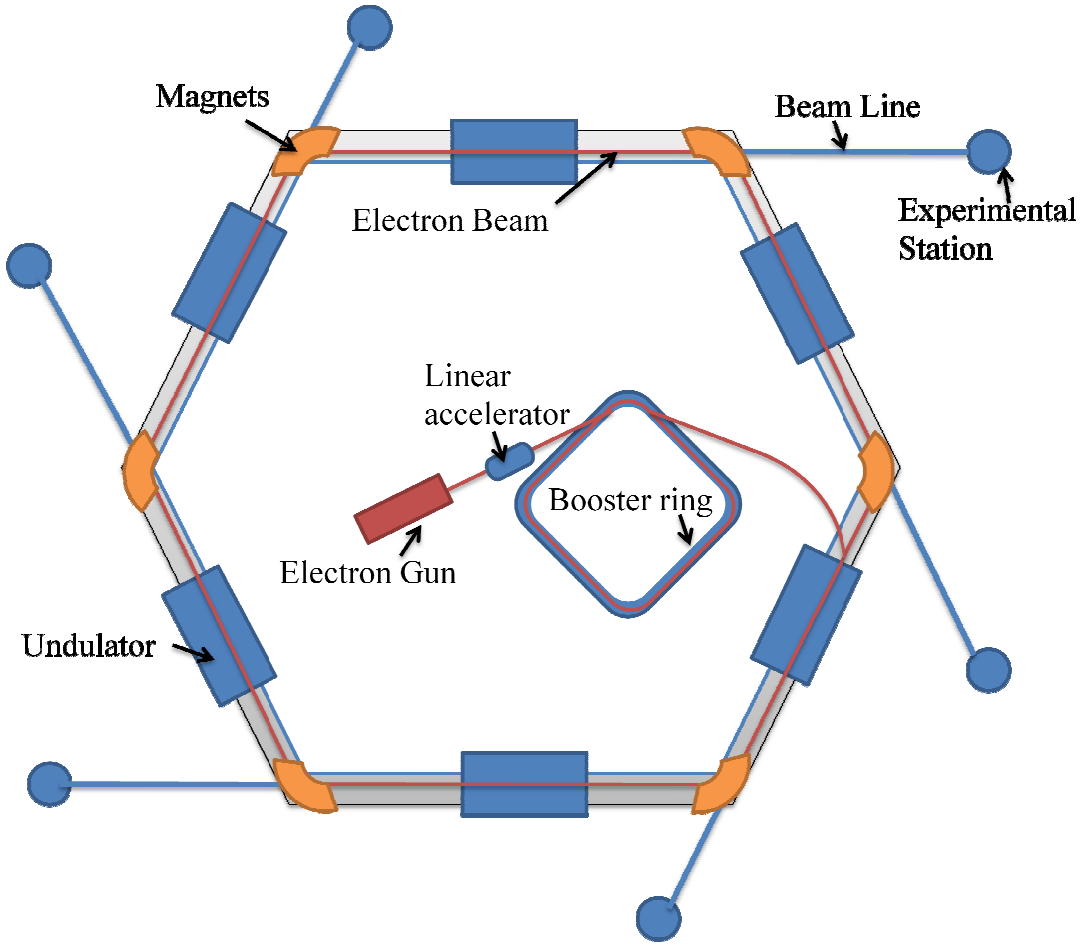

Figure 2.17: Schematic diagram showing how an electron beam emits synchrotron radiation when accelerated around the curved sections of a storage ring.

A heated cathode produces free electrons which are pulled through the end of the gun by an electric field. The stream of electrons are fed into a linear accelerator (linac) where high energy microwaves and radiowaves split the stream into pulses and accelerate the beam to 99% the speed of light. The linac then feeds into a booster ring which uses magnetic fields to force the electrons to travel in a closed loop and more

radio waves add more speed to the beam (approximately 99.998% of the speed of light) and ramps the energy of the electron stream to between 1.5 and 2.9 GeV which is enough energy to produce synchrotron light in the infrared to hard X-ray range.

The booster ring then feeds electrons into a storage ring which is typically made up of a series of straight tube sections connected in a polygon arrangement. The ring is maintained under ultra-high vacuum, and the beam remains at a constant energy. Focusing magnets placed in the straight sections of the storage ring keep the electron beam small and well-defined as the more focussed the beam, the brighter the radiation. If undulators are placed in the straight sections they cause the electrons to oscillate and radiate energy before reaching the corner sections of the storage ring [**16**]. The radiation emitted by this undulation will generate a much more intense, coherent beam of light. Finally, bending magnets deviate the electrons by several degrees and allow the beam to negotiate the curved corners of the ring. The change in electron momentum which occurs at the curved corners of the ring results in the tangential emission of a broad spectral range of synchrotron radiation by the electrons. The radiation is then extracted for use in beamlines, for a variety of techniques. The use of monochromators allows specific photon energies to be selected allowing for high resolution spectroscopy and maximum surface sensitivity, as the appropriate photon energy may be selected for a particular core level to minimise the electron escape depth.

2.3 Transmission electron microscopy

2.3.1 Principles of operation

Considering the Rayleigh criterion, the maximum resolution δ, which can be obtained with a light microscope, is given by

$$\delta = \frac{0.61\lambda}{\mu sin\beta} \approx \frac{\lambda}{2} \tag{2.9}$$

where λ is the wavelength of the photons that are being used to probe the sample, and $\mu sin\beta$ is defined as the numerical aperture (NA). It can therefore be seen that as the resolution is limited by the wavelength of the incident photons, and the maximum resolution for a microscope using visible light is approximately 160 nm. However, if wave/particle duality is considered, electrons can be considered to have both wave and particle properties with the wavelength λ given by ,

$$\lambda = \frac{h}{\sqrt{2meV}} \tag{2.10}$$

where h is Planck's constant, m and e are the mass and charge of the electron and V is the electron accelerating voltage. However, as the value of accelerating voltage used in electron microscopes is generally large, electrons can reach velocities comparable to speed of light and relativistic effects need to be taken into account. By replacing V with the relativistic accelerating voltage V_C given by

$$V_c = V[1 + eV/2m_0 c^2] \tag{2.11}$$

where c is the speed of light, and m_0 is the rest mass of the electron. These wave-like properties mean that a beam of high-energy electrons can be made to behave like an electromagnetic radiation beam and used to resolve features as small as 0.5 Å. This forms the basis for many modern microscopy techniques such as the scanning electron microscope (SEM) and transmission electron microscope (TEM), which is the technique used in this work.

Transmission electron microscopy (TEM) is a microscopy technique whereby a beam of high-energy electrons is transmitted through an ultra thin specimen, interacting with the specimen as it passes through. An image is formed from the interaction of the electrons transmitted through the specimen which is magnified and focused onto an imaging device, such as a fluorescent screen, or detected by a sensor such as a CCD camera. In this way TEM can be considered analogous to an optical instrument as the layout of the focusing optics is similar. The typical setup of such a microscope is shown in Figure 2.18

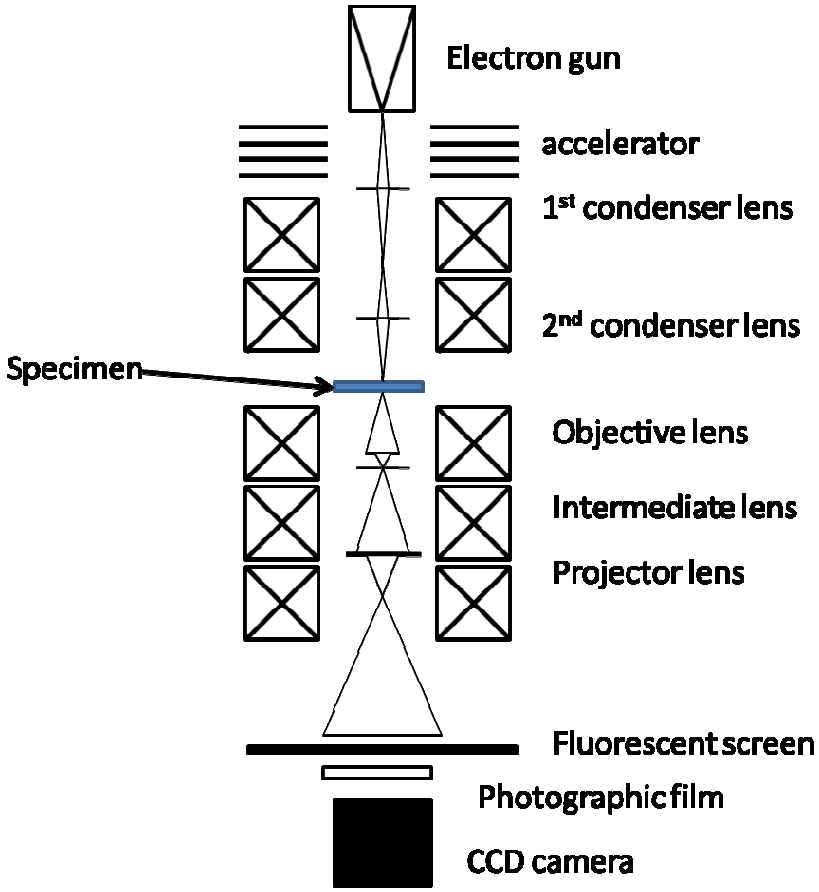

Figure 2.18: Schematic of TEM

Electrons are emitted from either a tungsten filament, or field emission gun and accelerated using high voltage (typically 80 kV to 200 kV) down the beam column, where the condenser lenses converge the electrons onto the specimen and control beam intensity and density. After interaction with the sample the electrons pass through the objective lens, which focuses the image. The intermediate lens is used to change between imaging modes and the projector lens provides final magnification before the electrons are detected by the combination of a fluorescent screen, photographic film and CCD camera. High vacuum is required within the system as the electron gun and all the electromagnetic lens focussing rely on a large mean free path.

Proper sample preparation is of vital importance to provide useful images. TEM specimens are required to be at most hundreds of nanometres thick, as samples need to have thicknesses comparable to the mean free paths of the electrons used. These

thicknesses are achieved by a combination of mechanical grinding, ion milling and focused ion beam etching.

Two modes of operation can be selected depending on the configuration of the lenses. If the focusing is set similarly to an optical microscope to form an image of the sample the microscope is said to be in contrast mode. Image contrast in TEM images can be obtained based on both the particle and wave properties of the electron. Electrons passing atoms of higher atomic number or thicker regions within the sample may not reach the detector due to absorption events. This will result in dark regions within the TEM image, allowing investigation of the structure and atomic composition of the sample. Within this mode images may be formed from the primary undeviated beam (bright-field) or from a diffracted beam satisfying the Bragg condition (dark-field).

The second mode of operation is achieved by using the sample as a diffraction grating focussing the beam to form a diffraction pattern. This is known as diffraction contrast, which uses the Bragg scattering of electrons from crystalline regions within the sample. Scattering changes the angular distribution of the electrons, allowing them to be detected separately from unscattered electrons. As such, crystalline regions may be identified as bright regions within the image [**17**] and can be used to provide information regarding crystal structure, lattice parameter and structural defects.

2.3.2 Energy Dispersive X-Ray Spectroscopy (EDX)

EDX is a complementary analysis technique which can be incorporated into a TEM. Essentially it can be seen this analogous to x-ray production in an XPS source in that the incident TEM electron beam may excite an electron in an inner shell, ejecting it from the shell creating an electron hole as schematically illustrated in Figure 2.19. An electron from an outer, higher-energy shell then fills the hole, and the difference in energy between the higher-energy shell and the lower energy shell may be released in the form of an X-ray.

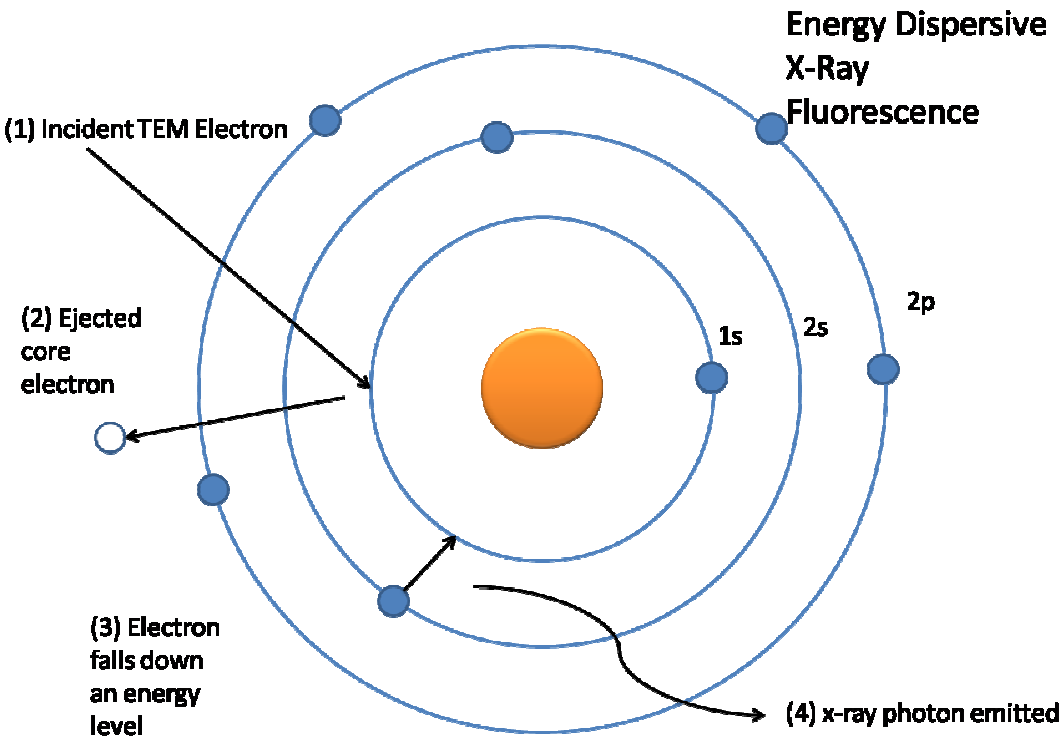

Figure 2.19: Concept of EDX

The energy of each X-ray photon is characteristic of the element which produced it. The EDX system collects the X-rays and plots them as a function of energy, and automatically identifies and labels the elements responsible for the peaks in the energy distribution. The EDX data are typically compared with either known or computer-generated standards to produce a full quantitative analysis showing the sample composition.

2.3.3 Electron Energy Loss Spectroscopy (EELS)

Electron Energy Loss Spectroscopy (EELS) is a further useful technique which can be integrated into TEM. After interaction with the sample, some of the incident beam electrons will have lost a certain amount of energy due to inelastic interactions with the sample. These inelastic events include phonon vibrations, plasmon excitations and inner shell ionizations. EELS is similar to EDX in that it also provides information on atomic composition and chemical bonding. However, unlike EDX, EELS works well at low atomic numbers and provides better spatial resolution when compared with EDX. The

amount of energy loss is measured with an electron spectrometer similar to the energy analyzer used in XPS and a plot of relative intensity vs. energy loss is plotted as shown in Figure 2.20.

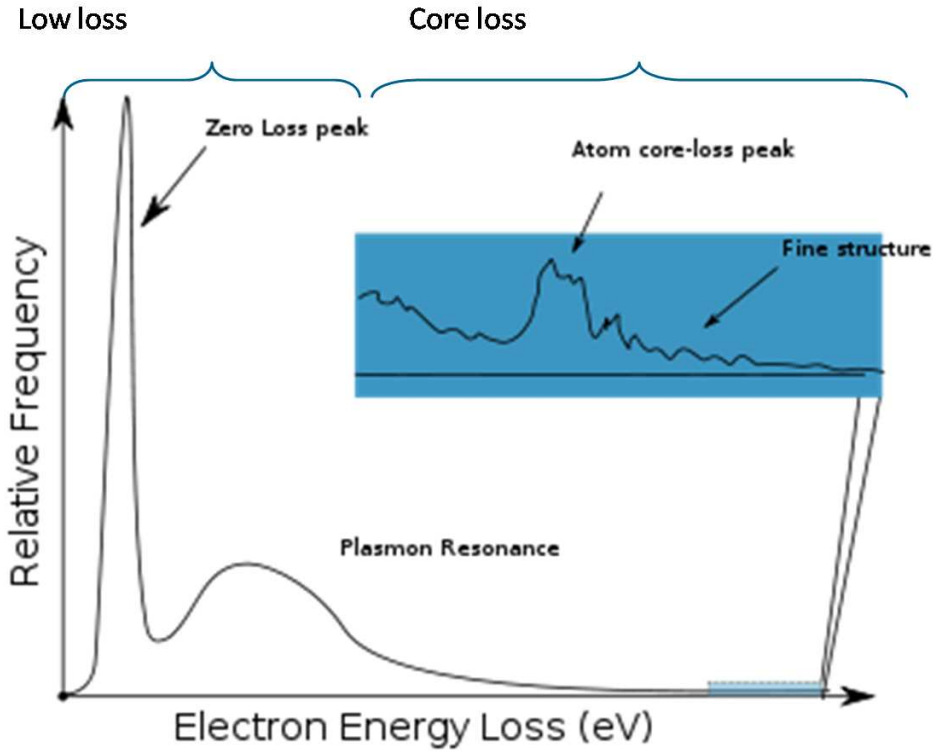

Figure 2.20: Typical EELS spectrum showing low loss and core loss regions

The Zero Loss peak consists of elastic forward-scattered electrons which have lost no energy. The Plasmon Resonance peak is due to the collective response to the electron beam by all valence electrons. The ratio of plasmon peak intensity to zero-loss peak intensity may estimate the sample thickness. Of most interest is the region of high-energy loss which contains core loss peaks. The peaks in this region are characteristic for each element and can provide chemical information. The fine structure of the peaks also contains information about the electronic structure (e.g. O peak in MnO is different than in NiO).

2.4 Atomic Force Microscopy

Atomic force microscopy (AFM) or scanning force microscopy is a very high resolution surface imaging technique, used to obtain topographical information from a sample surface at near atomic resolution [**2**]. The main benefit of AFM over other more sensitive techniques such as scanning tunnelling microscopy (STM) is that AFM may be used on a broader range of samples, including insulators, and may also be used in air. In the simplest terms, AFM operates by placing an atomically sharp tip at the end of a cantilever in close proximity to a sample surface and measuring the resultant force acting on the tip.

When two materials are brought into close proximity, inter-atomic forces are exerted between the two materials. AFM measures the magnitude of these forces, which include Van der Waals, electrostatic or magnetic forces, and uses them to determine characteristics of the surface being investigated [**18**].

The three modes of operation used for AFM are contact mode, tapping mode and non-contact mode. Contact mode AFM operates by rastering a sharp tip (made either of silicon or Si_3N_4 attached to a low spring constant cantilever) across the sample. An extremely low force (~10^{-9}N, interatomic force range) is maintained on the cantilever, thereby pushing the tip against the sample as it rasters across the sample surface and monitoring the changes in cantilever deflection. The force acting on the tip and the resulting cantilever deflection can be related using Hooke's law; $F = -kx$, where k is the spring constant of the cantilever and x is the deflection. The value of k may range from 0.01 N/m to 1.0 N/m, resulting in forces ranging from nN to μN for ambient AFM [**18**].

The tip is brought to its operating position in two stages. Firstly, the user brings the tip to a height above the surface of approximately 1 mm, using an optical microscope system which is designed to focus on surface features at an image distance of 1 mm. The tip is then engaged using a piezoelectric motor which lowers the tip in increments

of 10 μm (i.e. ~ 100 "steps") until the tip comes into contact with the surface. The sample surface is then scanned by moving it under the tip using a piezoelectric scanner.

As the surface is moved beneath the tip the cantilever is deflected by forces exerted on it by the surface. A laser beam aimed at the back of the cantilever–tip assembly reflects off the cantilever surface to a split photodiode, which detects the small cantilever deflections. A feedback loop, shown schematically in Figure 2.21, maintains constant tip–sample force by moving the scanner in the z direction to maintain the setpoint deflection. Without this feedback loop the tip would "crash" into a sample with even small topographic features.

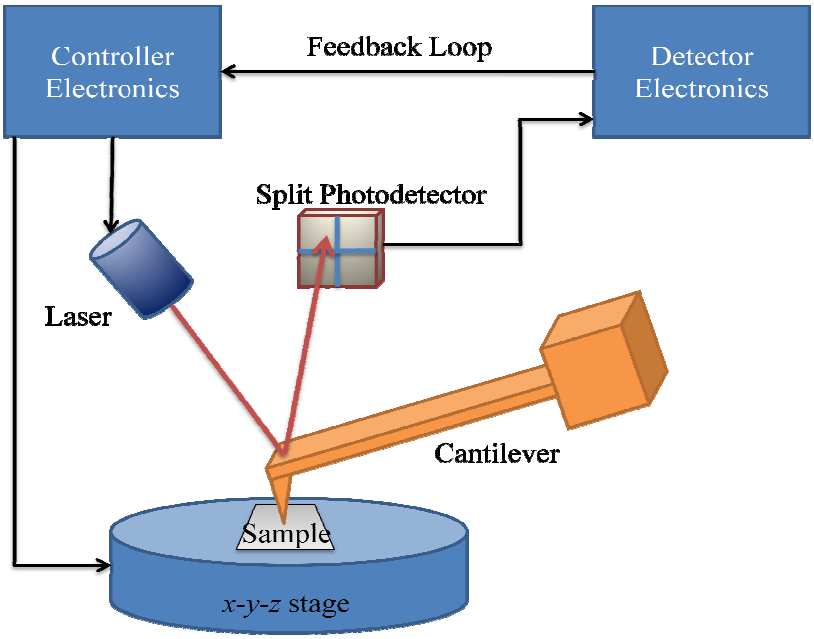

Figure 2.21 Operational diagram for AFM which shows how tip deflections are measured using laser light reflected from the back surface of the tip [18].

By maintaining a constant tip-sample force the seperation between the tip and the sample is calculated. The distance the scanner moves in the z direction is stored relative to the special variation in the x-y plane to generate a topographical image of the sample surface.

Using contact mode the surface may be scanned in two ways; either by keeping the tip position constant and monitoring the changes in cantilever reflection (constant height mode), or by maintaining a constant cantilever deflection by altering the position of the tip relative to the surface so as to keep a constant force between the two (constant force mode). The latter of these two is typically used when the initial state and smoothness of the surface is not known as it is not affected by the presence of contamination or rapid changes in the topography of the surface as is the case for constant height mode which can damage the tip. Constant height mode is only used when the surface is known to be relatively flat so as to avoid tip damage due to surface contamination or abrupt changes in topography. However, constant height mode can provide near atomic resolutions when the sample is known to be atomically clean and flat showing atomic corrugations and steps.

Although operating in contact mode is useful, it suffers from a number of drawbacks that limit its use on a number of sample types. Crucially the constant downward force on the tip often damages many surfaces including silicon. However this problem can be overcome be the use of tapping mode AFM. In tapping mode, the AFM tip/cantilever oscillates at the sample surface while the tip is being scanned; thus, the tip lightly taps the surface while rastering and only touches the sample at the bottom of each oscillation. This prevents damage to the surface due to surface contamination and overcomes problems associated with friction, adhesion and electrostatic forces. Tapping mode imaging is implemented by oscillating the cantilever assembly at or near the cantilever's resonant frequency using a piezoelectric crystal. The piezo motion causes the cantilever to oscillate with a high amplitude (typically from 20 nm to 100 nm [**18**].) when the tip is not in contact with the surface. The frequency of oscillation is kept constant by altering the position of the tip relative to the surface, which is again monitored using the position of the deflected laser beam. Non-contact mode is commonly used for soft samples, such as biological material, where physical contact may damage the surface. In this mode the cantilever oscillates above the surface, slightly

beyond its resonant frequency. It operates by measuring the attractive Van der Waals forces which extend from 1 nm to 10 nm above the surface, altering the tip position in order to maintain constant oscillation frequency.

2.5 References

[1] D. P. Woodruff and T. A. Delchar, *Modern Techniques of Surface Science*. `: Cambridge Solid State Science Series, 1986.

[2] J. C. Vickerman, *Suface Analysis: The Principle Techniques*, J. C. Vickerman, Ed. Wiley, 1997.

[3] L. C. Feldman and W. Meyer, *Fundementals of surface and thin film analysis*. Elsevier Science Publishing Co. Inc., 1986.

[4] D. Brigggs and J. T. Grant, *Surface Analysis by Auger and X-ray Photoelectron*. IM Publications, 2003.

[5] LaSurface. [Online]. http://lasurface.com

[6] NIST Database. [Online]. http://srdata.nist.gov/xps/

[7] J. F. Moulder, W. F. Stickle, P. E. Sobol, and K. D. Bomden, *Handbook of X-Ray Photoelectron Spectroscopy*, J. Chastain, Ed. United States of America: Perkin-Elmer Corporation, Physical Electronics Division, 1992, XPS Handbook.

[8] S. Oktyabrsky, et al., *Materials Science and Engineering B*, vol. 135, no. 3, pp. 272-276, 2006.

[9] G. Alverez and H. J. Silverstone, *Phys. Rev. A*, vol. 40, p. 3690, 1989.

[10] M. P. Seah and S. J. Spencer, "Ultrathin SiO2 on Si II. Issues in quantification of the oxide thickness ," *Surf. Interface Anal.*, vol. 33, pp. 640-652, May 2002.

[11] D. Briggs and M. P. Seah, *Practical Surface Analysis: Volume 1, Auger and X-ray*

Photoelectron Spectroscopy. Wiley, 1990.

[12] R. G. Vitchev, et al., *Appl. Surf. Sci.*, vol. 235, pp. 21-25, 2004.

[13] A. Jablonski and C. J. Powell, *Surface Science Reports*, vol. 47, p. 33, 2002.

[14] R. G. Vitchev, et al., *Journal of Electron Spectroscopy and Related Phenomena*, vol. 149, pp. 37-44, 2005.

[15] F. J. Himpsell, F. R. McFreely, A. Taleb-Ibrahimi, J. A. Yarmoff, and G. Hollinger, *Phys. Rev. B*, vol. 38, p. 6084, 1988.

[16] Wiedemann, *Synchrotron Radiation*. Springer, 2003.

[17] D. B. Williams and C. B. Carter, *Transmission Electron Microscopy Volume 1*. Plenum Publishing Corporation.

[18] V. M. G. Digital Instuments, *Nanoscope scanning probe microscope training manual*. 1999.

Chapter 3

Experimental Details

This chapter describes the ultra high vacuum (UHV) systems used for these experiments, along with the thin film deposition and surface cleaning techniques employed throughout the study.

3.1 Ultra High Vacuum Systems

In order to measure the kinetic energy of photoemitted electrons, with the minimum of error, XPS must be performed under ultra high vacuum (UHV) conditions. UHV is generally defined as the vacuum regime characterised by pressures lower than 10^{-9} mbar. At these pressures the mean free path of the remaining molecules in the system is of the range of kilometres hence any molecules inside the chamber will collide with the inner chamber components many times before colliding with each other.[**1**] This allows any photoemitted electrons from a sample surface to be counted by a closely placed electron spectrometer without experiencing any extra molecular collisions. Other reasons UHV conditions are necessary for surface science experiments relates to the operation of other equipment such as evaporators and mass spectrometers which require UHV in order to operate properly, and most importantly to minimise sample contamination.

The surfaces of solids which are exposed to atmosphere are significantly more complex than clean, reconstructed or relaxed surfaces. On exposure to the atmosphere, atoms and molecules may adsorb on the sample surface destroying any well-ordered surface structure. The presence of this contaminant layer prohibits any controlled, systematic investigation of surface properties. To enable atomically clean surfaces for study, such surfaces need to be maintained in a contamination-free state. Hence, by working at

UHV a clean sample surface can be maintained for the duration of the experiment. A number of different UHV systems were used throughout the course of this work, each with particular measurement capabilities for the range of experiments undertaken.

3.1.1 Surface Science Vacuum System

The majority of work in this study was carried out on the dedicated surface science chamber shown in Figure 3.1; which included *in-situ* thin film deposition techniques and high temperature resistive heating capabilities of the substrate for annealing and surface cleaning purposes. The system consisted of two chambers; a small load lock with a base pressure of 10^{-7}mbar which could hold up to three samples and a main chamber where a base pressure of better than 10^{-10} mbar was routinely achieved after a bakeout procedure with pumping carried out by a turbo molecular pump backed by a rotary roughing pump and a titanium sublimation pump.

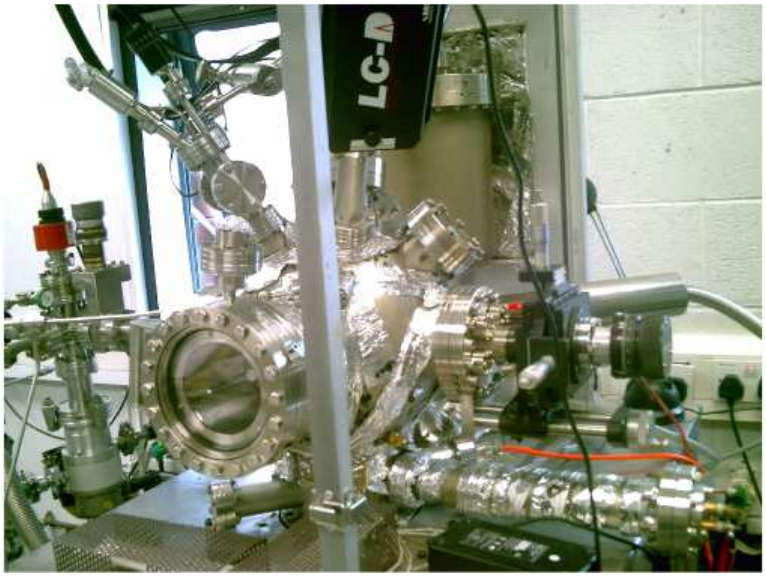

Figure 3.1 : UHV surface science chamber equipped with XPS, LEED, mass spectrometer, thermal gas cracker, e-beam and hot wire deposition capabilities

Samples were fixed to a sample stub, which could be heated *in-situ* up to 700 °C using resistive current heating. Sample temperatures up to 550 °C were measured by calibrating the heating stub using a thermocouple attached directly to the sample. A pyrometer was used to measure sample temperatures greater than 550 °C. The chamber is equipped with a dual anode X-ray source (Mg and Al) and a VG CLAM electron energy analyser with a triple channel electron multiplier as well as a four pocket mini e-beam evaporator and thermal evaporation sources for thin film deposition. A mass spectrometer was used as a residual gas analyser and a thermal gas cracker was also available for surface cleaning purposes. The system also contained low energy electron diffraction (LEED) optics which wasn't used in these experiments.

3.1.2 Dedicated XPS Chamber

The second XPS system shown in Figure 3.2 consisted of three vacuum chambers; a small load lock maintained at a pressure of 10^{-2} mbar for the introduction of multiple samples, a preparation chamber maintained at 10^{-7}mbar for in-situ anneals up to 500°C, and an analysis chamber with a base pressure of 10^{-10} mbar again equipped with a dual anode X-ray source (Mg and Al), and a VG CLAM electron energy analyser with a triple channeltron detector.

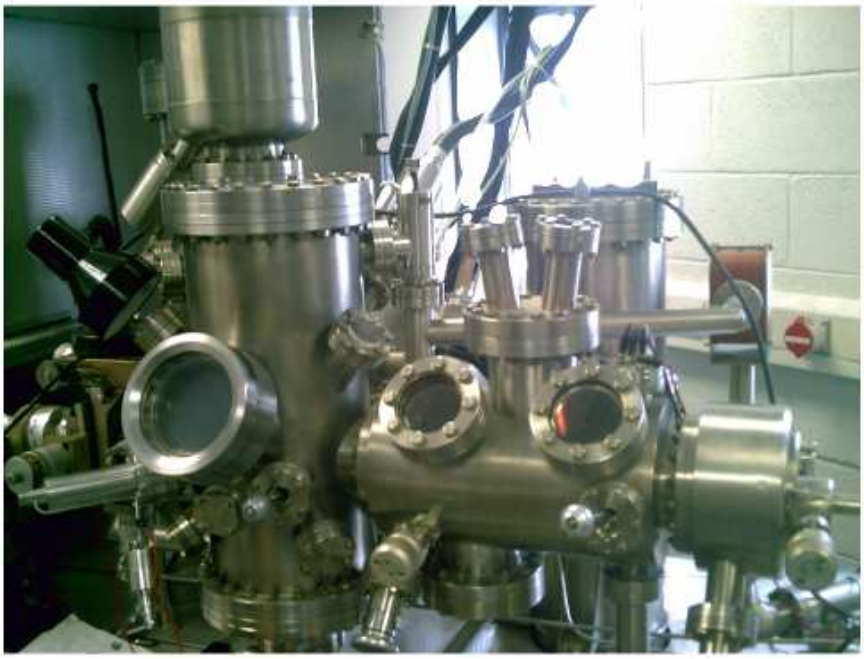

Figure 3.2 : Dedicated XPS system with 3 vacuum chambers to allow for rapid sample introduction to UHV

The chambers were pumped using diffusion pumps backed by rotary pumps. UHV conditions are achieved after a 12 hr bake at 150°C. The advantage of this system is that the three separate chambers, coupled with a sample holder stages within the load lock and analyser allows for rapid introduction of multiple *ex-situ* prepared samples to UHV conditions. The obvious disadvantage of the system is the lack of any in-situ deposition or sample cleaning techniques; meaning that deposited thin film samples were loaded after exposure to atmosphere. This system was used in

this work for the investigation of interdiffusion in thick copper/manganese films; this is presented in Chapter 5.

3.1.3 Dedicated Deposition Chamber

The system shown in Figure 3.3, was a dedicated Leybold Univex deposition chamber containing both hot filament and e-beam techniques allowing for sequential layer-by-layer growth studies of two materials. Film thicknesses were measured using a water cooled quartz crystal deposition monitor which could be positioned in front of either evaporation source. The resolution of the monitor enabled the measurement of deposition rates as low as 0.1Å/s.

Figure 3.3 : Dedicated Deposition Chamber

This system allowed for the rapid introduction of multiple samples as UHV was not required for the depositions. Chamber pressures of $<10^{-6}$ mbar were achieved after 3 hour pump down by turbomolecular pump backed by a rotary pump. Samples could be attached to a large sample holder which allowed for the deposition of identical films on

a multiple number of substrates at the same time. This system was used to grow the copper/manganese thick films investigated in Chapter 5.

3.1.4 Synchrotron based photoemission vacuum system

The final vacuum system used was at the ASTRID Synchrotron in the University of Aarhus, Denmark, where the photoemission studies presented in Chapter 4 were performed using the SX700 beamline shown in Figure 3.4.

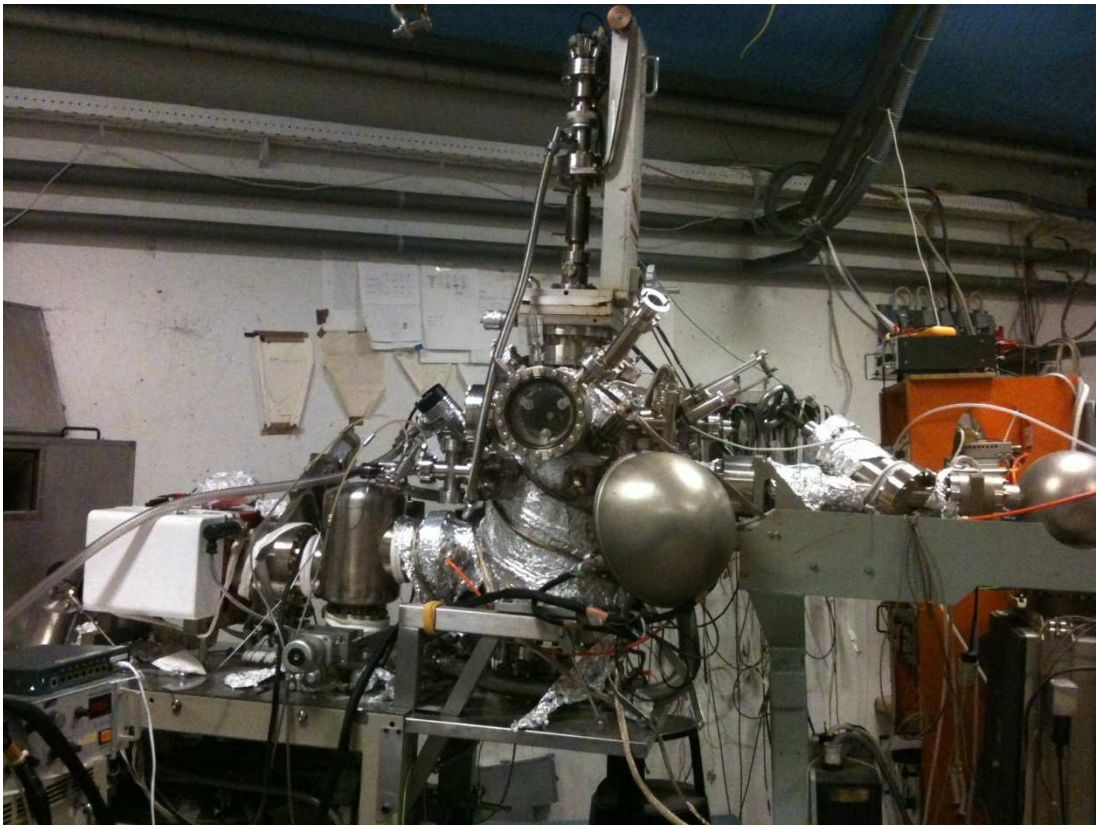

Figure 3.4 : SX700 beamline at the ASTRID synchrotron in Aarhus, Denmark

The ultrahigh vacuum system consists of a preparation chamber (5×10^{-10} mbar) and an analysis chamber held at 2×10^{-10} mbar. A schematic diagram of the Astrid synchrotron is shown in Figure 3.5.

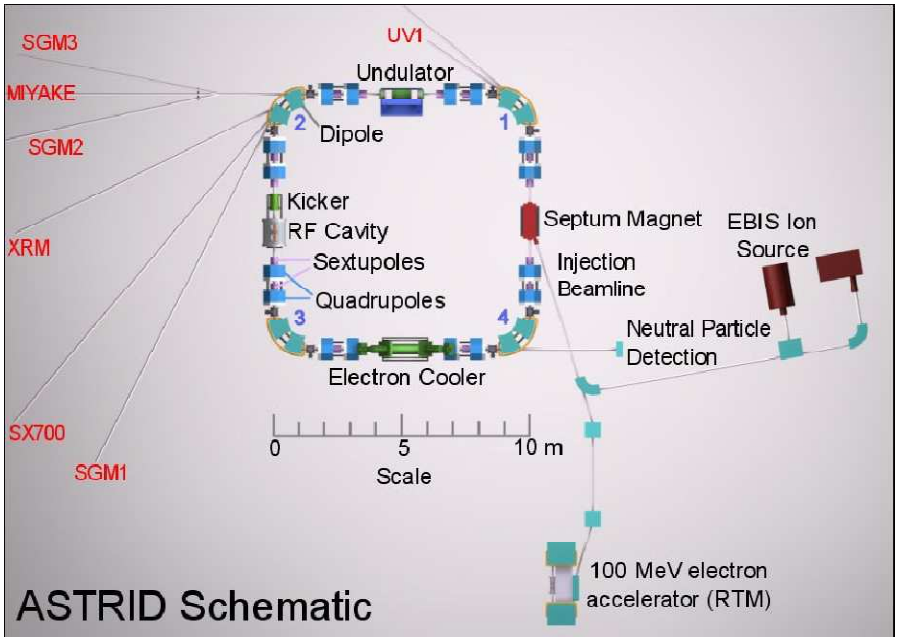

Figure 3.5 : Diagram of the ASTRID synchrotron in Aarhus, Denmark.

Photon energies from 30-700 eV can be selected allowing for core level, valence band and workfunction measurements to be taken at a range of surface sensitive energies. In the photoemission system, a single channeltron CLAM electron energy analyzer is used to detect the photoelectron signal.

3.1.4.1 XPS systems

The mode of operation of the dual anode X-ray sources (Mg and Al) used in the two conventional XPS systems described above is graphically illustrated in Figure 3.6.

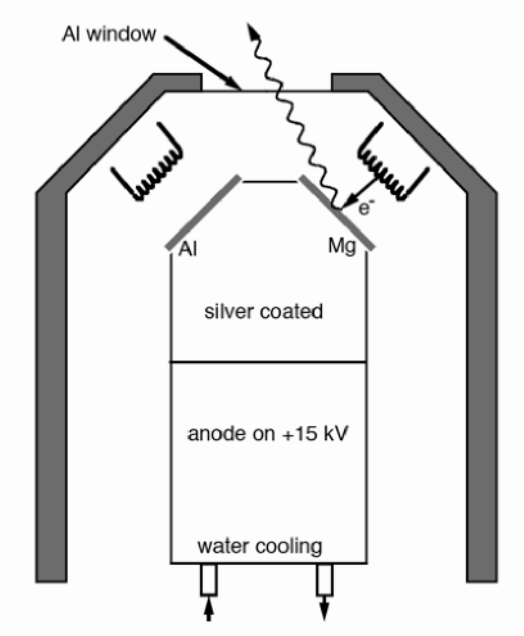

Figure 3.6 Diagram showing the operation of a dual anode X-ray source [2]

The x-ray source consists of a copper, water cooled anode target coated with thin films of aluminium and magnesium that can be selected independently. The anode typically operates at voltages ranging from 10-15 keV. This is placed in line with a filament cathode, which bombards the target with high energy electrons. The high electron flux necessitates water cooling of the target due to the high levels of heat generated, which would be enough to evaporate or damage the metal thin films on the surface of the anode.

The electron beam generates a continuous Bremsstrahlung energy distribution emission, with a maximum intensity at the Kα transition energy which results from the transition of an electron from the unresolved Al or Mg $2p$ doublet to the $1s$ core level. For the aluminium target this results in a peak energy of 1486.7 eV with a line width of 0.85 eV and for the Mg target, the value is 1253.6 eV with line width of 0.7 eV. The line

width is a reflection of the doublet separation of the $2p$ peak and is a composite of the natural line widths of the $2p_{3/2}$ and $2p_{1/2}$ peaks. For Al $2p$ the doublet separation of the component peaks is 0.43 eV, contributing to a relatively broad overall line width. The doublet separation for the Mg $2p$ is significantly smaller than that of the Al $2p$ peak, producing the narrower overall line width. Some Bremshtralung radiation produced along with the x-ray signal is partially removed by placing an Al foil (~ 2 µm thick) at the exit aperture of the x-ray source, while radiation which is not removed adds to the background of the spectrum.

The x-rays striking the sample surface result in the emission of photoelectrons, as described in Chapter 2. These photoelectrons are collected and focused into the electron energy analyser using an electrostatic electron lens. The acceptance angle of the lens depends on the analyser design. Increasing the acceptance angle would increase the overall electron yield it would result in a trade off between the total sampling area with an increased angle taking electrons from a wider surface area. This is especially critical for angular resolved XPS as it would result in electrons with different take off angles being collected creating discrepancies in the apparent electron escape depths. For angle resolved XPS, a small acceptance angle is preferred. The electrostatic lens is designed to generate an electric field which focuses the electrons to a focal point. This is typically carried out twice with the second focal point positioned at the entrance of the electron analyser in order to reduce the spread of the electrons due to the variation in the acceptance angle.

Upon focusing the stream of electrons pass into the electron analyser and are separated according to their kinetic energy. The standard electron analyser is the hemispherical analyser as shown in Figure 3.7. This consists of two concentric hemispherical plates of radii R_1 and R_2 such that the mean radius between the two is R_0.

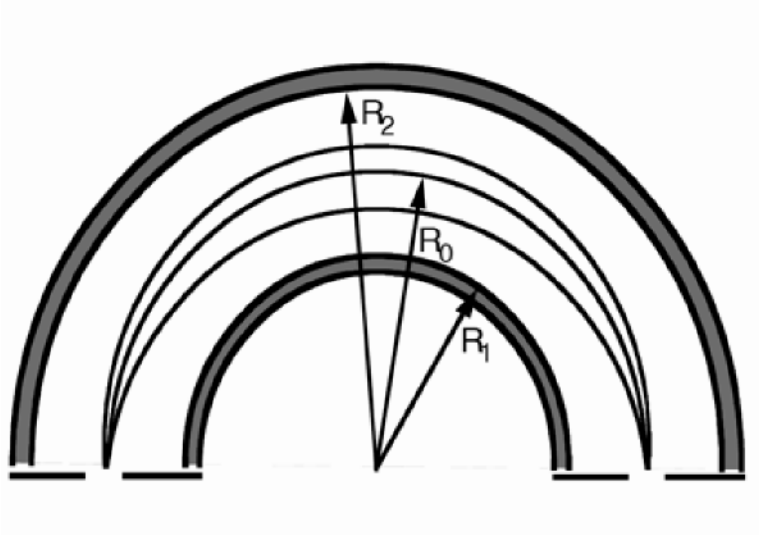

Figure 3.7 : Schematic of hemispherical analyser with R_0 the mean distance between R_1 and R_2 [4]

As the electrons enter the analyser after being focused by the lens with energy $E_0 = eV_0$, where V_0 is the retardation voltage applied to the grid, the voltage applied to the two hemispheres are adjusted so that only electrons that exactly match the pass energy are allowed to transverse along *Ro* between the two plates. This is achieved by applying a negative voltage with respect to V_0 to the outer hemisphere (V_2) which repels the electrons and a positive voltage with respect to V_0 to the inner hemisphere (V_1) which attracts the electrons. V_1 and V_2 are related to the radius of the hemispheres by the relationships:

$$V_1 = V_0\left(3 - 2\frac{R_0}{R_1}\right) \tag{3.1}$$

$$V_2 = V_0\left(3 - 2\frac{R_0}{R_2}\right) \tag{3.2}$$

so that the voltage between the plates is

$$V_2 - V_1 = V_0\left(\frac{R_2}{R_1} - \frac{R_1}{R_2}\right) \tag{3.3}$$

and $V_1 = 0.5(V_0)$ and $V_2 = (-1.33)V_0$.

As a result the retarded electron velocity is maintained. Electrons with large energy variations from E_0 will be lost to collisions with the hemispheres before they are able to transverse the full distance to the detector.

The electrons which pass through the hemispherical analyser are detected at the end of the analyser by either hitting a channel plate which is able to determine the energy of the electrons depending on where they hit the plate, i.e. the deviation from the expected position for E_0 along the plate, or by the use of a channeltron electron detector which, if there is only one, restricts the energy range around E_0 to a smaller value and hence passes a reduced number of electrons compared to the channel plate as well as a slight decrease in resolution. The channel plate which is essentially made up of a series of multipliers orientated in parallel is schematically shown in Figure 3.8 as is a single channeltron detector. [**5**]

The channeltron multipliers generally consist of a semiconductor glass tube with a funnel at the entrance to increase the acceptance angle of the electrons coming from the analyser with a length to diameter ratio of roughly 50. A potential difference of 2-4 kV is applied across the channeltron which causes an electron avalanche effect, with each successive collision releasing ever more electrons. In order to increase the number of collisions possible along the length of the tube as well as reduce ionic feedback generated in the collisions, the tube can be curved. The output of the multiplier is then measured as a pulse, providing an electron gain of 10^6 - 10^8 and potential count rates of greater than 10^6 counts per second (c.p.s.). Modern systems come equipped with multi-channel detectors giving significant increases to the count rates and sensitivities possible. The output from the pulse counters is then fed into analysis software that is

able to plot the (c.p.s) as a function of the electron binding energy. Multi-channel channeltrons are used in the CLAM analysers used throughout this work.

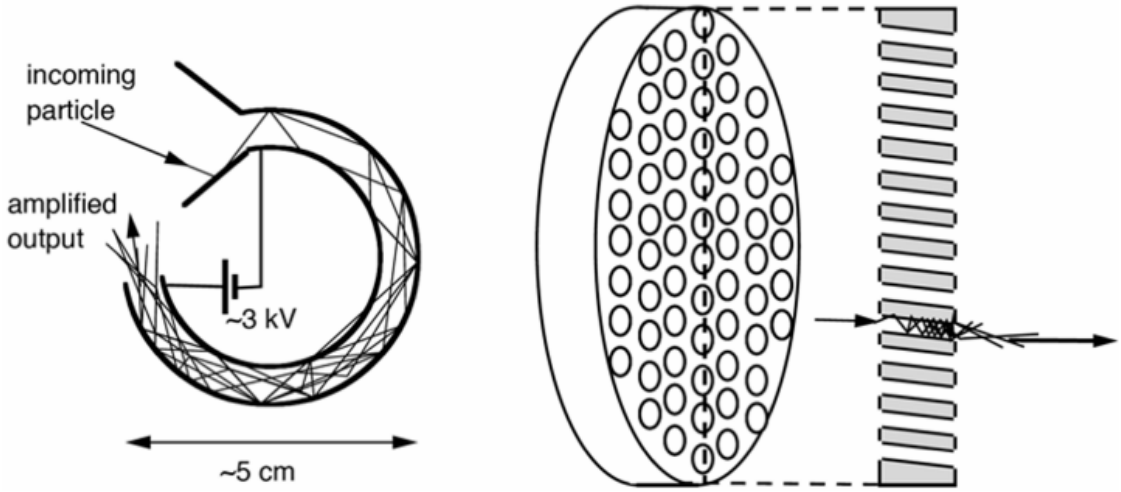

Figure 3.8 : Channeltron and channel plate consisting of a series of electron multipliers arranged in parallel

3.2 Surface Preparation methods

Three separate semiconductor substrate materials were used in this work. Most experiments were carried out on boron doped p-type Si(111) with a high quality thermally grown oxide 5.4nm thick as determined by TEM. These oxide layers were grown using a Semitool dry oxidation process in a Thermoco 9002 series furnace at 850 °C in the Tyndall National Laboratory. The second substrate studied consisted of a 640nm thick amorphous SiO_2 layer on Si(011). The final substrate studied was a prototype Aurora^{TM} carbon doped oxide (CDO) ultra low-κ (ULK) dielectric material with a dielectric constant of 2.4, as determined by elipsometry. The CDO layers had a thickness of ~ 350 nm as determined by TEM, with an open porosity of 15 % - 16 % and 30 % closed pore volume[**6**].

3.2.1 Standard organic cleaning of semiconductor surfaces

Prolonged exposure to ambient conditions results in the formation of predominantly carbon based impurities on the surface of semiconducting substrates. In this study the organic cleaning method used to remove these impurities before XPS studies consisted of successive 1 minute dips in acetone, methanol and isopropyl alcohol (IPA), with samples being subsequently dried in an N_2 gas flow before being loaded into the vacuum vessel. This procedure was used to clean both SiO_2 and CDO surfaces, however, it should be noted that as expected the XPS spectra taken in this study suggest that the procedure does not remove or alter the chemical composition of the oxide layers or the carbon content of the CDO.

3.2.2 HCl etching of Manganese

Manganese metal exposed to air results in the rapid formation of manganese oxide species on the surface. In some of the studies which will be discussed in the thesis, it was necessary to ensure the deposition of purely metallic manganese from the evaporation source. This was achieved by etching the manganese chips in dilute hydrochloric acid for 10 minutes to remove the surface oxides immediately prior to the manganese source being loaded into the UHV chamber. After loading, the UHV chamber was baked at 140 °C for 18 hours to remove water vapour and chamber contamination.

3.2.3 TEM sample preparation

TEM sample preparation is a complex procedure as the thickness of the samples investigated has to be comparable to the mean free path of the electrons which travel through the sample. The initial preparation step used in this work involved cutting two 5 mm×2 mm sections of a sample, which are sandwiched between four pieces of support silicon using a heat activated epoxy before being mechanically ground to a thickness of ~500 µm using a silicon carbide based abrasive. The sample is then polished using a liquid diamond based lubricant and mechanically ground again to a thickness of <100

μm before being placed in a dimple grinder which grinds the sample down to ~15 μm. Finally, the sample is ion milled until electron transparent and placed in a plasma cleaner where an oxygen plasma is used to reduce the surface carbon contamination immediately prior to it being loaded into the TEM. All TEM work shown in this thesis was carried out in the Materials Department in Oxford University.

3.3 Deposition Techniques

The ability to deposit high quality thin films is of critical importance to the creation of layered barrier structures. Two methods of thermal deposition were used to grow thin films throughout this work; electron beam deposition, and hot tungsten filament evaporation. The primary technique used to deposit manganese in this study was electron beam evaporation. Hot filament evaporation was also used to produce relatively thick manganese metal films which were grown in UHV and subsequently analysed using TEM. All copper films throughout the study were grown exclusively using electron beam evaporation.

3.3.1 E-Beam Deposition:

The primary metal deposition technique used in this work was electron beam (e-beam) deposition which is a physical vapour deposition (PVD) process where a high energy electron beam is focussed at a target anode containing a crucible with the evaporant. The e-beam heats the target which is then thermally deposited onto a sample situated in the line of sight of the anode.

Two separate e-beam evaporators were used throughout this study. The primary system used was an Oxford Applied Research EGC04 mini e-beam evaporator four pocket source seen in Figure 3.9, which allowed for *in-situ* deposition and analysis of various thin films in the surface science UHV chamber described in section 3.1.1. The evaporator is equipped with four separate pockets and uses either solid target rods or evaporant filled crucibles that are held at a high potential of 2 kV with respect to the

rest of the evaporator. Electrons emitted from a neighbouring tungsten filament which is held at earth potential are accelerated towards the crucible by the electric field and result in heating. The emitted electron beam has a maximum current setting of 100mA, giving a total power of 200W which is sufficient to evaporate a wide range of metal sources.

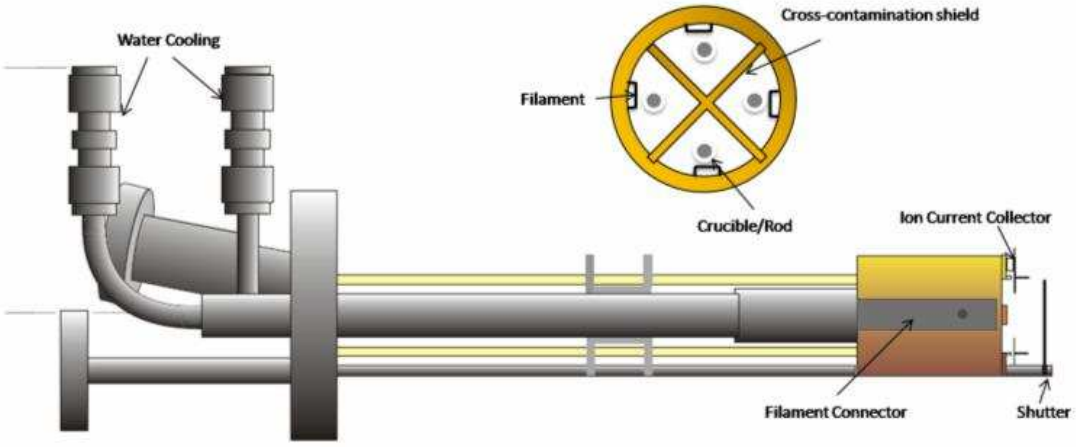

Figure 3.9 Diagram of the multi-pocket Oxford Applied Research EGC04 mini e-beam evaporator used in this study [7].

The evaporator is designed to detect the ionisation of target vapour which results in a measureable parameter and can be used as an indicator of the evaporation rate. Each pocket is shielded from contamination by neighbouring pockets through cross-contamination shielding. The simultaneous evaporation of two or more materials is achievable as each pocket is equipped with its own dedicated filament. The high heat generated by the thermal heating requires the main turret to be water cooled. The growth of the thin films can be controlled either by external power supply, or via software control which allowed direct control of evaporation rates and real-time monitoring of all parameters. The software also allowed for evaporation from all 4 pockets simultaneously, or from any selection of pockets.

The second e-beam evaporator used was a Ferrotec EV-1-8 electron beam evaporator, housed within the dedicated deposition chamber which allowed the deposition of films

at a base pressure of ~ 1 × 10^{-6} mbar. Given that this system was not equipped with any analysis techniques and also that all films were exposed to air after deposition, this system was only used in the deposition of thick copper manganese film studies in Chapter 5. In this system, illustrated in Figure 3.10, an electron beam originating from a heated tungsten filament is accelerated with a voltage of up to 5 keV and focused directly onto the source material using a system of electro-magnets which bend the beam through an angle of ~ 270 ° preventing line of sight contamination of the source material from the tungsten filament.

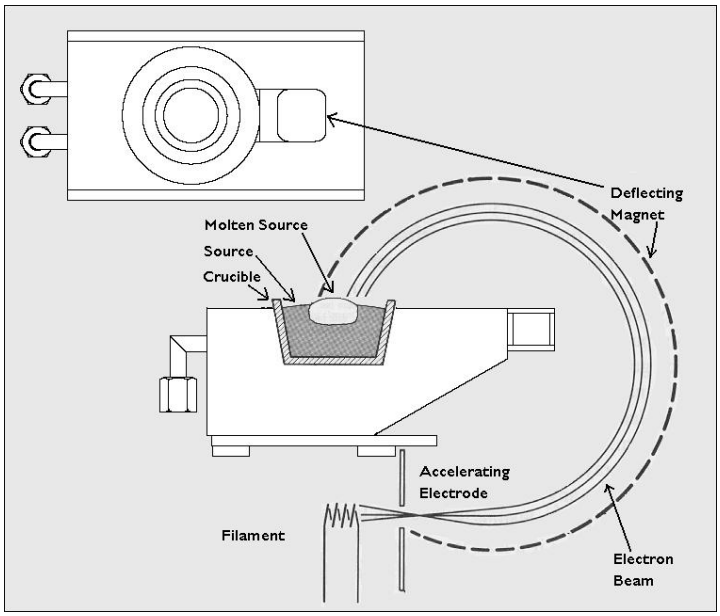

Figure 3.10: Schematic diagram of e-beam deposition showing the generation of electrons which are accelerated towards the source material using high voltage and a system of electro magnets [8]**.**

The size and direction of the electron beam is altered as required to achieve uniform heating of the source. The electron beam heats the target material placed in a crucible to a temperature where the target begins to evaporate and the sample is placed directly above the e-beam block. The localised nature of the electron beam on the material target allows much higher temperatures to be reached than with resistive heating meaning a greater range of materials, with higher melting points can be deposited. The metal vapours travel in straight lines from the source so the sample has to be placed

directly in front of the material source which is another reason for the placement of the tungsten filament away from the source. The target metal is placed in a crucible made of a high melting point material which is housed inside the e-beam block and again, due to the high temperature generated by the electron beam, the hearth, in which the crucible sits is water cooled to help dissipate the excess heat generated. The deposition rate, typically 0.01 nm/s, was monitored using a thin film thickness monitor which could be calibrated for each material used.

3.3.2 Thermal/Hot Filament Evaporation

The second deposition technique used was hot filament evaporation which is a direct method of depositing a thin film. The material to be deposited is placed in a tungsten basket as shown in Figure 3.11 which was resistively heated by a current up to the point where the material begins to evaporate.[**9**] High vacuum of better than 10^{-6} mbar is needed to prevent filament oxidation during the deposition process and to ensure metallic deposition from the evaporant. The basket heater itself is shielded from the rest of the chamber and other deposition sources to prevent cross contamination. Metal films can be evaporated from high purity (typically >99.9% purity) metal sources or metal oxides can be deposited by evaporating the metal in a background pressure of oxygen. Growth rates of < 0.1Å/s are achievable by careful control of the filament current allowing for good precision in terms of controlling the film thickness and >1 nm/s growth is easily achievable for thicker film growth.

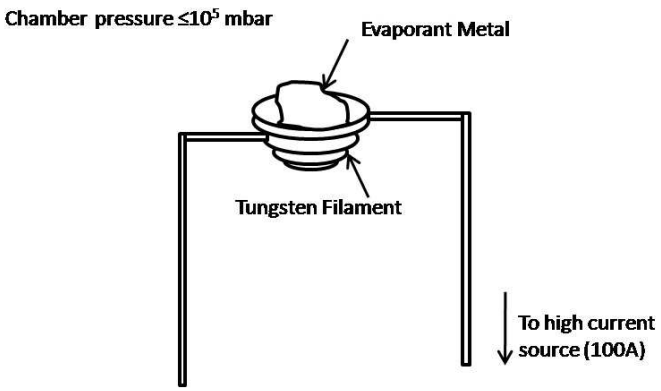

Figure 3.11: Hot Filament Evaporation

3.4 Spectral analysis of photoemission peaks

Curve fitting of photoemission spectra is used to obtain information relating to both the elemental and chemical composition of the sample surface. It has been shown in Chapter 2 that it is often possible to identify elements using the binding energy position of the photoemission peaks. However, given that contributions from different chemical species within a core level spectrum tend not to be separated by more than 5 eV, these peaks are often unresolved within the spectrum.

Therefore, in order to further analyse the various chemical states contained within the peak profile the spectrum must be fitted into a series of component peaks, each of which relating to a specific bonding environment. All curve fitting analysis presented in this study was carried as an iterative process using the AAnalyser software [**10**]. XPS core level spectra were curve fitted using Voigt profiles composed of Gaussian and Lorentzian line shapes in a 3:1 ratio and using a nonlinear Shirley-type background to account for the rise in the spectral background due to the emission of secondary electrons.

To achieve an accurate curve fit it is important to obtain accurate fitting parameters as a starting point. An example of this is the Si $2p$ spectrum shown in Figure 3.12, which was acquired from an ultra-thin ($\sim$ 1 monolayer) Si oxide on a silicon surface using synchrotron radiation based XPS. It can be seen from Figure 3.12 that identification of

the individual oxidation states of silicon from the measured "raw" spectrum requires detailed curve fitting, as they are not immediately apparent in the spectrum.

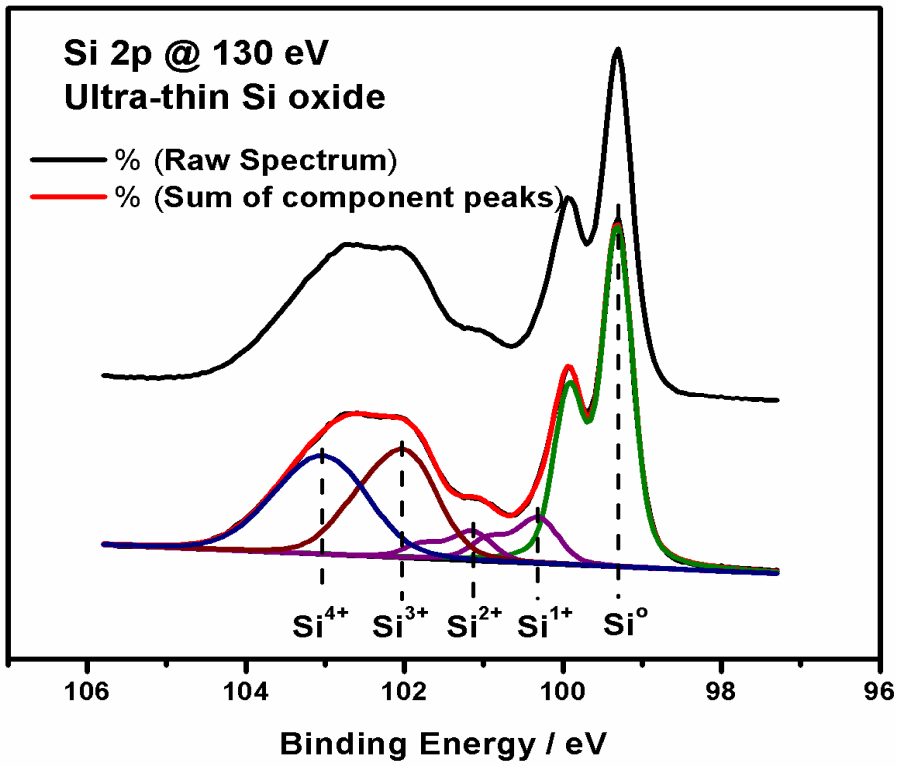

Figure 3.12 : Raw and curve fitted Si 2p spectra taken from an ultra-thin Si oxide layer using SRXPS. Curve fitting allows contributions from bulk Si (Si^o) and each of the four silicon oxidation states to be identified.

In this particular case for a thin silicon oxide, it is known that each component peak within the Si 2*p* spectrum is a doublet, with a spin-orbit splitting of 0.61 eV and an intensity ratio of 2:1 for the 2p 3/2 and 1/2 features. The full width half maximum (FWHM) of each component peak is a combination of both Lorentzian and Gaussian components. The Lorentzian width is related to the intrinsic lineshape due to the uncertainty principle, relating core-hole lifetime and the energy of the ejected electrons, and is independent of chemical composition. As such, for the spectra in Figure 3.12, the Lorentzian line width will be the same for each component. The Gaussian width is principally affected by instrumental broadening but may also depend on the chemically

homogeneity of a particular bonding state. As such, the Gaussian profile acts as a direct measure of the disorder within the local bonding environment, with more chemically disordered surfaces showing broader Gaussian peak widths. Himpsel *et al.* have reported a binding energy separation of ~0.9 eV between the Si bulk peak (Si^{o}) and each of the four Si oxidation states [**11**], however variations of ± 0.2 eV have also been reported [**12**]. Therefore, these separation values were fixed only for the initial stages of analysis, before allowing a best fit to be obtained. The curve fitting parameters used in Figure 3.12 are summarised in Table 3.1.

	Position	**Gaussian FWHM**	**Lorentzian FWHM**	**Peak Area**	**Spin-Orbit Splitting**
Si^{o}	99.33 eV	0.33 eV	0.18 eV	43.9 %	0.61 eV*
Si^{1+}	100.32 eV	0.45 eV	0.18 eV *	6.8 %	0.61 eV*
Si^{2+}	101.15 eV	0.44 eV	0.18 eV *	4.4 %	0.61 eV*
Si^{3+}	101.95 eV	0.79 eV	0.18 eV *	22.8 %	0.61 eV*
Si^{4+}	102.90 eV	1.02 eV	0.18 eV *	22.1 %	0.61 eV*

Table 3.1 : Peak fitting parameters relating to the Si 2p spectrum in figure 3.7, with * indicating a value which was fixed during the fitting process.

These parameters are used throughout this study as the starting point for curve fitting Si 2p spectra obtained using SRXPS. While increases in the Gaussian width can be attributed to chemical disorder, excessively large widths often indicate the presence of another chemical state. This may necessitate the addition of further component peaks, which must be justified with reference to published results, electronegativity values or thermodynamic data. As instrumental broadening may greatly affect photoemission line widths, the parameters used for synchrotron studies may differ substantially from those used for spectra taken using standard XPS. It should be noted that curve fitted spectra presented throughout this study does not distinguish between the raw spectrum and the sum of the component peaks. As such, in situations where the sum overlays the raw spectrum it is taken to be a measure of the accuracy of the peak fit.

Curve fitted Si 2p spectra taken from a Si native oxide surface using standard XPS, and the relevant fitting parameters, are shown in Figure 3.13 and Table 3.2 It can be seen that only the Si^{4+} oxidation component is used for the curve fit in Figure 3.13. This is due to a combination of reduced resolution and decreased surface sensitivity of standard XPS compared to SRXPS. This is further evidenced by curve fitted Si 2p spectra taken from the same surface using both conventional and synchrotron based XPS (Figure 3.14).

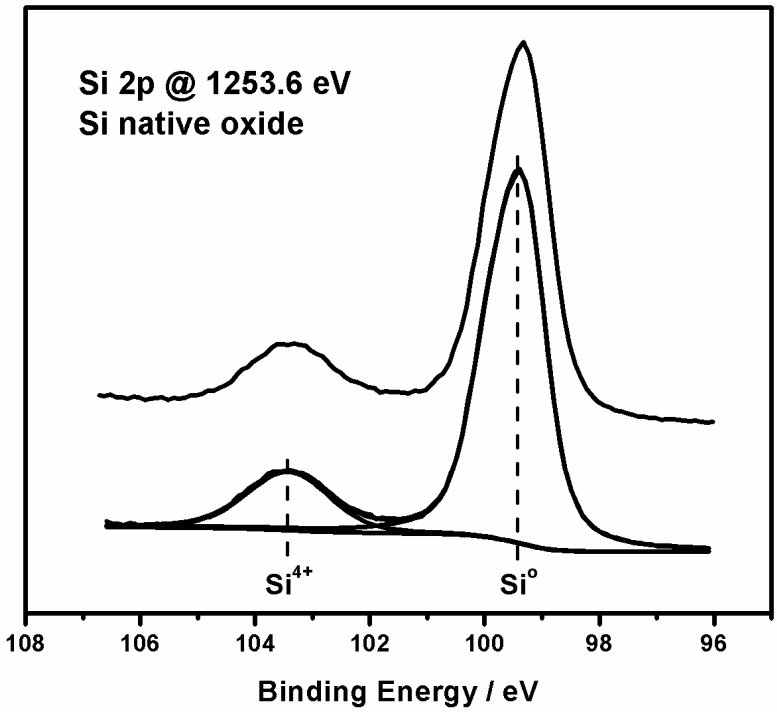

Figure 3.13 : Raw(top) and curve fitted(bottom) Si 2p spectra taken from a Si native oxide surface using conventional XPS.

	Position	Gaussian FWHM	Lorentzian FWHM	Peak Area	Spin-Orbit Splitting
Si°	99.30 eV	0.77 eV	0.30 eV	82.8 %	0.61 eV*

Si^{4+}	103.23 eV	1.28 eV	0.30 eV *	17.2 %	0.61 eV*

Table 3.2 : Peak fitting parameters relating to the spectrum in figure 3.8. The reduced surface sensitivity of conventional XPS allows only the Si^{4+} oxidation state to be resolved.

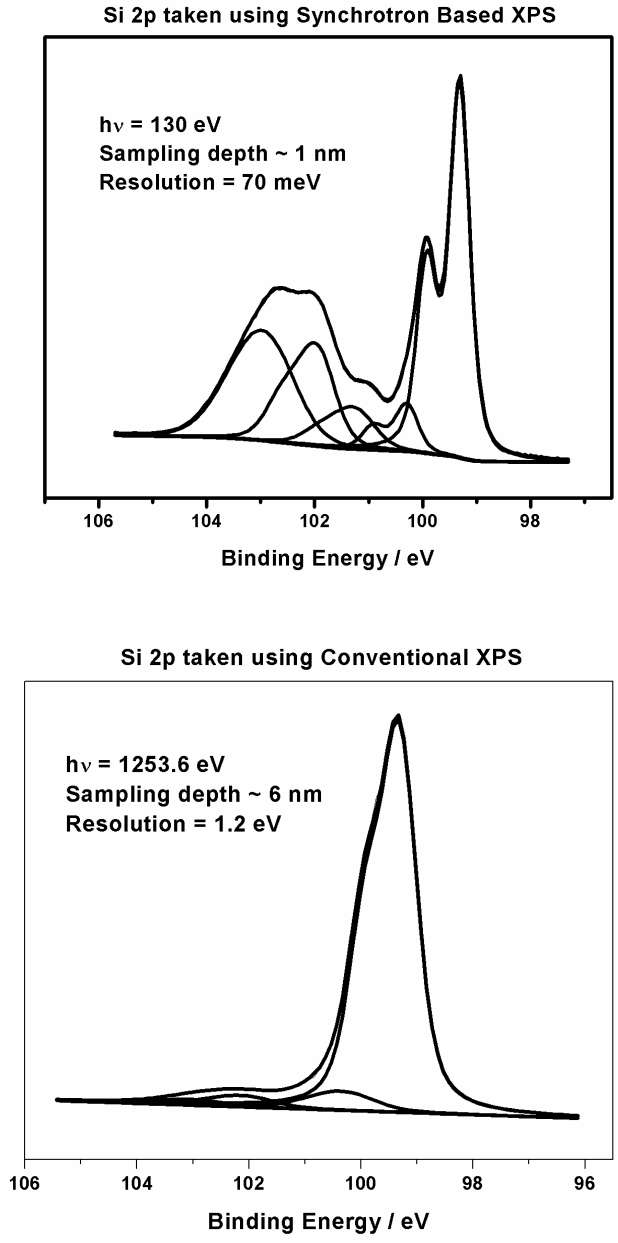

Figure 3.14 : Si 2p spectra taken from the same ultra-thin (~ 0.3 nm) Si oxide layer, using both synchrotron based and conventional XPS. Differences between the spectra clearly show the increased resolution and surface sensitivity achieved using SRXPS.

The parameters in Table 3.2 are again used throughout this study for Si 2p spectra taken using standard XPS. Apart from the Si 2p, the main core level spectra analysed in this study using curve fitting are the O 1s, Mn 2p, and Cu 2p.

3.5 TEM systems and image analysis

Two separate TEM systems were used in this study. The majority of high resolution TEM, high angle annular dark field (HAADF), EELS, and energy dispersive x-ray spectroscopy (EDX) in scanning-transmission electron microscopy (STEM) mode measurements were carried out on JEOL 2010FEG electron microscope similar to the one shown in Figure 3.15(a) based in Oxford University. High resolution EDX and EELS elemental maps were carried out using a Tecnai Osiris electron microscope shown in Figure 3.15(b). Both microscopes operated at 200 kV. Samples in cross section geometry XTEM were prepared by the conventional method of grinding and polishing followed by Ar^+ milling in a Gatan precision ion polishing system (PIPS) until electron transparent as mentioned above.

Figure 3.15 : a: JOEL 2010FEG Electron Microscope[13]**; b: Tecnai Osiris Electron Microscope**[14]

3.6 AFM image acquisition and interpretation

The atomic force microscope used in this study was a Dimension 3100 SPM equipped with an acoustic and vibration isolation hood and an anti-vibration table as shown in Figure 3.16. AFM images presented in this study were acquired exclusively using tapping mode.

Figure 3.16 : Dimension 3100 AFM

WSxM free software [**15**] was used to process the images, allowing information such as surface roughness and feature height to be acquired. Root mean square (RMS) surface roughness values quoted in this study are average values taken from a minimum of 8 sites across the sample surface.

3.7 References

[1] J. C. Vickerman, *Suface Analysis: The Principle Techniques*, J. C. Vickerman, Ed. Wiley, 1997.

[2] Twin anode x-ray source. [Online]. http://eapclu.iap.tuwien.ac.at/~werner/images/t_exp_pho.gif

[3] D. ,. W. ,. O. Heddle, *Electrostatic Lens Systems*, 2nd ed. Taylor & Francis, 2000.

[4] Electron Analyser. [Online]. http://eapclu.iap.tuwien.ac.at/~werner/images/t_exp_ana.gif

[5] Channeltron and Channel Plate. [Online]. http://eapclu.iap.tuwien.ac.at/~werner/images/t_exp_cha.gif

[6] I. Reid, Y. Zhang, A. DeMasi, G. Hughes, and K. E. Smith, *Thin Solid Films*, vol. 516, no. 4851, 2008.

[7] O. A. Research. OAR Electron beam evaporator. [Online]. http://www.oaresearch.co.uk/oaresearch/brochures/EGseries.pdf

[8] B. Y. University. Electron beam evaporator. [Online]. http://www.cleanroom.byu.edu/metal.parts/gun.JPG

[9] J. ,. S. Corneille, J. ,. W. He, and D. W. Goodman, *Surf. Sci.*, vol. 306, p. 269, 1994.

[10] A. Herrera-Gomez. AAnalyser. [Online]. http://qro.cinvestav.mx/~aanalyser/

[11] F. ,. J. Himpsel, F. ,. R. McFreely, A. Taleb-Ibrahimi, J. ,. A. Yarmoff, and G.

Hollinger, *Phys. Rev. B*, vol. 38, p. 6084, 1988.

[12] F. Jolly, F. Rochet, G. Dufour, C. Grupp, and A. Taleb-Ibrahimi, *Surface Science*, vol. 463, pp. 102-108, 2000.

[13] JOEL 2010FEG TEM. [Online].
http://www.campnano.org/web/uploads/picture/tem.png

[14] Tecnai Osiris TEM. [Online].
http://cfnewsads.thomasnet.com/images/large/840/840932.jpg

[15] Nanotec. WSxM Software. [Online].
http://www.nanotec.es/products/wsxm/index.php

4 Chapter 4

Growth and Analysis of Mn Silicate films on SiO_2

4.1 Introduction

Self forming Cu/Mn barrier layers have been proposed as a method of dispensing with the traditional sequential barrier deposition process by relying on the chemical interaction of the expelled Mn with the dielectric material to form an effective diffusion barrier layer [**1**,**2**]. The growth of Mn silicate based barrier layers through the deposition of metal Mn [**3**] and Mn/Cu alloys [**1**] on SiO_2 substrates have both been the subject of considerable interest due to their reported effectiveness as a barrier to Cu migration and improved Cu adhesion properties compared to other barrier layer candidates [**3**,**4**]. Several transmission electron microscopy (TEM) studies have shown that thin (2-3 nm) Mn silicate layers act as effective barriers to Cu, O and H_2O diffusion [**3**,**1**], while promising electrical characteristics have also been reported for Cu interconnects on Mn silicate using techniques such as sheet resistance and capacitance measurements [**4**,**5**].

However, comparatively few studies have focused on the interfacial chemistry and thermal stability of the chemical bonding present at the Mn/SiO_2 interface. In addition to this, studies using analysis techniques such as electron energy loss spectroscopy (EELS) and secondary ion mass spectroscopy (SIMS) have produced contradictory results relating to the chemical composition of the barrier layer. In particular, doubt remains over the presence of manganese oxide [**6**], Mn silicate [**4**] or both [**7**], within the Mn/SiO_2 interfacial region. A possible reason for this inconsistency is the reported

electron screening interaction which occurs between metallic Mn and Cu atoms, which is known to affect the profile of EELS Mn-L3 spectra [**7**] and Mn photoemission [**8**] spectra taken from Mn/Cu alloys. This interaction is reported to affect EELS spectra such that the electronic state measured from Mn atoms in a Cu/Mn alloy is similar to that of Mn atoms in the barrier layer region [**7**]. Similarly, Mn photoemission spectra taken from Mn/Cu alloys exhibit a spectral component on the higher binding energy (HBE) side of the metallic Mn peak [**8**] which may be interpreted as indicating the presence of an oxidised Mn species. As such, it is extremely difficult to determine the chemical composition of the barrier layer region using EELS or photoemission spectra taken from device structures containing both Mn and Cu. In addition to this the *ex-situ* sample preparation methods required for techniques such as EELS may result in the ambient oxidation of Mn [**9**] or the incorporation of H_2O into the films, creating uncertainty as to whether Mn oxide species are present due to air exposure or due to the inherent chemical interactions within the barrier layer.

In this study *in-situ* analysis of Mn silicate growth is performed in the absence of Cu, in order to identify the key chemical interactions which lead to barrier layer formation. Synchrotron based photoelectron spectroscopy (SRPES) is used to investigate the chemical composition of barrier layers formed following the deposition of a thin metallic Mn layer onto a 5.4 nm thermally grown SiO_2 film and subsequently annealed to high temperature. While numerous studies have focused on barrier growth using Mn/Cu alloys [**1**,**6**,**7**] it has recently been suggested that the deposition of Mn metal may be preferential to the use of alloys [**3**] as the presence of residual Mn impurities within Cu during thermal annealing restricts Cu grain growth, leading to an increase in the final resistance of the interconnect [**4**]. Therefore, it is suggested that investigations into the growth of barrier layers using metal Mn are not only subject to less inherent experimental uncertainty than Mn/Cu alloy studies, but may also be of significant technological relevance.

The following photoemission studies show that this growth method of the Mn silicate layer is self limiting at high temperature, with the maximum thickness of the silicate calculated to be approximately 2 nm, resulting in the presence of residual metallic Mn on the surface following annealing. Previous studies [**5**] have shown that unreacted metallic Mn remaining after barrier layer formation can diffuse to the surface of the deposited Cu interconnect during high temperature annealing and can be subsequently removed using an oxidation process. However, as mentioned previously the presence of Mn within Cu during thermal annealing restricts Cu grain growth, leading to an increase in the final resistance of the interconnect. Therefore, it would be preferable if the Mn silicate growth reaction could be controlled more accurately in order to determine the thickness of the $MnSiO_3$ layer and prevent the presence of residual metallic Mn.

Ablett et al [**2**] have previously discussed the factors which determine the initial stages of Mn silicate growth on silica based dielectrics. It was suggested that adsorbed water on dielectric surfaces leads to the presence of –OH groups, which interact with deposited Mn to form Mn oxide, with these Mn oxide species in turn reacting with silicon in the SiO_2 to form $MnSiO_3$. It has also been suggested that the absence of adsorbed water species on thermally grown SiO_2 layers reduces Mn oxide formation, hence limiting the maximum thickness of Mn silicate layers which can be formed on the surface. However, the precise role of SiO_2, metallic Mn and Mn oxide species within the Mn silicate formation process has not been investigated experimentally. Therefore, the focus of the second part of this study is to determine if the thickness of Mn silicate barrier layers grown on thermally grown SiO_2 surfaces is limited by the presence of additional oxygen species, beyond that found within the SiO_2 layer.

The chemical interactions between metallic Mn, partially oxidized Mn and fully oxidized Mn thin films on thermally grown SiO_2 were systematically investigated *in-situ* using conventional x-ray photoelectron spectroscopy (XPS). The formation of Mn oxide species on the surface of dielectric materials through the presence of surface –OH

groups, as described by Ablett et al [**2**], would be very difficult to control experimentally. Therefore, the experimental approach adopted in this study was to form partially oxidised and fully oxidised Mn thin films in UHV conditions through the evaporation of metallic Mn in a controlled oxygen background pressure. Also, given that barrier layer formation and XPS analysis was performed *in-situ* in the UHV analysis chamber, this allowed the role of both oxidised and metallic Mn species could be investigated without the complicating influence of air exposure oxidation effects. Following the completion of XPS analysis, a protective copper capping layer (20-30 nm) was deposited on selected samples before they were removed from vacuum and subsequently analysed by transmission electron microscopy (TEM), in order to accurately determine the thickness and uniformity of the silicate layers.

4.2 Experimental Procedure

High quality thermally grown SiO_2 layers on silicon substrates, were grown using the Semitool dry oxidation process in a Thermoco 9002 series furnace at 850 °C in the Tyndall National Laboratory. The XPS survey scan in Figure 4.1 displays photoemission peaks which originate from the silicon oxide, the silicon substrate and surface carbon contamination.

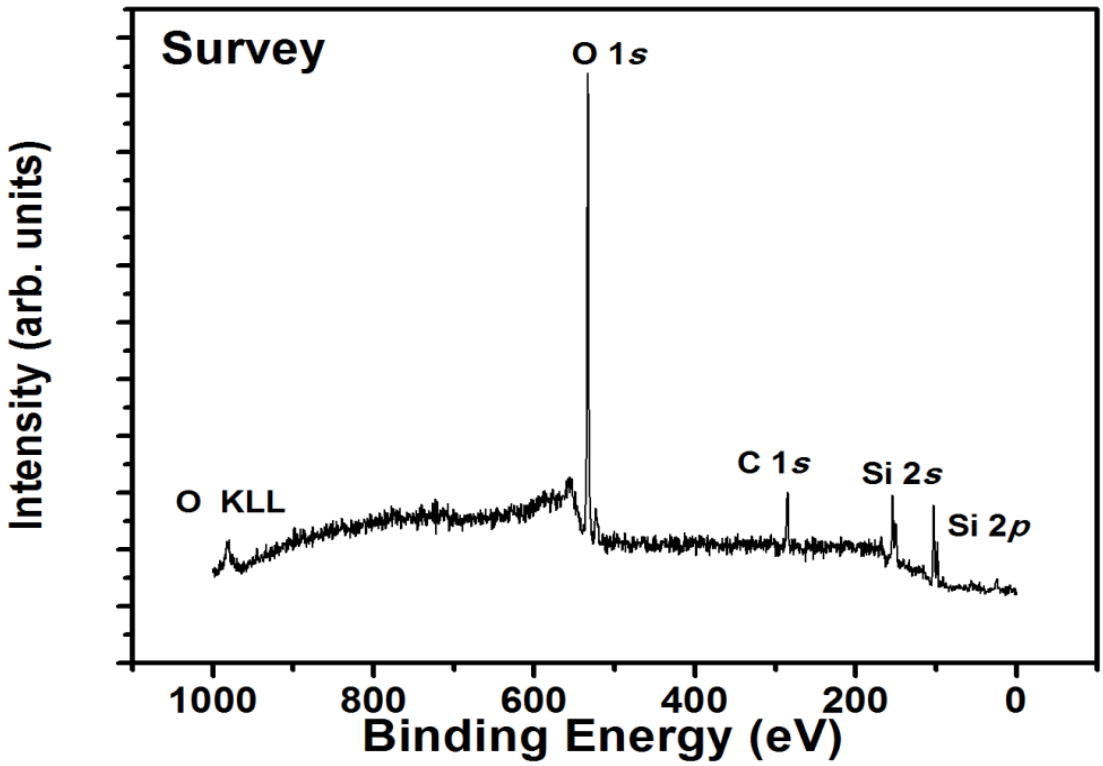

Figure 4.1: XPS spectrum of the 5.4 nm SiO_2 oxide on a silicon substrate

TEM thickness calculations yielded an approximate SiO_2 overlayer thickness of 5.4 nm as shown in Figure 4.2 and Table 4.1.

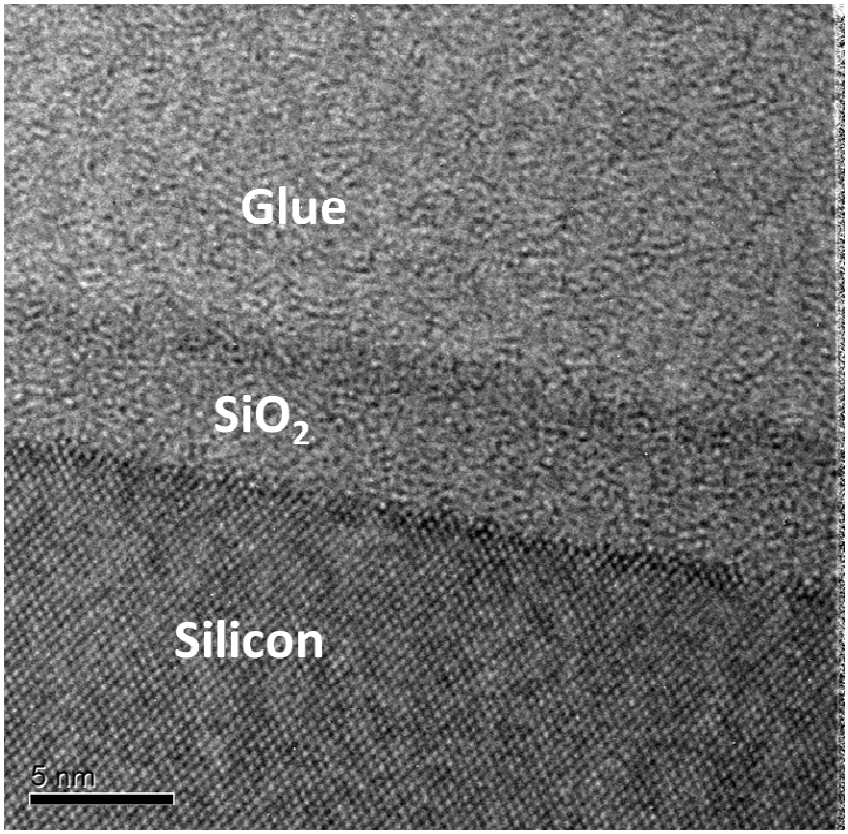

Figure 4.2: TEM of 5.4nm thermally grown SiO_2

Micrograph	Thickness SiO_2 (nm)	Micrograph	Thickness SiO_2 (nm)
1	5.230	6	5.309
2	5.228	7	5.474
3	5.365	8	5.251
4	5.592	9	5.339
5	5.381	10	5.494
		Average	5.366

Table 4.1: Average thickness values of SiO_2 overlayer from TEM measurements

The thickness of the thermal oxide was chosen so that the Si substrate (Si°) and SiO_2 component peaks of the Si $2p$ core level profile could be observed throughout all experimental stages, allowing the extent of SiO_2 to silicate conversion to be approximated using XPS curve fitting techniques as shown in the Si $2p$ spectrum in Figure 4.3. The SiO_2 surfaces were prepared using the standard degreasing procedure of successive dips in acetone, methanol and isopropyl alcohol (IPA) as described in Chapter 3, Section 2.1 before being loaded into the UHV deposition and analysis system. Samples were then degassed at ~ 200 °C for 2 hours, with the UHV chamber reaching a maximum pressure of 1×10^{-9} mbar during degassing.

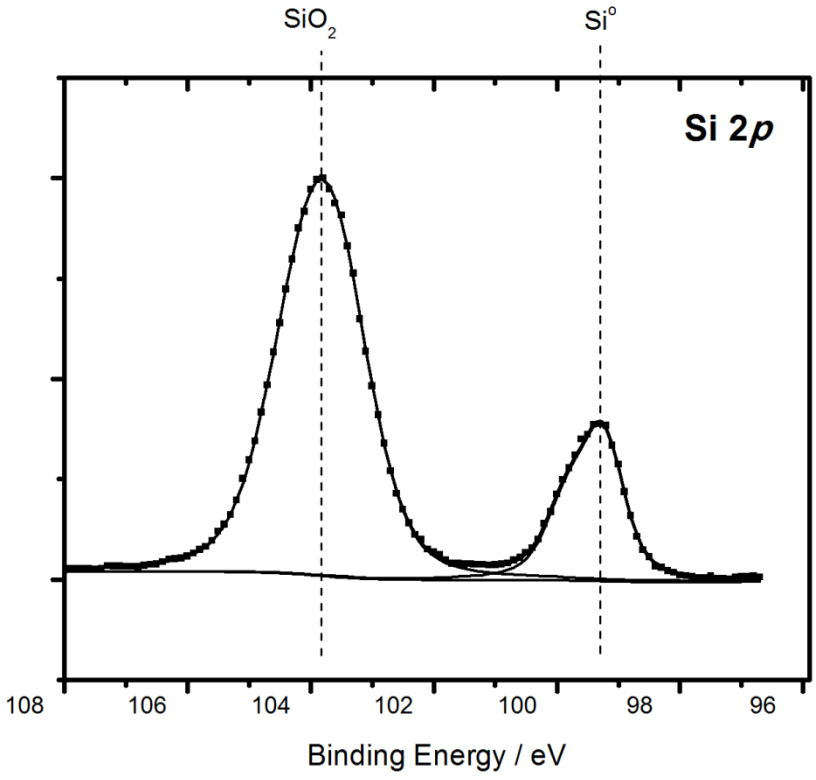

Figure 4.3: Si $2p$ spectra of 5.4nm SiO_2 sample showing the Si substrate, and the 5.4nm SiO_2 overlayer

The SRPES experiments were carried out on the SX700 beamline at the Astrid synchrotron in the University of Aarhus described in Chapter 3, Section 1.4 in the ultra high vacuum (UHV) system maintained at $< 1 \times 10^{-10}$ mbar. The photon energies used to acquire the various core level spectra were; Si 2p (130 eV), O 1s (600 eV) and Mn 3p (197 eV). Metallic manganese (99.9 % purity) thin film deposition was performed at room temperature using the Oxford Applied Research EGC04 mini electron-beam evaporator, described in Chapter 3, Section 3.1, at a chamber pressure of 5×10^{-9} mbar. High temperature vacuum annealing studies were performed at pressures $\leq 5 \times 10^{-9}$ mbar, with samples being held at the target temperature for 60 minutes in agreement with similar studies performed by Gordon *et al.* [**3**] and Lee *et al.* [**10**]. Annealing temperatures between 350 °C and 500 °C were measured using a thermocouple attached directly to the sample. The core level spectra were curve fitted using Voigt profiles composed of Gaussian and Lorentzian line shapes in a 3:1 ratio and using a Shirley-type background. The full width at half maximum (FWHM) of the Si 2*p* SiO_2 peak was 1.1 eV, with sub-stoichiometric Si oxide, Mn silicide and Mn silicate component peaks in the range 0.8 eV to 1.1 eV. The metallic Mn component of the Mn 3*p* peak profile was curve fitted using an asymmetric doublet peak with a spin-orbit splitting value of 0.4 eV. The FWHM of the metallic Mn component was acquired using the Mn 3*p* reference spectra taken from a thick (~ 10 nm) Mn film, which showed no evidence of O 1*s* or C 1*s* core level features within the detection limit of SRPES (~ 0.1 %). All curve fitting analysis presented in this study was performed using AAnalyser and Win-Spec curve fitting software programs.

The conventional XPS experiments were carried out in the dedicated surface science chamber described in Chapter 3, Section 1.1. The XPS analysis was carried out using a VG Microtech electron spectrometer at a base pressure of 1×10^{-9} mbar. The photoelectrons were excited with a conventional Mg Kα ($h\nu = 1253.6$ eV) x-ray source similar to the one described in Chapter 3, Section 1.4.1 and an electron energy analyser

operating at a 20 eV pass energy, yielding an overall resolution of 1.2 eV. High temperature annealing studies were carried out in vacuum at a pressure of 5×10^{-9} mbar, with samples kept at the target temperature for 60 minutes. Hydrochloric acid (HCl) etched Mn chips, with a purity of ~ 99.9 %, were used as a source material for the deposition of oxygen free metallic Mn thin films using electron beam evaporation. Metallic manganese thin film deposition was performed at elevated substrate temperature (150 °C) again using the Oxford Applied Research EGC04 mini electron-beam evaporator, at a chamber pressure of 5×10^{-9} mbar. The deposition of both partially and fully oxidised Mn films was carried out by the controlled introduction of O_2 gas into the UHV chamber during metallic Mn deposition. The XPS core level spectra were again curve fitted using Voigt profiles composed of Gaussian and Lorentzian line shapes in a 3:1 ratio and using a Shirley-type background. The full width at half maximum (FWHM) of the Si 2p bulk peak was 0.9 eV, with SiO_2 and Mn silicate component peaks in the range 1.1 eV to 1.2 eV. The FWHM of the O 1s SiO_2 component was 1.2 eV with Mn silicate and Mn oxide peaks in the range of 1.2 eV to 1.1 eV.

It should be noted that curve fitting of the Mn $2p$ spectrum could not be performed given that XPS ghost peaks [**11**] emanating from the Mn $2p^{1/2}$ are present within the peak profile of the Mn $2p^{3/2}$ component. As such, only non-curve fitted Mn 2p spectra are included in the second part of the study. The Mn 2p spectra are primarily used to identify the presence of metallic Mn and oxidised Mn species on the sample surface as these component peaks are easily identified from the Mn $2p^{3/2}$ peak profile without curve fitting. However, Mn $2p$ spectra could not be used to conclusively identify the presence of differing oxidised Mn species such as Mn silicate and Mn oxide, therefore these chemical species are identified in this study using curve fitted O 1s and Si 2p spectra.

High resolution transmission electron microscopy (HRTEM) studies were performed using a JEOL-JEM 3000 F and JEOL-JEM 4000EX electron microscopes operating at

300 and 400 kV, respectively. Samples in cross section geometry were prepared by the conventional method of grinding and polishing followed by Ar^+ milling in a Gatan PIPS until electron transparent. The HRTEM micrographs were calibrated using the silicon (111) planes spacing as a reference.

4.3 Synchrotron radiation photoemission study of in-situ manganese silicate formation

The curve fitted Mn $3p$ spectrum in Figure 4.4 taken after ~ 1.5 nm room temperature deposition of Mn shows the presence of a single asymmetric spectral component peak at a binding energy (B.E.) position of 47.1 eV, which has been attributed to metallic Mn in agreement with previous reports [**12**] and spectra acquired from the thick (> 10 nm) metallic Mn reference film. The presence of a single metallic peak suggests that the deposited Mn does not react with the SiO_2 surface at room temperature. This is confirmed by the corresponding O $1s$ and Si $2p$ spectra taken after Mn deposition (Figure 4.5) which are also curve fitted using single spectral components.

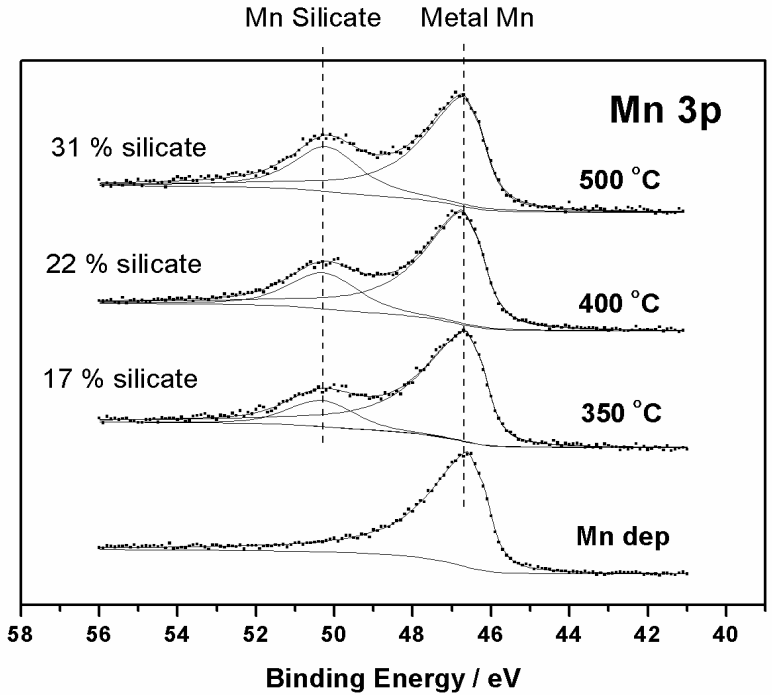

Figure 4.4: Mn 3p (197 eV) spectra showing the self limiting growth of Mn silicate following high temperature annealing of metallic Mn on a thermally grown 5.4 nm SiO_2 surface. The percentage thickness of metal Mn converted to Mn silicate is shown following each anneal.

It should be noted that the Si 2*p* spectrum taken from the SiO_2 surface before Mn deposition shows the presence of a small component peak, separated from the SiO_2 peak by 1.6 eV, which has been attributed to the Si^{3+} surface oxidation state as previously reported [**13**].

A series of high temperature anneals between 350 °C and 500 °C were then performed on the sample. The curve fitted Mn 3*p* spectra in Figure 4.4 show that high temperature annealing results in the growth of an additional spectral component, separated from the metallic Mn peak by 3.6 eV on the higher binding energy side.

The corresponding O 1*s* and Si 2*p* spectra in Figure 4.5 show the concurrent growth of additional spectral components following the 350 °C and 500 °C anneals, separated from the SiO_2 substrate components by 1.4 eV and 1.3 eV, respectively. It should be noted that the 350 °C Si 2*p* spectrum also shows evidence for the growth of a small peak at a B.E. position of 98.4 eV, which has been attributed to Mn silicide in agreement with the relative electronegativity values of Si (1.90) O (3.44) and Mn (1.55). However, due to the low levels of silicide formation, a Mn silicide component could not be accurately included in the Mn 3p peak fit. The concurrent changes seen in the Si 2p, Mn 3p and O 1s spectra following annealing suggests the formation of a single chemical species containing each of these elements. As such, the results are attributed to the growth of a thin (1 – 2 nm) Mn silicate interfacial region, in agreement with previous photoemission studies of metal silicate species [**14**,**15**]. Using the photo-ionisation cross section values published by Yeh *et al.* [**16**] the stoichiometry of this Mn silicate was calculated to be $MnSi_{0.9}O_{2.9}$. This value is consistent with that of $MnSiO_3$, the silicate composition reported previously [**7**,**2**] in barrier layer studies.

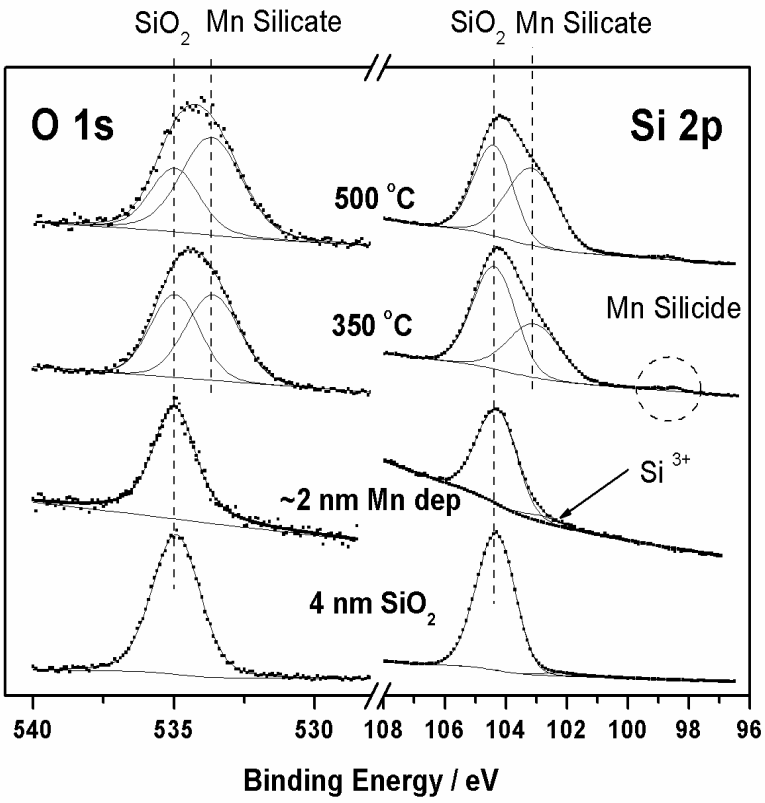

Figure 4.5: O 1s (600 eV) and Si 2p (130 eV) core level spectra corresponding to Figure 4.4 **after Mn deposition showing growth of Mn silicate following high temperature annealing. Spectra also show no evidence for the presence of Mn oxide at the Mn-SiO_2 interface.**

As stated previously, the Mn 3*p* and O 1*s* spectra in Figure 4.4 and Figure 4.5 only show evidence for the growth of a single oxidised species following high temperature annealing, which has been attributed to Mn silicate. As such, there is no evidence for the formation of manganese oxide following Mn deposition on SiO_2 and subsequent high temperature annealing. However, in addition to metal silicate formation, the growth of metal oxide species within the barrier layer region may also be of technological interest given that the reduction of SiO_2 is reported to lead to the diffusion of Si into the Cu film, increasing interconnect resistance [**17**]. Given that there is a broad range of stoichiometry values reported for Mn oxide species, and that the Mn 3p components of

these oxide species fall in a broad binding energy range [**18**], it is difficult to rule out the presence of Mn oxide based solely on the energy position of the Mn 3*p* HBE spectral component in Figure 4.4. However, the reported B.E. range for the O 1*s* component of all stable Mn oxide species is between 529 eV - 530 eV [**18**], which offers further evidence that the O 1s component in Figure 4.5 which grows following annealing (532.1 eV) is due to Mn silicate and not Mn oxide. Furthermore, the Mn 3p and O 1s spectra in Figure 4.4 and Figure 4.5 only show evidence for the growth of a single oxidised Mn species, which has been attributed to Mn silicate due to the concurrent changes seen in the Si 2*p* peak. However previous reports have shown that when both metal oxide and metal silicate species are present, they can be identified as separate spectral components within the relevant oxygen and metal photoemission peaks [**15**,**19**]. Therefore, it can be stated that there is no evidence for the formation of manganese oxide following Mn deposition on SiO_2 and subsequent high temperature annealing. This result is in contrast to the findings of Otsuka *et al.* [**7**] and Chung *et al.* [**6**] who reported the presence of Mn oxide within the barrier layer region following Mn/Cu alloy deposition. Given that the Mn/Cu interactions mentioned previously complicate the interpretation of the interface chemistry [**20**,**8**], further studies need to be undertaken in order to understand interface formation in the presence of Cu. However, based on the results of this work it can be said that Mn silicate barrier layers free from Mn oxide can be formed using metal Mn deposition.

The absence of Mn oxide following Mn deposition onto SiO_2 is in agreement with the proposed reaction mechanism of metals on SiO_2 as described in previous studies [**21**,**22**]. Ndwandwe *et al.* [**22**] have investigated the interaction between SiO_2 surfaces and a variety of metals, suggesting that metals can be classified as either reactive or non-reactive on SiO_2. It has been shown that the deposition of reactive metals commonly results in the concurrent formation of both metal-silicide and metal-oxide species [**22**], which can be subsequently converted to metal-silicate using high temperature annealing [**14**]. However, the suggested growth mode for some rare earth metals on SiO_2 is the

direct formation of metal-silicate upon annealing, without the intermediate growth of metal oxide or metal silicide species [**22**]. Based upon thermodynamic data it has been suggested [**22**] that Mn has chemically reactive properties which lie between that of highly reactive species such as Mg, and un-reactive species such as Pd. The Si 2p spectra in Figure 4.5 are in agreement with this analysis as they show no evidence of Mn silicide growth upon Mn deposition and the growth of an extremely small Mn silicide peak following the 350 °C anneal, amounting to approximately 0.6 % of the total Si 2p spectral intensity. As such, it is suggested that the behavior of metallic Mn on SiO_2 is closer to that of rare-earth metals such as Yb, resulting in the direct formation of Mn silicate without the appreciable growth of metal oxide or metal silicide species [**22**]. Therefore, the interaction of Mn with SiO_2 may be preferable to that of other metal barrier layer candidates such as Mg and Al, which have been reported to release Si into the Cu film following the reduction of SiO_2 to form metal oxide species [**1**,**17**].

In addition to investigating the chemical composition of the interface, it can also be inferred from the SRPES spectra that Mn silicate growth on SiO_2 surfaces is self limiting at high temperature. The Mn 3p spectra in Figure 4.4 show that the subsequent vacuum anneals between 350 °C and 500 °C result in the growth of the Mn silicate peak, from 17 % to 31 % of the total spectral integrated intensity, suggesting that ~ 0.9 nm of Mn was converted to Mn silicate following the 500 °C anneal, with most of the deposited Mn remaining in a metallic state. However, a further 1 hour anneal at 500 °C has no effect on the interface chemistry which suggests that the growth of Mn silicate on thermally grown SiO_2 is self limiting at this temperature, and estimated to be less than 2nm thick. This result is in agreement with the work of Ablett *et al.* [**2**] who reported that it is not possible to form Mn silicate layers thicker than 1 nm on high quality thermally grown Si oxide films.

A thin Cu film was subsequently deposited on the surface; however, as shown in the Mn 3*p* spectra in Figure 4.6 it proved extremely difficult to interpret the results seen following Cu deposition, which also included changes to the Si 2p and O 1s spectra.

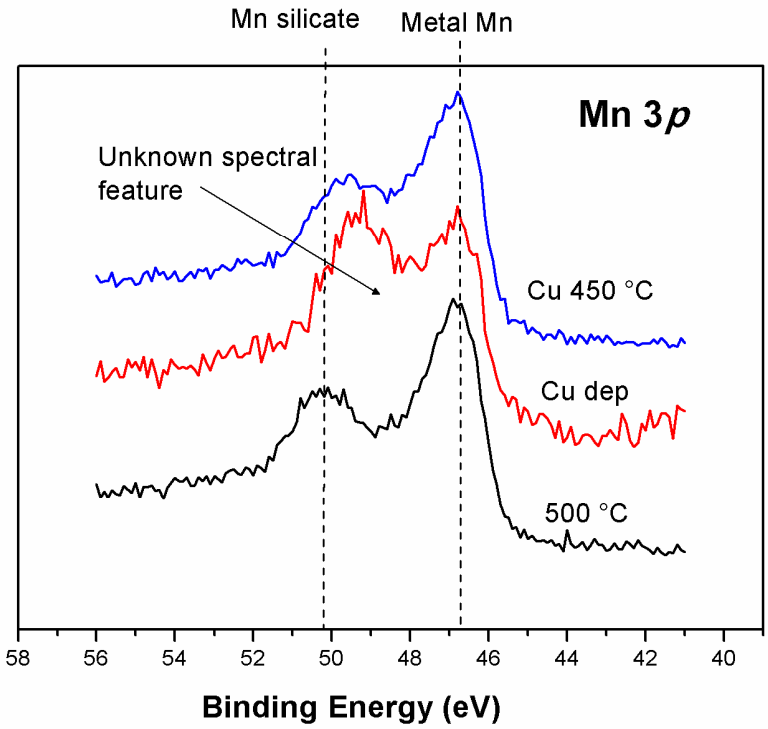

Figure 4.6: Change in profile of the Mn 3p core level spectrum following Cu deposition

The reason for this difficulty is due to an inherent reaction which takes place between metallic Mn and metallic Cu, which was clearly shown from the Mn $2p$ spectra in Figure 4.7, taken from a separate experiment in which a thin (~ 2 nm) Cu film was deposited onto a thick (~ 20 nm) Mn layer.

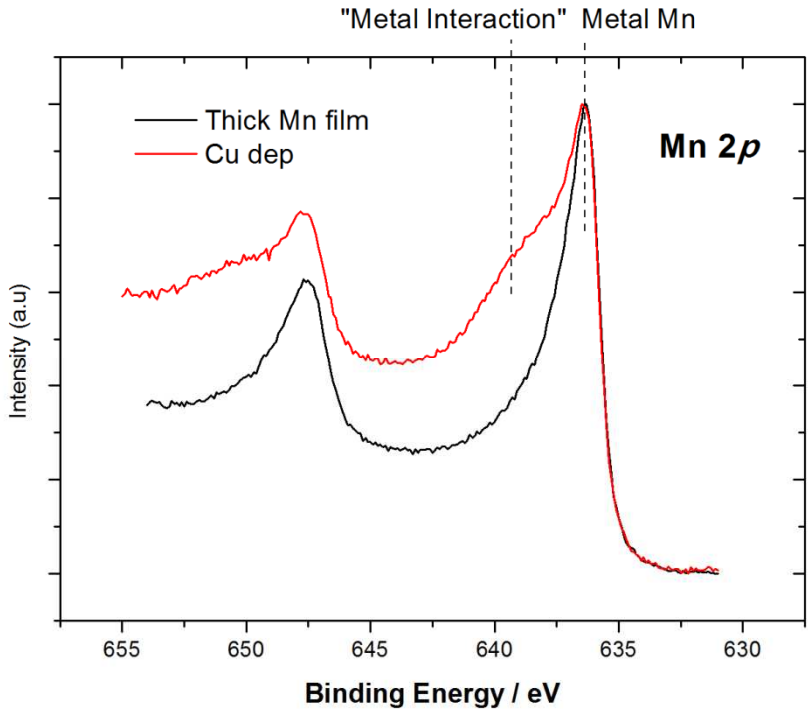

Figure 4.7 Normalised Mn 2p spectra taken from a thick (~20 nm) Mn surface, using conventional XPS, show that interaction between metal Mn and Cu results in the growth of a spectral component at HBE with respect to the metal Mn peak.

As conventional XPS spectra taken from the surface showed no evidence for O 1s or C 1s peaks it can be clearly stated that the changes seen in Figure 4.7 are due to an interaction between the Mn and Cu metallic species. However, it should also be noted that Cu 2p spectra taken following deposition (not shown) are identical to those taken from Cu reference films and as such show no evidence for the presence of any Mn-Cu interaction. While the occurrence of this metallic interaction has been reported [**23**,**8**] some questions remain as to the exact nature of the interaction. It has been suggested in a number of reports [**8**,**23**] that the changes seen in Mn photoemission spectra are due to differing levels of electron screening experienced by Mn atoms as the Mn/Cu surface alloy forms. However, this proposal does not explain the changes seen in the Si 2p and O 1s seen in experiments following Cu deposition. Alternatively, Koike *et al* [**20**] have reported that metallic Mn present within a Cu alloy becomes ionised, losing

electrons which are not transferred directly to the Cu, but instead migrate through the Mn silicate region creating a dipole charge across the barrier layer. The loss of electrons from metallic Mn directly explains the growth of the HBE component seen in Figure 4.7, a spectral change which may be easily mistaken for the presence of oxidised Mn in thin film studies where oxidised species are present. As the electrons lost by the metallic Mn are not transferred directly to the Cu, this also explains why Cu 2p spectra taken from the surface show no evidence of chemical interaction. Also, the creation of a dipole field across the barrier layer region may cause surface band bending which can be used to explain the changes seen in the O 1s and Si 2p spectra, as previously reported for the Si/SiO_2 system [**24**].

4.4 Chemical and structural investigation of the role of Mn oxide in the formation of Mn silicate

The above experiment was subsequently repeated using conventional XPS to further investigate the details of the chemical interactions and the effect of the controlled oxidation on the silicate formation process. The curve fitted O 1s and Si 2p core level spectra taken from the 5.4 nm thermal SiO_2 surface are shown in Figure 4.8. . In this instance, because of the greater sampling depth of XPS over the synchrotron radiation photon energies used in the previous section, photoemitted electrons from the silicon substrate can be observed in the Si $2p$ core level spectra. The corresponding Mn spectra taken following the deposition of a ~ 1 nm metallic Mn thin film onto the SiO_2 surface at elevated substrate temperature (150 °C) are also shown in Figure 4.9. Curve fitting analysis shows small changes to the core levels profiles suggesting that Mn deposition resulted in the growth of small additional component peaks in both the O 1s and Si 2p spectra separated from the SiO_2 components by 1.4 eV and 1.3 eV respectively. These peaks are attributed to the growth of the Mn silicate species $MnSiO_3$, in agreement with the previous photoemission results. A series of high temperature vacuum anneals between 300 °C and 500 °C were then performed on the sample.

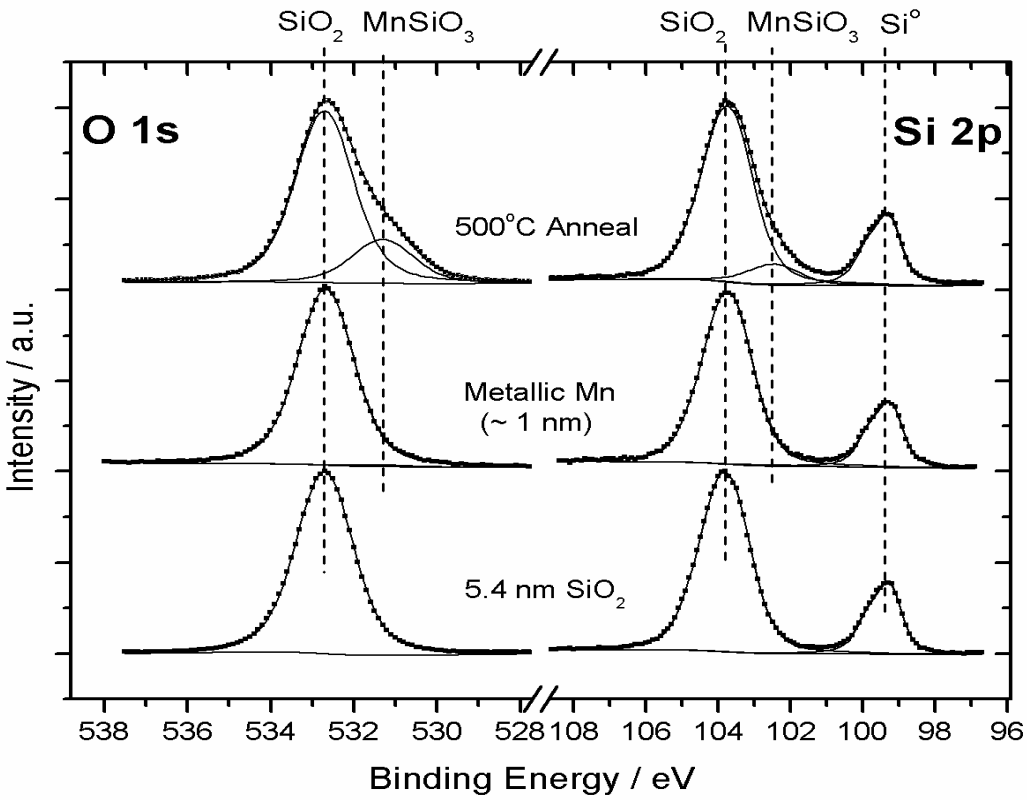

Figure 4.8 : Curve fitted O 1s and Si 2p spectra showing the growth of Mn silicate (MnSiO3) following the deposition of metallic Mn (~ 1 nm) onto SiO2 thermal oxide surface and subsequent UHV annealing.

The spectra in Figure 4.8 show evidence for further Mn silicate formation following these anneals, and this is supported by changes in the Mn 2p spectrum in Figure 4.9 which show the growth of an oxidised Mn component peak on the higher binding energy (HBE) side of the metallic Mn peak [**8**].

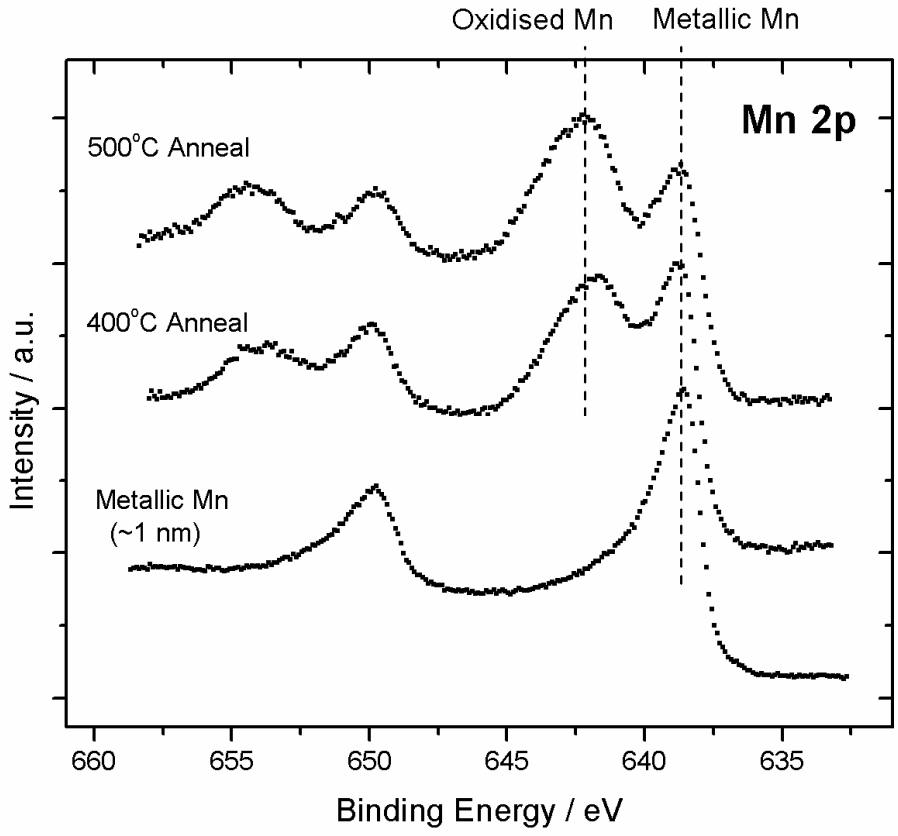

Figure 4.9 : Mn 2*p* spectra, corresponding to Figure 4.8, show the presence of residual metallic Mn on the surface following 500 °C annealing. This result suggests that the interaction of metallic Mn and SiO_2 is self limiting at high temperature.

As before within the Mn 3p spectra, the presence of residual metallic Mn following the 500 °C anneal suggest that the interaction of metallic Mn with SiO_2 is self limiting at this temperature [**2**]. Rudimentary peak fitting (not shown) of the Mn 2p spectra in Figure 4.9 suggests that only ~0.5 nm of the deposited Mn film was converted to Mn silicate following the 500 °C anneal. This limited scale of Mn silicate growth can also be seen from the corresponding Si 2p spectrum which shows that only ~ 12 % of the SiO_2 component peak was converted to Mn silicate. The results shown in Figure 4.8 and Figure 4.9 again suggest that the thickness of manganese silicate barrier layers formed

through the deposition of purely metallic Mn is self limiting at high temperature. Based on photoemission thickness calculations [**25**] the limiting thickness of the $MnSiO_3$ was calculated to be approximately 2 nm following the 500 °C vacuum anneal. In order to determine if the chemical reactivity of metallic Mn on SiO_2 surfaces is limited by the presence of additional oxygen species, specifically in the form of Mn oxide, a partially oxidised Mn film was deposited onto the SiO_2 surface and annealed to high temperature.

Figure 4.10 shows Mn 2p spectra taken following the deposition of metallic Mn in an O_2 partial pressure of 5×10^{-8} mbar, leading to an O_2 exposure of ~ 30 Langmuir (L) onto the SiO_2 surface at elevated substrate temperature (150 °C). The Mn 2p spectrum clearly shows the presence of both metallic Mn and oxidised Mn spectral components, with curve fitting analysis suggesting a metallic Mn:oxidised Mn ratio of 5:1. Angular resolved Mn 2p spectra (not shown) indicate no evidence for depth segregation between the oxidised and metallic species, which suggests that the oxygen content is homogenously distributed throughout the deposited film.

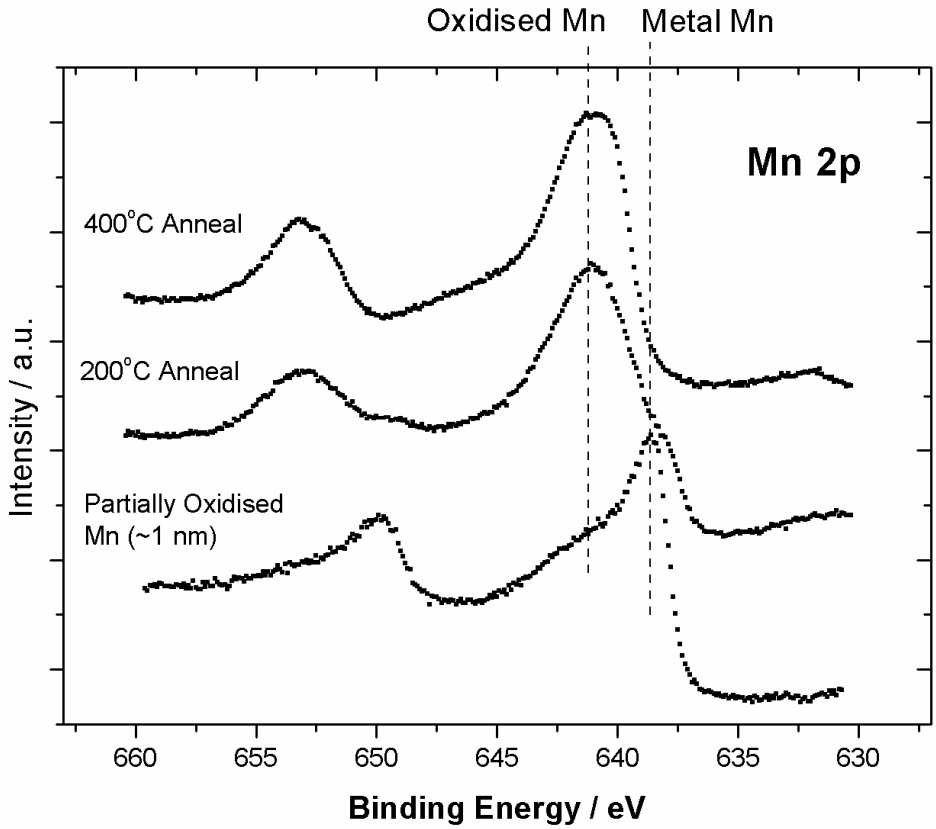

Figure 4.10 : Mn 2p spectra taken following the deposition of partially oxidised Mn (~ 1 nm) onto SiO_2 show the presence of both metallic Mn and oxidised Mn component peaks. Spectra taken following 400 °C annealing show the complete conversion of metallic Mn to Mn silicate.

While detailed chemical analysis of Mn species cannot be achieved by curve fitting the Mn 2p spectrum as mentioned previously, the curve fitted O 1s and Si 2p spectra in Figure 4.11 can be used to determine the chemical species present on the SiO_2 surface following deposition of the partially oxidised Mn film. It can be seen from Figure 4.11 that O 1s spectra show the presence of two additional component peaks on the lower binding energy (LBE) side of the SiO_2 component following deposition. The peak at 531.3 eV is again attributed to the presence of Mn silicate which formed upon deposition, which is confirmed by the growth of a Mn silicate component peak in the corresponding Si 2p spectrum at 102.6 eV (Figure 4.11).

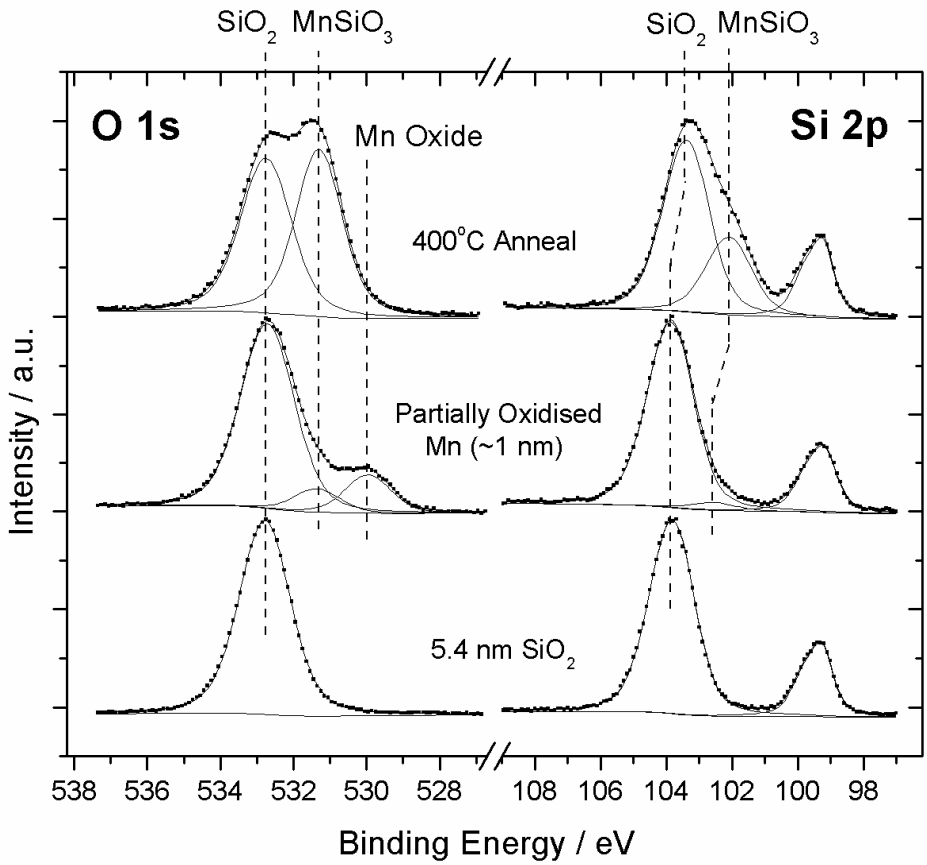

Figure 4.11 : Curve fitted O 1*s* and Si 2*p* spectra corresponding to Figure 4.10. Spectra show the complete conversion of both metallic Mn and Mn oxide to form $MnSiO_3$, resulting in higher levels of silicate growth than that seen in Figure 4.8 which indicates the increased reactivity of partially oxidised Mn films on SiO_2.

In addition to this, the O 1*s* spectrum also shows evidence for a third component peak at a binding energy position of 530.0 eV, which is attributed to the presence of Mn oxide in agreement with previous studies [**18**]. The formation of Mn oxide species following ~ 30 L O_2 exposure is in agreement with the work of B. Lescop [**26**] who has shown that the oxidation of Mn can occur at oxygen exposure levels less than 20 L. Based on this analysis it is apparent that the chemical species present on the surface prior to high temperature annealing are metallic Mn, Mn oxide, Mn silicate and SiO_2.

The sample was subsequently annealed to 400 °C in UHV and the corresponding photoemission spectra are also shown in Figure 4.10 and Figure 4.11. It can be seen from Figure 4.11 that annealing to 400 °C has resulted in considerable growth of Mn silicate, as evidenced by growth of the $MnSiO_3$ component peaks in both the O 1s and Si 2p spectra. Curve fitting of the Si 2p spectrum following annealing suggests that 48 % of the SiO_2 component peak was converted to Mn silicate, which is a considerably larger value than that seen following the deposition of metallic Mn in Figure 4.9. XPS thickness calculations [**25**] suggest that the thickness of this silicate layer is ~ 3 nm. It is suggested that this increased thickness may be attributed to an increase in the chemical reactivity of the partially oxidised Mn species on SiO_2, compared to that of the purely metallic Mn film. This increased chemical reactivity of the partially oxidised Mn film is also shown by the Mn 2p spectra in Figure 4.10 which show no evidence for the presence of any residual metallic Mn following 400 °C annealing, again in contrast to the results seen following the deposition of metallic Mn in Figure 4.9.

Figure 4.12 shows TEM images taken from the 5.4 nm thermal SiO_2 surface (5a), as well as images taken following the growth of barrier layers using partially oxidised Mn (5b) and metallic Mn (5c). The images are used to more accurately quantify the thickness of the barriers layers formed on both samples, and as such offer further evidence for the increased chemical reactivity of partially oxidised Mn. The TEM thickness values in Table 4.2 indicate that the thickness of the barrier layer formed using purely metallic Mn is ~1.7 nm (Figure 4.12c), while the Mn silicate layer formed using partially oxidised Mn is measured to be 2.6 nm (Figure 4.12b). It should be noted that the TEM thickness values shown in Table 4.2 are in close agreement with the corresponding values calculated using XPS, suggesting the photoemission calculations used in this study are accurate. It should also be noted that XPS thickness calculations suggest that the deposited thickness of Mn in both films was the same (~ 1 nm). Therefore, the increased thickness of the Mn silicate layer shown in Figure 4.12b is attributed to an

increase in the chemical reactivity of the partially oxidised Mn film compared to that of the purely metallic Mn film.

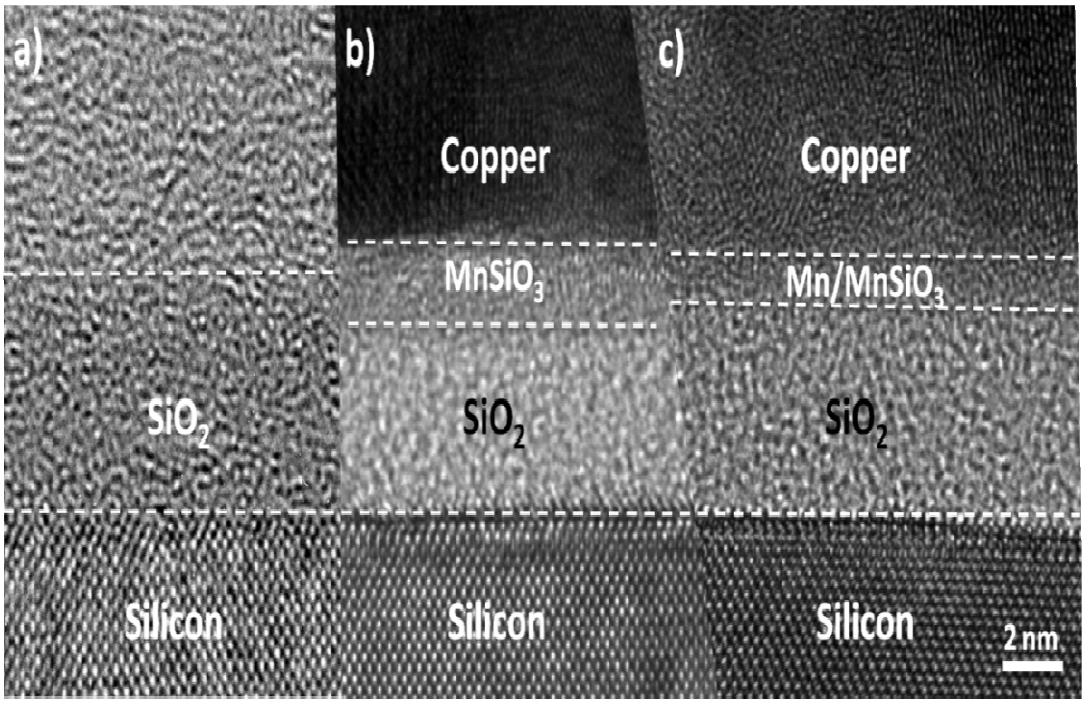

Figure 4.12 : TEM images taken from the as grown SiO_2 thermal oxide (5a), the barrier layer formed using partially oxidised Mn (5b) and the barrier layer formed using metallic Mn (5c). Images clearly show that the $MnSiO_3$ layer formed using partially oxidised Mn is considerably thicker than formed using metallic Mn. It can also be seen that $MnSiO_3$ growth has resulted in a corresponding reduction in SiO_2 thickness, indicating the conversion of SiO_2 to $MnSiO_3$ during barrier layer formation.

It should also be noted that while the partially oxidised Mn film consisted of ~15 % oxidised Mn, the remaining oxygen required to form the fully oxidised $MnSiO_3$ layer must come from the conversion of SiO_2 to Mn silicate, given that all experimental stages were carried out in UHV. The conversion of SiO_2 to $MnSiO_3$ during barrier layer growth

is confirmed by the TEM images in Figure 4.12 which clearly show that the increased barrier layer thickness seen in Figure 4.12b results in a corresponding reduction in the thickness of the underlying SiO_2.

	SiO_2 thickness (nm)	**Mn barrier layer thickness (nm)**
Thermally grown SiO_2 (5a)	5.4	--
Partially oxidised Mn (5b)	4.1	2.6
Metallic Mn (5c)	4.5	1.7

Table 4.2 : TEM thickness values corresponding to the images shown in Figure 4.12.

This observation is analogous to a comparable study by Copel et al [**19**] who investigated the interaction of La_2O_3 films on SiO_2 surfaces and reported that the growth of La silicate through thermal annealing resulted in a corresponding reduction in SiO_2 thickness. The reduction of SiO_2 thickness during the conversion of SiO_2 to $MnSiO_3$ is quantified in Table 4.2, with TEM thickness values suggesting that the presence of Mn oxide species within the partially oxidised film allowed for increased levels of SiO_2 conversion. Therefore, it is suggested that the presence of Mn oxide allows Mn silicate layers of increased thickness to be formed by facilitating the conversion of both SiO_2 and Mn to $MnSiO_3$.

It should be noted that the shift to LBE seen in the SiO_2 component of the Si 2p spectra in Figure 4.11 is attributed to the thinning of the SiO_2 layer following Mn silicate growth. It has been shown by Iwata et al. [**27**] that the binding energy (B.E.) separation between the Si° and SiO_2 components of the Si 2p profile may be increased as a function of increasing SiO_2 thickness, due to the build up of surface electronic charge during the photoemission process. In agreement with this, curve fitting

techniques suggest that the Si° - SiO_2 B.E. separation is reduced from an initial value of 4.4 eV for the 5.4 nm SiO_2 surface to 4.0 eV following the growth of Mn silicate and corresponding reduction in SiO_2 thickness. The effects of surface charging are accommodated during the peak fitting process by linking the B.E. position of the Mn silicate component to that of the SiO_2 component, using a B.E. separation of 1.4 eV in agreement with previous studies.

Along with the conversion of metallic Mn, the O 1*s* spectra in Figure 4.11 also show evidence for the complete conversion of Mn oxide to Mn silicate following high temperature annealing. This result indicates that $MnSiO_3$ layers free from metallic Mn and Mn oxide can be formed by the thermal annealing of partially oxidised Mn on SiO_2 surfaces. The conversion of Mn oxide to Mn silicate is in contrast to the finding of Gordon et al [**3**,**4**,**28**] who have suggested that Mn oxide is unreactive on SiO_2 surfaces. However, the chemical reactivity of Mn oxide species within a metallic Mn matrix may be different to that of fully oxidised Mn oxide films. Therefore, a metal free Mn oxide layer, with a thickness of ~ 1 nm, was deposited in order to determine the chemical stability of fully oxidised Mn on SiO_2. The fully oxidised Mn film was formed by evaporation of metallic Mn in an O_2 oxygen background pressure of 1×10^{-7} mbar at elevated substrate temperature of 150 °C. A post deposition anneal at the same temperature and O_2 background pressure was then performed leading to a total O_2 exposure of ~ 400 L. The Mn 2p spectrum taken following post-deposition annealing is shown in Figure 4.13 and displays no evidence for the presence of metallic Mn on the surface, showing that the film is fully oxidised. 'The corresponding O 1s spectrum in Figure 4.14 shows the presence of a Mn oxide component at a binding energy position of 530.2 eV, which is close to that previously attributed to the Mn oxide species MnO [**18**]. Given the difficulty in curve fitting Mn 2p spectrum obtained using conventional non-monochromated XPS, the exact stoichiometry of the Mn oxide species deposited in this study cannot be established. However, it can be clearly stated that the film is fully oxidised and free from metallic Mn.

A series of high temperature vacuum anneals between 300 °C and 500 °C were then performed on the sample. In agreement with the results of the partially oxidised Mn film, it can be seen from both the O 1s and Si 2p spectra in Figure 4.14 that high temperature annealing results in the conversion of Mn oxide to Mn silicate. Given that there is no evidence for the presence of metallic Mn on the surface of this sample, this experimental result shows that fully oxidised Mn can also be converted to Mn silicate following high temperature annealing on SiO_2 surfaces. This result is in agreement with previous studies which have reported the conversion of metal oxide species to metal silicate during thermal annealing for other metals such as Mg [**14**] and La [**19**]. The scale of Mn silicate growth is again quantified using curve fitting techniques, with the Si 2p spectra in Figure 4.14 showing that 36 % of the SiO_2 component peak being converted to Mn silicate. It should be noted that the SiO_2 component of the Si 2*p* spectrum in Figure 4.14 does not show the same shift to LBE previously observed in Figure 4.11 following the reduction of SiO_2 thickness, and the corresponding reduction of surface electronic charging effects. It is suggested that these charging effects were not reduced to the same extent in Figure 4.14, given that lower levels of SiO_2 conversion to $MnSiO_3$ were observed in this sample. Also, the presence of Mn oxide species, with comparatively high resistivity, on the SiO_2 surface in Figure 4.14 may have also increased the level of photoemission surface charging affects compared to that seen in Figure 4.11.

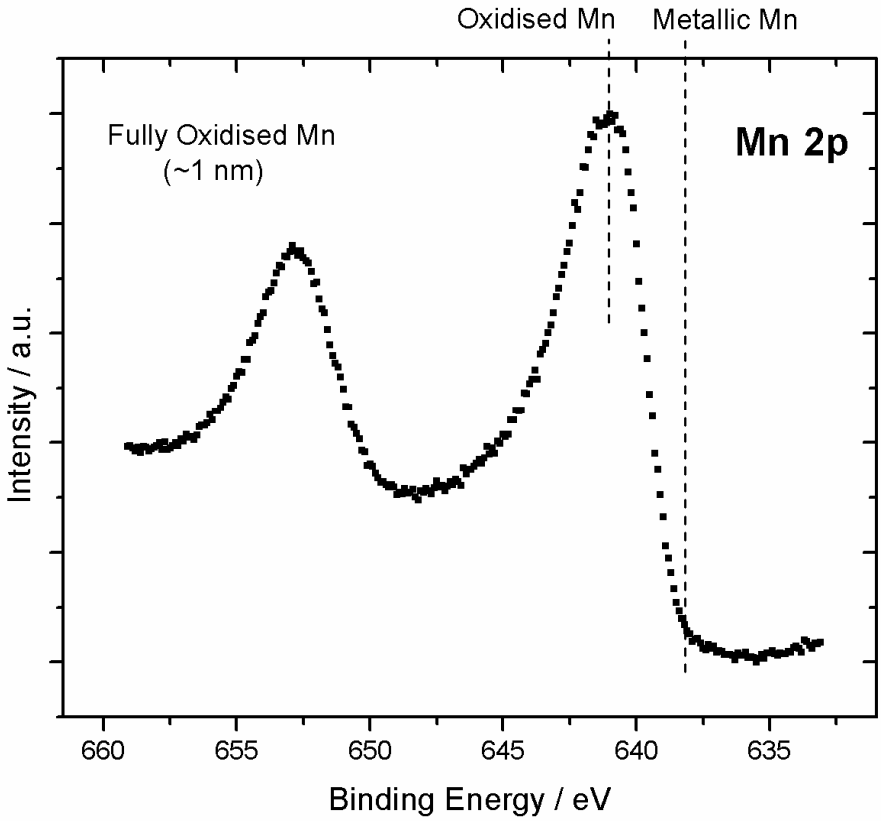

Figure 4.13 : Mn 2p spectrum following the deposition of a fully oxidised Mn film (~ 1 nm).

Further experiments (not shown) involving the deposition of partially oxidised Mn films of greater thickness (>1.5 nm) were also carried out in order to determine if the deposited film thickness is also a limiting factor in Mn silicate growth. Spectra taken after 500 °C annealing showed evidence for greater levels of Mn silicate growth than that seen in Figure 4.10 and Figure 4.11, however there was also evidence for the presence of residual metallic Mn which had not been converted to Mn silicate at this temperature. Therefore, based on the results of this study it is suggested that even when sufficient levels of Mn oxide are present on the surface the thickness of Mn silicate layers formed on SiO_2 is still self limiting at high temperature.

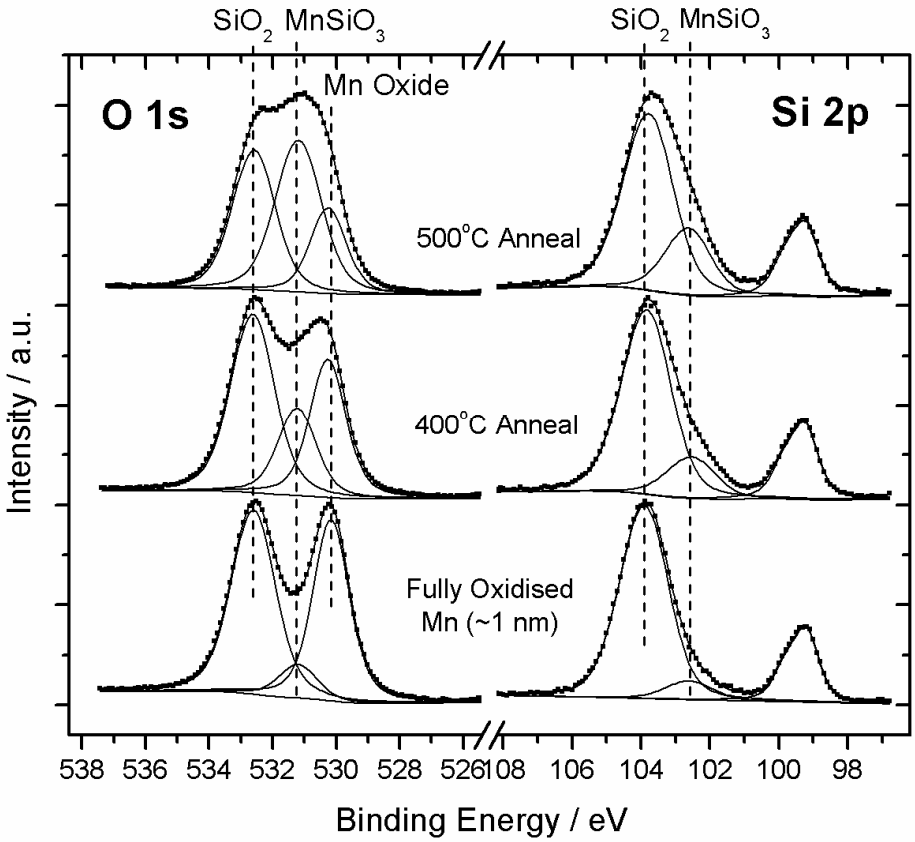

Figure 4.14 : Curve fitted O 1s and Si 2p spectra showing the conversion of Mn oxide to Mn silicate following high temperature UHV annealing. This result shows that the conversion of oxide to silicate species can occur for fully oxidised Mn films, in the absence of metallic Mn.

4.5 Chapter Conclusions

In summary, in the absence of deposited Cu which serves to complicate the analysis of chemical composition data [**7**,**8**], it has been shown that vacuum annealing of metal Mn on thermally grown SiO_2 between 350 °C and 500 °C results in the formation of a Mn silicate interfacial region with an approximate thickness of 2 nm. Using photo-ionisation cross section values the stoichiometry of the Mn silicate region was found to be consistent with $MnSiO_3$ in agreement with previous studies. Curve fitted SRPES spectra suggest that Mn oxide is not present within the Mn/SiO_2 interfacial region, in contrast to previous reports but in agreement with the reported reaction mechanism of metals on SiO_2. Based on previous studies from the literature [**1**,**17**] it is suggested that the absence of both Mn oxide and Mn silicide from the barrier layer region may make Mn a more favourable candidate than other metals such as Mg and Al for the formation of Cu diffusion barrier layers.

The second part of this study showed that the growth of the Mn silicate barrier layers on SiO_2 surfaces is self limited by the availability of additional oxygen, beyond that which is present within the SiO_2 layer. It has been shown that a ~ 1 nm metallic Mn film cannot be fully converted to Mn silicate following 500 °C annealing. As a result, Mn silicate layers with a thickness greater than ~1.7 nm cannot be formed following the deposition of purely metallic Mn and subsequent UHV annealing on a thermally grown SiO_2 layer. It has also been shown that a partially oxidised Mn film of similar thickness (~ 1 nm), containing approximately 15 % Mn oxide, can be fully converted to form a Mn silicate layer of greater thickness (~2.6 nm) which is free from metallic Mn and Mn oxide. TEM images taken from these samples show that $MnSiO_3$ growth causes a corresponding reduction in the SiO_2 layer thickness. This result is attributed to the conversion of SiO_2 to Mn silicate during UHV annealing and suggests that while the presence of Mn oxide is required to achieve full conversion of 1 nm Mn films to Mn silicate, the remaining oxygen required for silicate growth can be obtained from the SiO_2

film. Therefore, only low levels of additional oxygen are required to increase film reactivity. This may be of relevance for the practical implementation of $MnSiO_3$ barrier layer formation processes in device fabrication, given that the integration of excess oxygen into the Mn layer may decrease the reportedly high diffusivity of metallic Mn within Cu layers [**2**], one of the main factors which has led to the investigation of Mn based barriers layers for Cu interconnects. It has also been shown in this study that fully oxidised Mn films, free from metallic Mn, can be converted to Mn silicate using thermal annealing on SiO_2 surfaces. Given that conformal deposition techniques such as ALD are more suited to the deposition of metal oxide species than contaminant free metallic films, the use of fully or partially oxidised Mn films may offer a route to integrate Mn silicate structures into ultrathin barrier layer formation. However, it should be noted that the chemical reactivity of Mn oxide films on SiO_2 may depend greatly on factors such as oxide stoichiometry and film deposition method.

4.6 References

[1] J. Koike and M. Wada, "Self-forming diffusion barrier layer in Cu-Mn alloy metallization," *Appl. Phys. Lett*, vol. 87, no. 041911, Jul. 2005.

[2] J. M. Ablett, J. C. Woicik, Z. Tokei, and S. List, "Phase identification of self-forming Cu-Mn based diffusion barriers on p-SiOC:H and SiO2 dielectrics using x-ray absorption fine structure," *Appl. Phys. Lett.*, vol. 94, no. 042112, Jan. 2009.

[3] Y. Au, et al., "Selective Chemical Vapor Deposition of Manganese Self-Aligned Capped Layer for Cu Interconnections in Microelectronics," *J. Electrochem. Soc.*, vol. 157, no. 6, pp. 341-345, Apr. 2010.

[4] R. G. Gordon and H. Kim, "Self-Aligned Barrier Layers for Interconnects," U.S. Manufacturing WO 2009/117670 A2, Sep. 24, 2009.

[5] J. Iijima, Y. Fujii, K. Neishi, and J. Koike, "Resistivity reduction by external oxidation of Cu-Mn alloy films for semiconductor interconnect application," *J. Vac. Sci. Technol., B*, vol. 27, no. 4, pp. 1963-1968, Jul. 2009.

[6] S. ,. M. Chung and J. Koike, "Analysis of dielectric constant of a self-forming barrier layer with Cu-Mn alloy on TEOS-SiO2," *J. Vac. Sci. Technol, B.*, no. 27, p. 28, Sep. 2009.

[7] Y. Otsuka, J. Koike, H. Sako, K. Ishibashi, and N. Kawasaki, "Graded composition and valence states in self forming barrier layers at Cu-Mn/SiO2 interface," *Appl. Phys. Lett*, vol. 96, no. 012101, Jan. 2010.

[8] U. Manju, D. Topwal, G. Rossi, and I. Vobornick, "Electronic structure of the two-

dimensionally ordered Mn/Cu(110)," *Phys. Rev. B*, vol. 82, no. 035442, Jul. 2010.

[9] C. Yoon and D. L. Cocke, "Oxidation studies of copper-manganese alloys - A basis for model catalyst preparation," *Appl. Surf. Sci.*, vol. 31, no. 118, pp. 118-150, Aug. 1988.

[10] C. Lee and Y.-L. Kuo, "The Evolution of Diffusion Barriers in Copper Metallization," *JOM*, pp. 44-49, Jan. 2007.

[11] M. ,. Krause and J. ,. G. Ferreira, *J. Vac. Sci. Technol.* , vol. 27, p. 1963, 2009.

[12] S. Rubini, et al., "GaAs nanowires by Mn-catalysed molecular beam epitaxy," in *International Conference on Nanoscience and Technology*, 2007, pp. 992-996.

[13] P. Morgen, A. Bahari, U. Robenhagen, and J. F. Andersen, "Roads to ultrathin silicon oxides," *J. Vac. Sci. Technol. A*, vol. 23, no. 1, pp. 201-208, Jan. 2005.

[14] P. Casey and G. Hughes, "Photoemission study of the SiO2 conversion mechanism to magnesium silicate," *J. Appl. Phys*, vol. 107, no. 074107, Apr. 2010.

[15] J. J. Chambers and G. N. Parsons, "Physical and electrical characterization of ultrathin yttrium silicate insulators on silicon," *J. Appl. Phys.*, vol. 90, no. 2, pp. 918-933, Apr. 2001.

[16] J. J. Yeh and I. Lindau, "Atomic subshell photoionization cross sections and asymmetry parameters," *At. Data Nucl. Data Tables*, vol. 32, no. 1, Jan. 1985.

[17] M. J. Frederick, R. Goswami, and G. Ramanah, "Sequence of Mg segregation, grain growth, and interfacial MgO formation in Cu-Mg alloy films on SiO2 during vacuum annealing," *J. Appl. Phys.*, vol. 93, no. 10, pp. 5966-5972, May 2003.

[18] A. A. Audi and P. M. Sherwood, "Valence-band x-ray photoelectron spectroscopic

studies of manganese and its oxides interpreted by cluster and band structure calculations," *Surf. Interface Anal.*, vol. 33, pp. 274-282, Dec. 2001.

[19] M. Copel, E. Cartier, and F. M. Ross, "Formation of a stratified lanthanum silicate dielectric by reaction with Si(001)," *Appl. Phys. Lett.*, vol. 78, no. 11, pp. 1607-1609, Mar. 2001.

[20] M. Haneda, J. Iijima, and J. Koike, "Growth behavior of self-formed barrier at Cu--Mn/SiO2 interface at 250--450 C," *Appl. Phys. Lett.*, vol. 90, no. 252107, 2007.

[21] R. Beyers, "Thermodynamic considerations in refractory metal-silicon-oxygen systems," *J. Appl. Phys.*, vol. 56, no. 1, pp. 147-152, Jul. 1984.

[22] O. M. Ndwandwe, Q. Y. Hlatshwayo, and R. Pretorius, "Thermodynamic stabily of SiO2 in contact with thin metal films," *Mater. Chem. Phys.*, vol. 92, pp. 487-491, Jan. 2005.

[23] A. A. S. Kimura, T. Kambe, T. Xie, S. Watanabe, and M. Taniguchi, *Phys. Rev. B*, vol. 115416, no. 76, 2007.

[24] H. Ofner, et al., *Phys. Rev B.*, vol. 15120, no. 50, 1994.

[25] M. P. Seah and S. J. Spencer, *Surf. Interface Anal.*, vol. 33, pp. 640-652, May 2002.

[26] B. Lescop, *Appl. Surf. Sci.*, vol. 2276, p. 252, 2006.

[27] S. Iwata and A. Ishizaka, *J. Appl. Phys.* , vol. 6653, no. 79, 1996.

[28] R. G. Gordon, K. Hoon, Y. Au, H. Wang, and H. B. Bhandari, in *Advanced Metallization Conference*, California, 2008.

Chapter 5

The effect of Cu on the chemical and structural composition of $MnSiO_3$ barrier layers formed on SiO_2

5.1 Introduction

As discussed in Chapter 1 copper has recently replaced aluminium as the metal of choice for interconnects in microelectronic devices, due to its lower resistivity and increased resistance to electromigration [**1**] [**2**] [**3**]. The requirement of a physical barrier isolating the interconnect and preventing both the diffusion of Cu into the insulating SiO_2 based dielectric materials, and the diffusion of O and H_2O into the Cu [**3**] has been known for some time. The chemical and physical composition of manganese silicate ($MnSiO_3$) for use as the copper barrier layer has been investigated in Chapter 4 of this thesis. However, while the inherent chemical interactions between Mn and SiO_2 have been investigated, it has not yet been conclusively determined if the presence of Cu at the Mn/SiO_2 interface during barrier formation alters the chemical composition of the $MnSiO_3$ layer.

As also stated in Chapter 1, promising results have been obtained through the deposition of Mn/Cu alloys; forming $MnSi_xO_y$ barriers of 3–4 nm [**4**] [**5**]. However, TEM based investigations of these alloy based barriers have in some cases produced contradictory results with regards to the chemical composition of the layers. For example, when analyzing electron energy loss spectroscopy (EELS) spectra, Koike *et al.* [**7**] first reported a Mn^{3+} valence state consistent with Mn_2O_3 being the main

constituent of the barrier; while Abblet *et al.* [**8**] reported the valence state of Mn in the barrier as +2 by means of x-ray absorption near-edge spectroscopy and extended x-ray absorption fine structure, being mainly constituted of a mixture of MnO and $MnSiO_3$. Recently, Otsuka *et al.* [**8**] refined the previous work of Koike and reported a graded composition for the self-forming diffusion barrier, with a gradual increase in the valence state from +2 to +3, consistent with the presence of nanocrystalline MnO and amorphous $MnSiO_3$ layers. These varying results could be partially due to the fact that the main efforts to date have been concentrated on investigating the Cu-Mn alloy interaction with the insulating substrate rather than the individual Cu and Mn elemental interactions. Therefore, the chemical interaction between pure metallic manganese and the SiO_2 as a function of annealing temperature and between Cu and Mn layers could reveal important information on the nature of the interactions between these materials at the elevated temperatures used in barrier layer formation.

The focus of this chapter is to investigate the role of copper in barrier layer formation, both in the diffusion properties of Cu-Mn alloys and also the effect of copper on Mn/SiO_2 interfacial chemistry. The chapter is divided into three sections which addresses various aspects of the introduction of copper into the Mn barrier system. The first section investigates the chemical and structural composition of thermally deposited Cu layers on the 5.4 nm SiO_2 substrate used in the previous chapter both before and after anneal in order to determine the extent of interdiffusion of Cu across the interface caused by the thermal anneal. The second section investigates the interdiffusion of thermally evaporated Mn-Cu heterostructures, using both photoemission spectroscopy and a range of TEM techniques.

Finally, the effect of copper on the chemical composition of the Mn/SiO_2 barrier region is investigated in the last section of this chapter.

5.2 Experimental Details

The substrates principally employed in this chapter were 5.4 nm SiO_2 surfaces on silicon, identical to the samples used in the experiments described throughout Chapter 4, which were again grown using the Semitool dry oxidation process in a Thermoco 9002 series furnace at 850 °C. These SiO_2 surfaces were prepared for experiments by using the standard degreasing procedure of successive dips in acetone, methanol and isopropyl alcohol (IPA) before being loaded into UHV. For the first part of the study, approximately 5 nm of pure Cu (99.99 %) was deposited on the 5.4 nm SiO_2 dielectric layer using the Applied Research EGC04 mini electron-beam evaporator, at a chamber pressure of 1×10^{-8} mbar. XPS analysis was carried within the surface science system outlined in Chapter 3, Section 1.1. High temperature annealing studies were carried out in vacuum at a pressure of 1×10^{-8} mbar, with samples kept at the target temperature for 1 hour. Atomic Force Microscopy (AFM) analysis of both an as-deposited control sample and the annealed copper sample was performed in ambient conditions using the Digital Instruments Dimension 3100 AFM described in Chapter 3, Section 6. All AFM images were acquired using tapping mode and the surface roughness data was taken from at least ten different 2 μm × 2 μm areas of the surface.

For the TEM section of the study, a series of bilayer samples consisting of 20 nm of metallic Cu deposited on 30 nm of metallic Mn layers were grown in the Leybold Univex deposition chamber at a vacuum pressure of 2×10^{-6} mbar. As the emphasis in this work was on characterising the interdiffusion between the two metal layers, the substrates employed were 640 nm of amorphous SiO_2 on silicon. The samples were studied using XPS both as deposited, and after subsequent annealing under a vacuum of 10^{-8} mbar at 450 ° C for 2 hours. High resolution TEM, high angle annular dark field (HAADF), EELS, and energy dispersive x-ray spectroscopy (EDX) in scanning-transmission electron microscopy (STEM) mode measurements were carried out on JEOL 2010FEG and Tecnai Osiris electron microscopes, similar to those described in

Chapter 3, both operating at 200 kV. Samples in cross section geometry (XTEM) were prepared by the conventional method of grinding and polishing followed by Ar_+ milling in a Gatan PIPS until electron transparent. XPS analysis in the second section of the chapter was carried out using a VG Microtech electron spectrometer in the analysis chamber of the dedicated XPS system described in Chapter 3, Section 1.2 at a base pressure of 5×10^{-9} mbar. The photoelectrons were excited with a conventional Al Kα ($h\nu = 1486.7$ eV) x-ray source and an electron energy analyser operating at a 20 eV pass energy, yielding an overall resolution of 1.2 eV.

All experiments in the final section of the chapter were carried out on the high quality 5.4 nm thermally grown SiO_2 layers. Analogous to the work described in Chapter 4, every stage of the experimental process; including thin film growth and analysis, were again performed entirely *in-situ* without removal from ultra high vacuum conditions. Samples were degassed at ~ 200 °C for 2 hours, with the UHV chamber reaching a maximum pressure of 5×10^{-9} mbar during degassing. It has been previously shown in Chapter 4, Section 4 that $MnSiO_3$ layers with a thickness of ~3 nm can be formed on the SiO_2 surface through the evaporation of metallic Mn in an O_2 background pressure, forming partially oxidised Mn films on the SiO_2. However, in order to prevent the unwanted oxidation of Cu during the deposition of MnO_x/Cu alloys, all MnO_x films deposited in this study were evaporated from a partially oxidised Mn source which did not require the addition of extra O_2 to the UHV system during deposition. The deposition of both partially oxidised manganese and copper thin films were performed using the Oxford Applied Research EGC04 mini electron-beam evaporator, at a chamber pressure of 1×10^{-8} mbar. The deposition of partially oxidised Mn/Cu alloys was achieved by the simultaneous evaporation of partially MnO_x and Cu from the e-beam evaporator, at a deposition pressure of 1×10^{-8} mbar. XPS analysis was again carried out using the same VG Microtech electron spectrometer. High temperature annealing studies were carried out in vacuum at a pressure of 5×10^{-9} mbar, with samples kept at the target temperature for 60 minutes.

The XPS core level spectra were again curve fitted according to the parameters used in Chapter 4 of this thesis.

Again, it should be noted that curve fitting of the Mn 2p spectrum could not be performed given that XPS ghost peaks [**10**] emanating from the Mn $2p^{1/2}$ are present within the peak profile of the Mn $2p^{3/2}$ component. As such, only non-curve fitted Mn 2p spectra are included in this study. In agreement with the previous chapter the Mn $2p$ spectra shown in this study are primarily used to identify the presence of metallic Mn and oxidised Mn species on the sample surface, with O $1s$ and Si $2p$ spectra used to conclusively identify the presence of differing oxidised Mn species such as Mn silicate and Mn oxide. Furthermore, it should be noted that the behaviour of Mn atoms in a Cu alloy matrix has been reported to change the peak profile of the Mn $2p$ spectrum [**11**]. Given that the spectral component resulting from the interaction of metallic Mn and Cu has a similar binding energy position to that of oxidised Mn, Mn $2p$ spectra are not used for interfacial chemical analysis in situations where both metallic Mn and Cu are present of the surface. Electron energy loss spectroscopy (EELS) measurements in this final section were carried out on a JEOL 2010FEG electron microscope operating at 200 kV. TEM samples were again prepared by the conventional method of grinding and polishing followed by Ar^+ milling in a Gatan PIPS until electron transparent.

5.3 Characterisation of thermally deposited Cu layers on SiO_2

Figure 5.1 shows a survey spectrum (0-600 eV) taken following the room temperature deposition of ≈7 nm Cu on 5.4 nm SiO_2 surface. The spectrum shows the expected copper core level peaks, with no evidence of O 1*s* or C 1*s* peaks to within the detection limit of conventional XPS (~0.1 %). The film is sufficiently thick to completely suppress the SiO_2 substrate signal. The corresponding Cu 2*p* spectrum for this film shown in Figure 5.2 is identical to that taken from a 20 nm Cu reference sample, suggesting that the deposited copper film is in a purely metallic state.

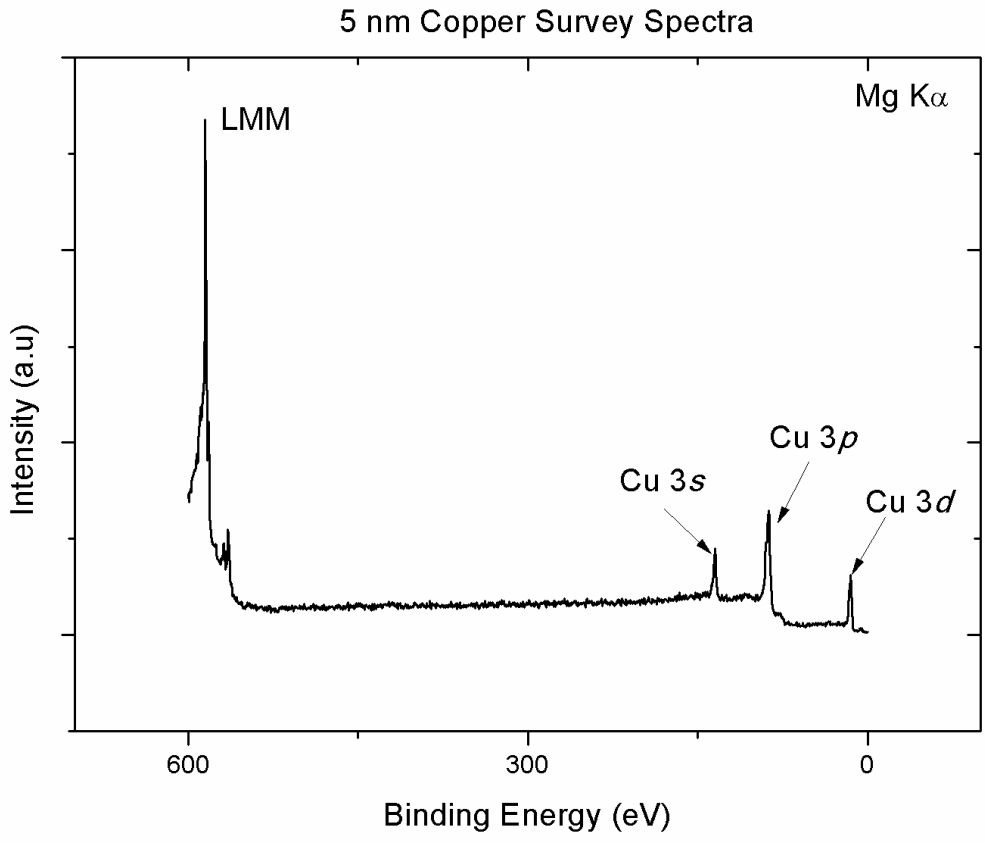

Figure 5.1: Survey spectra of 5 nm Cu film on SiO_2

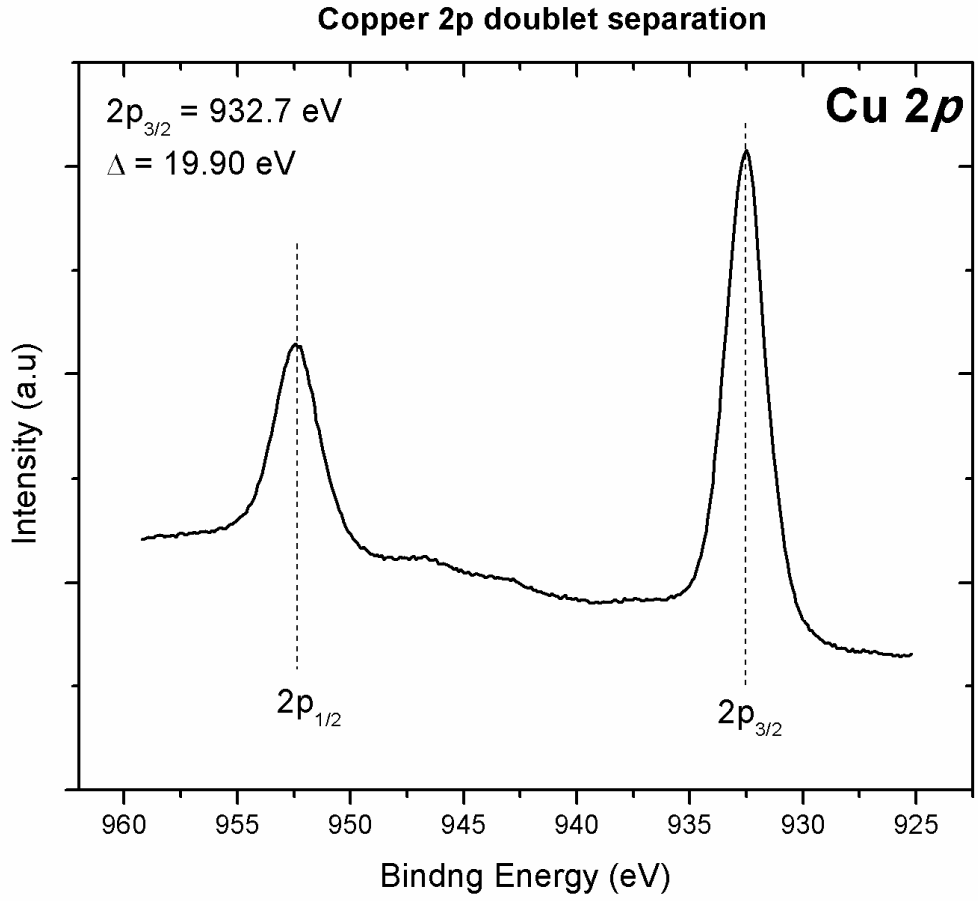

Figure 5.2: Corresponding Cu 2*p* spectra from 5 nm film on SiO_2 showing no signs of oxidation.

The complete lack of shake-up features characteristic of copper oxide [**12**], in the Cu 2*p* doublet shown in Figure 5.2 would indicate that the deposition resulted in no oxide formation. It is worth noting, that the position of the Cu 3*p* (75.3eV) is comparatively close to the Si 2*p* (99eV) which is relevant as it allows relative changes in the signal intensities to be observed after thermal annealing of the sample.

The photoemission spectra in Figure 5.3 show the changes induced in the relative intensities of the copper and the substrate signals following a 500°C anneal. The Si 2*p* spectrum which was fully attenuated following Cu deposition re-appears following the anneal.

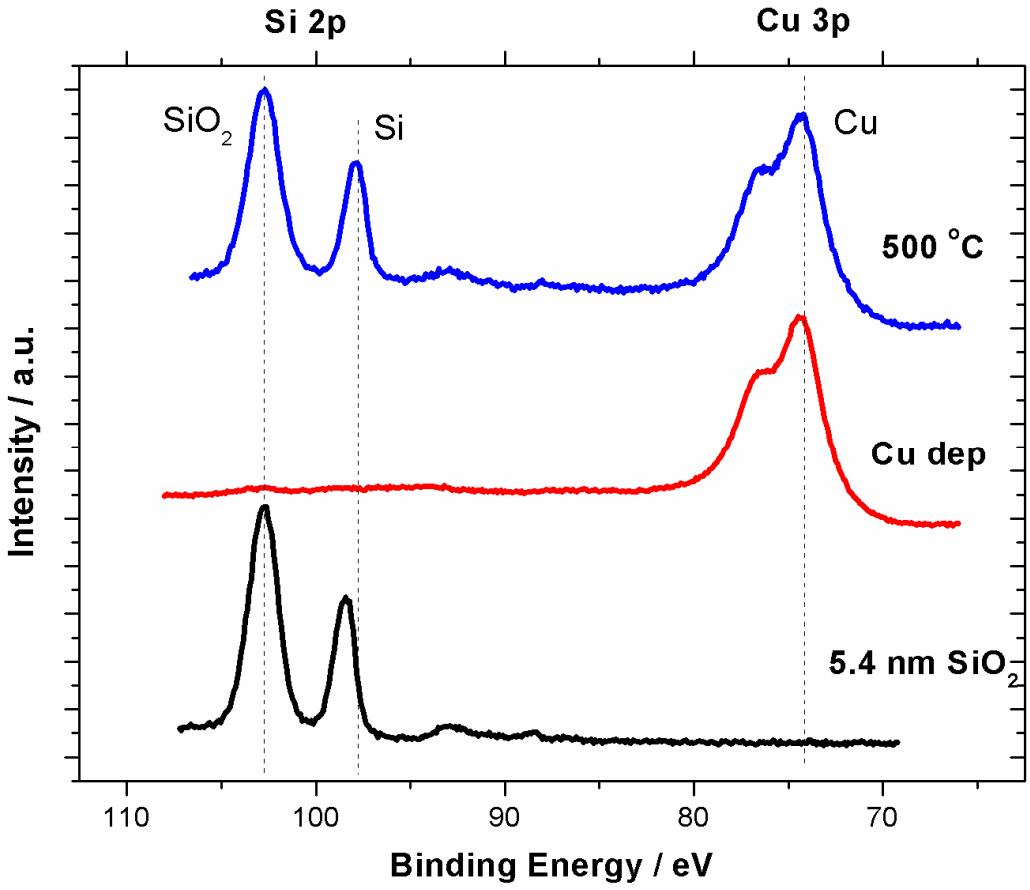

Figure 5.3: Si 2p and Cu 3p spectra showing uncovering of silicon substrate

This re-emergence can be explained either by the diffusion of Cu into the SiO_2 and the silicon or by the formation of Cu islands which exposes or uncovers the underlying substrate. By comparing the intensities of the Cu and Si related peaks between normal emission and 60° off normal, as shown in Figure 5.4, there is little change in the relative intensity of the SiO_2 and Cu $3p$ peaks while the silicon substrate signal has been suppressed. This change in intensities with takeoff angle is indicative of a layered structure with the Cu residing on top of the silicon oxide layer which is above the silicon substrate.

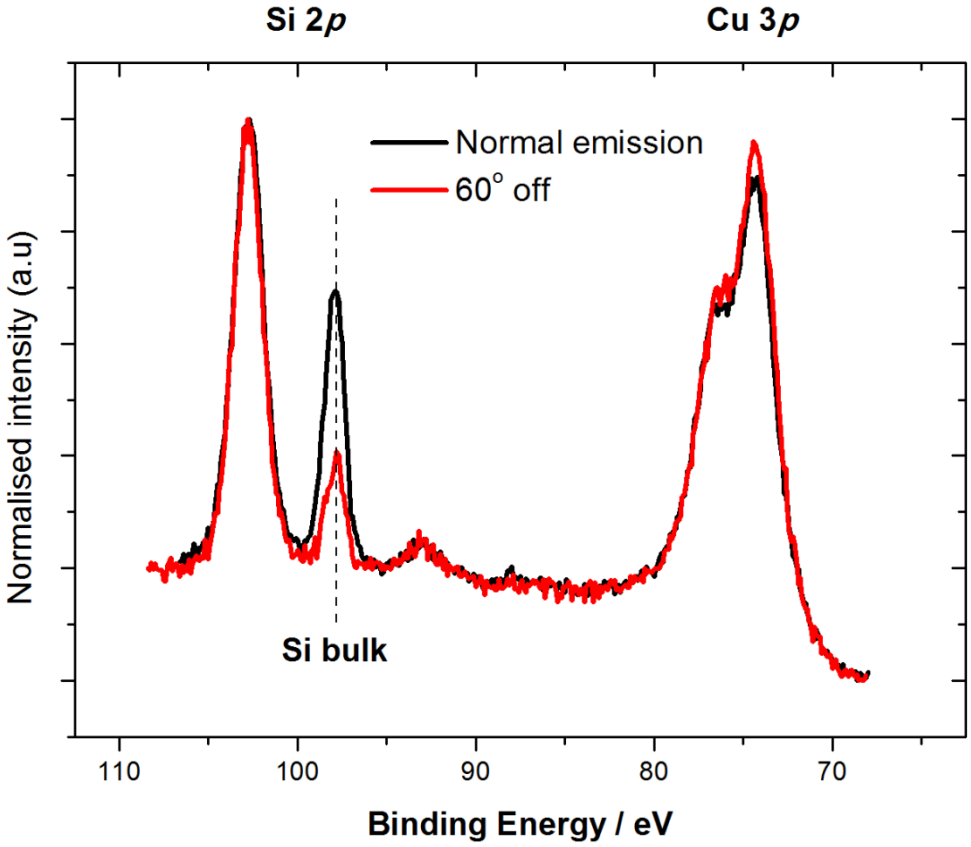

Figure 5.4: Comparison of Si 2*p* and Cu 3*p* relative intensities as a function of takeoff angle.

It can be seen in Figure 5.4 that the off angle scans show little change in the relative intensity of the SiO_2 and Cu 3*p* peaks. Therefore it can be suggested that the majority of the Si signal is not coming from SiO_2 which is beneath Cu i.e. the majority of the Si signal is coming from uncovered SiO_2 surface. It can also be seen that the Si bulk peak has been suppressed considerably off angle; however, the off angle scan shown in Figure 5.5 which is taken from an ordinary 5.4 nm SiO_2 surface shows that the suppression of the bulk peak is simply due to the presence of the oxide layer and not due to Cu.

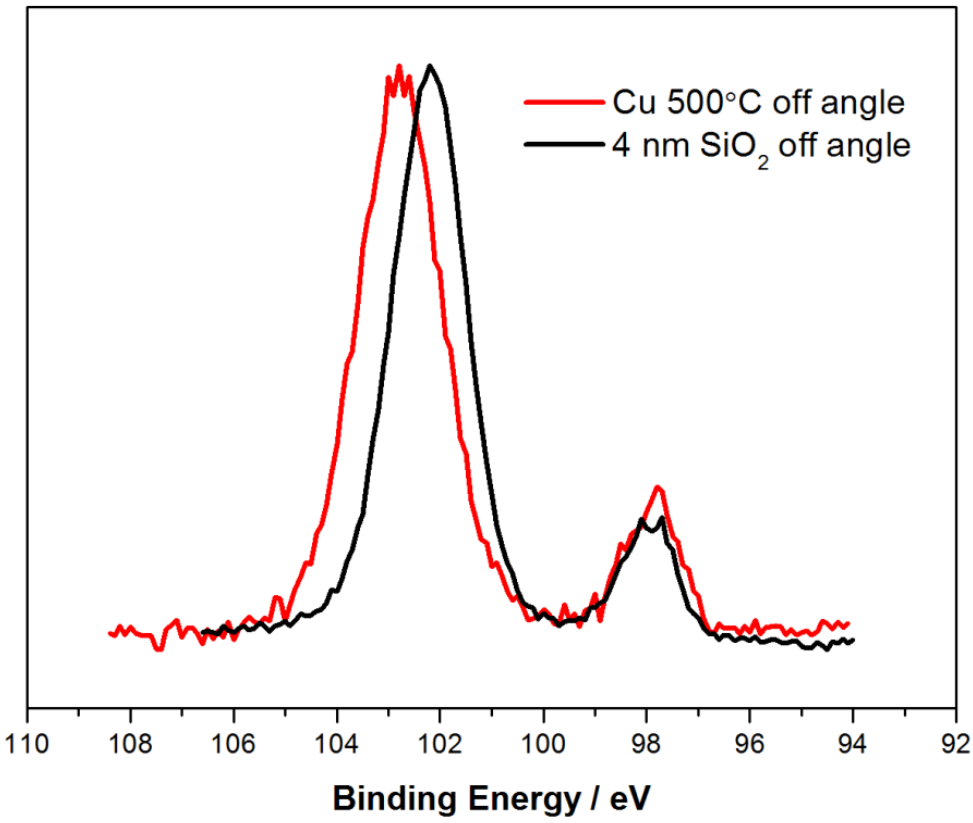

Figure 5.5: Si 2p spectra showing no relative change in oxide and bulk silicon after cu dep.

These results would suggest that following a 500 °C anneal areas of uncovered SiO_2 are revealed, which leads to the re-emergence of the Si $2p$ peaks. The AFM images shown in Figure 5.6 are taken from the as deposited and 500 °C annealed samples.

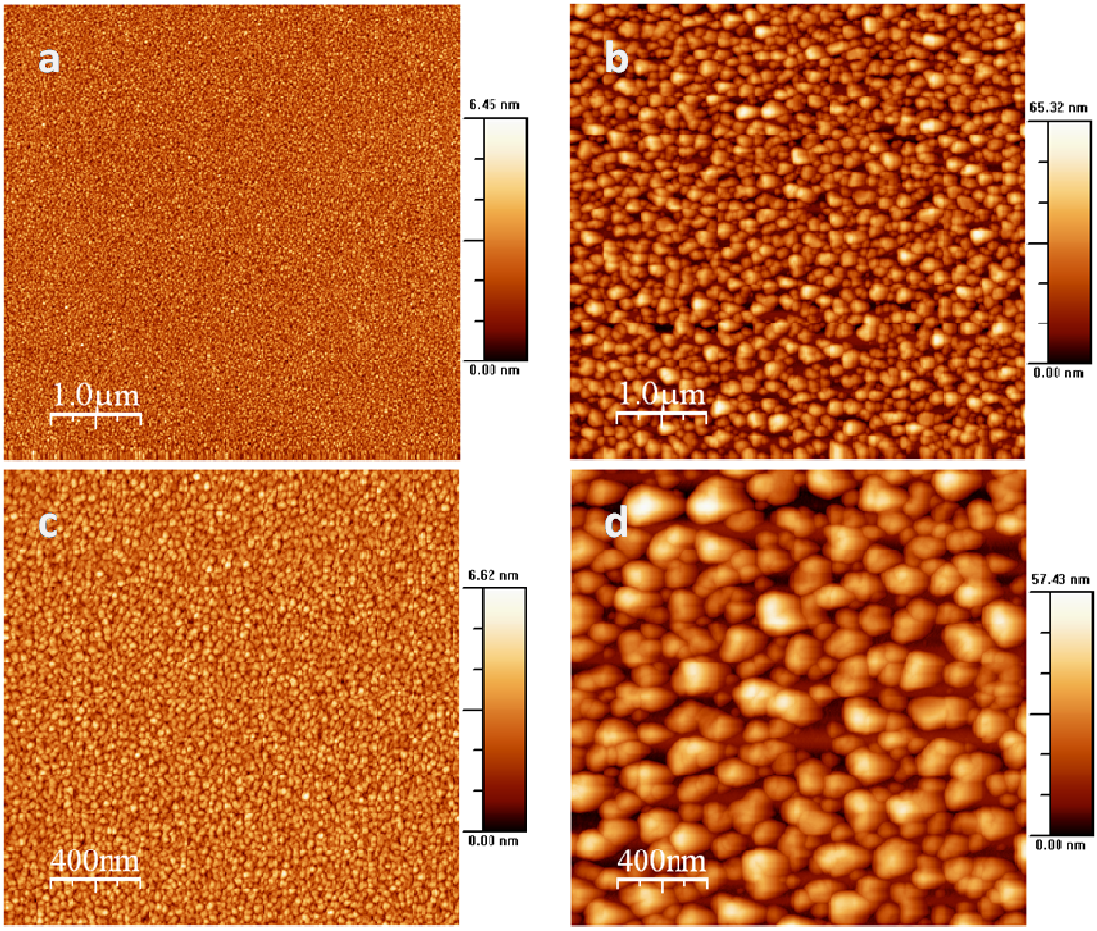

Figure 5.6 AFM images of annealed Cu sample indicating island formation. a: low magnification image of control sample, b: low magnification image of annealed sample, c: high magnification image of control sample, d: high magnification of annealed sample.

	RMS roughness	Average roughness	Max. roughness
Cu on Si control	0.8 nm	2.9 nm	6.6 nm
Cu 500 °C	10.1 nm	20.4 nm	57.7 nm

Table 3: RMS roughness values of annealed and control Cu samples

The flatness of the control sample in Figure 5.6 (a) and (c); and the roughness of the annealed sample in Figure 5.6 (b) and (d) would suggest that the Cu is forming islands confirming the photoemission results.

The spectra in Figure 5.5 show that after the 500 °C anneal there is a measurable increase in the binding energy separation between the bulk and oxide peaks. Given that Cu is reported to be un-reactive with SiO_2 up to 800 °C [**26**] this change is attributed to a change in the oxide charging and not a chemical reaction between the Cu and SiO_2. Also the Cu $3p$ spectra taken after 500 °C annealing is identical to that taken after Cu deposition so there's no evidence that the Cu has chemically reacted with the SiO_2.

5.4 TEM study of interdiffusion in thermally evaporated Mn/Cu heterostructures on SiO_2 substrates

In order the investigate the inherent diffusion interactions between metallic Cu and Mn, a series of thick Cu/Mn samples, as described in the experimental section, were prepared as shown schematically in Figure 5.7 and individually annealed for various times and temperatures before being analysed by both XPS and TEM. While the total thickness of the deposited films was significantly larger than the XPS sampling depth, evidence of interdiffusion was obtained from these measurements.

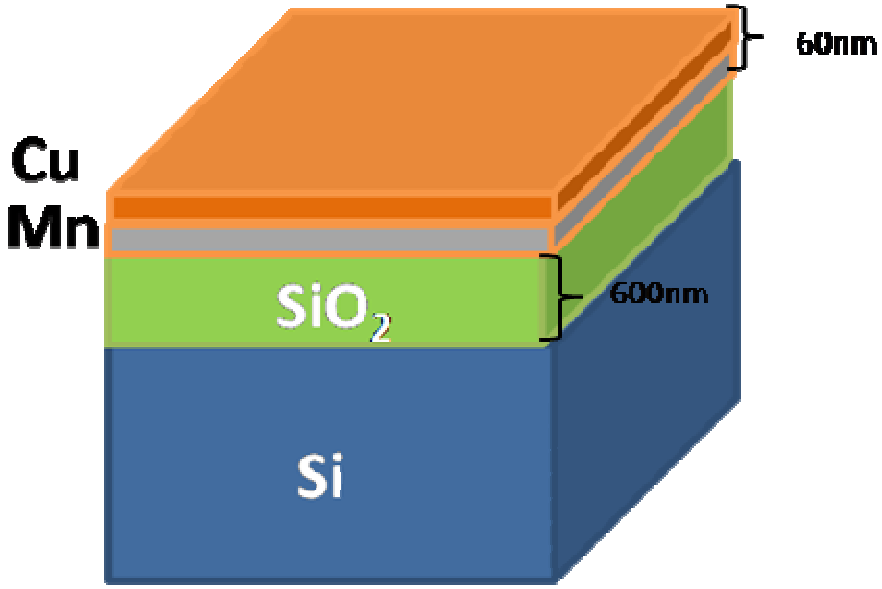

Figure 5.7: Schematic diagram of thick layered structure.

Identical layered structure samples were then annealed for 1 hour at 300° C and 2 hours at 450° C and analysed using both XPS and TEM. From the survey scan shown in Figure 5.8 it can be seen that the spectrum taken before anneals is characteristic of a

metallic copper film as expected for a 25 nm thick layer. However, after the first anneal the Mn *2p* peak appears at 639 eV. It's important to note that the position of the copper Auger lines overlap with the Mn 2*p* spectra, but after anneal the manganese 2*p* core level is clearly observed in the spectrum.

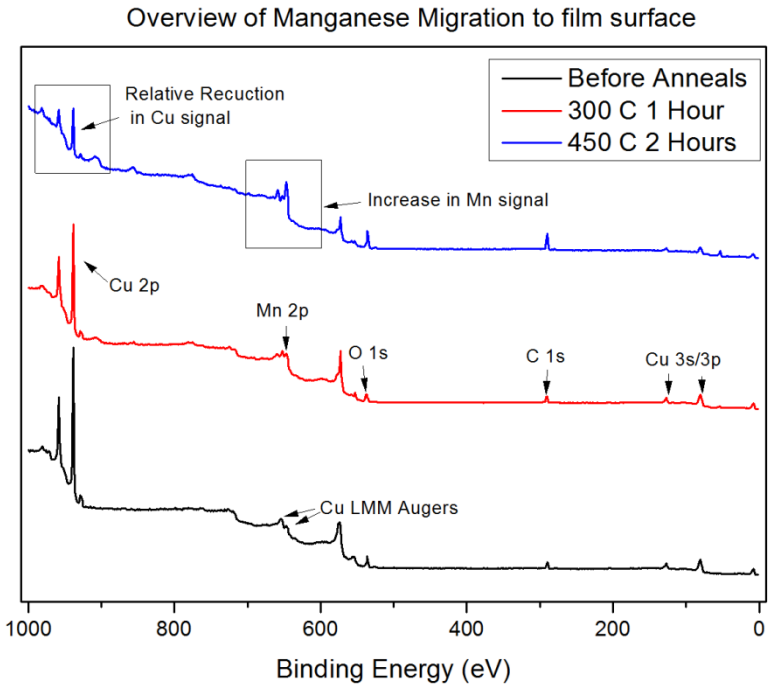

Figure 5.8: XPS Survey scans of thick layered samples before and after anneals.

The high-angle annular dark-field (HAADF) image in Figure 5.9 confirms this as a darker layer is clearly evident at the Cu surface. Since the difference in contrast in the images obtained with this technique is directly related to the difference in Z number of the elements that are present, these darker regions must contain an element or compound with an average Z number higher than that of Cu. Hence, these dark regions are attributed to the manganese that has diffused through the copper layer to the surface. This TEM image was taken on a sample which had been annealed at 450°

C for 2 hours where the presence of manganese at the surface of the copper is most evident. The TEM measurements of the thickness of the layers was seen to change after anneal as the Mn layer decreased from ~40 nm to ~36 nm and the Cu layer was seen to increase from ~25nm to ~32 nm. This is worth noting as it suggests that despite the change in thickness of the individual layers the total amount of material deposited remained constant throughout the anneals.

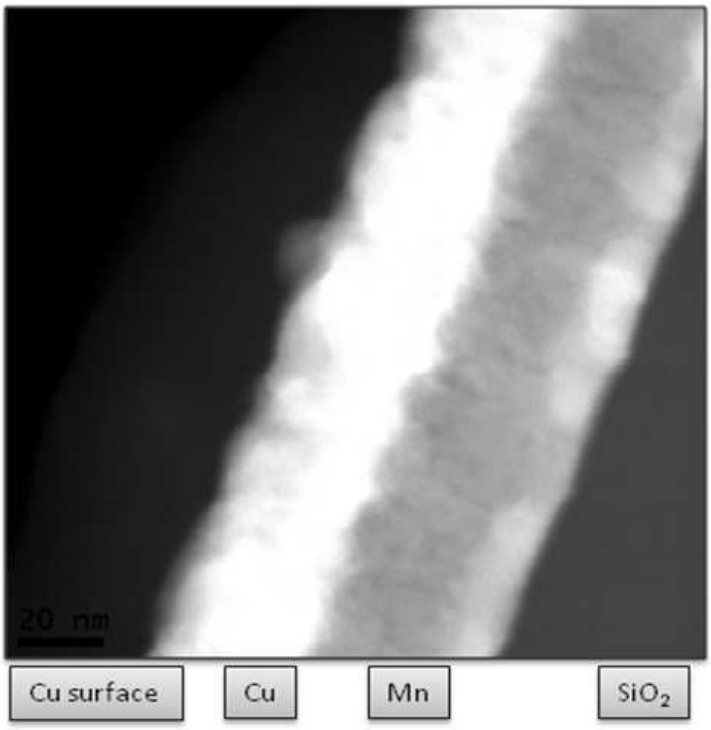

Figure 5.9: TEM image showing the outward diffusion of manganese after 450°C anneal

The changes in the peak intensities in the narrow XPS scans of the Cu $2p$ and Mn $2p$ core levels for this sample shown in Figure 5.10 and Figure 5.11 respectively, are consistent with the migration of the manganese through the copper layer to the surface. The peak shape of the Mn $2p$ spectra indicates that the manganese is in an oxidised state. However, the precise oxidation state of the migrated manganese could not be

determined due to the aforementioned difficulties in curve-fitting the Mn $2p$ spectrum. However the EDX data for this sample indicated the manganese layer was mostly in the form of MnO, hence it is assumed that the main peak is in the form of MnO. In contrast, the copper spectra would indicate the presence of metallic copper as the Cu $2p$ peak profile appears identical to a reference spectrum from a pure metallic layer.

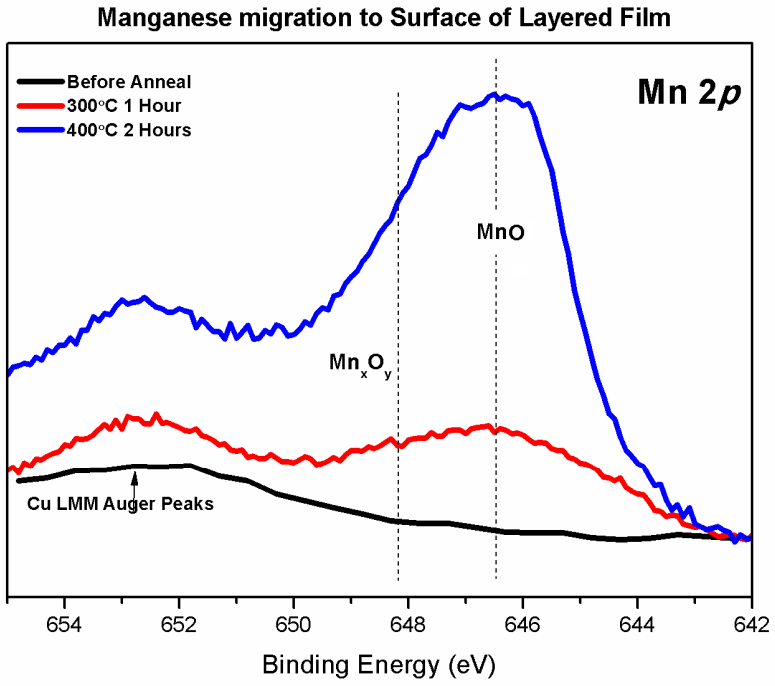

Figure 5.10 : XPS scans of the Mn $2p$ spectra showing the re-emergence of the Mn $2p$ peak after anneal

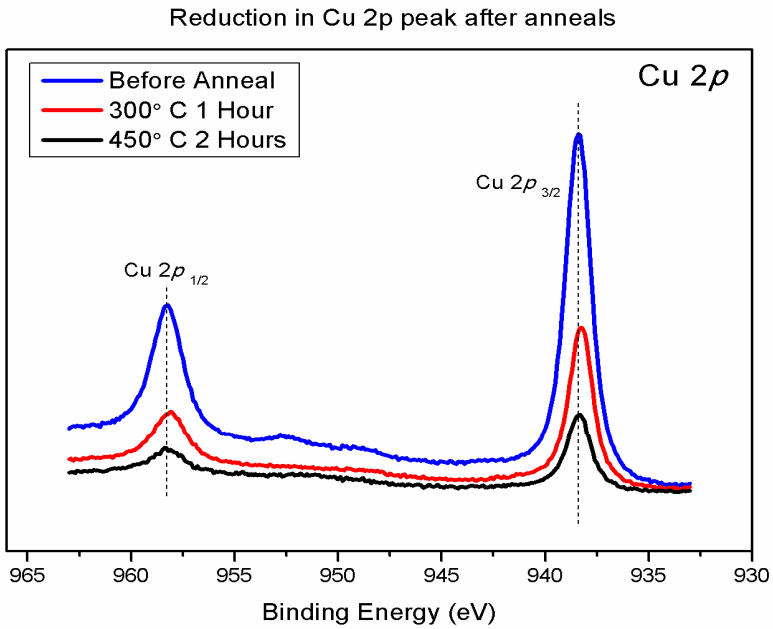

Figure 5.11: XPS Scans showing the decrease in intensity of the Cu 2*p* spectra after thermal anneal

Again EDX spectra were taken for the various layers and interfaces in the structure and the results are shown in Table 4 and Figure 5.12.

Layer	**%Mn**	**%Cu**	**%O**
SiO_2 Interface	63.0	2.8	34.2
Mn layer	56.3	0.5	43.2
Cu layer	8.0	83.3	8.7
Cu Surface	25.6	36.9	37.6

Table 4: EDX elemental composition of layers and interfaces after anneal

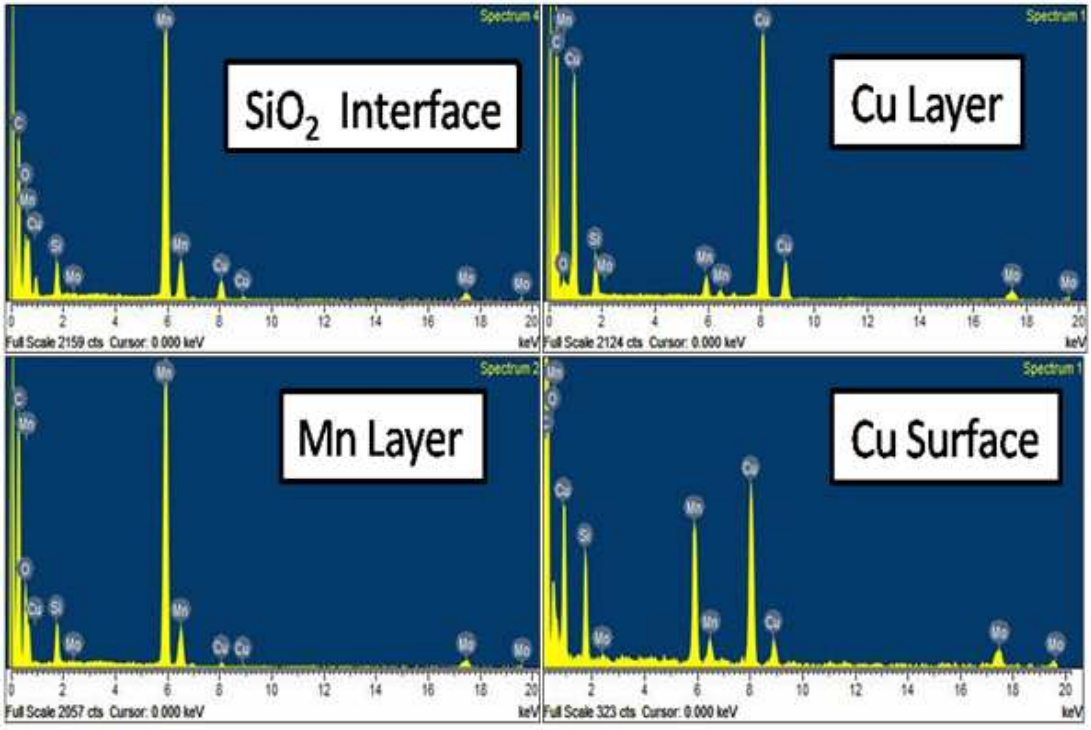

Figure 5.12: EDX spectra of thick layers and interfaces

The elemental data from EDX for the 450° C annealed sample concurs with the XPS scans and TEM images studied. The copper surface contains a large amount of manganese and oxygen which agrees with the Mn $2p$ oxide peak seen in the XPS scans.

It's interesting to note that a higher percentage of Mn is detected at the surface of the Cu layer than in the bulk of the film and that a higher percentage of Cu is observed at the interface than in the Mn layer. This would suggest that both the copper and manganese have the ability to migrate through the layers but only accumulate at the interface and the surface.

The HAADF micrograph shown in Figure 5.13 shows an unexpected bright contrast in a region approximately 10 nm thick above the interface between the Mn layer and the SiO_2. Since the difference in contrast in the images obtained with this technique is directly related to the difference in Z number of the elements that are present, these

brighter regions must contain an element or compound with an average Z number higher than that of Mn.

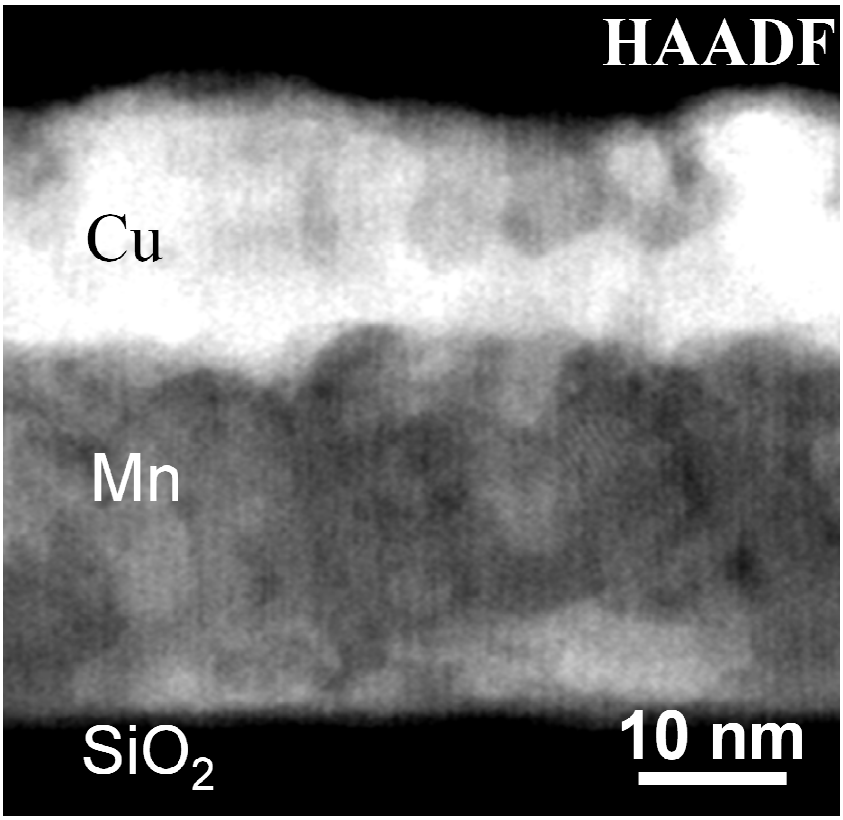

Figure 5.13: HAADF micrograph of the Cu/Mn heterostructure showing an unexpected contrast at the interface Mn / SiO_2

To confirm this, EELS elemental maps were recorded along the different layers in STEM mode with a nominal probe size of 1 nm and a size of 100×100 pixels so that every spectrum image therefore contains 10^4 spectra. Figure 5.14(a) shows the Cu extracted signal map obtained after background subtraction and multivariate statistical analysis noise reduction, [**13**] considering a Hartree–Slater step function to take into account sample thickness effects and integrating the remaining signal under the Cu *L* peak. The same procedure was used for the Mn *L,* Si *K* and O *K* edges, and the results are displayed in Figure 5.14(b), (c) and (d), respectively. The barrier region is

represented by the thin area outlined at the SiO_2/Mn interface. As expected, a relatively large amount of segregated Mn was found in the Cu layer.

However, there is also a noticeable increase in the Cu signal in certain areas of the region close to the interface between the Mn and the dielectric, which is attributed to the migration of Cu toward the interface region during the annealing process. In addition, this diffused Cu appears to encapsulate areas where a higher Mn and lower O signals are observed in Figure 5.14(b) and Figure 5.14(d), respectively. The oxygen arises from the oxidation of the TEM sample as a consequence of exposure to environmental conditions and is more accentuated in the bulk of the Mn layer with the exception of these areas. This indicates that the Cu surrounding Mn clusters close to the interface is preventing this Mn from being as heavily oxidized as the rest of the layer on ambient exposure and, therefore, the metallic Mn signal intensity is higher. It is worth mentioning that no Cu trace is detected in the SiO_2, which can be attributed to the formation and effectiveness of a diffusion barrier layer.

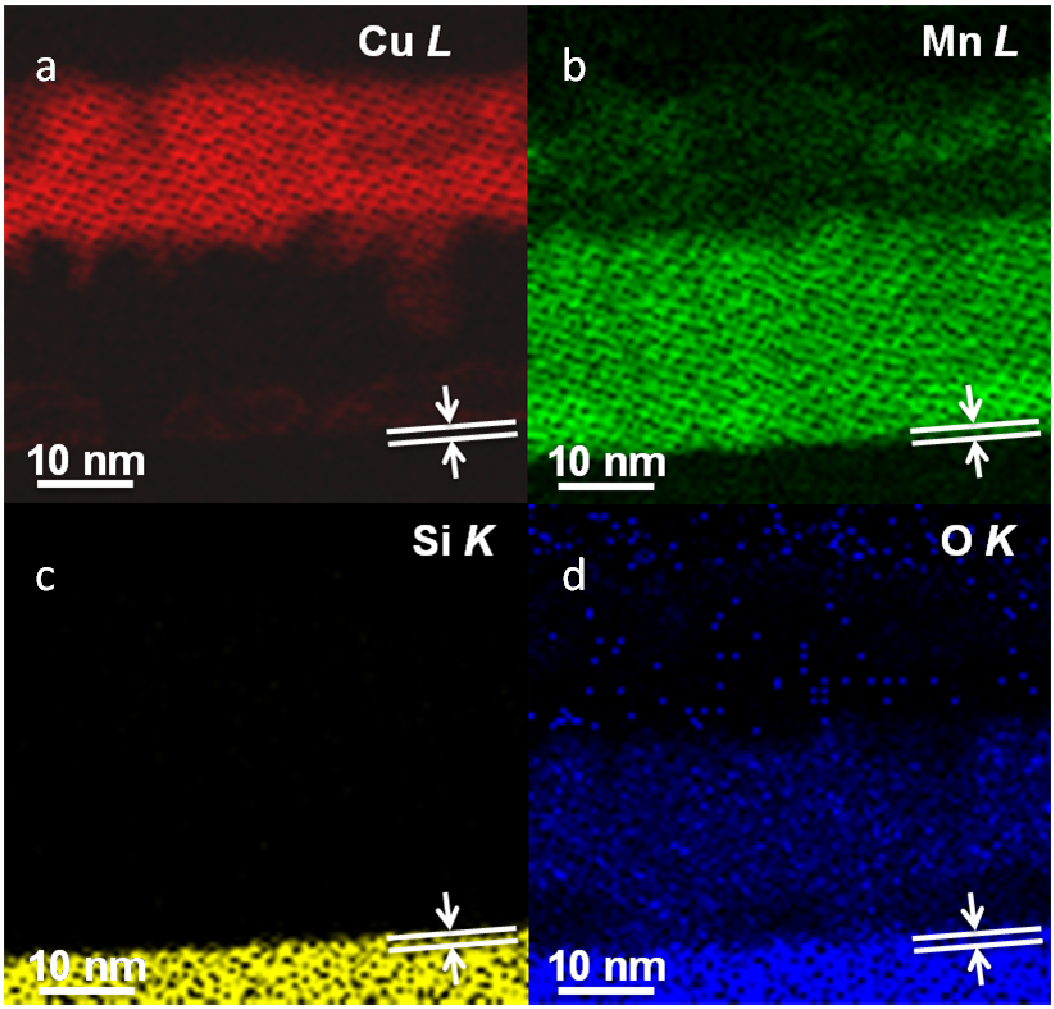

Figure 5.14: EELS extracted signal maps for a Cu L, b Mn L, c Si K and d O K edges.

These results were confirmed by EDX mapping measurements of the different layers. Figure 5.15 shows a set of elemental line scans perpendicular to the layers. These line scans not only confirmed the EELS results but also show that the 2–3 nm thin layer immediately below the segregated Cu and the surface of the SiO_2 is primarily composed of Mn, O, and Si, in agreement with previously reported results for self-forming diffusion barriers in Cu Mn alloys.

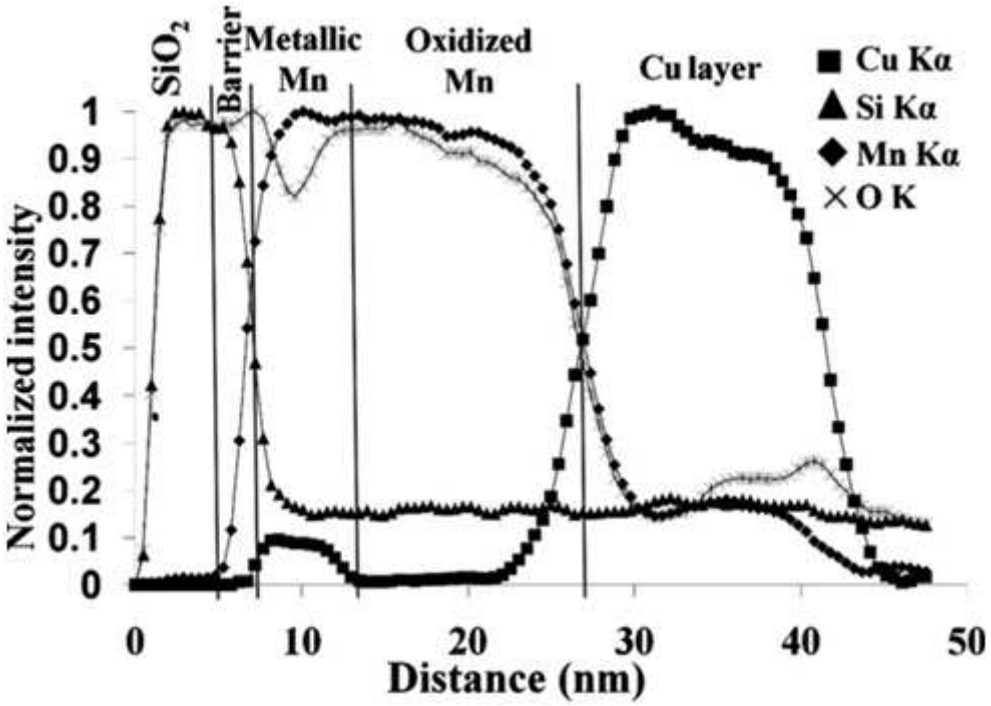

Figure 5.15: EDX integrated line scan of the heterostructure layer displaying the Cu, Si, Mn, and O signals.

The nature of the chemical reactions at the Mn/SiO_2 interface to form a diffusion barrier is now explored. EELS is accepted as a very powerful technique to evaluate the valence states of transition metals either in heterophase materials or in thin films. [**14**] It is known that manganese presents two characteristic EELS lines, L_2 and L_3, which are due to the transitions from $2p_{3/2}$ and $2p_{1/2}$ core states to unoccupied $3d$ states localized on the excited Mn ions. Rask *et al.* [**15**] showed for a series of manganese oxides that the $(I)L_3/\ (I)L_2$ white line intensity ratio is characteristic of the oxidation state of the manganese ions, as the intensity ratio increases with decreasing oxidation state. Here, we have estimated the Mn peaks $(I)L_3/(I)L_2$ intensity ratio to investigate possible variations in the Mn valency in the different regions of the Mn layer using associated EELS elemental maps. First, due to the lack of available data in the literature for typical EELS spectra of metallic manganese reference spectra shown in Figure 5.16 were taken from a sample consisting of deposited Mn kept under vacuum

conditions of 1×10^{-9}mbar during the whole process to avoid oxidation, and an average intensity ratio of 1.23±0.2 was calculated. For the valency of Mn in different oxides, we rely on the data from Schmidt *et al.* [**14**] which is tabulated in Table 5. While the air exposure makes it difficult to definitively identify the chemical state of the Mn at the Mn layer and Mn/SiO_2 interface, it highlights the compositional changes in the film following annealing as is displayed in Figure 5.17. Different regions can be easily distinguished: a first one corresponding to the main bulk of the oxidized Mn layer where the L_{23} intensity ratio values range approximately from 1.8–2, i.e., an intermediate value between that of metallic Mn and those reported for the different oxides. This could be caused by the overlapping of the spectra arising from the metallic Mn sandwiched between the two thin layers of Mn surface oxide top and bottom of TEM sample. Second, some areas close to the Mn / SiO_2 interface with a lower L_{23} intensity ratio 1.2–1.5 that corresponds to the encapsulated Mn.

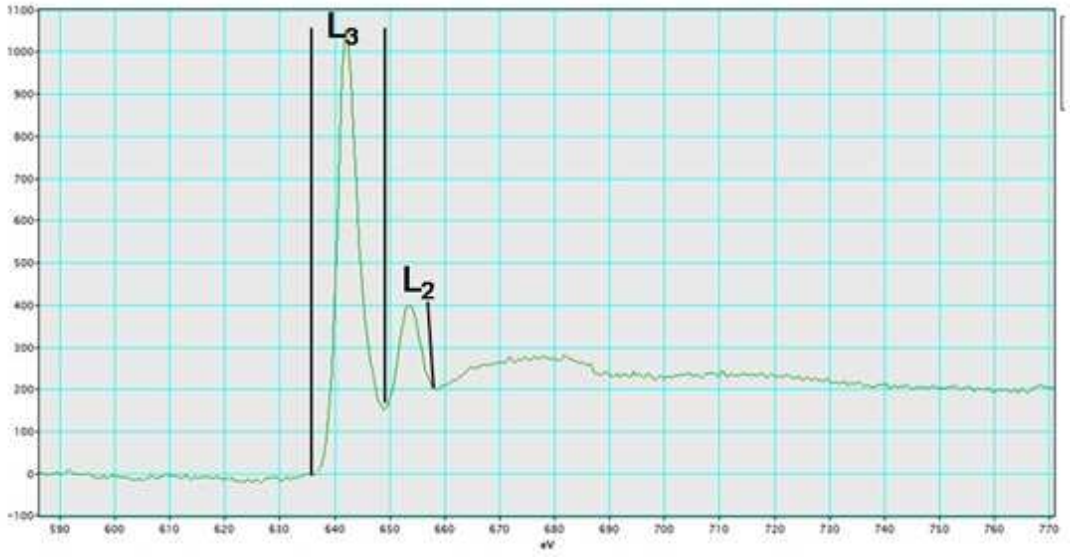

Figure 5.16: L_3 / L_2 intensity EELS spectra taken from metallic Mn reference spectra.

Phase	Mn	$MnCO_3$	MnO	Mn_3O_4	Mn_2O_3	MnO_2
Oxidation state	0	2+	2+	2+, 3+	3+	4+
Intensity ratio (L_3/L_2)	1.7	4.1	3.9	2.8	2.4	2.0

Table 5: Intensity ratios of various Mn compounds[14].

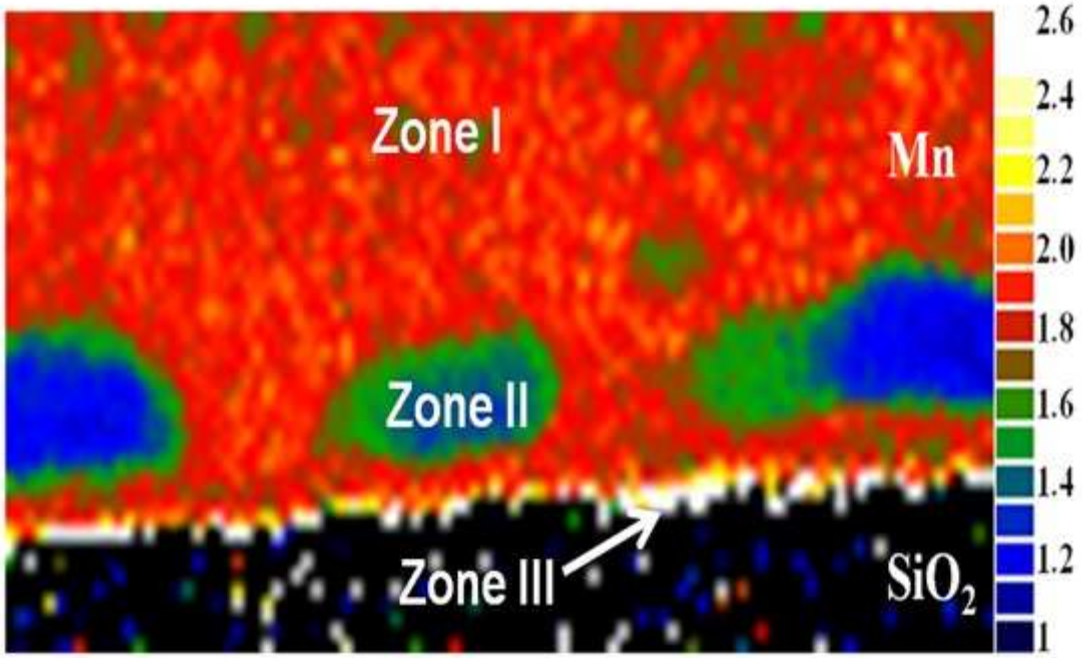

Figure 5.17: Colour online EELS L23 intensity ratio map of Mn and Mn / SiO_2 interface indicating areas with different Mn valency values.

This corroborates the previous EELS and EDX observations showing that the less oxidized Mn regions appear to be encapsulated by Cu which diffused into the thick Mn film during annealing preventing those regions from being as oxidized as the rest of the layer and therefore it is mainly in a metallic state. Finally, a thin layer located at the Mn/SiO_2 interface with a thickness of 2–3 nm shows a higher L_{23} intensity ratio of 2–2.6 which, according to the values reported by Schmidt should correspond to a mixture of +2 and +3 valences of Mn, in agreement with previously reported results for self-forming diffusion barriers in Cu Mn / SiO_2 structures. [**9**] [**16**] It is also worth mentioning that, since this is a method that applies to the determination of the oxidation state in Mn oxides, in those areas where this element is not present, such as SiO_2, it fails and therefore the values displayed in this region can be ignored.

While the diffusion of Mn in Cu in Cu(Mn) alloys have been widely reported in the literature, little published data exists regarding diffusion of Cu in Mn in thick layered structures. It is well known that Cu diffuses mainly through the grain boundaries into polycrystalline materials like Pb [**17**] or C–Mn steel [**18**] layers. Therefore, it is proposed that similar to copper diffusion in other metals, the polycrystalline nature of the Mn layer is the reason for the presence of Cu in this layer. The small average Mn and Cu grain sizes creates numerous paths for the migration of these elements into the neighbour layer and, therefore, the 450 ° C anneal of the Cu/Mn layered structure results in a number of Mn clusters fully or partially surrounded by a thin layer of Cu in the regions close to the interface, forming an non-homogeneous Mn(Cu) alloy heterostructure on the nanometer scale. In the same way, Mn atoms will diffuse into the Cu to form a non-homogeneous Cu(Mn) alloy in the upper layer. This can be mainly enhanced by the presence of residual amounts of oxygen contamination, [**19**] present during the deposition process and subsequent handling, to form MnO via the displacement reaction $Cu_2O + Mn \rightarrow 2MnO$ during the vacuum annealing. Equivalently, for the solute Cu in the Mn matrix lower layer, it is expected that Cu atoms will migrate to the Mn / SiO_2 interface to form a more stable oxide. However,

there is no evidence of Cu in the SiO_2 beyond this interfacial layer indicating its effectiveness at preventing interdiffusion. Given that the thickness of this interfacial region is below 3 nm even though it was formed in the presence of excess Mn, it suggests that the barrier formation process is self limiting at this temperature. This study shows that while the thick Mn film does not in itself prevent copper diffusion, the thin interfacial $MnSiO_3$ region is effective at preventing Cu diffusion into the SiO_2 substrate.

5.5 Photoemission Study of the effect of Cu on the chemical composition of $MnSiO_3$ barrier layers formed on SiO_2

In order to study the interfacial chemistry and thermal stability of the chemical species present at the Cu/Mn/SiO_2 interface, a series of Cu/Mn samples, as described in the experimental section, were prepared before being analysed by both XPS and TEM.

Curve fitted O 1*s* and Si 2*p* core level spectra taken from the 5.4 nm thermal SiO_2 surface are shown in Figure 5.18. The corresponding spectra taken following the deposition of a ~ 1 nm partially oxidised Mn (MnO_x) thin film onto the SiO_2 surface at room temperature are also shown in Figure 5.18.

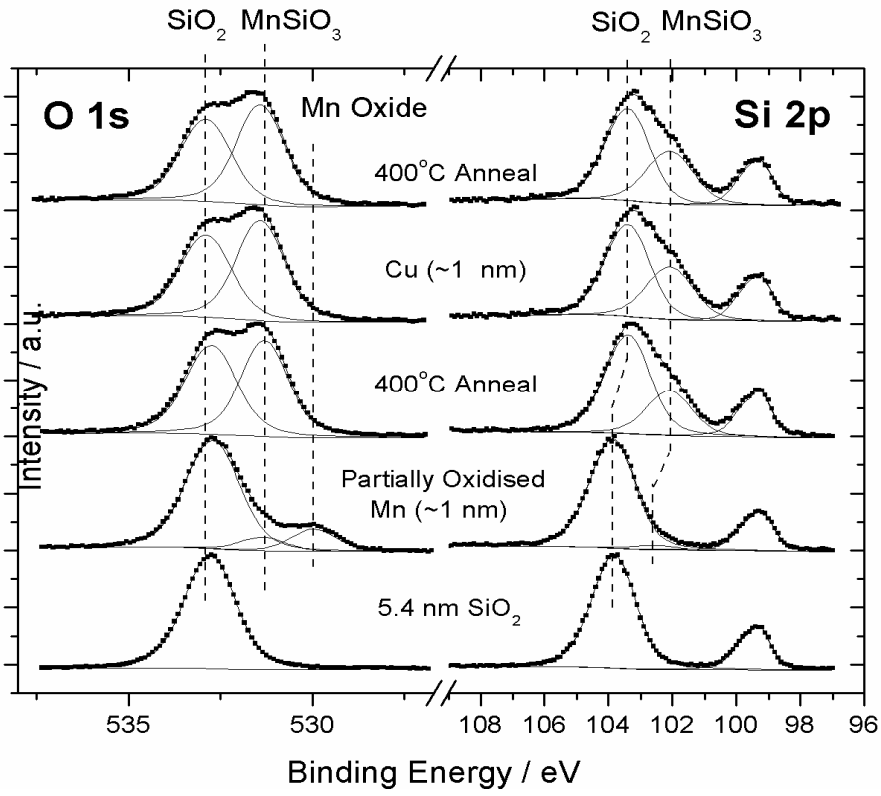

Figure 5.18: Curve fitted O 1s and Si 2p spectra showing the growth of $MnSiO_3$.

Curve fitting analysis shows small changes to the core level profiles suggesting that Mn deposition resulted in the growth of additional component peaks in both the O 1s and Si 2p spectra separated from the SiO_2 components by 1.4 eV and 1.3 eV respectively. These peaks are attributed to the presence of the Mn silicate species, $MnSiO_3$, in agreement with the previous photoemission results.

In addition to this, the O 1*s* spectrum also shows evidence for a third component peak at a binding energy position of 530.0 eV, which is attributed to the presence of Mn oxide in agreement with previous studies [**20**]. The corresponding Mn 2*p* spectrum in Figure 5.19 clearly shows the presence of both metallic Mn and oxidised Mn spectral components, with curve fitting analysis suggesting a metallic Mn:oxidised Mn ratio of 5:1. Angular resolved Mn 2*p* spectra (not shown) indicate no evidence for spatial segregation between the oxidised and metallic species, which suggests that the oxygen content is homogenously distributed throughout the deposited film. Following deposition the sample was annealed to 400 °C in UHV, resulting in the growth of Mn silicate on the surface as evidenced by the growth of $MnSiO_3$ component peaks in both the Si 2*p* and O 1*s* spectra. It should be noted that O 1*s* spectrum taken following annealing suggests the full conversion of Mn oxide to Mn silicate, in agreement with the previous results in Chapter 4. In addition to this, the corresponding Mn 2*p* spectrum in Figure 5.19 also shows the full conversion of metallic Mn to $MnSiO_3$, suggesting the formation of a $MnSiO_3$ barrier layer free from both metallic Mn and Mn oxide.

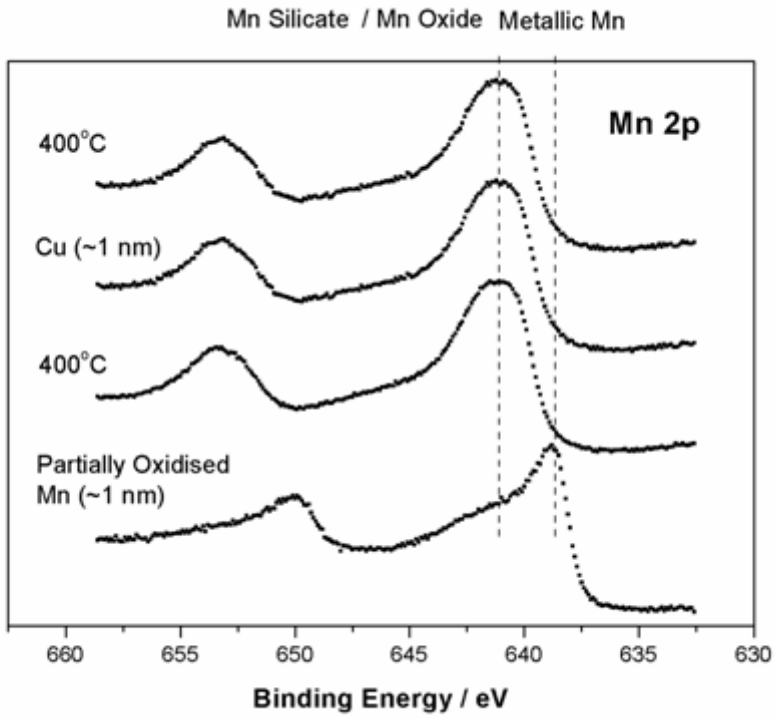

Figure 5.19: Mn 2*p* spectra showing the full conversion of Mn metal to silicate and no chemical interaction after copper deposition or subsequent 400 C anneal.

As stated previously, the full conversion of metallic Mn to Mn silicate prior to Cu deposition is of significant importance as the interaction of metallic Mn and Cu [**11**] is known to alter the profile of the Mn 2*p* photoemission peak, complicating chemical analysis. Therefore, in the absence of metallic Mn, the Mn 2*p* core level was used to investigate the chemical interaction of $MnSiO_3$ with a deposited Cu layer.

A ~ 1 nm Cu thin film was deposited on the $MnSiO_3$ surface at room temperature using electron beam evaporation, and subsequently annealed to 400 °C. Si 2*p* and O 1*s* spectra taken from the surface following annealing, in Figure 5.18, show no changes in peak profile suggesting that no chemical interaction occurred between the $MnSiO_3$ barrier layer and the deposited Cu film at 400 °C. The Mn 2*p* spectrum in Figure 5.19 also shows no changes in peak profile following 400 °C annealing, which again suggests that there was no chemical interaction between the Cu and $MnSiO_3$ layers. In addition

to this it should be noted that the Cu 2p spectrum taken from the surface following 400 °C annealing (not shown) is identical to that taken before annealing, and showed no evidence for the presence of Cu oxide. This result is of significance given that one of the primary functions of the $MnSiO_3$ barrier layer is to prevent the oxidation of the Cu interconnect during thermal annealing [**2**]. Furthermore, the work of Willis *et al* [**21**] has suggested that the formation of Cu oxide acts as an intermediate step in the diffusion mechanism of Cu through SiO_2. Therefore, within the detection limits of conventional XPS it can be suggested that $MnSiO_3$ acts as an effective barrier layer to copper migration following 400 °C annealing. However, it should be noted that conventional XPS is not the analysis technique best suited to investigate the effectiveness of $MnSiO_3$ as a barrier layer to the diffusion of Cu. Therefore, after the completion of XPS analysis a protective Cu capping (~ 10 nm) layer was deposited onto the surface, with the sample being removed from UHV and subsequently analysed using TEM related techniques.

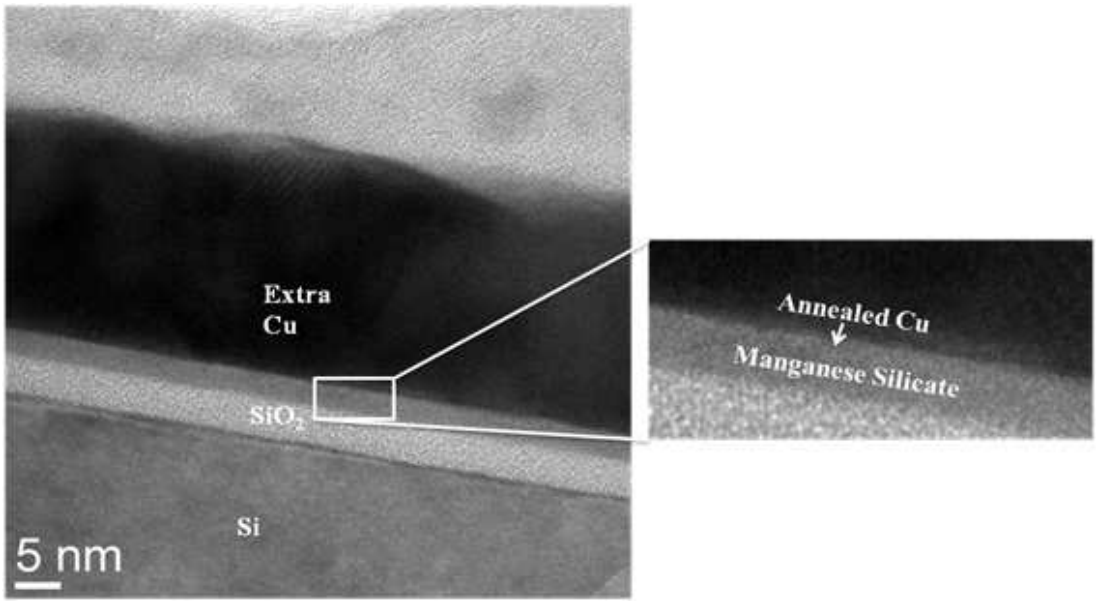

Figure 5.20: HRTEM micrograph of copper capped pre-formed silicate sample in cross section.

The HRTEM and low magnification TEM images shown in Figure 5.20 taken from the same sample as that was analysed using XPS in Figure 5.18 and Figure 5.19 show that all the layers are quite uniform and, with the exception of the Mn silicate/annealed Cu layer have sharp interfaces. The silicate and the annealed Cu layers appear to have an amorphous structure, while the extra copper capping layer seems polycrystalline. HAADF micrographs shown in Figure 5.21 show a layer approximately 1nm thick located between the silicate and the extra capping Cu with an unexpected dark contrast. High resolution EELS spectra using a 5 angstrom diameter probe shown in Figure 5.22 indicates that this dark layer corresponds to the thin annealed copper film and contains a certain amount of Mn and O, indicating that the silicate may be somewhat incorporated into the thin annealed copper layer.

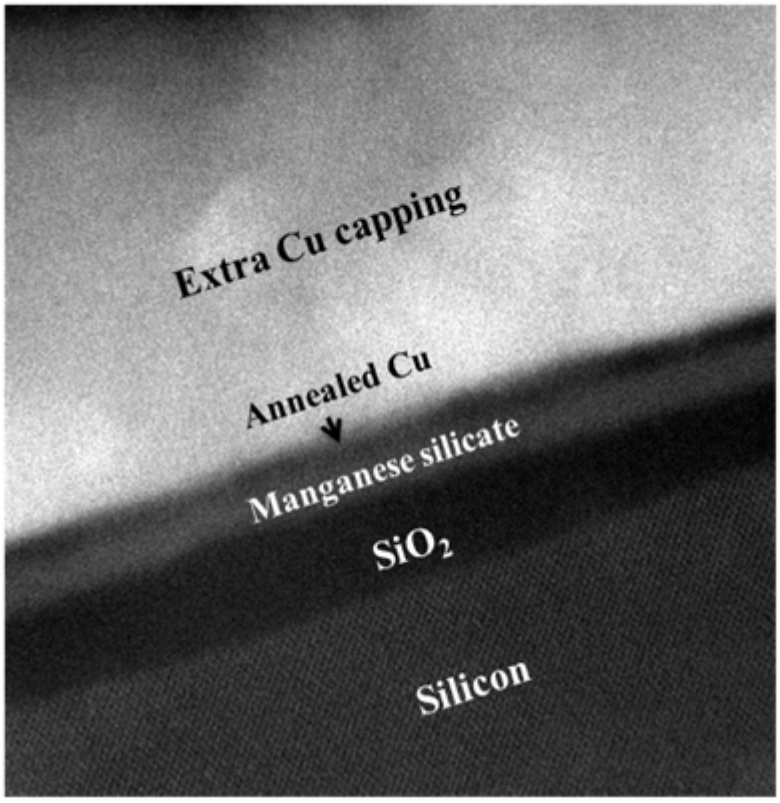

Figure 5.21: High resolution STEM-HAADF micrograph of the pre-formed silicate sample.

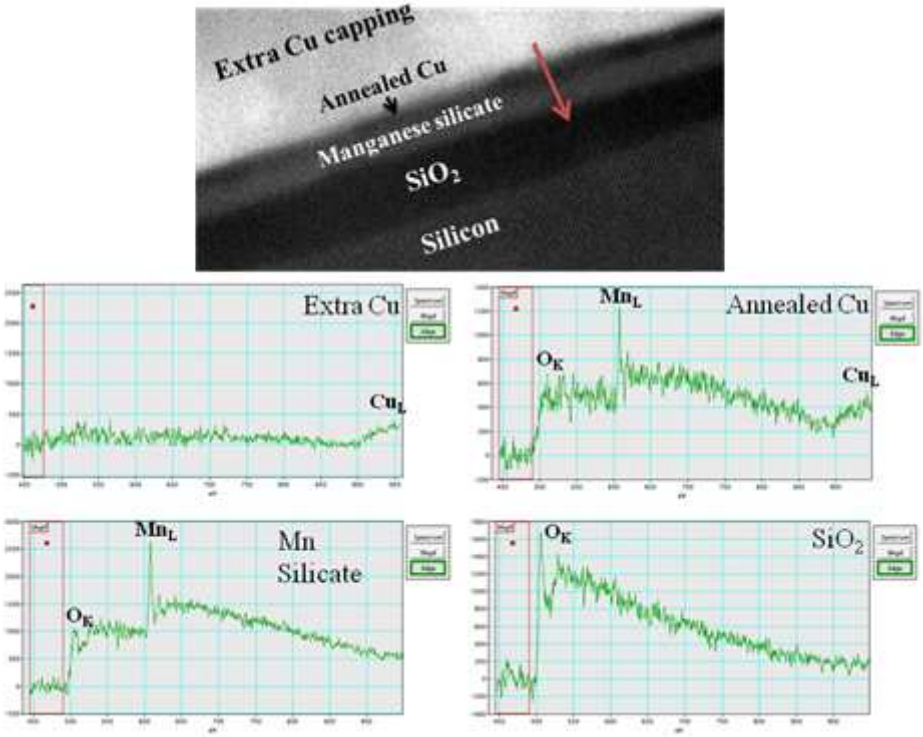

Figure 5.22: EELS spectra of the different layers indicating that the dark layer in the annealed copper film.

The calculated thicknesses of the different layers, using the Si (111) planes in the HR-STEM micrographs for calibration, are shown in Table 6. The incorporation of the SiO_2 into the manganese silicate layer is observed by the ≈25% thinning of the 5.4 nm SiO_2 substrate.

Layer	**Thickness (nm)**
Extra Cu	24
Annealed Cu	0.85
Mn silicate	2.50
SiO_2	3.90

Table 6: Thickness values of individual layers.

Figure 5.23 shows the EELS line profile which clearly indicates the presence of the four distinct regions within the sample, namely the Cu capping layer, the annealed copper layer, ~ 3 nm $MnSiO_3$ barrier layer and the underlying 5.4 nm thermal SiO_2 film. While there is a slight overlapping between the $MnSiO_3$ and Cu capping layer regions, to within the detection limit of the technique, it can be clearly seen that the Cu signal falls to zero within the SiO_2 region. Therefore, based on the combined XPS and EELS results shown in this study it can be stated that $MnSiO_3$ layers with a thickness of ~3 nm act as effective barrier to Cu diffusion following 400 °C annealing, and also show no evidence of chemical interaction at this temperature.

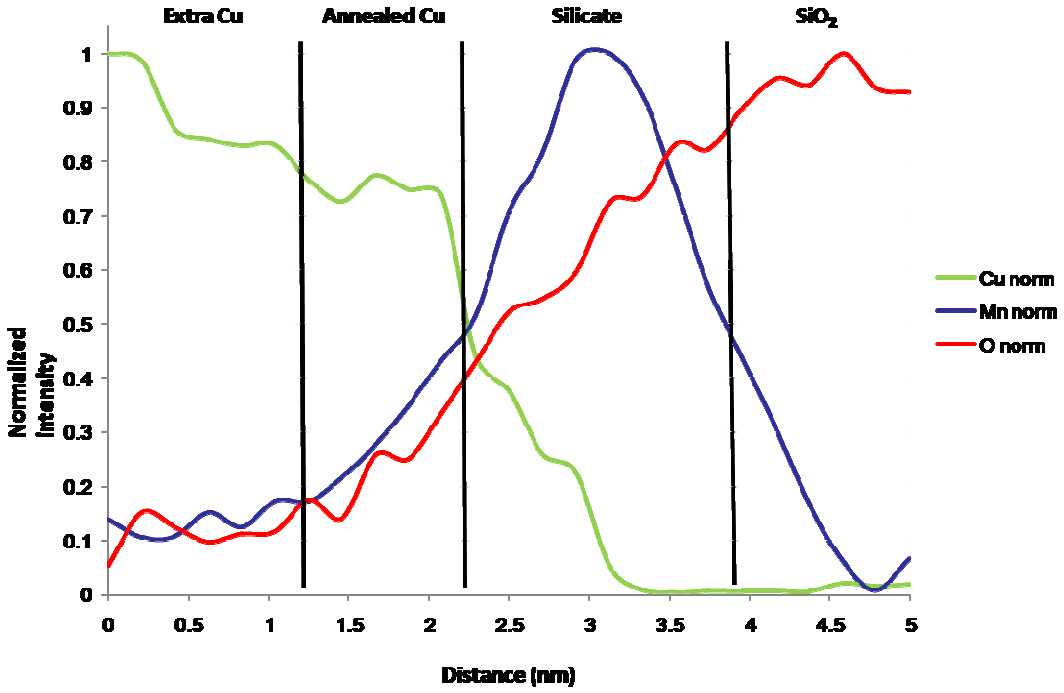

Figure 5.23: Normalized EELs composition linescan across the layers indicating barrier formation.

While the spectra in Figure 5.18 and Figure 5.19 show that there is no chemical interaction at high temperature between Cu and pre-formed $MnSiO_3$ barrier layers, further studies were performed in order to investigate the interaction of Mn and Cu

during barrier layer formation. This was achieved through the initial deposition of a ~ 1 nm partially oxidised Mn film, followed by the deposition of a ~ 1 nm Cu film prior to annealing. This experiment allowed the inherent chemical interactions which occur at the MnO_x/Cu interface to be investigated using a more simplistic experimental system than a MnO_x/Cu alloy.

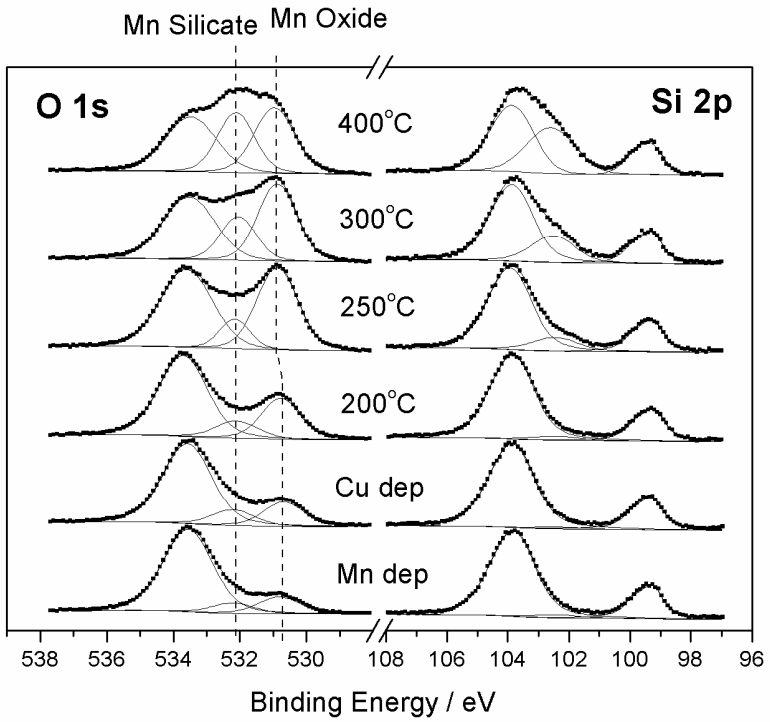

Figure 5.24: Curve fitted O 1*s* and Si 2*p* spectra showing the formation of both Mn silicate and Mn oxide when the barrier is formed in the presence of copper.

Figure 5.24 shows O 1*s* and Si 2*p* spectra taken from the 5.4 nm SiO_2 surface before and after then deposition of a ~ 1 nm partially oxidised Mn film. In agreement with Figure 5.18, spectra show evidence for the growth of $MnSiO_3$ upon deposition and also show evidence for Mn oxide species within the partially oxidised Mn film. A ~ 1 nm Cu film was subsequently deposited on the surface, which resulted in no changes in the O 1*s* and Si 2*p* spectra, as seen in Figure 5.24. However, the corresponding Mn 2*p* spectra in Figure 5.25 show considerable changes in peak profile following Cu deposition, which are attributed to the previously mentioned interaction between metallic Mn and Cu [**11**]. A

series of high temperature vacuum anneals between 200 °C and 400 °C were then performed on the sample and the corresponding core level spectra are shown in Figure 5.24 and Figure 5.25. The O 1*s* and Si 2*p* spectra taken following 200 °C show evidence for the growth of $MnSiO_3$, in agreement with the results of Figure 5.18, as seen by the growth of component peaks at 531.3 eV and 102.6 eV respectively. However, the O 1*s* spectrum also shows evidence for the growth of Mn oxide on the surface following 200 °C annealing, in contrast to results seen in Figure 5.18 of this study. Further evidenced for the growth of Mn oxide can also be seen from O 1s spectra taken following subsequent anneals to 250 °C and 300 °C. It can also be seen that further annealing to 300 °C and 400 °C resulted in the conversion of these Mn oxide species to Mn silicate, as evidenced by the reduction of the Mn oxide component and concurrent growth in the Si 2p and O 1s $MnSiO_3$ component peaks. The high levels of Mn oxide growth seen in Figure 5.25 are in contrast to results seen for $MnSiO_3$ growth in the absence of Cu, indicating that the presence of Cu at the Mn/SiO_2 interface alters the chemical composition of the barrier layer. It should also be noted that the profile of the Cu 2*p* spectra was unaltered following 400 °C annealing, suggesting that the chemical composition of the Cu layer was not changed during the formation of $MnSiO_3$ and Mn oxide species.

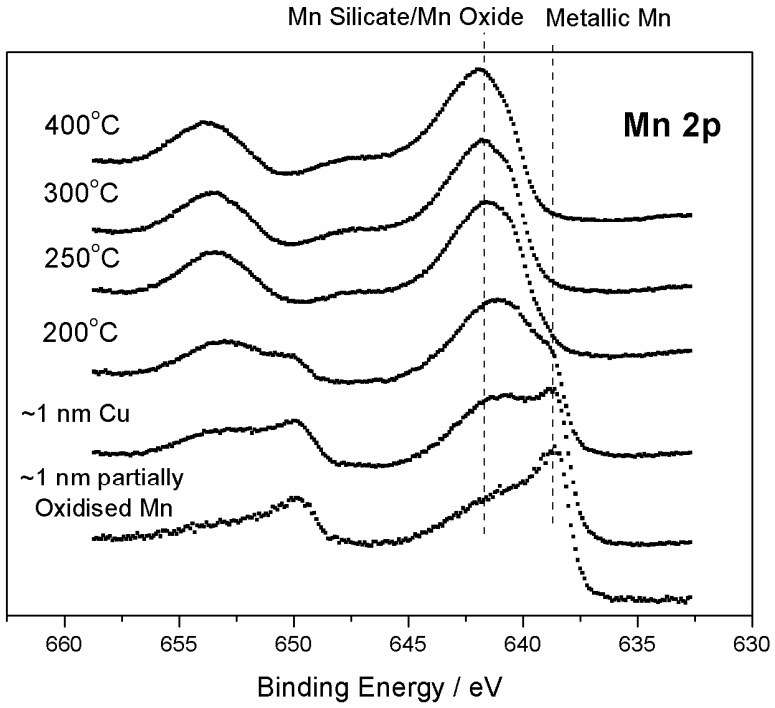

Figure 5.25: Mn 2p spectra showing the Cu/Mn metal interaction when forming the silicate layer in the presence of copper.

In order to further investigate how the presence Cu at the MnO_x/SiO_2 interface during $MnSiO_3$ growth affects the chemical composition of the barrier layer, a ~2 nm alloy containing approximately 60 % partially oxidised Mn and 40 % Cu was deposited onto the 5.4 nm SiO_2 surface. Angular resolved XPS measurements showed no evidence of spatial segregation between the Mn and Cu, which suggests that the alloy was homogenous. It should be noted that the Mn:Cu ratio used in this experiment was considerably more Mn rich than that used in previous publications [**16**]. However, in order to form a $MnSiO_3$ layer of sufficient thickness to be easily investigated using conventional XPS then the thickness of deposited Mn could not be reduced below ~ 1 nm. Furthermore, the low sampling depth and high surface sensitivity of XPS places an upper limit on the total alloy thickness which could be deposited without attenuating the underlying Si 2p and O 1s core level spectra. As such, it is suggested that while the Mn:Cu ratio used in this experiment is different to that used in previous publications,

the study still serves to highlight the inherent chemical interactions which occur between Mn/Cu alloys on SiO_2 surfaces.

Figure 5.26 shows O 1s and Si 2p spectra taken from the SiO_2 surface before and after Mn/Cu alloy deposition. The spectra show evidence for the growth of Mn silicate upon alloy deposition, in agreement with results in Figure 5.18 and Figure 5.24, while the O 1s spectrum again shows evidence for the presence of Mn oxide within the partially oxidised Mn film. Mn 2p spectra taken following alloy deposition are shown in Figure 5.27. As stated previously, changes in the Mn 2p peak profile due to the interaction of metallic Mn and Cu complicate the analysis of the chemical state of Mn within the alloy. However, given that this interaction does not affect the peak profile of the Cu 2p core level [**11**] it can be stated that the Cu present within the alloy is in the form of un-oxidised metallic Cu.

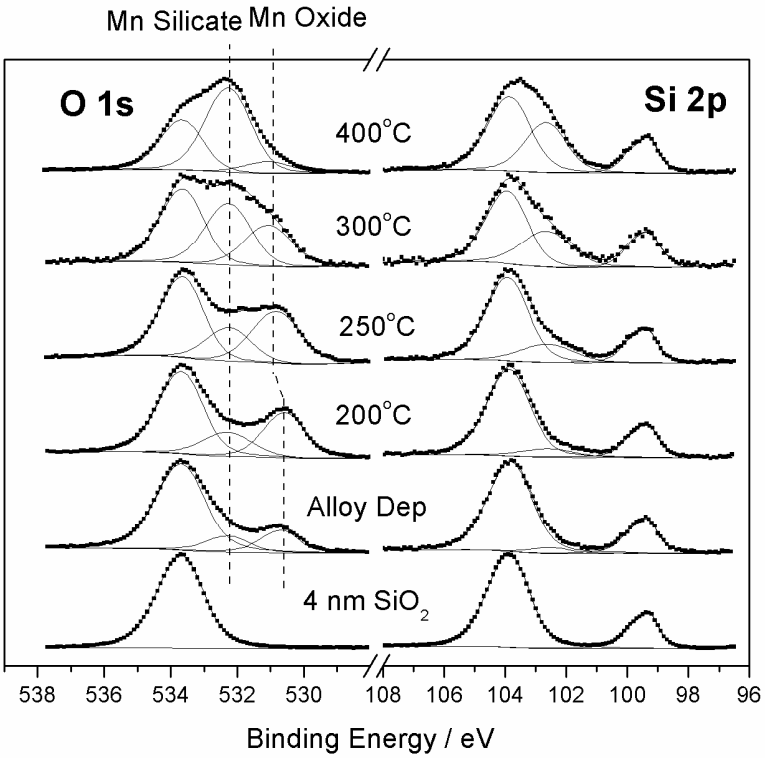

Figure 5.26: Curve fitted O1s and Si2p spectra showing deposition of Mn/Cu alloy and subsequent formation of Mn silicate and Mn oxide after anneal

A series of high temperature vacuum anneals between 200 °C and 400 °C were performed on the sample and the O 1s and Si 2p spectra taken from these anneals are shown in Figure 5.26. The O 1s and Si 2p spectra show evidence for the growth of $MnSiO_3$ following 200 °C annealing. However, the O 1s spectrum again shows evidence for the growth of Mn oxide on the surface following annealing, in agreement with results seen in Figure 5.24. The spectra in Figure 5.26 also show that annealing to 250 °C results in further growth of Mn oxide within the barrier layer, while subsequent anneals to 300 °C and 400 °C result in the conversion of Mn oxide to $MnSiO_3$ in agreement with the results of Figure 5.24. Based on the results of Figure 5.24 and Figure 5.26 it can be stated that the presence of Cu at the Mn/SiO_2 interface during the formation of $MnSiO_3$ barrier layers leads to the growth of Mn oxide, a result which is not seen for barrier layers formed in the absence of Cu.

While the results of this study suggest that the Mn oxide species formed on the surface can be converted to Mn silicate using thermal annealing, the work of Fredrick *et al* [**22**] has shown that the formation of metal oxide species through the reduction of SiO_2 may result in the release of Si into the Cu overlayer, increasing the resistance of the interconnect. Therefore, the origin of the Mn oxide species may be of significance to the properties of the barrier layer.

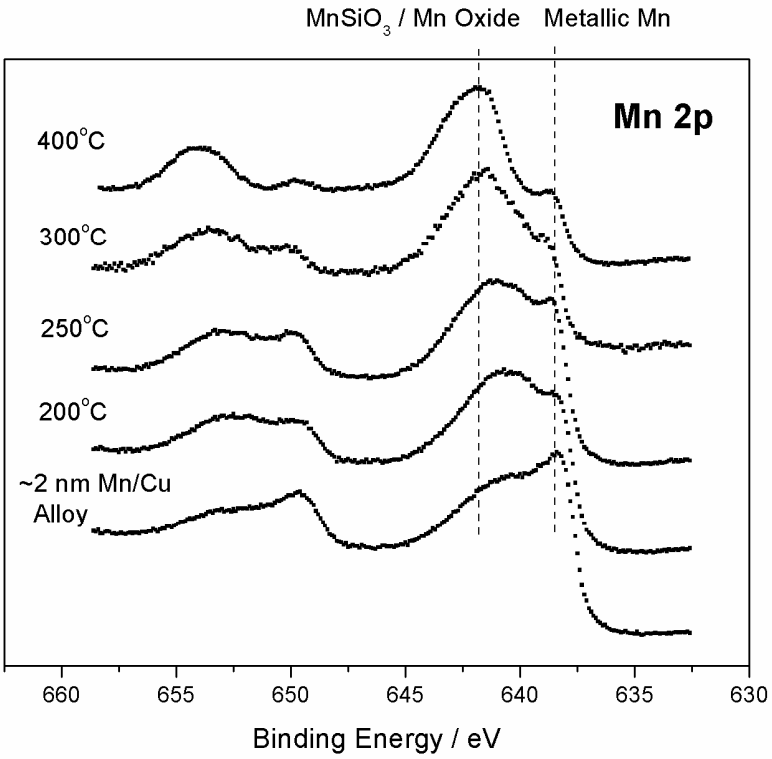

Figure 5.27: Mn 2p spectra after alloy deposition and annealing show the reduction in metallic Mn and shift to HBE in the peak profile. The presence of residual metallic Mn prevents in depth analysis of the spectra.

It is suggested that the two possible oxygen sources within the experimental set up are the SiO_2 substrate and gaseous oxygen present within the UHV chamber during annealing. While all thermal anneals performed in this study were carried out at pressures 5×10^{-9} mbar, the work of B. Lescop [**23**] has shown that the oxidation of Mn can occur within UHV conditions, at oxygen exposure levels less than 20 L. However, this growth method would necessitate the addition of extra oxygen to the surface, which would have lead to a corresponding attenuation of the Si 2p core level concurrent with the growth of Mn oxide species. Given that such an attenuation was not seen in this study it is suggested that Mn oxide species were not formed due to the presence of gaseous O_2 within the UHV system. In addition to this, the presence of a Cu overlayer on the surface of the 1 nm Mn film in Figure 5.24 may have inhibited the

formation of Mn oxide through interaction with gaseous O_2 within the UHV chamber. Therefore, it is suggested that the reduction of SiO_2 is the primary source of Mn oxide growth, seen during the formation of $MnSiO_3$ in the presence Cu.

While the results of this study show that the presence of Cu at the MnO_x/SiO_2 interface changes the chemical composition of the barrier layer, the reasons for this are not fully understood. It has been suggested by Ablett et al [**8**] that the interaction of metallic Mn and Cu leads to the ionization of Mn, therefore it may be proposed that this ionization may lead to changes in the chemical reactivity of the Mn and may cause the formation of Mn oxide on the surface in Figure 5.24 and Figure 5.26. However, it should be noted that this has not been conclusively shown in this study.

The differing chemical composition of Mn silicate barrier layers formed in the presence of Cu to those formed without Cu shown in this study is also in agreement with published results. While Koike *et al* [**7**] have reported the formation of a mixed Mn silicate and Mn oxide barrier layer following the deposition of a Mn/Cu alloy, Gordon et al [**3**] have reported the formation of a purely $MnSiO_3$ layer following the deposition of Mn without Cu.

The Mn 2*p* spectra in Figure 5.28 show a similar trend to that seen in Figure 5.19 and Figure 5.25, with a reduction of metallic Mn and shift to HBE which is indicative of both Mn silicate and Mn oxide growth. However, it should be noted that there is still evidence for the presence of residual metallic Mn following 350 °C annealing, which is in contrast to the previous results shown in Figure 5.19 and Figure 5.25. This discrepancy can be attributed to either the deposition of too much Mn, given the self limiting nature of the silicate reaction discussed previously in Chapter 4; or the diffusion of metallic Mn away from the interface, towards the surface of the alloy layer.

Given that care was taken to ensure that all Mn deposition settings were kept consistent between all experiments it is thought unlikely that there was a great discrepancy between the amounts of Mn deposited in the samples corresponding to Figure 5.19 and

Figure 5.25. Evidence that metallic Mn may have diffused away from the interface and towards the surface of the film is shown by angular resolved Mn 2p spectra taken after 350 °C annealing shown in Figure 5.28 which suggests that the residual metal Mn was more surface localised than the interfacial silicate.

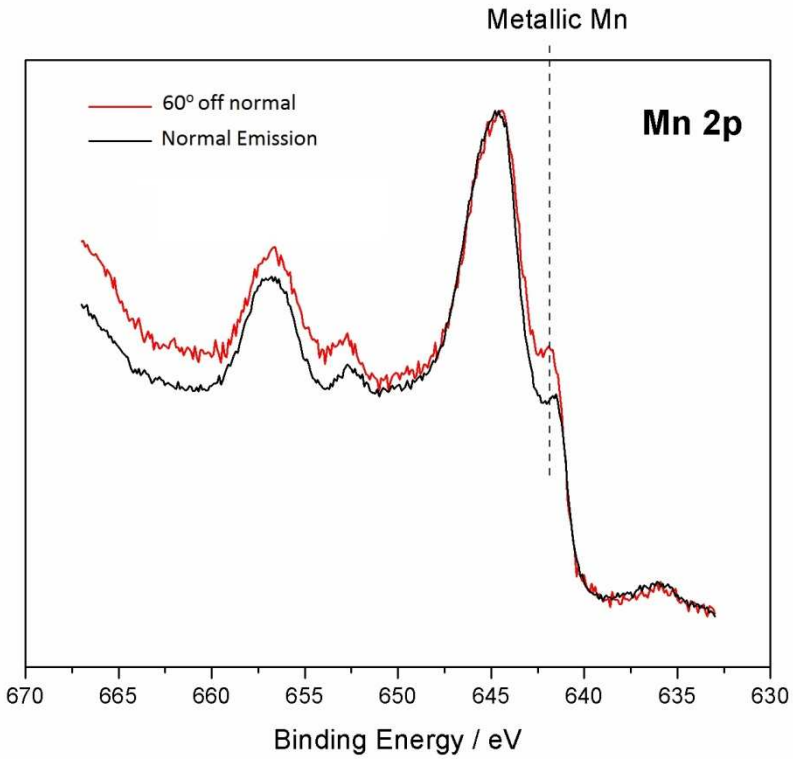

Figure 5.28: Normal emission and 60° off normal Mn 2p spectra showing that residual metallic Mn is surface localized with respect to the Mn silicate barrier layer.

Regardless of the reasons for the presence of this residual metallic Mn, the interaction between Mn and Cu described earlier prevents in-depth analysis of the Mn 2p spectra. However, it is suggested that the O 1s and Si 2p spectra shown in Figures 5.24 and 5.26 show sufficient evidence to suggest that both Mn silicate and Mn oxide species are formed following alloy deposition. This result is again in contrast to that seen following the initial deposition of Mn followed by high temperature annealing, before Cu deposition onto the preformed silicate layer.

5.6 Chapter Conclusions

In summary, it has been shown that the thermal deposition of metallic Cu on SiO_2 substrates shows no evidence for chemical reaction upon deposition. The reappearance of SiO_2 substrate signal upon vacuum anneal is shown using XPS. AFM analysis indicates that this reappearance is due to the formation of Cu islands highlighting the reported adhesion problem in copper interconnects [**24**] [**25**]. However, no chemical reaction is seen between the Cu and the substrate even after a series of thermal anneals. The second section of the chapter deals with the deposition of thick (30 nm) Mn/Cu heterostructures on SiO_2, investigated by both XPS and TEM related techniques. XPS and low resolution TEM images show the migration of Mn atoms through the 30 nm copper layer to the surface of the sample. EELS and EDX maps indicate the occurrence of interdiffusion between the Mn and Cu layers, confirming that the Mn tends to diffuse toward the surface of the structure, while the Cu atoms diffuse toward the Mn / SiO_2 interface surrounding clusters, where a higher content of metallic Mn is detected. EELS analysis indicates that the chemical composition of the 2–3 nm interfacial layer is primarily Mn in +2 and +3 oxidation states which is reported as being effective at preventing Cu diffusion into the dielectric layer [**7**].

The final section of the chapter deals with the introduction of Cu into the Mn silicate/SiO_2 structures discussed in Chapter 4. The results of this study confirms that Mn silicate ($MnSiO_3$) barrier layers, free from Mn oxide and metallic Mn, can be formed on SiO_2 surfaces through the deposition of partially oxidised Mn (MnO_x) from a partially oxidised Mn source without the presence of Cu. The chemical and thermal stability of Cu layers on $MnSiO_3$ has also been investigated, with conventional XPS showing that subsequent deposition of Cu onto the preformed silicate surface showed no evidence of chemical interaction between Cu and $MnSiO_3$ following 400 °C annealing. Spectra taken after Cu deposition and 300 °C annealing again showed no evidence for the formation of Mn oxide species. It has also been shown using EELS analysis that a

$MnSiO_3$ layer with a thickness of ~ 3 nm acts as an effective barrier layer to Cu diffusion following 400 °C annealing. Separate experiments investigating the growth of barrier layers through the sequential deposition of MnO_x and Cu layers and the deposition of MnO_x/Cu alloys have also been performed. It has been shown that when Cu is present at the MnO_x/SiO_2 interface during $MnSiO_3$ growth, Mn oxide species are also formed within the barrier. The presence of both Mn oxide and Mn silicate has been shown following the sequential deposition of Mn and Cu films prior to annealing, and has also been shown to occur following the co-deposition of a Mn / Cu alloy. Results indicate that Mn oxide species form due to the reduction of SiO_2, which is reported to lead to the diffusion of Si into the Cu layer, increasing the resistivity of the interconnect [**22**]. It is suggested that growth of Mn oxide at the $Cu/MnO_x/SiO_2$ interface may be due to the ionization of Mn due to the interaction of metallic Mn and Cu [**8**], however, this has not been conclusively shown in this study.

Based on these results it is suggested that the deposition and annealing sequence used during barrier layer formation has a large affect on the chemical composition of the barrier layer. In particular it is suggested that the presence of Cu within the interfacial region during silicate formation results in the formation of Mn oxide species. The reasons for this are not entirely clear, as Cu spectra taken from the surface show no evidence for the creation of Cu bonds to other chemical species, regardless of the deposition sequence used. However, it has been suggested in previous publications that the interaction between Cu and metallic Mn results in the ionisation of the metallic Mn layer. It is suggested that this ionisation may affect the chemical reactivity of the Mn layer, which in turn results in changes to the chemical composition of the barrier layers formed using deposition processes which involve the initial interaction of Cu and Mn prior to silicate formation. This proposed reaction mechanism is further supported by the fact that there is no observed interaction between Cu and Mn silicate in the absence of residual metallic Mn.

5.7 References

[1] C. Lee and Y.-L. Kuo, "The Evolution of Diffusion Barriers in Copper Metallization," *JOM*, pp. 44-49, Jan. 2007.

[2] R. G. Gordon, K. Hoon, Y. Au, H. Wang, and H. B. Bhandari, "Chemical Vapor Deposition (CVD) of Manganese Self-Alighned Diffusion Barriers for Cu Interconnections in Microelectronics," in *Advanced Metallization Conference*, California, 2008.

[3] R. G. Gordon and H. Kim, "Self-Aligned Barrier Layers for Interconnects," U.S. Manufacturing WO 2009/117670 A2, Sep. 24, 2009.

[4] Y. Au, et al., "Selective Chemical Vapor Deposition of Manganese Self-Alighned Capped Layer for Cu Interconnections in Microelectronics," *J. Electrochem. Soc.*, vol. 157, no. 6, pp. 341-345, Apr. 2010.

[5] M. Haneda, J. Iijima, and J. Koike, "Growth behavior of self-formed barrier at Cu--Mn/SiO2 interface at 250--450 C," *Appl. Phys. Lett.*, vol. 90, no. 252107, 2007.

[6] S.-M. Yi, K.-H. Jang, J.-U. An, S.-S. Hwang, and Y.-C. Joo, "The self-formatting barrier characteristics of Cu–Mg/SiO2 and Cu–Ru/SiO2 films for Cu interconnects," *Microelectron. Reliab.*, vol. 48, no. 5, pp. 744-748, May 2008.

[7] J. Koike and M. Wada, "Self-forming diffusion barrier layer in Cu-Mn alloy metallization," *Appl. Phys. Lett*, vol. 87, no. 041911, Jul. 2005.

[8] J. M. Ablett, J. C. Woicik, Z. Tokei, and S. List, "Phase identification of self-forming Cu-Mn based diffusion barriers on p-SiOC:H and SiO2 dielectrics using x-

ray absorption fine structure," *Appl. Phys. Lett.*, vol. 94, no. 042112, Jan. 2009.

[9] Y. Otsuka, J. Koike, H. Sako, K. Ishibashi, and N. Kawasaki, "Graded composition and valence states in self forming barrier layers at Cu-Mn/SiO2 interface," *Appl. Phys. Lett*, vol. 96, no. 012101, Jan. 2010.

[10] M. O. Krause and J. G. Ferreira, *J. Phys. B: At. Mol. Phys.*, vol. 8, no. 12, 1975.

[11] U. Manju, D. Topwal, G. Rossi, and I. Vobornick, "Electronic structure of the two-dimensionally ordered Mn/Cu(110) magnetic surface alloy," *Phys. Rev. B*, vol. 82, no. 035442, Jul. 2010.

[12] J. F. Moulder, W. F. Stickle, P. E. Sobol, and K. D. Bomden, *Handbook of X-Ray Photoelectron Spectroscopy*, J. Chastain, Ed. United States of America: Perkin-Elmer Corporation, Physical Electronics Division, 1992, XPS Handbook.

[13] S. Lozano-Perez, V. de Castro Bernal, and R. J. Nicholls, "Achieving sub-nanometre particle mapping with energy-filtered TEM," *Ultramicroscopy*, vol. 109, no. 10, pp. 1217-1228, Sep. 2009.

[14] H. K. Schmid and W. Mader, "Oxidation states of Mn and Fe in various compound oxide systems," *Micron*, vol. 37, no. 5, pp. 426-432, Jul. 2006.

[15] J. H. Rask, B. A. Miner, and P. R. Buseck, "Determination of manganese oxidation states in solids by electron energy-loss spectroscopy," *Ultramicroscopy*, vol. 21, no. 4, pp. 321-326, 1987.

[16] J. Koike, M. Haneda, and J. Iijima, "Growth kinetics and thermal stability of a self-formed barrier layer at Cu-Mn/SiO2 interface," *J. Appl. Phys.*, vol. 102, no. 043527, Aug. 2007.

[17] H. Gleiter, "The segregation of copper at high angle grain boundaries in lead," *Acta*

Metall, vol. 18, no. 1, pp. 117-121, Jan. 1970.

[18] R. Roy and S. K. Sen, "The study of diffusion of copper in thin films of silver and Ag---Al alloys as a function of increasing aluminium concentration," *Thin Solid Films*, vol. 223, no. 1, pp. 189-195, Jan. 1993.

[19] I. Katayama, K. Oura, F. Shoji, and T. Hanawa, "Oxygen-Enhanced Surface Segregation of Mn in Cu-Mn and Ag-Mn Alloy Films Studied by ISS/AES," *Jpn. J. Appl. Phys.*, vol. 27, no. L1822, 1988.

[20] A. A. Audi and P. M. Sherwood, "Valence-band x-ray photoelectron spectroscopic studies of manganese and its oxides interpreted by cluster and band structure calculations," *Surf. Interface Anal.*, vol. 33, pp. 274-282, Dec. 2001.

[21] B. G. Willis and D. V. Lang, "Oxidation mechanism of ionic transport of copper in SiO2 dielectrics," *Thin Solid Films*, no. 467, pp. 284-293, Apr. 2004.

[22] M. J. Frederick, R. Goswami, and G. Ramanah, "Sequence of Mg segregation, grain growth, and interfacial MgO formation in Cu-Mg alloy films on SiO2 during vacuum annealing," *J. Appl. Phys.*, vol. 93, no. 10, pp. 5966-5972, May 2003.

[23] B. Lescop, *Appl. Surf. Sci*, vol. 252, no. 2276, 2006.

[24] T. Waechtler, S. Oswald, and N. Roth, "Copper Oxide Films Grown by Atomic Layer Deposition from Bis copper acetylacetonate on Ta, TaN, Ru, and SiO2," *Journal of The Electrochemical Society*, no. 156, pp. 453-459, Apr. 2009.

[25] R. Saxena, M. J. Frederick, G. Ramanath, W. N. Gill, and J. L. Plawsky, "Kinetics of voiding and agglomeration of copper nanolayers on silica," *Phys Rev B.*, no. 72, pp. 1-7, Sep. 2005.

[26] O. M. Ndwandwe, Q. Y. Hlatshwayo, and R. Pretorius, "Thermodynamic stabily of SiO2 in contact with thin metal films," *Mater. Chem. Phys.*, vol. 92, pp. 487-491, Jan. 2005.

Chapter 6

Growth and Analysis of Mn silicate barrier layers on carbon doped oxide surfaces

6.1 Introduction

While the majority of studies to date have focused on the formation of $MnSiO_3$ barrier layers on SiO_2 surfaces [**1**] [**2**], the growth of Mn based barrier layers on ultra low dielectric constant (ULK) materials has also been the subject of some interest [**3**] [**4**] [**5**] [**6**] [**7**]. The use of ULK interlayer dielectric materials in microelectronic devices acts to reduce the parasitic capacitance affects which are known to cause resistance-capacitance delay problems [**8**]. One of the ULK dielectric materials thought to be most compatible with modern device fabrication are carbon doped oxides (CDO) which are formed by replacing Si-O bonds in the SiO_2 with the less polar Si-CH_3 bond. The reduced polarity of this bonding structure and the introduction of voids within the CDO, schematically illustrated in Figure 6.1, acts to reduce the κ value of the substrate, with some low-κ CDO materials currently been investigated having reported dielectric constant values as low as 2.0 [**9**]. However, it has been shown that the low polarity Si-CH_3 bond is considerably weaker than Si-O bonds, which can reduce the reliability of the material in the device processing steps used in microprocessor fabrication [**7**]. It has also been reported that a wide range of processing steps can cause the depletion of C from CDO dielectrics, resulting in an increase of dielectric constant [**8**]. However, comparatively few

studies have focused on the growth of self forming barrier layer materials on CDO surfaces, and its effect on the carbon content of the dielectric material.

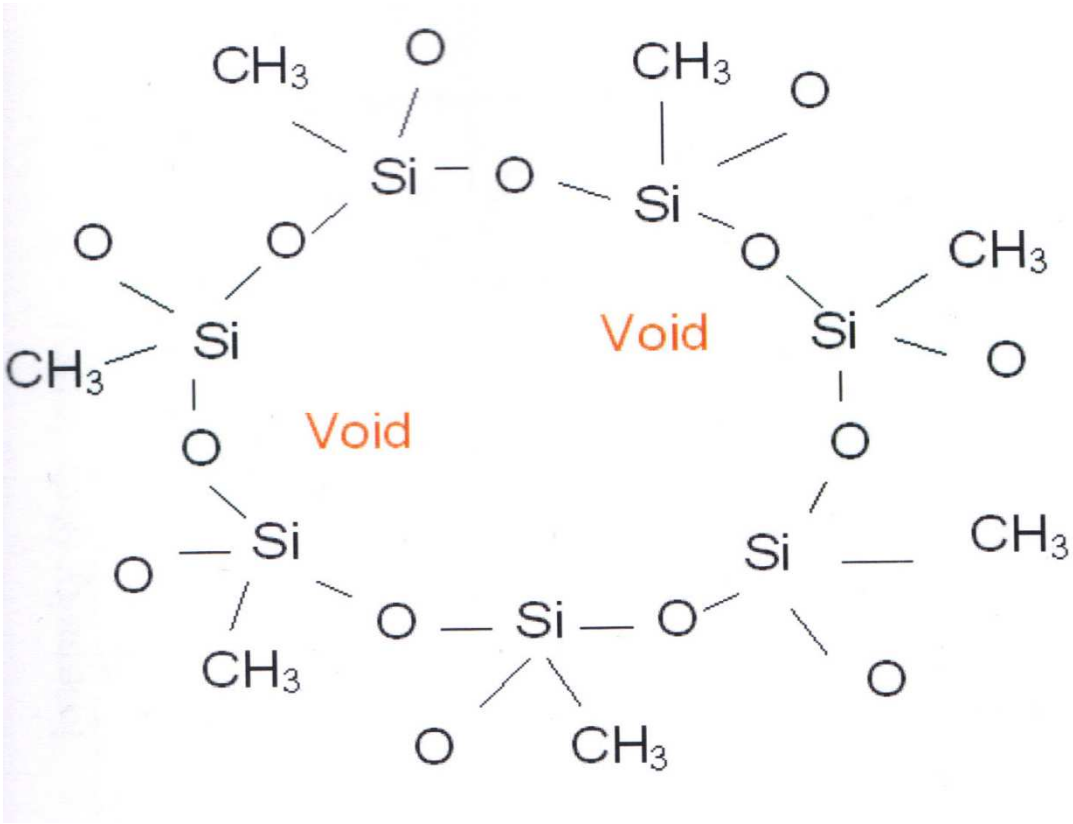

Figure 6.1: Schematic illustration of void formation within Aurora™ CDO

This chapter presents an initial investigation into the growth and analysis of Mn barrier layers on these ultra low-κ CDO surfaces. The chapter is divided into two sections which focus on two separate aspects of the use of the low-κ substrate. The first section introduces the Aurora™ CDO used throughout the study and details the XPS study which investigated the chemical and structural properties of thermally deposited Cu thin films on the CDO substrate both before and after thermal anneal. These investigations, in contrast to the similar study on SiO_2 in Chapter 5, shows evidence for the formation of copper oxide after anneal which may have a negative impact on the overall performance of the interconnect and indicate the increased importance of the barrier layer for low-κ materials. In the second section of this study the chemical interactions which occur between metallic Mn, partially oxidized Mn and fully oxidized

Mn thin films on CDO surfaces are systematically investigated. In-situ XPS is used to determine how changes in the stoichiometry of the deposited Mn film can cause changes in the chemical composition of the barrier. Given the importance of retaining carbon within CDO dielectrics in order to maintain their low-κ value, this study focused on developing a barrier layer growth process which prevented the depletion of carbon from the CDO layer during $MnSiO_3$ growth. Chapter 4 of this thesis showed that $MnSiO_3$ layers formed on thermally grown SiO_2 surfaces are self-limited by the availability of additional oxygen, beyond that found within the dielectric layer. It was shown that the maximum thickness of $MnSiO_3$ barrier layers formed on SiO_2 surfaces following the deposition of metallic Mn was >2 nm, while $MnSiO_3$ layers with a thickness of ~ 3nm could be formed following the deposition of partially oxidised and fully oxidised Mn layers. In this study in-situ XPS analysis is used to determine if the growth of $MnSiO_3$ barrier layers on CDO surfaces is similarly self-limited by the availability of Mn oxide species within the deposited layer.

6.2 Experimental Details.

An Aurora™ CDO ULK dielectric material with a dielectric constant of 2.4, as determined by elipsometry, was used in this study. The CDO layers have a thickness of ~ 350 nm as determined by transmission electron microscopy as illustrated in Figure 6.2, with an open porosity of 15 % - 16 % and 30 % closed pore volume [**10**]. The CDO surfaces were prepared using a standard degreasing procedure of successive dips in acetone, methanol and isopropyl alcohol (IPA) before being loaded into an ultra high vacuum (UHV) deposition and analysis system. Ablett et al [**5**] have previously suggested that the growth of $MnSiO_3$ surfaces on low-κ surfaces may be affected by the presence of adsorbed hydroxyl species, therefore, all samples were degassed prior to Mn deposition in order to remove residual water species adsorbed within the porous dielectric structure. Samples were degassed at ~ 200 °C for 2 hours, with the UHV chamber reaching a maximum pressure of 5×10^{-9} mbar during degassing. The XPS analysis was carried out in the vacuum system described in Chapter 3. High temperature annealing studies were carried out in vacuum at a pressure of 5×10^{-9} mbar, with samples kept at the target temperature for 60 minutes. Room temperature e-beam evaporation of copper thin films was performed using a Cu source material of 99.9 % purity, at a deposition pressure of 5×10^{-9} mbar. Hydrochloric acid (HCl) etched Mn chips, with a purity of ~ 99.9 %, were used as a source material for the deposition of oxygen free metallic Mn thin films using electron beam evaporation. Metallic manganese thin film deposition was performed at room temperature using the Oxford Applied Research EGC04 mini electron-beam evaporator, at a chamber pressure of 5×10^{-9} mbar. The deposition of partially oxidised Mn films was carried out by the controlled introduction of O_2 gas into the UHV chamber during metallic Mn deposition, resulting in an O_2 partial pressure of 4×10^{-8} mbar. The XPS core level spectra were curve fitted using Voigt profiles composed of Gaussian and Lorentzian line shapes in a 3:1 ratio and using a Shirley-type background. The full width at half maximum (FWHM) of the Si 2p CDO substrate peak was 1.4 eV, with a Mn silicate component peak FWHM of 1.5 eV.

The FWHM of the O 1s CDO component was 1.5 eV with Mn silicate and Mn oxide peaks in the range of 1.4 eV to 1.6 eV. The FWHM of the C 1s CDO component was 1.3 eV with a Mn carbide peak FWHM of 1.2 eV.

Again, it should be noted that curve fitting of the Mn 2p spectrum could not be easily performed given that XPS ghost peaks [**11**] emanating from the Mn $2p^{1/2}$ are present within the peak profile of the Mn $2p^{3/2}$ component. As such, only non-curve fitted Mn $2p$ spectra are included in this study. In agreement with previous Chapters, the Mn $2p$ spectra shown in this study are primarily used to identify the presence of metallic Mn and oxidised Mn species on the sample surface, with O $1s$ and Si $2p$ spectra used to conclusively identify the presence of differing oxidised Mn species such as Mn silicate and Mn oxide.

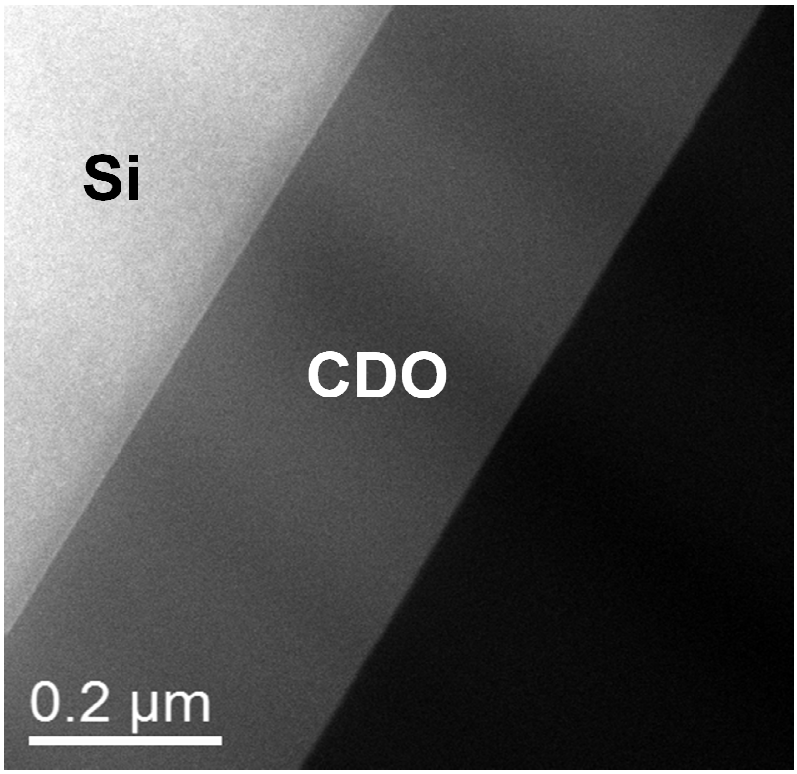

Figure 6.2: Low resolution TEM micrograph of Aurora™ CDO

6.3 Chemical characterisation of thermally deposited Cu films on CDO

Shown in Figure 6.3 is the survey spectrum (0-700 eV) of the CDO substrate taken immediately upon loading into the XPS system. The spectrum shows the expected Si 2*p* and O 1*s* core level peaks characteristic of a SiO_2 substrate, but also the addition of an increased C 1*s* signal due to the Si-CH_3 bonds within the substrate. Initial XPS chemical composition calculations [**10**] estimate the carbon content to be ~15%. No change is seen in the survey spectra upon 200 °C degassing indicating that the chemical composition of the substrate has not been significantly altered upon removal of any adsorbed species.

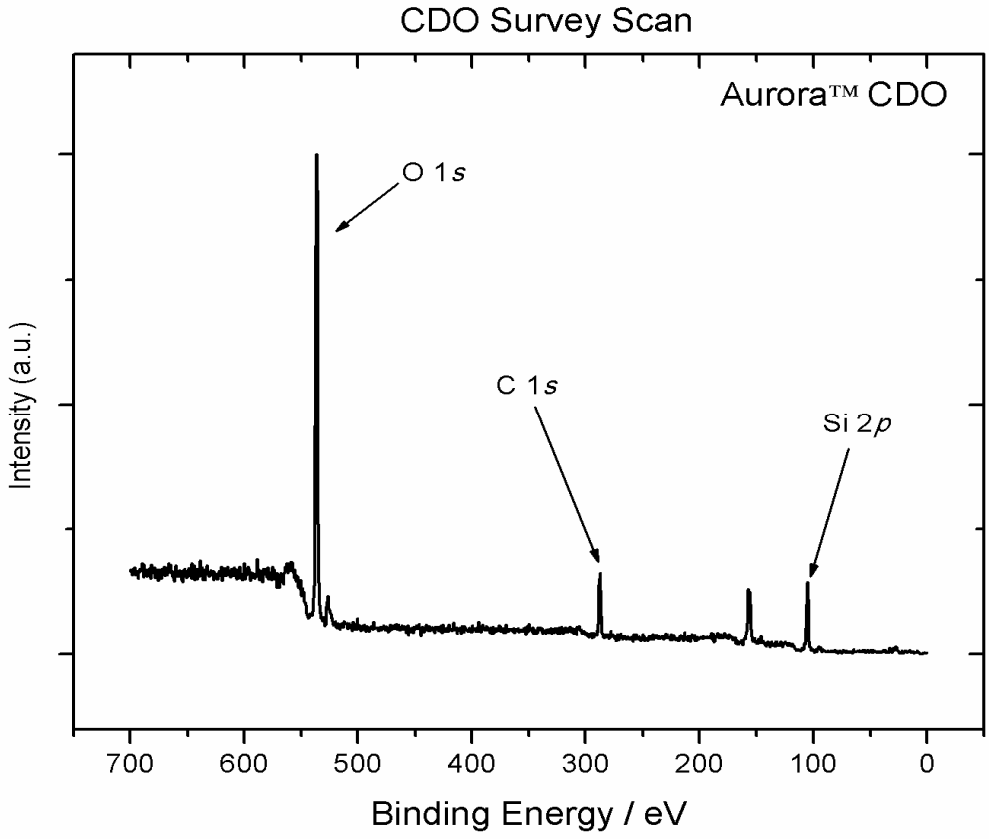

Figure 6.3: XPS survey spectra of Aurora™ CDO substrate

Figure 6.4 shows normalised narrow scans of the Si 2p and O 1s spectra taken from a degassed CDO sample compared with the corresponding reference spectra taken from the 5.4 nm SiO_2 substrate used throughout the previous studies in Chapter 4 and 5.

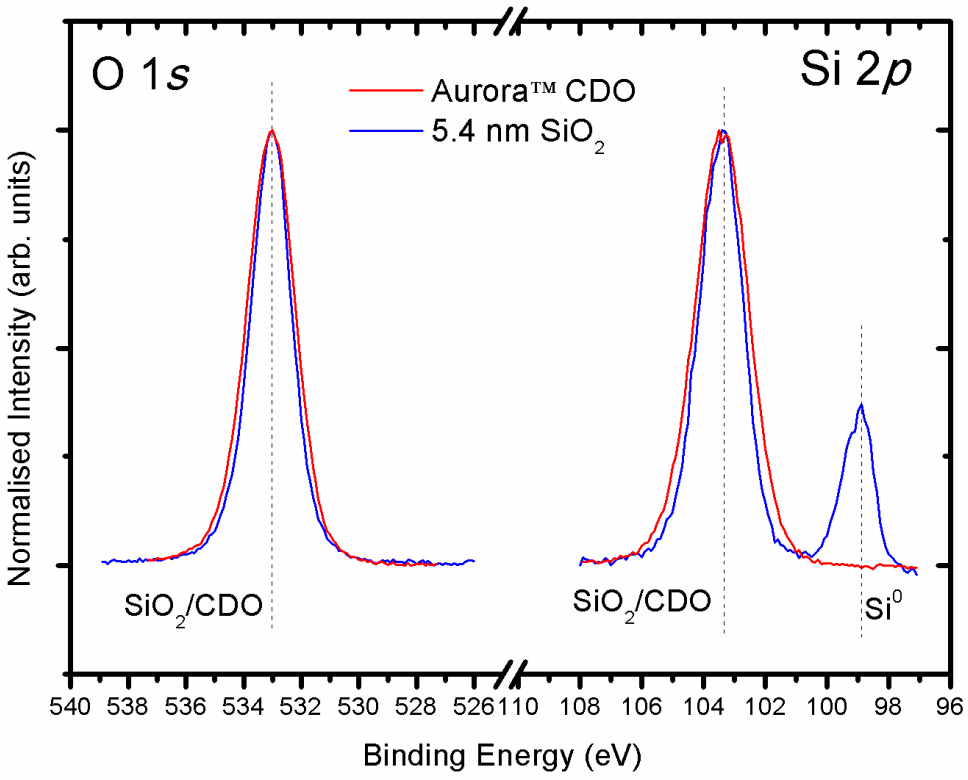

Figure 6.4: Comparison of Si 2*p* and O 1*s* spectra taken from CDO substrate with spectra from 5.4 nm SiO_2

The Si 2p spectra confirms that, unlike the 5.4 nm SiO_2 substrate, the CDO layer is too thick to see the silicon substrate making any Mn silicate thickness calculations used in Chapter 4 impossible. The slight increase in the FWHM of the Si 2*p* and O 1*s* spectra indicate that the CDO may be in a more complex chemical state than the SiO_2. However, the peak positions and relative peak shape of both the Si 2p and O 1s spectra suggests that the CDO may be comparable to the 5.4 nm SiO_2 substrate in terms on Mn silicate formation.

Approximately 2 nm of metallic Cu was subsequently deposited onto the CDO substrate at room temperature and annealed at 300 °C and 600 °C. The Cu 2*p* spectrum shown in Figure 6.5 indicates that the deposited copper film is in a purely metallic state and there has been no chemical reaction upon deposition. Following a 300°C anneal, an additional spectral component at HBE becomes evident which is attributed to copper oxide. The further growth of this additional component is seen following the 600 °C anneal.

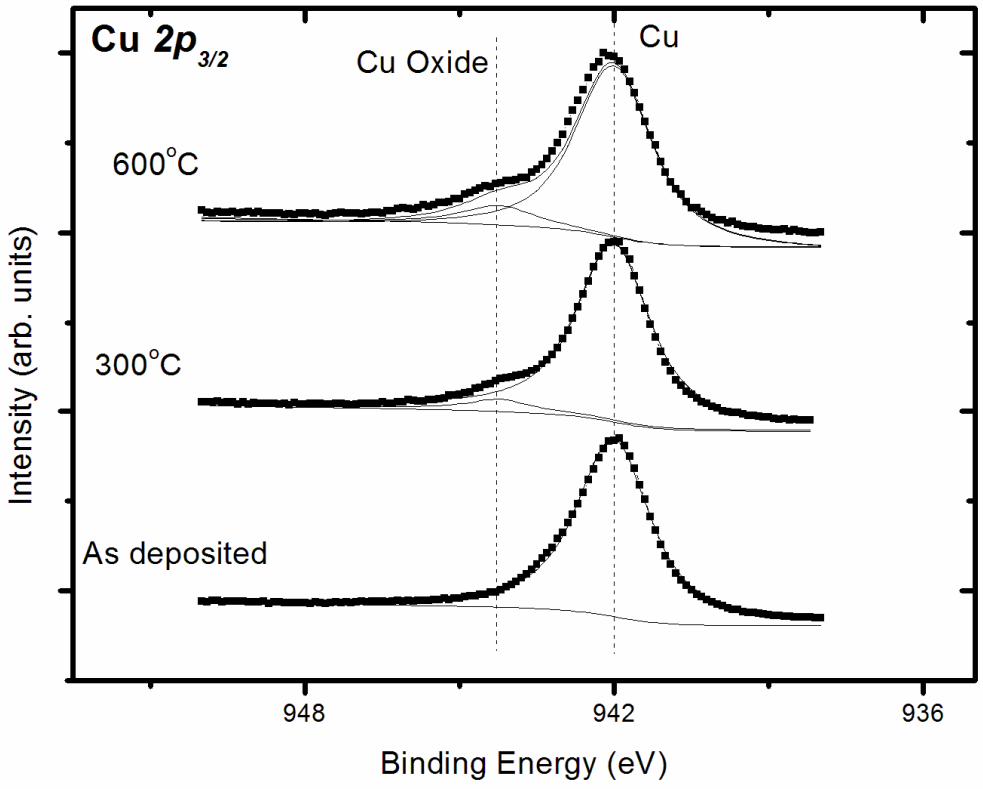

Figure 6.5: Curve fitted Cu 2*p* spectra showing the formation of a second chemical state after anneal

The corresponding O 1*s* spectra in Figure 6.6 confirms the growth of Cu oxide after anneal. It has been previously reported that it is this growth of Cu oxide, and the subsequent formation of Cu ions, which leads to diffusion of Cu into the interlayer dielectric [**12**]. Furthermore, the formation of the copper oxide may cause the chemical degradation of the CDO surface through breaking of weaker Si-O bonds which may increase the κ value of the CDO above that of SiO_2 negating any advantages of using the low- κ and freeing up elemental silicon which may then diffuse into the interconnect material.

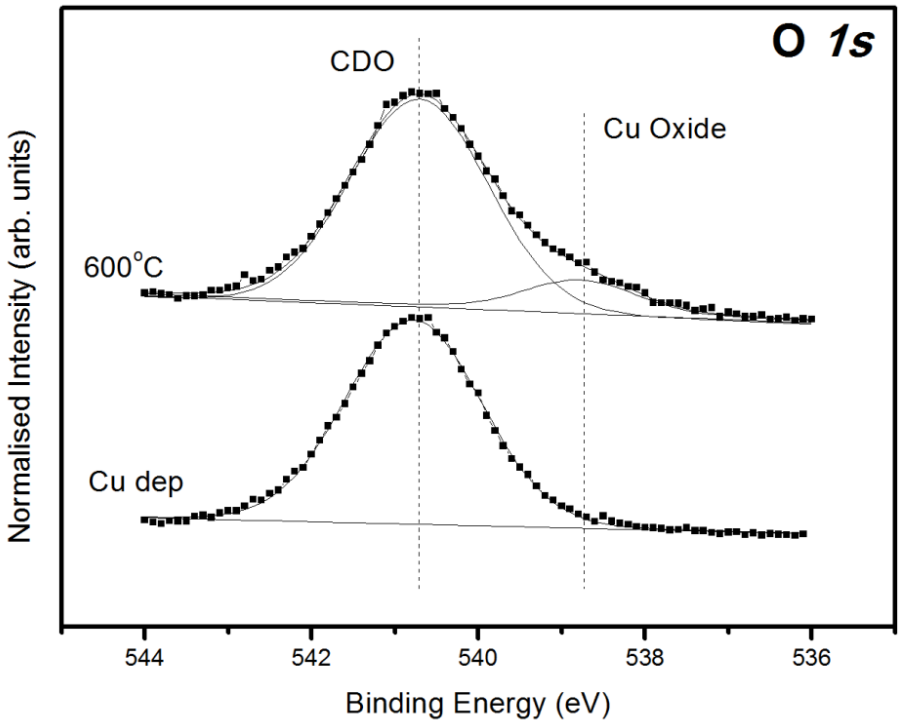

Figure 6.6: Curve fitted O 1*s* spectra corresponding to Figure 6.5 confirming the growth of Cu oxide following thermal anneal

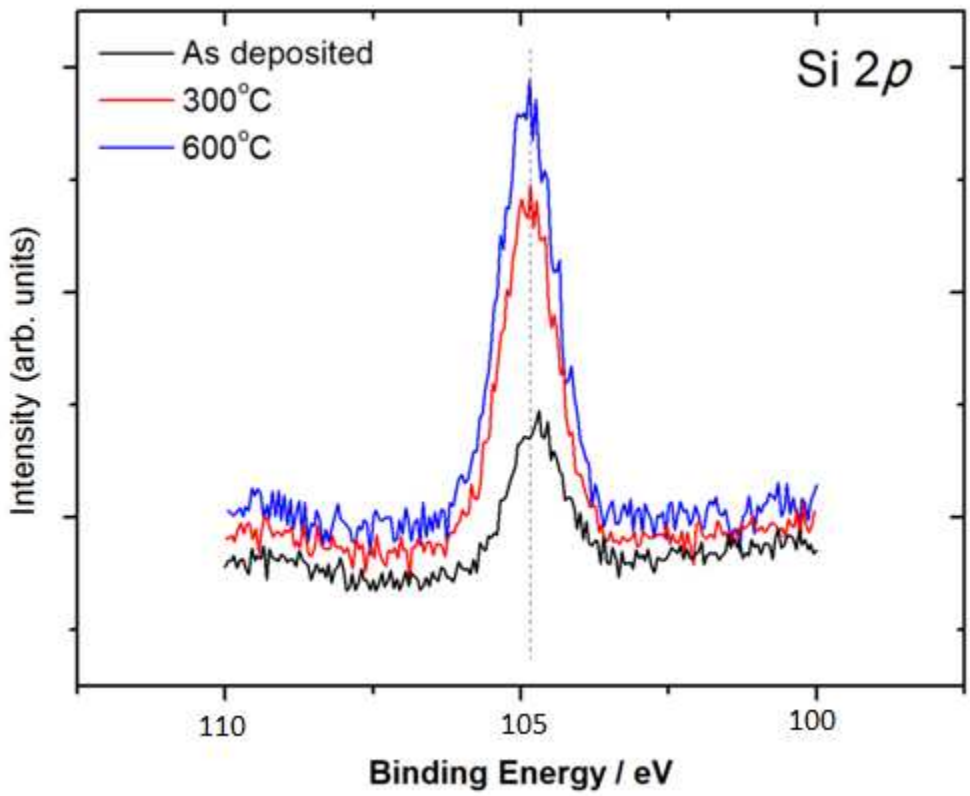

Figure 6.7: Increase in Si 2*p* signal due to uncovering of SiO_2 substrate

The XPS spectrum in Figure 6.7 shows the partial suppression of Si 2*p* signal suggesting that the copper film is less than 5 nm in thickness. The 300 °C anneal results in the reappearance of the Si 2*p* spectrum and is again attributed to the uncovering of the CDO substrate due to island formation similar to the results shown in Chapter 5. These results further highlight the increased importance of an effective barrier layer between the interlayer dielectric and the interconnect in terms of preventing copper oxidation. The fact that in this CDO study it is possible to see direct evidence of the interaction of copper with the dielectric material, means that the effectiveness of the barrier layer at preventing this oxidation can be assessed. The next section of the chapter is concerned with the growth of the Mn silicate based barrier on the Aurora™ CDO.

6.4 Photoemission study of carbon depletion from ultra low-κ CDO surfaces during the growth of Mn silicate barrier layers

Curve fitted O 1*s* and Si 2*p* spectra taken from the carbon doped oxide (CDO) surface are shown in Figure 6.8. Given that the measured thickness of the CDO layer was approximately 350 nm, the Si substrate signal was not within the sampling depth of XPS. As such, the Si 2p spectrum is fitted with a single component peak at 103.5 eV, which is attributed to oxidised silicon within the CDO layer. The changes induced in these core level spectra following the deposition of ~ 1 nm of metallic Mn are also shown in Figure 6.8. Curve fitting analysis shows that the Si 2*p* spectrum is unchanged following deposition, suggesting that no Mn silicate growth occurred upon deposition in contrast to previous results seen on SiO_2 surfaces.

In agreement with this, the corresponding O 1s spectrum taken following Mn deposition shows no evidence for Mn silicate growth and is again fitted with a single component peak attributed to the CDO layer. It should also be noted that the full width at half maximum (FWHM) of the O 1s spectrum was reduced following Mn deposition, a result which may indicate the formation of a more chemically homogenous bonding environment for the oxygen on the CDO surface. Curve fitted C 1s spectra taken from the CDO surface before and after Mn deposition are shown in Figure 6.9. The C 1s spectrum taken following deposition clearly shows the growth of an additional component peak, separated from the CDO component by 2.3 eV on the lower binding energy side. This peak has been attributed to the formation of Mn-C bonds, in agreement with the relative electronegativity values of C (2.55), Si (1.90) and Mn (1.55). While the peak at 287.1 eV shows the presence of a new chemical species containing Mn-C bonds, it can be seen from the spectra in Figure 6.8 that there is no

evidence for the growth of additional component peaks in the O 1s or Si 2p spectra, with the only component peak present being that of the CDO substrate.

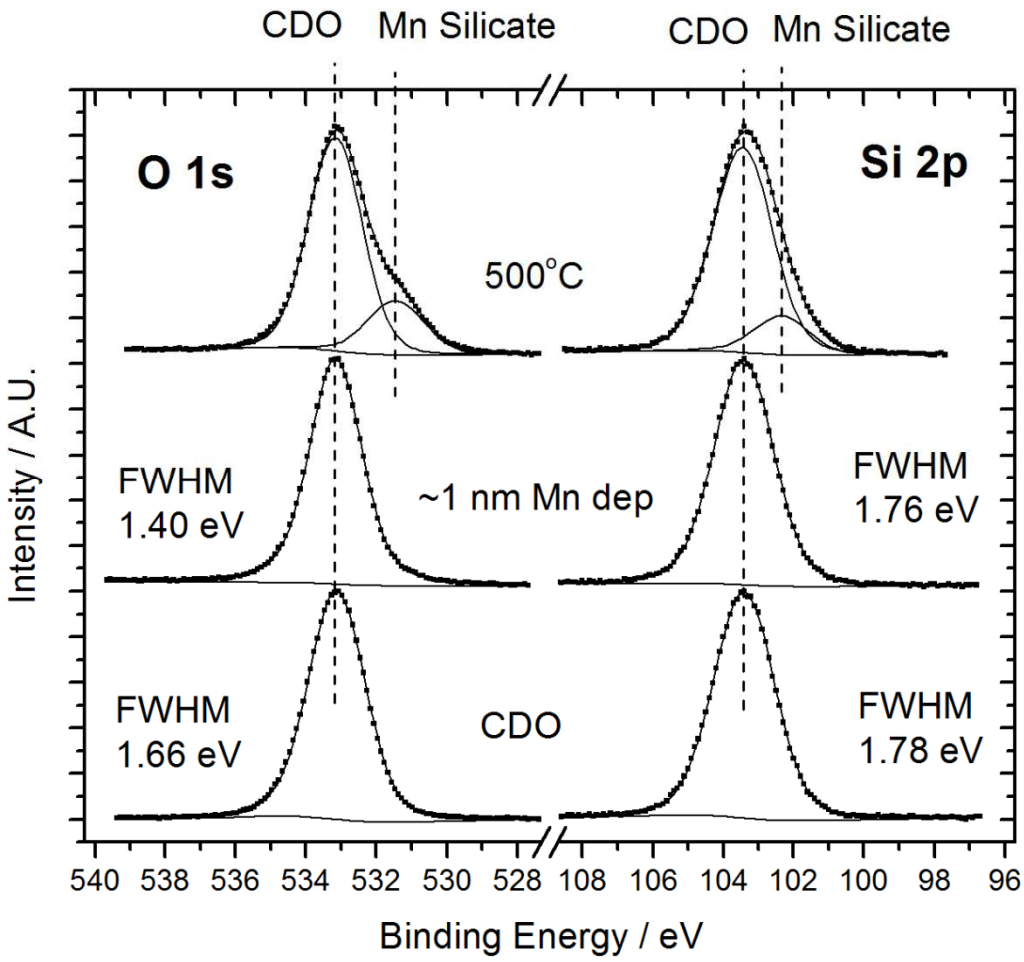

Figure 6.8 : Curve fitted O 1s and Si 2p spectra taken following the deposition of ~1 nm metallic Mn on to the CDO surface and subsequent thermal annealing to 500 °C.

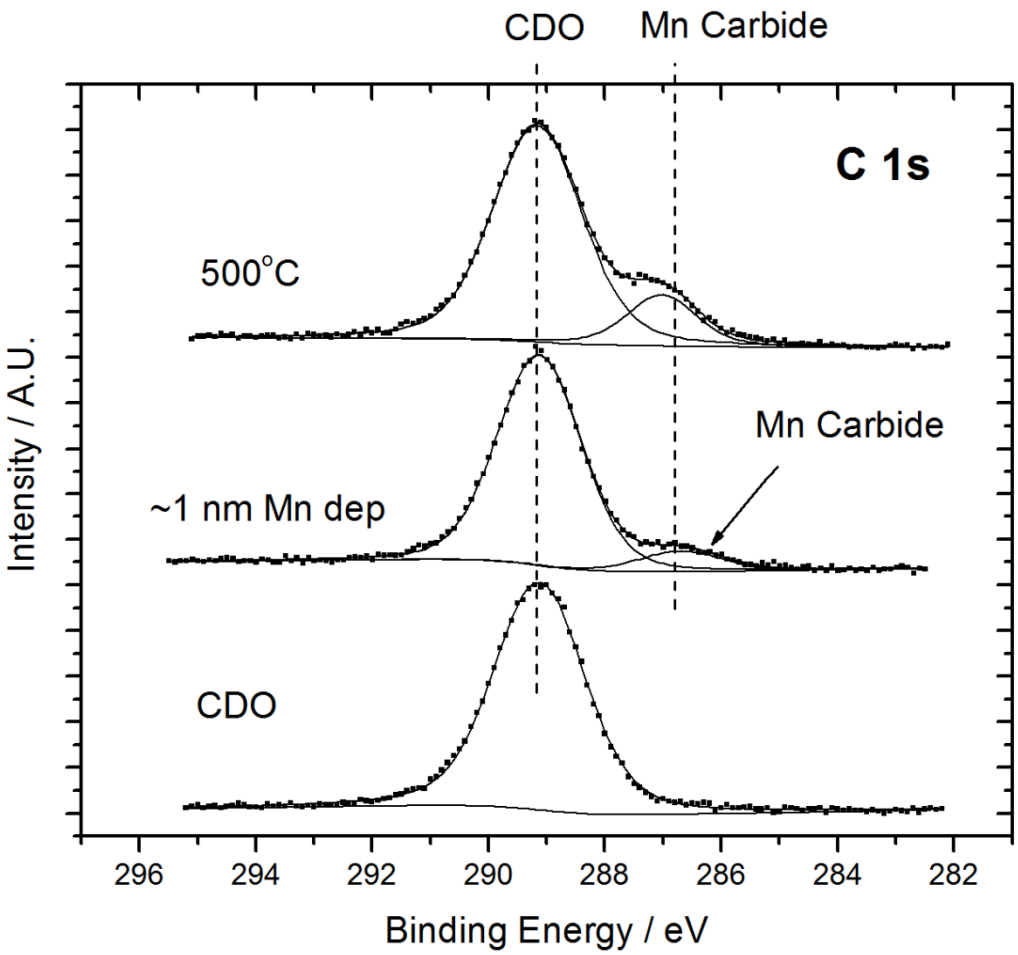

Figure 6.9 : Curve fitted C 1s spectra corresponding to Figure 6.8. The growth of an additional component peak following Mn deposition is attributed to the formation of a Mn carbide species.

Therefore, it can be concluded that no additional chemical species involving Mn-O or Mn-Si bonds have been formed following Mn deposition. As such it is suggested that the C-Mn based species identified in Figure 6.9 does not contain either O or Si. Therefore, the C 1s component peak at 282.1 eV is attributed to the formation of a manganese carbide species, due to the depletion of C from the CDO material. It should be noted that carbon is introduced into the CDO structure in the form of CH_3 [**8**][**10**] and as such hydrogen may also be present with the Mn carbide species. However, given that XPS analysis cannot be used to identify the presence of hydrogen on the surface, the exact chemical composition of this C-Mn based species has not been determined in this study,

and is therefore referred to as Mn carbide. The Mn 2p spectrum taken from the surface following Mn deposition is shown in Figure 6.10. The asymmetric peak shape is indicative of metallic Mn, suggesting either that the Mn 2p spectrum is not sensitive to chemical changes between Mn-Mn and Mn-C bonds, or alternatively that the scale of Mn carbide growth at the Mn/CDO interface was not large enough to impact on the overall profile of the Mn 2p spectrum.

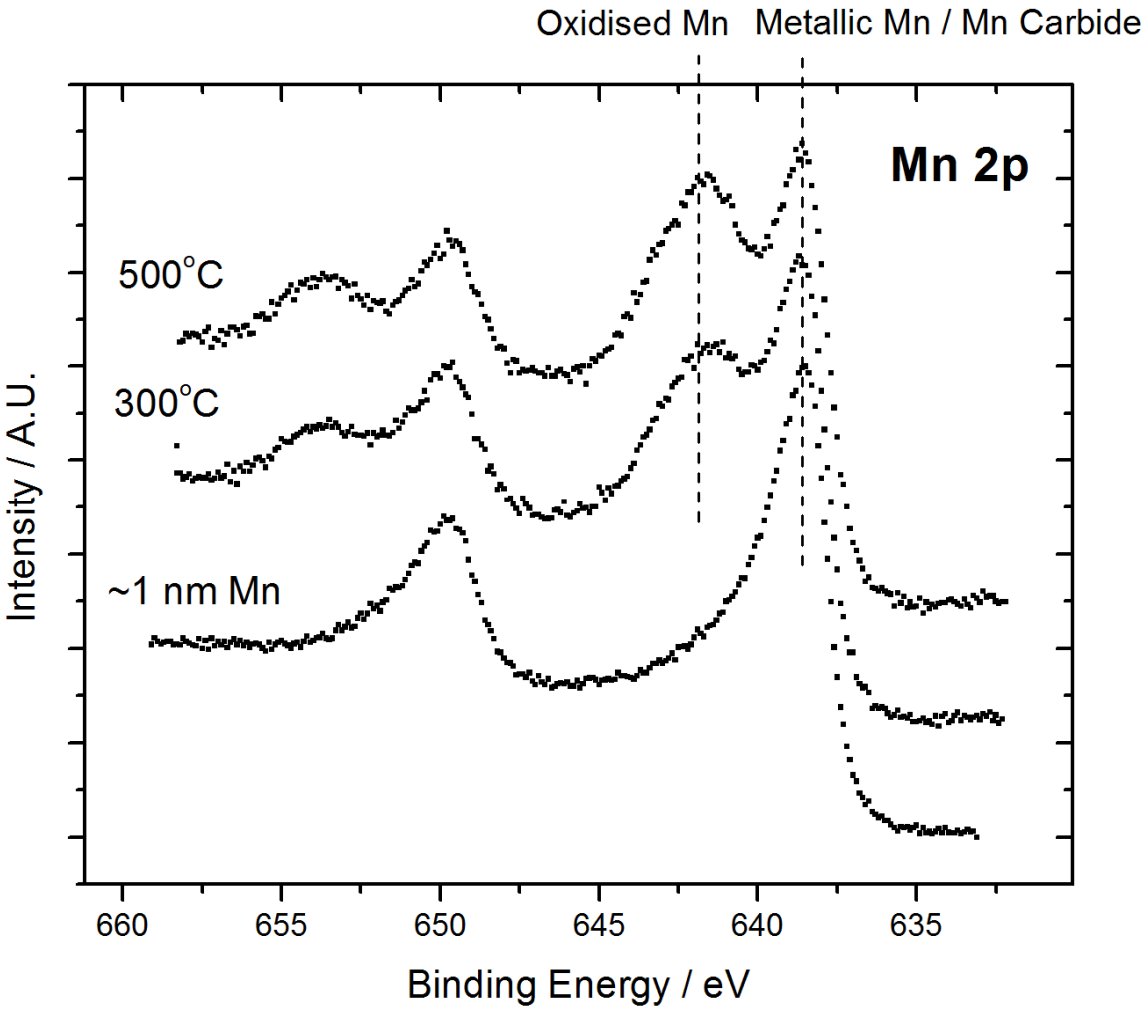

Figure 6.10 : Mn 2p spectra corresponding to Figures 6.8 and 6.9, show the presence of residual metallic Mn following 500 °C annealing suggesting that the interaction of Mn on CDO is self limiting.

The sample was then annealed to 500 °C in UHV, with curve fitted O 1s and Si 2p spectra taken following the anneal shown in Figure 6.8. These spectra show the growth

of additional component peaks in both the O 1s and Si 2p core levels separated from the substrate component peaks by 1.6 eV and 1.1 eV, respectively and are attributed to the presence of the Mn silicate species $MnSiO_3$, in agreement with previous photoemission results[**5**]. Curve fitting analysis of the Si 2p spectrum suggests that ~ 17 % of the CDO component peak was converted to Mn silicate.

The corresponding C 1s spectra in Figure 6.9 show an increase in the intensity of the Mn carbide peak following annealing, suggesting that the growth of $MnSiO_3$ results in the concurrent depletion of C from the CDO lattice. It should also be noted that the corresponding Mn 2p spectrum in Figure 6.10 shows the presence of residual metallic Mn on the surface following 500 °C anneal, indicating that the growth of $MnSiO_3$ on CDO is self limiting. Previous studies[**5**] have shown that the growth of $MnSiO_3$ on SiO_2 surfaces is limited by the presence of additional oxygen, beyond that found within the SiO_2 substrate, and that $MnSiO_3$ barrier layers of increased thickness can be formed through the deposition of partially oxidised Mn layers (MnO_x where $x < 1$) containing both metallic Mn and oxidised Mn species. In order to determine if the interaction of Mn with CDO surfaces is also self limited, the interaction of CDO with a partially oxidised Mn layer was also investigated.

Figure 6.11 shows the O 1s and Si 2p spectra taken from the CDO surface before and after the deposition of a thin (~ 1 nm) MnO_x layer. Curve fitting analysis indicates the growth of Mn silicate on the surface following MnO_x deposition, as evidenced by the growth of additional component peaks at 102.3 eV and 531.4 eV within the Si 2p and O 1s core levels respectively. The room temperature growth of Mn silicate is in contrast to results seen in Figure 6.8 and is attributed to the increased chemical reactivity of MnO_x on CDO surfaces. In addition to this, the O 1s spectrum also shows evidence for a third component peak at a binding energy position of 530.0 eV, which is attributed to the presence of Mn oxide within the deposited MnO_x film, in agreement with previous studies[**12**].

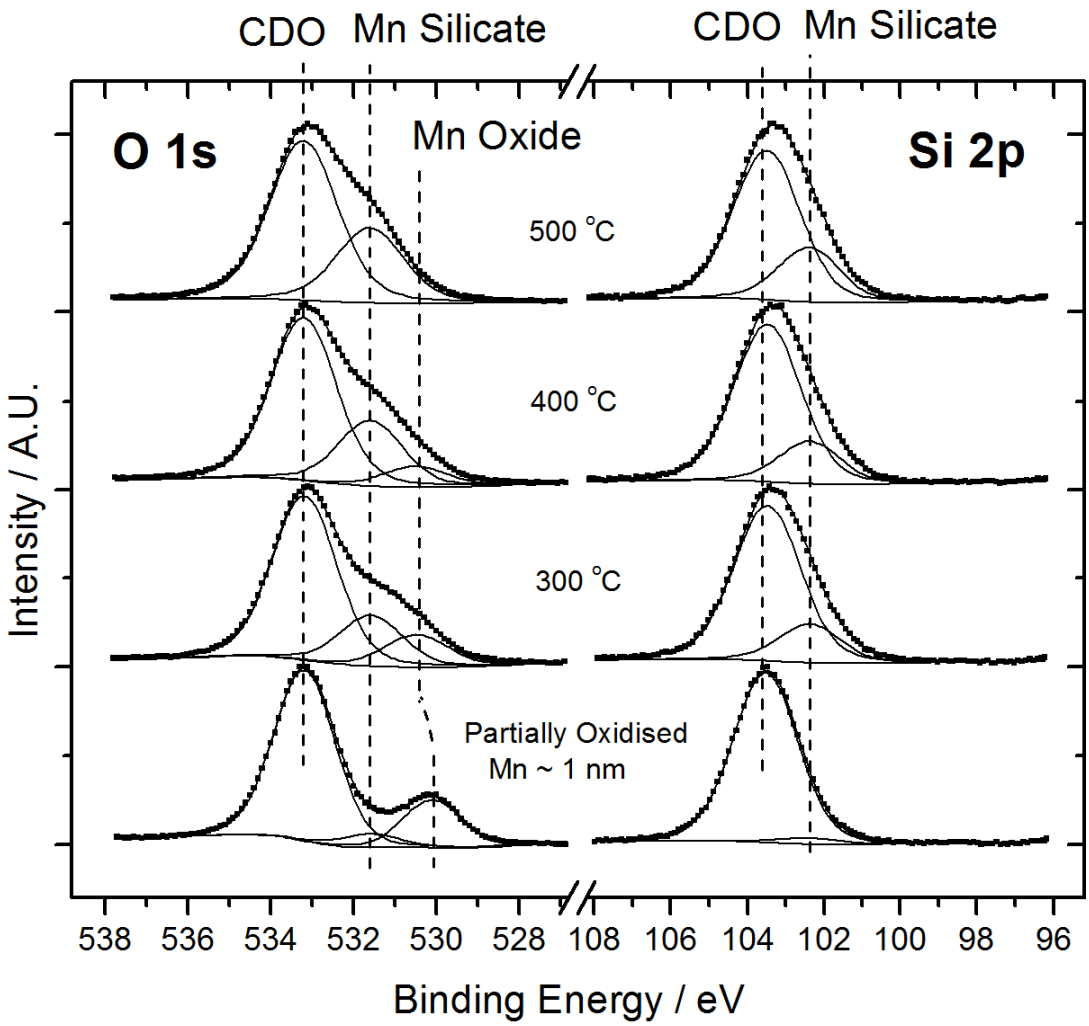

Figure 6.11 : Curve fitted O 1s and Si 2p spectra taken following the deposition of ~1 nm partially oxidised Mn layer on CDO. Spectra taken following thermal annealing show increased levels of Mn silicate growth compared to Figure 6.8 and also show the conversion of Mn oxide to silicate.

The corresponding Mn 2*p* spectrum in Figure 6.12 clearly shows the presence of both metallic Mn and oxidised Mn spectral components, with rudimentary curve fitting analysis (not shown) suggesting a metallic Mn:oxidised Mn ratio of 2:1. Angular resolved Mn 2p spectra (not shown) indicate no evidence for spatial segregation between the oxidised and metallic species, which suggests that the oxygen content is

homogenously distributed throughout the deposited film. Curve fitted C 1s spectra taken from the surface and shown in Figure 6.13 show the growth of an additional component peak at 282.1 eV following MnO_x deposition, which is again attributed to the growth of Mn carbide through the depletion of C from the CDO lattice. This result shows that Mn carbide will grow on the CDO surface following the deposition of either metallic Mn or partially oxidised Mn films.

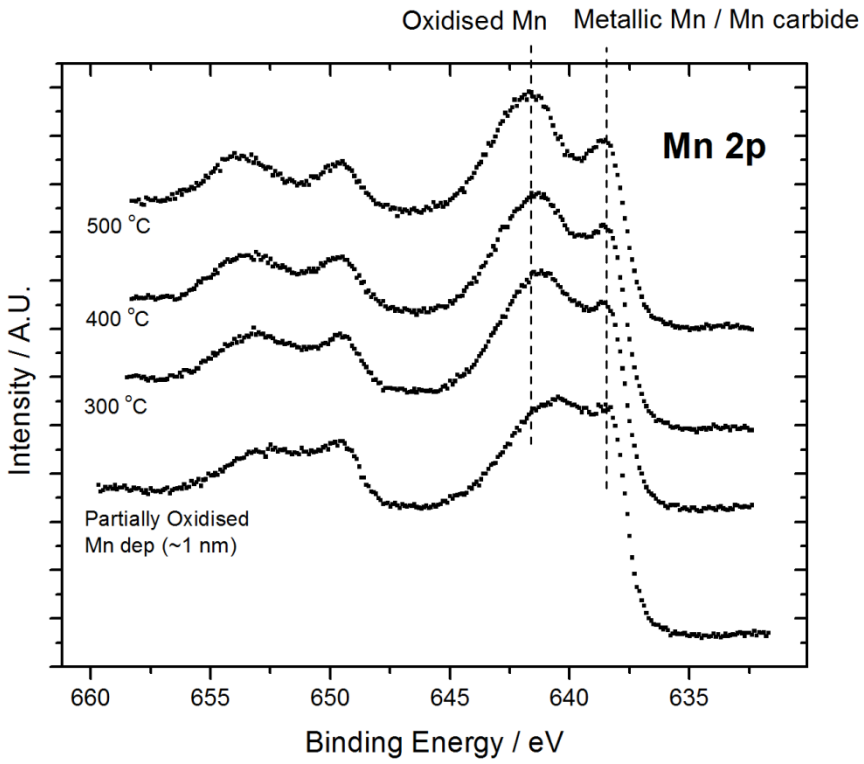

Figure 6.12 : Mn 2*p* spectra corresponding to Figure 6.11, show the presence of both oxidised Mn and metallic Mn within the deposited MnO_x layer and the conversion of Mn to Mn silicate following annealing.

A series of high temperature UHV anneals between 300 °C and 500 °C were then performed on the sample. The relevant O 1s and Si 2p spectra in Figure 6.11 show that annealing results in the formation of Mn silicate, in agreement with previous results. Spectra taken following 500 °C annealing also suggest the complete conversion of Mn oxide to Mn silicate, in agreement with previous findings on SiO_2 surfaces[**13**].

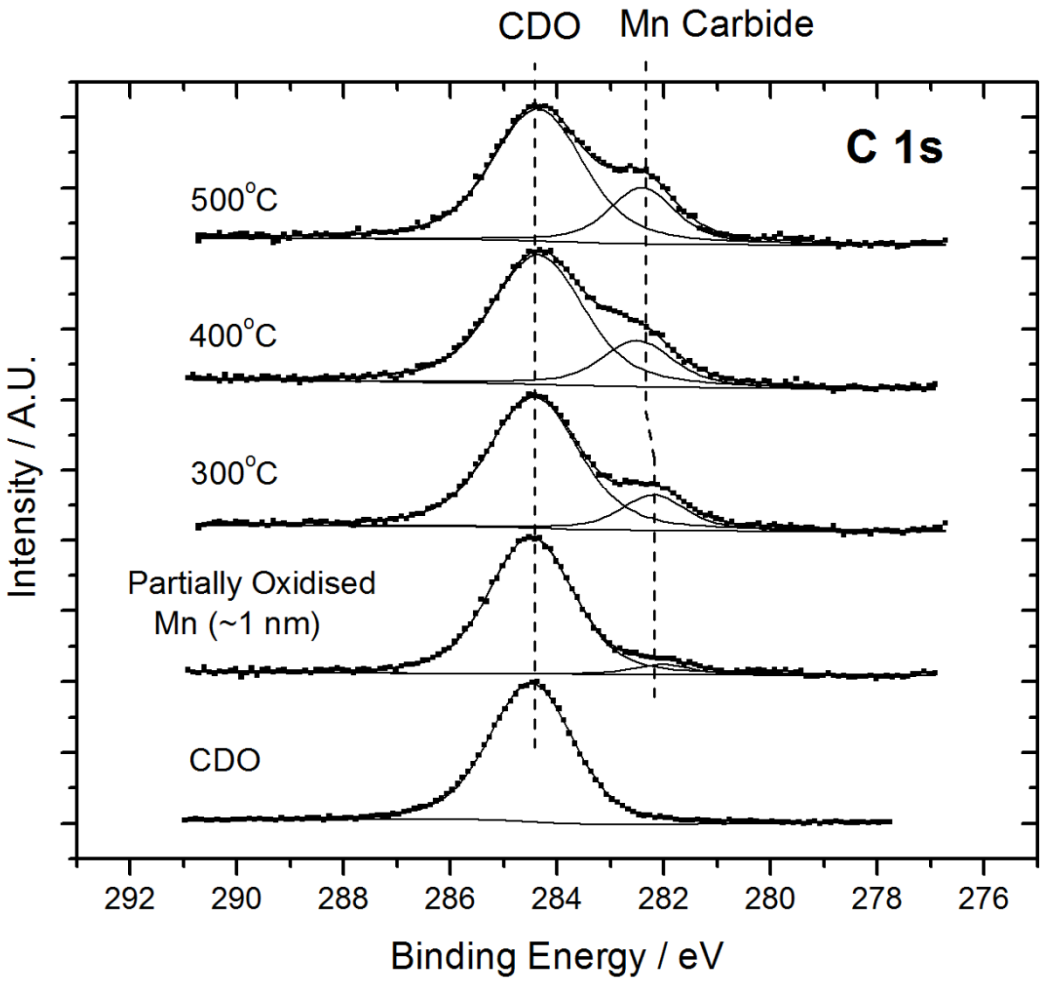

Figure 6.13 : Curve fitted C 1s spectra corresponding to Figures 6.11 and 6.12 show the formation of Mn carbide on the surface following annealing, indicating the formation of a mixed Mn silicate and Mn carbide barrier layer.

Curve fitting analysis of the Si 2p spectrum suggests that ~ 26 % of the CDO component peak was converted to Mn silicate, a value which is considerably larger than that seen following metallic Mn deposition in Figure 6.8. It is suggested that this increased thickness may be attributed to an increase in the chemical reactivity of the partially oxidised Mn species on CDO, compared to that of the purely metallic Mn film. However, the curve fitted C 1s spectra in Figure 6.13 clearly show that high temperature annealing of MnO_x thin films on CDO also results in considerable growth

of the Mn carbide species, resulting in a mixed phase Mn silicate/Mn carbide barrier layer. Given that CH_3 species are introduced into the CDO structure in order to reduce the dielectric constant of the layer [**8**], the depletion of C from the CDO during Mn carbide growth may result in an effective increase of the dielectric constant of the CDO, which is reported to have a detrimental effect on the switching speed of devices containing low-κ materials [**8**]. Therefore, it would be beneficial for the performance of the barrier layer device if the growth of Mn carbide species could be prevented during $MnSiO_3$ barrier layer formation. Given that the results of Figure 6.8 and Figure 6.11 suggest that Mn carbide growth is due to the interaction of metallic Mn and CDO, the formation of a $MnSiO_3$ barrier layer through the use of fully oxidised Mn may prevent the depletion of C from the CDO lattice. Previous results in Chapter 4 have shown that fully oxidised Mn species may be converted into $MnSiO_3$ on SiO_2 surfaces without the presence of metallic Mn. In this study, MnO_x films were deposited onto CDO surfaces and subsequently exposed to O_2 in order to investigate the interaction of CDO surfaces with fully oxidised Mn.

Figure 6.14 shows O 1s and Si 2p spectra taken before and after the deposition of ~ 1 nm of MnO_x on the CDO surface, while the corresponding C 1s and Mn 2p spectra are shown in Figure 6.16 and Figure 6.15, respectively. In agreement with the previous results of this study, the spectra in Figure 6.14, Figure 6.16 and Figure 6.15 show the presence of both metallic Mn and Mn oxide within the deposited film, along with clear evidence for the growth of $MnSiO_3$ and Mn carbide on the CDO surface.

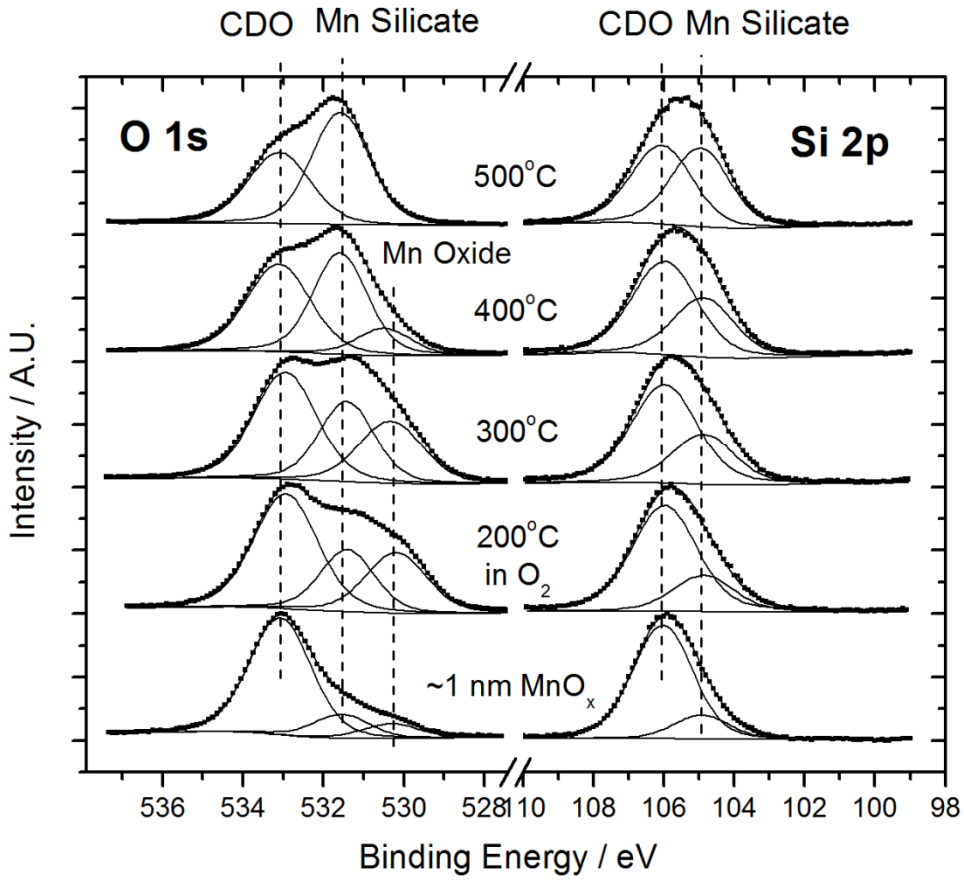

Figure 6.14 : O 1s and Si 2p spectra taken following the deposition of a ~1 nm MnOx followed by thermal annealing in an O2 partial pressure to form fully oxidised Mn. Spectra show the complete conversion of fully oxidised Mn to Mn silicate on the CDO surface following 500 °C annealing.

The sample was then annealed to 200 °C in an O_2 partial pressure of 1×10^{-7} for 1 hour, resulting in a total O_2 exposure of 360 L. The curve fitted O 1s spectrum in Figure 6.14 shows considerable evidence for the growth of Mn oxide species following O_2 annealing, as evidenced by the growth of the component peak at 530.3 eV. While this binding energy position is close to that previously attributed to the Mn oxide species MnO [**12**], the difficulty in curve fitting Mn 2*p* spectra obtained using conventional non-monochromated XPS, means that the exact stoichiometry of the Mn oxide species formed following O_2 exposure cannot be established.

However, the corresponding Mn 2p spectra in Figure 6.15 show no evidence for the presence of metallic Mn, and as such it can be clearly stated that the film is fully oxidised and free from metallic Mn. Therefore the fully oxidised Mn species may be referred to as MnO_y (where $y \geq 1$). The complete conversion of metallic Mn to Mn oxide following an O_2 exposure of 360 L is in agreement with the work of B. Lescop[**14**] who has shown that the oxidation of Mn can occur at oxygen exposure levels less than 20 L, while experiments in Chapter 4 have suggested similar findings.

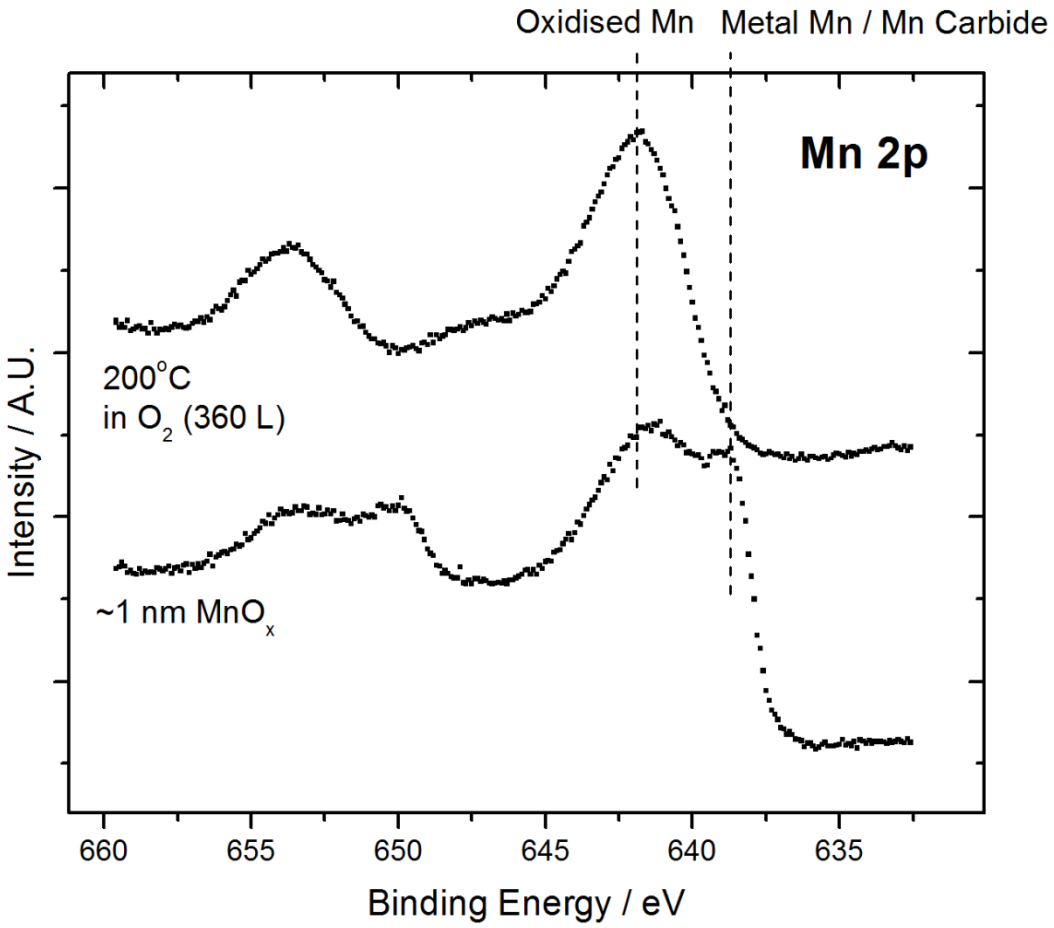

Figure 6.15 : Mn 2p spectra show no evidence for the presence of metallic Mn or Mn carbide following O2 exposure.

Along with the full conversion of metallic Mn to Mn oxide, the C 1s spectra in Figure 6.16 clearly show that O_2 exposure resulted in the removal of Mn carbide from the CDO surface which is in contrast to results seen in Figure 6.13 where the continued growth of Mn carbide species was observed following successive anneals up to 500 °C.

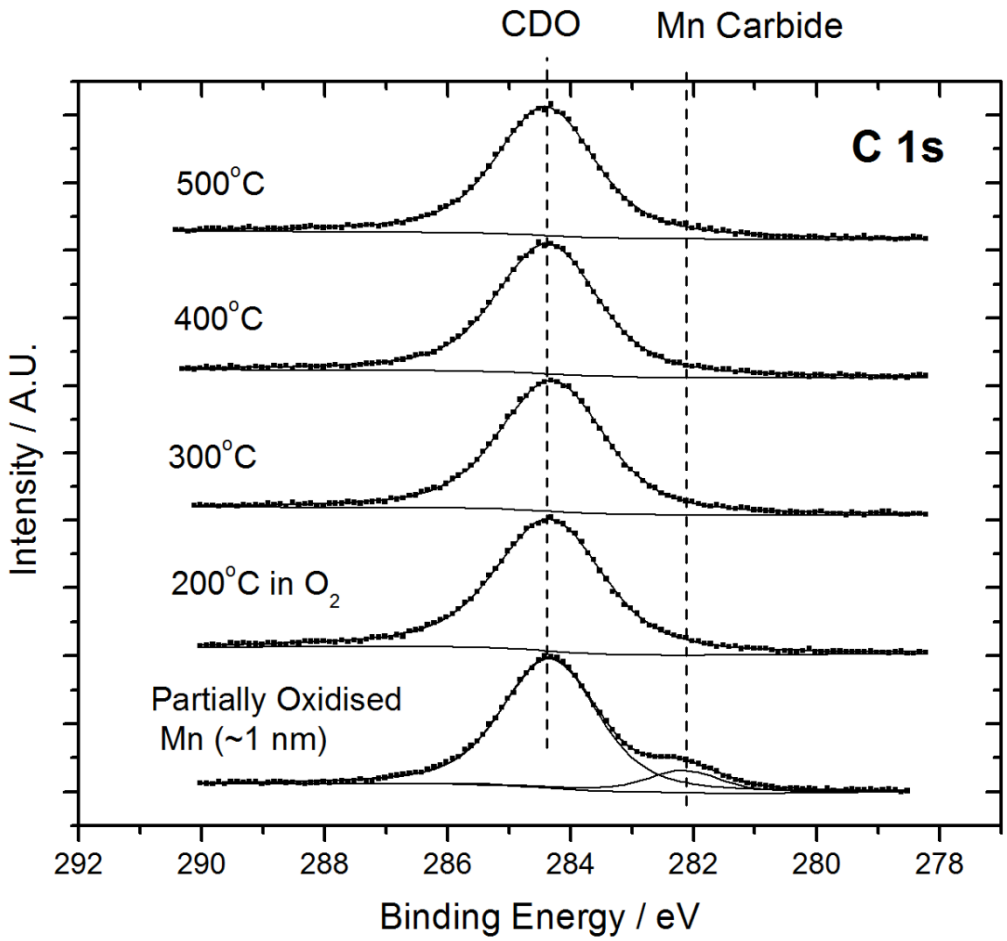

Figure 6.16 : Curve fitted C 1s spectra corresponding to Figure 6.14 show the removal of Mn carbide from the surface following oxygen exposure. Importantly there is no evidence for the regrowth of Mn carbide following high temperature annealing, suggesting that Mn carbide is not formed due to the interaction of fully oxidised Mn with CDO.

A series of high temperature UHV anneals were then performed on the sample, with XPS analysis being performed after each annealing treatment. Curve fitted O 1s and Si 2p spectra in Figure 6.14 show the conversion of Mn oxide to Mn silicate, with O 1s spectra taken after the 500 °C anneal indicating that all Mn oxide species present on the surface were converted to $MnSiO_3$. The conversion of fully oxidised Mn to $MnSiO_3$ on CDO surfaces is in agreement with previous results which have shown the growth of $MnSiO_3$ barrier layers on SiO_2 surfaces in the absence of metallic Mn. Crucially, it should be noted that C 1s spectra in Figure 6.16 show no evidence for the re-growth of Mn carbide species following high temperature annealing of fully oxidised Mn on CDO surfaces. This is in contrast to the results seen in Figure 6.9 and Figure 6.13 of this study and indicates that Mn carbide formation is due to the interaction of the metallic Mn with C groups within the CDO. Therefore, results suggest that $MnSiO_3$ barrier layers free from Mn carbide, Mn oxide and metallic Mn can be formed on CDO surfaces through the initial deposition of MnO_x, followed by the complete oxidation of metallic Mn through O_2 exposure and subsequent annealing to 500 °C. It should be noted that curve fitting analysis of the Si 2p spectrum suggests that ~ 50 % of the CDO component peak was converted to Mn silicate, suggesting the formation of a thicker Mn silicate layer than that seen from the spectra in Figure 6.8 or Figure 6.11. XPS thickness calculations [**15**] suggest the thickness of the $MnSiO_3$ layer was ~ 4.0 nm Given that peak fitting analysis [**15**] also indicates that the thickness of Mn deposited in all 3 experiments was approximately the same (~1 nm), it can be suggested that the increased $MnSiO_3$ growth in Figure 6.14 was due to the absence of Mn carbide, allowing all the deposited Mn to contribute to the formation of the barrier layer. Therefore, results of this study indicate that when Mn carbide species are formed on the surface through interaction with metallic Mn results in both the depletion of C from the CDO surface and also a reduction in the effective thickness of the $MnSiO_3$ barrier layer.

As discussed in Chapter 5, the conversion of all metallic Mn to Mn silicate before Cu deposition is crucial due to the interaction between metallic Mn and Cu [**17**]. Hence, in

order to determine the effectiveness of the barrier layer at preventing Cu oxidation, a ~2 nm Cu thin film was deposited on the fully converted $MnSiO_3$ surface. The deposition was performed at room temperature using electron beam evaporation, and the sample was subsequently annealed to 500 °C. The Cu 2*p* spectra shown Figure 6.17 taken from the surface upon deposition is identical to that taken from the 20 nm Cu reference sample, suggesting that the deposited copper film is in a purely metallic state. There was no discernable change in peak profile suggesting that no chemical interaction occurred between the $MnSiO_3$ barrier layer and the deposited Cu film. In addition to this, the Cu 2*p* spectra taken following 500 °C anneal shows no evidence for the presence of Cu oxide.

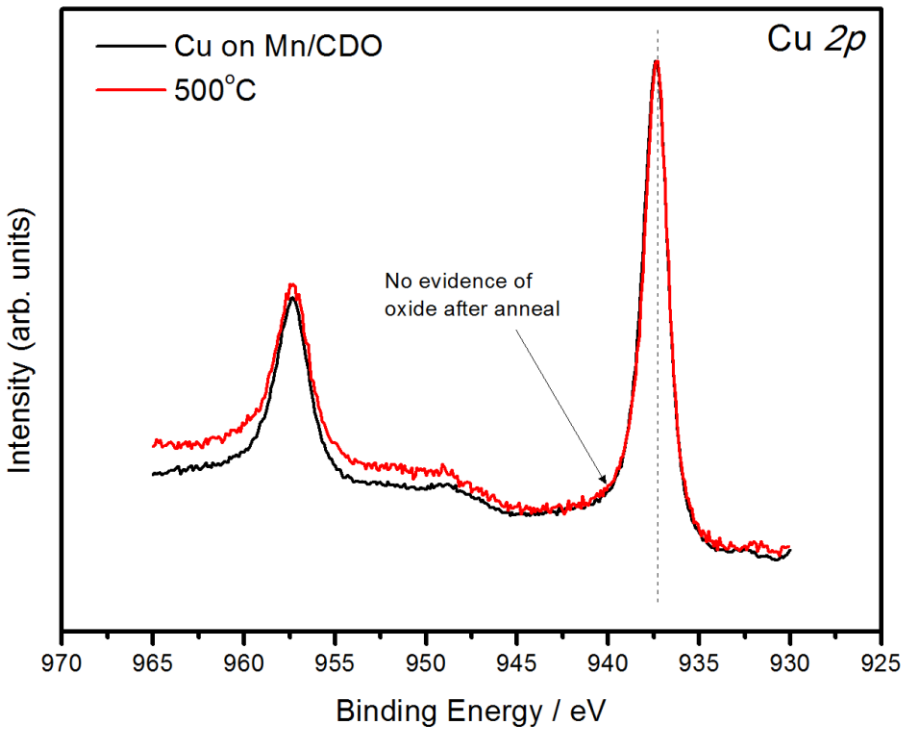

Figure 6.17: Cu 2*p* spectra showing the prevention of copper oxide formation due to the presence of $MnSiO_3$ layer.

This result is in contrast to the spectra shown in Figure 6.5 taken following the deposition of copper directly onto the CDO substrate in the absence of a barrier layer. Therefore, within the detection limits of conventional XPS it can be suggested that $MnSiO_3$ acts as an effective barrier layer to out diffusion of oxygen from the dielectric following 500 °C annealing. As previously stated this may be of significance given that one of the primary functions of the $MnSiO_3$ barrier layer is to prevent the oxidation of the Cu interconnect during thermal annealing [**18**]. Furthermore, the work of Willis *et al* [**17**] has suggested that the formation of Cu oxide acts as an intermediate step in the diffusion mechanism of Cu through SiO_2.

6.5 Conclusions

In the first section of this chapter it was shown that the deposition and subsequent thermal anneal of metallic Cu on CDO results in the formation of Cu islands on the surface, similar to previous experiments carried out on SiO_2 which were described in Chapter 5. However, unlike experiments on SiO_2, the growth of copper oxide is seen following thermal anneal which is attributed to the breaking of Si-O bonds which may lead to increase in dielectric constant of the CDO, and diffusion of Cu ions into the dielectric material causing decrease in performance within the device.

In the second section of the study, the growth of Mn silicate barrier layers on ultra low-κ carbon doped oxide (CDO) surfaces has been investigated through interaction with metallic Mn, partially oxidised Mn (MnO_x where $x < 1$) and fully oxidised Mn (MnO_y where $y \geq 1$) films. The deposition studies of metallic Mn and MnO_x layers have shown that the presence of metallic Mn on CDO surfaces results in the formation of Mn-C bonds. This result is attributed to the growth of a Mn carbide species on the surface, free from O and Si. Therefore it is suggested that the growth of Mn carbide may result in the depletion of C from the CDO surface, which is reported to cause an increase in the effective dielectric constant of the CDO layer. In a separate experiment a ~1 nm MnO_x was deposited and subsequently exposed to 360 L of O_2, resulting in the complete oxidation of metallic Mn and also the removal of Mn carbide species from the surface. High temperature UHV annealing studies have shown that this fully oxidised Mn film can be converted to form a $MnSiO_3$ layer with a thickness of ~ 4.0 nm on the CDO surface, with no evidence of Mn carbide bond formation. In agreement with the previous results on SiO_2 surfaces, XPS analysis has also shown that the growth of $MnSiO_3$ on the CDO surfaces is limited by the presence of additional oxygen species, beyond that found within the CDO substrate.

Finally, as a simple test of barrier effectiveness it was shown that deposition of Cu on a pre-formed manganese silicate layer results in a film free of Cu oxide after 500 °C anneal suggesting effective barrier formation.

6.6 References

[1] Y. Otsuka, J. Koike, H. Sako, K. Ishibashi, and N. Kawasaki, "Graded composition and valence states in self forming barrier layers at Cu-Mn/SiO2 interface," *Appl. Phys. Lett*, vol. 96, no. 012101, Jan. 2010.

[2] J. Koike and M. Wada, "Self-forming diffusion barrier layer in Cu-Mn alloy metallization," *Appl. Phys. Lett*, vol. 87, no. 041911, Jul. 2005.

[3] J. M. Ablett, J. C. Woicik, Z. Tokei, and S. List, "Phase identification of self-forming Cu-Mn based diffusion barriers on p-SiOC:H and SiO2 dielectrics using x-ray absorption fine structure," *Appl. Phys. Lett.*, vol. 94, no. 042112, Jan. 2009.

[4] C. J. Wilson, et al., *Microelectron Eng.*, vol. 87, no. 398, 2010.

[5] Z. Tokei, K. Croes, and B. G. P., *Microelectron Eng.*, vol. 87, no. 348, 2010.

[6] F. Y, R. Wolters, H. Roosen, J. H. M. Snijders, and R. Hoofman, *Microelectron Eng.*, vol. 76, no. 25, 2004.

[7] Y. Ohoka, et al., in *International Interconnect Technology Conference IEEE 67*, 2007.

[8] I. Reid, Y. Zhang, A. DeMasi, G. Hughes, and K. E. Smith, *Thin Solid Films*, vol. 516, no. 4851, 2008.

[9] M. O. Krause and J. G. Ferreira, *J. Phys. B: At. Mol. Phys.*, vol. 8, no. 12, 1975.

[10] B. G. Willis and D. V. Lang, "Oxidation mechanism of ionic transport of copper in SiO2 dielectrics," *Thin Solid Films*, no. 467, pp. 284-293, Apr. 2004.

[11] A. A. Audi and P. M. Sherwood, "Valence-band x-ray photoelectron spectroscopic studies of manganese and its oxides interpreted by cluster and band structure calculations," *Surf. Interface Anal.*, vol. 33, pp. 274-282, Dec. 2001.

[12] V. K. Dixit, N. Neishi, N. Akao, and J. Koike, *IEEE Trans. Device Mater. Reliab.*, vol. 11, no. 295, 2011.

[13] B. Lescop, *Appl. Surf. Sci*, vol. 252, no. 2276, 2006.

[14] M. P. Seah and S. J. Spencer, "Ultrathin SiO2 on Si II. Issues in quantification of the oxide thickness ," *Surf. Interface Anal.*, vol. 33, pp. 640-652, May 2002.

[15] U. Manju, D. Topwal, G. Rossi, and I. Vobornick, "Electronic structure of the two-dimensionally ordered Mn/Cu(110) magnetic surface alloy," *Phys. Rev. B*, vol. 82, no. 035442, Jul. 2010.

[16] R. G. Gordon and H. Kim, "Self-Aligned Barrier Layers for Interconnects," U.S. Manufacturing WO 2009/117670 A2, Sep. 24, 2009.

Chapter 7

Conclusions and Future Work

7.1 Conclusions

In this study the use of Mn silicate as an interconnect barrier layer material in copper based microelectronic interconnect, has been investigated. While the main focus of the work has been the use of x-ray photoelectron spectroscopy to analyse the Mn/interlayer dielectric interface formation, other techniques such as TEM and AFM have also been employed.

7.1.1 Mn silicate formation on SiO_2

In Chapter 4, synchrotron radiation photoelectron spectroscopy (SRPES) was used to investigate the *in-situ* formation of ultra thin Mn silicate layers on SiO_2, which has relevance for copper diffusion barrier layers in microelectronic devices. High temperature vacuum annealing of metallic Mn (~ 1.5 nm) deposited on a 5.4 nm thermally grown SiO_2 film resulted in the self limiting formation of a manganese silicate layer, the stoichiometry of which is consistent with the formation of $MnSiO_3$. Curve fitted Mn $3p$ SRPES spectra showed no evidence for the presence of a manganese oxide phase at the Mn/SiO_2 interface, in contrast to previous reports [**1**].

Subsequently, Mn silicate ($MnSiO_3$) barrier layers were formed on thermally grown SiO_2 using both metallic Mn and oxidized Mn films, in order to investigate the role of oxygen in determining the extent of the interaction between the deposited Mn and the SiO_2 substrate. Using X-ray photoelectron spectroscopy (XPS) it has been shown that a metallic Mn film with an approximate thickness of 1 nm cannot be fully converted

to Mn silicate following vacuum annealing to 500 °C. Transmission electron microscopy (TEM) analysis suggests the maximum $MnSiO_3$ layer thickness obtainable using metallic Mn is ~ 1.7 nm. In contrast, a ~ 1 nm partially oxidized Mn film can be fully converted to Mn silicate following thermal annealing to 400 °C, forming a $MnSiO_3$ layer with a measured thickness of 2.6 nm. TEM analysis also clearly shows that $MnSiO_3$ growth results in a corresponding reduction in the SiO_2 layer thickness. It has also been shown that a fully oxidized Mn oxide thin film can be converted to Mn silicate, in the absence of metallic Mn. Based on these results it is suggested that the presence of Mn oxide species at the Mn/SiO_2 interface facilitates the conversion of SiO_2 to $MnSiO_3$, in agreement with previously published studies [**2**].

7.1.2 The role of copper in Mn silicate formation

In Chapter 5, the introduction of copper into the barrier layer stack was investigated using a variety of techniques. XPS and AFM analysis indicates that the high temperature vacuum annealing of metallic Cu (~ 7 nm) deposited on a 5.4 nm thermally grown SiO_2 film results in the formation of Cu islands highlighting the adhesion problem inherent to copper interconnects [**3**] [**4**].

In the second section of Chapter 5, Mn/Cu heterostructures were thermally evaporated onto SiO_2 and subsequently annealed before being investigated by TEM related techniques in order to study the diffusion interactions which lead to barrier layer formation. Energy dispersive x-ray spectroscopy and electron energy loss spectroscopy provide evidence for the interdiffusion between the Mn and Cu layers following a 450 °C anneal, where the Mn diffuses toward the surface of the structure, while Cu diffuses toward the Mn/SiO_2 but does not propagate into the dielectric. The chemical composition of the 2–3 nm interfacial layer is primarily a mixture of +2 and +3 Mn valences, in agreement with previously reported results [**5**].

Finally in this chapter, XPS was used to investigate the effect of copper on the chemical composition of barrier layers formed on SiO_2 through the deposition of

partially oxidised Mn (MnO_x), sequential layers of MnO_x and Cu, and also through the deposition of MnO_x/Cu alloys. It has been shown that Mn silicate ($MnSiO_3$) barrier layers, free from Mn oxide and metallic Mn, can be formed on SiO_2 surfaces through the deposition of MnO_x and annealing to 400 °C. However, it has also been shown that when Cu is present at the MnO_x/SiO_2 interface during $MnSiO_3$ growth, Mn oxide species are also formed within the barrier. The chemical stability of a ~ 1 nm Cu film on $MnSiO_3$ barrier layers was also investigated, with results suggesting that no chemical interaction occurs between Cu and $MnSiO_3$ following 400 °C annealing. The barrier layer properties of $MnSiO_3$ thin films have also been investigated using electron energy loss spectroscopy (EELS), with results suggesting that a $MnSiO_3$ layer with thickness of ~ 3 nm acts as an effective barrier layer to Cu diffusion following 400 °C annealing.

7.1.3 Mn silicate barrier formation on low-k dielectric layers

The final studies in the thesis dealt with the growth of Mn silicate ($MnSiO_3$) barrier layers on ultra low dielectric constant (ULK) carbon doped oxide (CDO) surfaces. High temperature vacuum annealing of metallic Cu (~ 2 nm) deposited on a 5.4 nm thermally grown SiO_2 film resulted in the formation of copper oxide, attributed to the breaking of Si-O bonds which may lead to increase in dielectric constant of the CDO and the diffusion of Cu ions into the interlayer dielectric.

Mn silicate barriers were then grown on Aurora™ CDO samples, using both metallic Mn and oxidized Mn films, in order to determine the growth method best suited to preventing the depletion of carbon from the CDO surface. Using x-ray photoelectron spectroscopy (XPS) it has been shown that deposition of metallic Mn and partially oxidised Mn (MnO_x where $x < 1$) films on CDO surfaces results in the formation of both $MnSiO_3$ and a Mn carbide species within the barrier layer region. Analysis suggests that Mn carbide species are formed through the depletion of C from the CDO structure, which may increase the dielectric constant of the CDO. In a separate

experiment it was shown that the interaction of a fully oxidised Mn (MnO_y where $y \geq 1$) layer on CDO resulted in the growth of a $MnSiO_3$ barrier layer free from Mn carbide, metallic Mn and Mn oxide. These studies indicate that Mn carbide is only formed on CDO surface in the presence of metallic Mn and will not occur through the interaction of CDO with fully oxidised Mn layers. It has also been shown that the growth of $MnSiO_3$ layers on CDO is self-limited by the availability of additional oxygen, beyond that found within the CDO layer, in agreement with the previous studies on SiO_2 surfaces. Finally, it was shown that deposition of Cu on a pre-formed manganese silicate layer on the CDO substrate results in a film free of Cu oxide after 500 °C anneal suggesting effective barrier formation.

7.2 Future Work

The primary aspects arising from this study which require further investigation are outlined as follows.

7.2.1 Further optimisation of the growth of Mn silicate

In Chapter 4 the growth and characterisation of Mn silicate ($MnSiO_3$) on SiO_2 was outlined. The use of additional oxygen beyond that within the substrate was shown to assist in the growth of the silicate layer. However, further investigations into the optimisation of the $MnSiO_3$ are worthy of additional study. A possible method of driving silicate formation which could be investigated would be the use of a controlled supply of oxygen during the barrier formation process. This may determine whether the thickness of the barrier layer may be increased above 3 nm.

Also, while Chapter 5 discussed the introduction of copper into the barrier layer stack, further segregation studies into binary Cu/Mn alloys using TEM on thicker Cu/Mn layers are currently being pursued.

7.2.2 Electrical Characterization of Mn silicate barrier layers

The chemical and structural analysis techniques used in both Chapter 5 and Chapter 6 suggest that ultra-thin Mn silicate layers act as an effective barrier to copper diffusion following thermal anneal. However, the ultimate effectiveness of copper diffusion barriers can only be fully determined using electrical characterisation in the presence of an applied electric field [**2**]. Previous publications have shown that capacitance-voltage (C-V) and current-voltage (I-V) sheet resistance measurements may be used to determine if the resistance of copper interconnects has been altered by the diffusion of Cu into the underlying dielectric layer [**6**].

Initial studies addressing this particular aspect may simply consist of electrical measurements to quantify the resistivity of thin Mn silicate barrier layers and of

blanket Mn/Cu alloy films. The four-point probe technique could be used with a view to monitoring any change in resistivity in the overlying alloy layer due to the migration and incorporation of the Mn from the alloy, to the dielectric interface after thermal anneal.

Further electrical characterisation can then be carried through the fabrication of capacitor structures on various dielectric materials with differently formed barrier layers. C-V measurements may be employed in order to determine the barriers effectiveness at preventing copper diffusion both after thermal anneal and, upon application of electrical stress.

7.2.3 Challenges relating to TEM analysis

Throughout the course of this work various challenges arose with regards to the use of transmission electron microscopy (TEM) to study the barrier region in cross section. Both Chapter 4 and Chapter 5 successfully utilised TEM analysis of deposited Mn layers in the presence of copper, both as a capping layer in order to prevent oxidation, and as an integral part of the layered structure respectively. However, any TEM characterization of ultrathin Mn layers in the absence of the thick Cu capping layer proved to be especially difficult to analyse, as the thin metallic Mn layers have proven to be particularly radiation sensitive at high beam voltages used in high resolution imaging. It is suggested that the reason for this problem in the absence of a copper layer is due to the Cu acting as heat dissipation path for the electron beam. The possible solution suggested to solve this problem is the use of a lower voltage electron beam (80 kV) with a corresponding loss of signal and resolution.

Another issue faced with regard to TEM analysis was encountered in the attempted characterization of Mn silicate barrier layers on the CDO substrates detailed in Chapter 6. In contrast to results on SiO_2, Cu and Mn are difficult to detect on CDO substrates and no layered structure is visible. These results are in contradiction with XPS experiments which clearly indicate successful deposition of both Mn and Cu

layers. It is therefore suggested that this problem may be due to an adhesion problem between the metal layers and the CDO substrate. A possible solution to this problem may be the use of focussed ion beam (FIB) during TEM sample preparation. If this issue is addressed, the same methodology successfully used during barrier formation on SiO_2 substrates may be applied for the TEM characterization of diffusion barriers on CDO substrates from thin Mn layers and Cu/Mn alloys.

With regard to the basic diffusion processes which result in the formation of the barrier layers from alloy Mn/Cu composition layer, a heating stage in the 4000EX TEM microscope would allow the *in-situ* observation and TEM analysis of the formation of the barrier layer on both SiO_2 and low-κ substrates.

Finally, the utilisation of a scanning confocal electron microscope (SCEM) may allow the 3-dimensional characterization of the diffusion barrier layer structures. This technique is suitable for the 3D reconstruction of laterally extended objects, as opposed to conventional STEM tomography and is under development on the double aberration corrected microscope at Oxford University.

7.2.4 Barrier formation on industrially relevant CDO

Chapter 6 of the thesis dealt exclusively with the formation and chemical characterisation of Mn silicate barriers on a prototype ULK carbon doped oxide. However, if Mn silicate is to be used as the diffusion barrier in future devices then the interactions between Mn and other more industrially relevant CDO substrates must also be investigated.

Using a similar methodology to that successfully employed on the Aurora™ substrates, further investigations into silicate formation on a more technologically relevant lower carbon content CDO are required to understand the impact of the presence of carbon on the nature of chemical interactions resulting in manganese silicate formation at the interface. Also, the controlled removal of any surface carbon in

order to prevent the growth of Mn carbide species may be achieved via an oxygen plasma treatment of the CDO surface before Mn deposition.

Finally, further Mn deposition and barrier formation studies need be undertaken using a variety of industrially relevant CDO substrates such as porous CDO and porous CDO with pore sealants which present many material challenges.

7.2.5 Alternative barrier layer materials

While this thesis deals exclusively with the use of manganese as a barrier layer material, several other elements have attracted research attention within the field [**7**] [**8**] [**9**] [**10**]. For example, recent publications have suggested the use of ruthenium as another possible barrier candidate due to its excellent adhesion to the Cu layer, high thermal stability, and the ease of electrodeposition of copper on Ru [**8**]. Titanium has also been suggested due to its favourable adhesion properties and its marked improvement in resistivity over conventional Ta/TaN barrier layers [**7**].

Future investigations into the use of these materials as barrier layer alternatives, both on their own, and as an alloying element in a barrier layer stack need be carried out using the same approach successfully applied in this study of the interactions of Mn with dielectric materials.

.

7.3 References

[1] S. ,. M. Chung and J. Koike, "Analysis of dielectric constant of a self-forming barrier layer with Cu-Mn alloy on TEOS-SiO2," *J. Vac. Sci. Technol, B.*, no. 27, p. 28, Sep. 2009.

[2] R. G. Gordon and H. Kim, "Self-Aligned Barrier Layers for Interconnects," U.S. Manufacturing WO 2009/117670 A2, Sep. 24, 2009.

[3] T. Waechtler, S. Oswald, and N. Roth, "Copper Oxide Films Grown by Atomic Layer Deposition from Bis copper acetylacetonate on Ta, TaN, Ru, and SiO2," *Journal of The Electrochemical Society*, no. 156, pp. 453-459, Apr. 2009.

[4] R. Saxena, M. J. Frederick, G. Ramanath, W. N. Gill, and J. L. Plawsky, "Kinetics of voiding and agglomeration of copper nanolayers on silica," *Phys Rev B.*, no. 72, pp. 1-7, Sep. 2005.

[5] J. M. Ablett, J. C. Woicik, Z. Tokei, and S. List, "Phase identification of self-forming Cu-Mn based diffusion barriers on p-SiOC:H and SiO2 dielectrics using x-ray absorption fine structure," *Appl. Phys. Lett.*, vol. 94, no. 042112, Jan. 2009.

[6] J. Iijima, Y. Fujii, K. Neishi, and J. Koike, "Resistivity reduction by external oxidation of Cu-Mn alloy films for semiconductor interconnect application," *J. Vac. Sci. Technol., B*, vol. 27, no. 4, pp. 1963-1968, Jul. 2009.

[7] K. Kohama, K. Ito, and Y. Sonobayashi, "Structure Analyses of Ti-Based Self-Formed Barrier Layers," *Japanese Journal of Applied Physics*, no. 50, pp. 1-5, Apr. 2011.

[8] T. N. Arunagiri, Y. Zhang, and O. Chyan, "5 nm ruthenium thin film as a directly plateable copper diffusion barrier," *Applied Physics Letters*, no. 86, pp. 1-4, Feb. 2005.

[9] C. J. Liu and J. S. Chen, "Low leakage current Cu(Ti)/SiO2 interconnection scheme with a self-formed TiO diffusion barrier," *Applied Physics Letters*, vol. 80, Apr. 2002.

[10] B. H. Choi, Y. H. Lim, J. H. Lee, and Y. B. Kim, "Preparation of Ru thin film layer on Si and TaN/Si as diffusion barrier by plasma enhanced atomic layer deposition," *Microelectronic Engineering*, vol. 87, Dec. 2010.